Habib, Rabeeah (2022) *On the dynamics of heat transfer and combusting flows in porous media*. PhD thesis.

http://theses.gla.ac.uk/83182/

On the dynamics of heat transfer and combusting flows in porous media

Rabeeah Habib

Submitted in fulfilment of the requirements for the Degree of Doctor of Philosophy in Mechanical Engineering

School of Engineering

College of Science and Engineering

University of Glasgow

January 2022

This thesis is dedicated to my parents and my brothers

for their continuous love and support.

Abstract

Dynamics of heat transfer and combusting flows has attracted increased attention in porous media in recent years. A growing number of technologies require prediction of unsteady forced convection in porous media when the inlet flow is unsteady. Also, in practical combustion systems fluctuations in the fuel flow rate can occur and result in flame destabilisation, in particular in lean and ultra-lean modes of operation. This is due to heat transfer being dominant in combusting flows in porous media. To address these challenges a joint numerical and experimental approach is adopted.

A numerical study of heat convection response of a reticulated porous medium to the harmonic and ramp disturbances in the inlet flow is investigated taking a pore-scale approach. The developed model consists of ten cylindrical obstacles aligned in a staggered arrangement with set isothermal boundary conditions. A few types of fluids, along with different values of porosity and Reynolds number, are considered. Assuming laminar flow, the system is first modulated by sine waves superimposed on the inlet flow velocity, and the spatio-temporal responses of the flow and temperature fields are calculated. The results are then utilised to assess the linearity of the thermal response represented by the Nusselt number on the obstacles. In general, it is found that for low Reynolds numbers, the dynamics of heat convection can be predicted decently by taking a transfer function approach. However, the dynamical relations between the inlet flow fluctuations as the input and those of Nusselt number as the output, can be non-linear. Second, the thermal system is subject to a ramp disturbance superimposed on the entrance flow temperature/velocity. A response lag ratio (RLR) is defined to further characterise the transient response of the system. The results reveal that an increase in amplitude increases the RLR and interestingly, the Reynolds number has almost negligible effects upon RLR.

An experimental investigation is undertaken to examine the response of ultra-lean flames, stabilised in a porous burner, to the fluctuations imposed on the fuel flow rate. The employed porous burner includes layers of silicon carbide porous foam placed inside a quartz tube. The burner is equipped with a series of axially arranged thermocouples and is imaged by a digital camera. The fuel streams are measured and controlled separately by programmable mass flow controllers, which impose sinusoidal fluctuations with variable amplitude and frequency on the steady flow. To replicate realistic fluctuations in the fuel flow rate, the period of oscillations is chosen to be in the order of minutes. The flame embedded in porous media is imaged while the fuel flow is modulated. First, methane and blends of methane and carbon dioxide (mimicking biogas) are mixed with air and then fed to the burner at equivalence ratios below 0.3. Amplitude of the flame oscillations for methane is found to be higher than that for biogas. Further, it is observed that exposure of the burner to the fuel fluctuations for a long time (180s) eventually results in flame destabilisation. In a separate set of experiments, the hydrogen and methane blends are premixed with air at equivalence ratios below 0.275 and fed to the porous burner. It is found that fuel mixtures are noted to be rather insensitive to hydrogen flow fluctuation with a modulation amplitude below 30% of the steady flow. This study reveals the strong effects of unsteady heat transfer in porous media upon the fluctuations in flame position.

Table of Contents

List of Tables

List of Figures

Acknowledgements

First and foremost, I would like to thank Allah - the infallible teacher and the supreme solver – for granting me this noble opportunity to pursue a PhD.

I would like to express my sincere gratitude to my supervisors, Dr Nader Karimi, Dr Bijan Yadollahi and Dr Andrea Cammarano for their invaluable guidance, continuous support throughout my PhD.

I cannot begin to express my thanks to Dr Nader Karimi, who's enthusiasm, motivation, and vast wealth of knowledge has deeply inspired me. I have faced numerous obstacles and challenges throughout the course of my PhD but your cool, calm, and kind nature has always been a beacon of hope to get me through difficult times. You have played a key role in my personal development for which I will be forever grateful. It has been an honour and privilege.

I would also like to thank Ali Saeed for being an exceptional lab assistant and friend for the duration of my experiment. Your attention to detail and quick learning abilities have played a monumental role in the success of my experiment. This experiment could not have become functional without the safety expertise and technical knowledge of Colin Roberts and David Carr to whom I am particularly grateful.

I am elated to thank my fellow colleagues for their support and encouragement. A special thanks to Dr Graeme Hunt, Dr Loizos Christodoulou, Dr Tata Sutardi and Dr Linwei Wang. A big thank you to my friends who supported me throughout my doctorate studies. Azhar Sheikh, Sara Khan, Sohaib Ashraf and Hassan Khalid – Thank you

Finally, I would like to thank my parents, my family and my wife for their continued love, support and encouragement, without which I wouldn't be where I am today.

Declaration

The author confirms that the work presented in this thesis is the results of the author's own research. This thesis is composed by the author. The standard referencing practices are applied to any ideas or techniques from published works.

X

Rabeeah Habib - January 2022

Publications stemming from this work

Journal Papers

R. Habib, N. Karimi, B. Yadollahi, M.H. Doranehgard, L.K.B. Li, A pore-scale assessment of the dynamic response of forced convection in porous media to inlet flow modulations, *International Journal of Heat and Mass Transfer*. 153 (2020) 119657. https://doi.org/10.1016/j.ijheatmasstransfer.2020.119657.

R. Habib, B. Yadollahi, N. Karimi, M.H. Doranegard, On the unsteady forced convection in porous media subject to inlet flow disturbances-A pore-scale analysis, *International Communications in Heat and Mass Transfer*. 116 (2020) 104639. https://doi.org/10.1016/j.icheatmasstransfer.2020.104639.

R. Habib, B. Yadollahi, N. Karimi, A Pore-Scale Investigation of the Transient Response of Forced Convection in Porous Media to Inlet Ramp Inputs, *Journal of Energy Resources Technology*. 142 (2020) 1-14. https://doi.org/10.1115/1.4047968.

R. Habib, B. Yadollahi, A. Saeed, M.H. Doranehgard, L.K.B. Li, N. Karimi, Unsteady ultra-lean combustion of methane and biogas in a porous burner - An experimental study, *Applied Thermal Engineering*. 182 (2021) 116099. https://doi.org/10.1016/j.applthermaleng.2020.116099.

R. Habib, B. Yadollahi, A. Saeed, M.H. Doranehgard, N. Karimi, On the Response of Ultralean Combustion of CH 4 /H 2 Blends in a Porous Burner to Fluctuations in Fuel Flow—an Experimental Investigation, *Energy & Fuels*. 35 (2021) 8909–8921. https://doi.org/10.1021/acs.energyfuels.1c00081.

Conference Paper

R. Habib, B. Yadollahi, N. Karimi, Numerical Investigation of Thermal Dynamic Response in Porous Media—A Pore-Scale Study, in: *Advances in Heat Transfer and Thermal Engineering*, Springer Singapore, Singapore, 2021: pp. 385–389, *Proceedings of the 16th UK National Heat Transfer conference, Nottingham, UK, 2019*. https://doi.org/10.1007/978-981-33-4765-6_66.

Nomenclature

a_f	sinusoidal amplitude = $\big(max.sin(2\pi \cdot f \cdot t) - min.sin(2\pi \cdot f \cdot t)\big)/2$
a_r	ramp amplitude = $max.u - min.u$
c_p	specific heat capacity (J K^{-1} kg^{-1})
C	capacitance (F)
d	obstacle distance from the inlet (m)
D	obstacle diameter (m)
f	frequency (Hz)
$\mathcal{F}$	Fourier transform
h_o	external heat loss coefficient (W m^{-2} K^{-1})
H	height (m)
k	thermal conductivity (W K^{-1} m^{-1})
l	length (m)
$\dot{m}$	mass flow rate (kg s^{-1})
m	mass (kg)
n	Euclidean distance of the normalized Nusselt number at each obstacle
Nu	Nusselt number (-)
o	Discrete Fourier transform single sided amplitude spectrum of the normalized Nusselt number at each obstacle
p	pressure (Pa)
P	thermal power (kW)
Pe	Peclet number (-)
Pr	Prandtl number (-)
q''	heat flux (W m^{-2})
R	resistance (Ω)
Re	Reynolds number (-)
St	$(f \cdot D)/u$
t	time/period (s)
T	temperature (K)
u	flow velocity (m s^{-1})
u_m	mixture velocity = air and fuel flow velocity (m s^{-1})
X_C	capacitive reactance (Ω)

Greek Symbols

μ	dynamic viscosity (kg m^{-1} s^{-1})
ε	porosity
ρ	density (kg m^{-3})
φ	phase
ϕ	Equivalence ratio
ω	angular frequency (rad s^{-1})
δ	measure of non-linearity
ψ	temperature/velocity

Superscript

$\bar{}$	mean

Subscripts

amb	ambient
$delay$	delay
c	cut-off
D	based on Darcy
f	fluid
i	obstacle number
in	inlet
L	based on obstacle diameter size
$ramp$	function of ramp
ref	reference
x, y, z	Cartesian coordinates

Abbreviations

Al_2O_3	alumina
CO	carbon monoxide
CO_2	carbon dioxide
CH_4	methane
H_2O	water vapour
LHV	lower heating value
MFC	mass flow controller
ppi	pores per inch
$ppcm$	pores per centimetre
ppm	parts per million
NO	nitric oxide
NO_x	nitrogen oxides
O_3	ozone
REV	representative elementary volume
RGB	red green blue
SiC	silicon carbide

Chapter 1 Introduction

Climate change remains one of the world’s leading problems since the late 20th century [1] . This global crisis has substantially affected the complex architecture of numerous ecosystems resulting in the extinction of multiple species [2]. Climate change is defined as ‘an alteration in global or regional climate patterns, mainly associated with raised levels of atmospheric carbon dioxide (CO_2)’ [3]. The surge of CO_2 in the earth’s atmosphere alongside variation in temperature and rainfall, negatively impacts forest cover, leading to a gradual inevitable decline in human well-being [4].

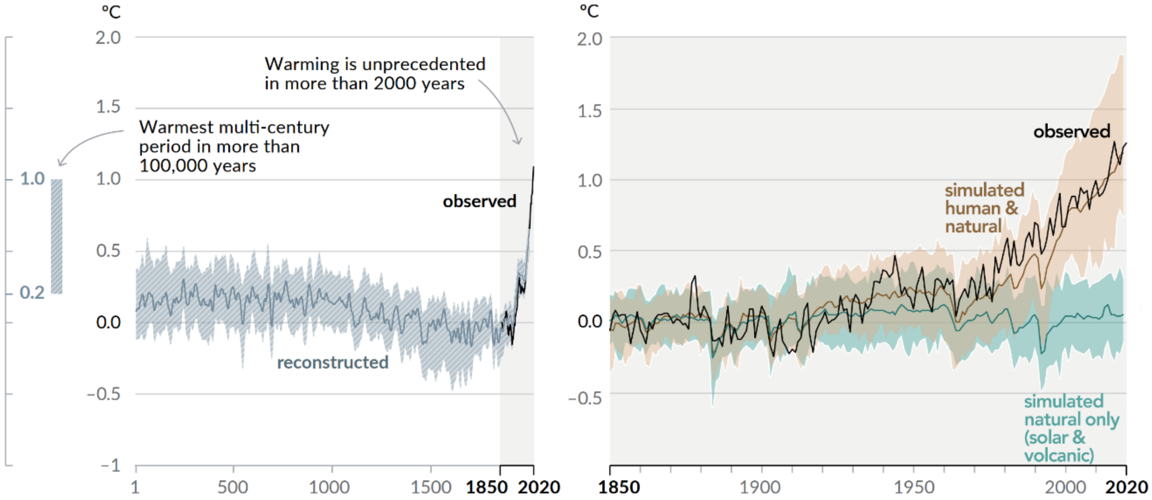

Figure 1-1: (a) Variation in global surface temperature as reconstructed and observed (b) Variation in global surface temperature as observed and simulated [5].

Greenhouse gases have a direct effect on the formation of climates [6]. The former are essential in ensuring that the temperature of the earth is suitable for human life [7]. The greenhouse gas effect phenomenon primarily materialises from gases such as carbon dioxide (CO_2), methane (CH_4), water vapour (H_2O), nitric oxide (NO), and ozone (O_3) [8]. In the absence of greenhouse gases, heat released by the earth from its surface into the atmosphere would result in inhabitable freezing temperatures. However, in reality only a portion of heat is absorbed, with most of the heat being transmitted back to earth, thus leading to an increase in the temperature of earth’s surface [9] (Figure 1-1). A contributing factor to climate change is the upward trend of energy consumption. Other problems that have developed include an increase in air pollution, melting of glaciers and rise in ocean levels – threatening countries to be submerged under water in the near future [10]. Fresh water resources will also become under threat with the rise in ocean levels [11].

1.1 Climate change mitigation

The concept of climate change mitigation is any action taken to mitigate global warming or halt any of its related effects [12]. Climate change mitigation techniques can be categorised into three primary methods. The first method includes the use of technology and practices to lessen CO_2 emissions [13] [14]. This can include utilising nuclear power, renewable energy, and the use of carbon neutral fuels. Most of these are seasoned technologies and carry a low-level managed risk.

However, the second method employs technology and processes that have been newly offered. They function to seize and isolate CO_2 in the atmosphere and are commonly known as “negative emissions technologies” [15]. Such carbon dioxide removal methods can include enhanced weathering, carbon capture and storage, afforestation, ocean enhancement and mineral carbonation [16] [17] [18].

Lastly, the third method entails changing the earth’s radiation balance by controlling the solar and planetary radiation. The most important aim is to reduce temperature or to keep it constant and this can be accomplished with no modifications to greenhouse gas concentrations in the atmosphere [19]. This method includes, cirrus cloud thinning, marine sky brightening and numerous radiation control techniques [20]. Many of these processes and techniques are either at the testing phase or are surrounded by ambiguity and high risk with regards to a comprehensive operation [21]. The three methods for climate change mitigation are illustrated in Figure 1-2.

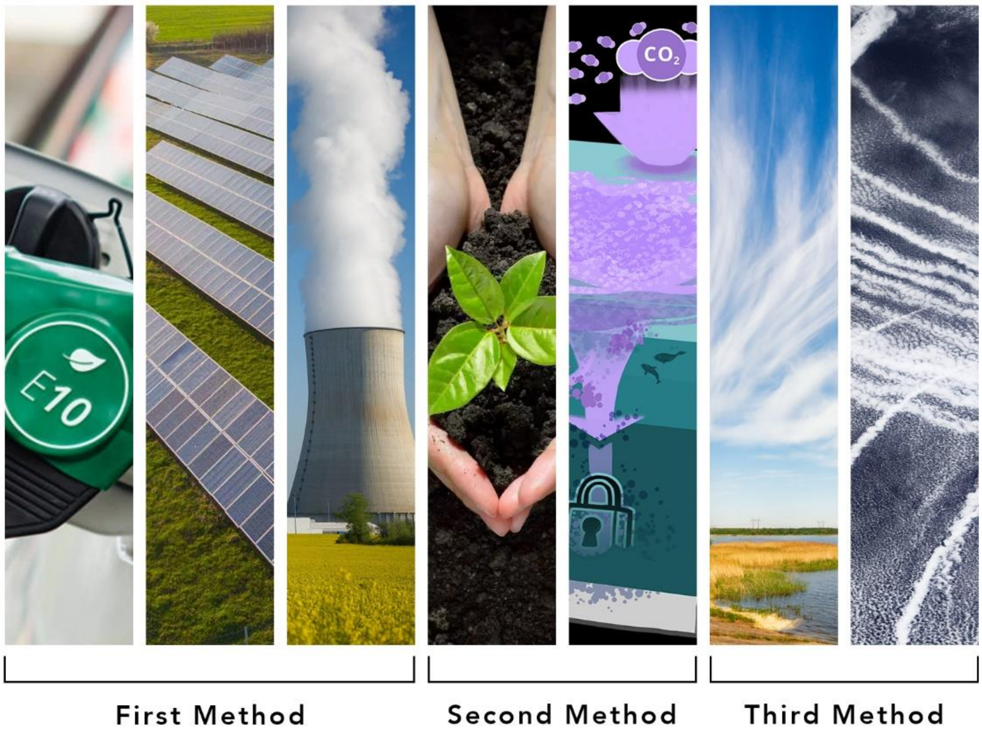

Figure 1-2: The three primary methods deployed for climate change mitigation.

1.1.1 UK and Worldwide greenhouse gas emissions

UK greenhouse gas emissions have predominately seen a decline since the year 1990 (Figure 1-3). CO_2 emissions in particular were conditionally projected to reduce by approximately 11% in 2020 since 2019, along with overall greenhouse gas emissions to decrease by around 9%. After 1990, the UK national emissions were projected to plummet by a staggering 49% up till 2020. Also, the constraints placed in the UK due to the coronavirus pandemic stemmed a negative growth economy in the year 2020, thus, a substantial effect on the overall UK emissions was predicted in 2020 [22].

The current UK data shows a 44% reduction was recorded in the overall national greenhouse gas emissions in 2019, since 1990. 27% of greenhouse gas emissions in 2019 were produced by the transport sector alone (Figure 1-4). Additionally, the energy supply sector reduced their emissions up to 66% from 1990 but represent only 21% of emissions in 2019 [22].

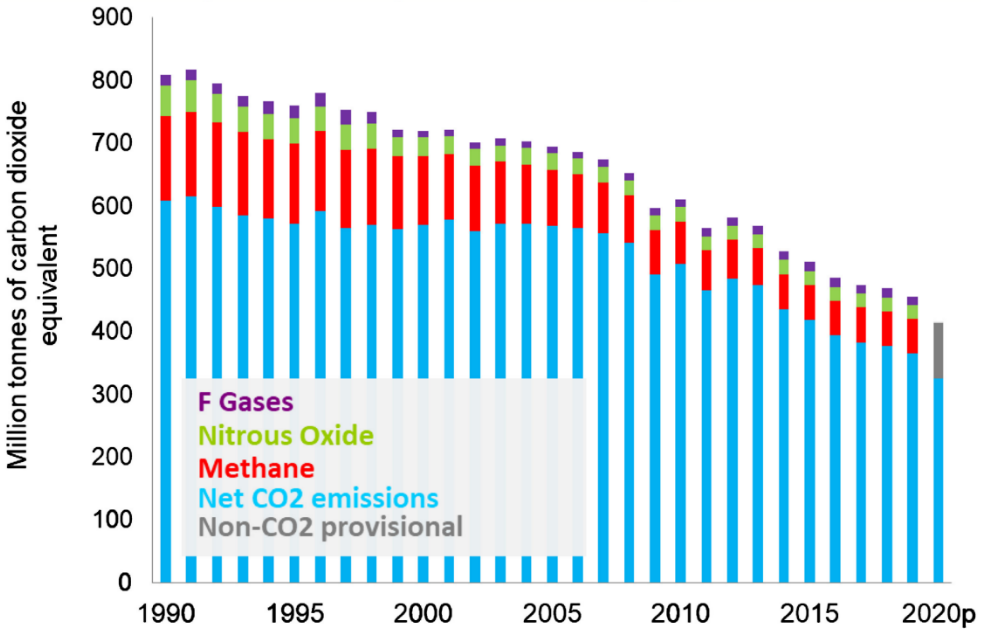

Figure 1-3: UK greenhouse gas emissions by gas type [22].

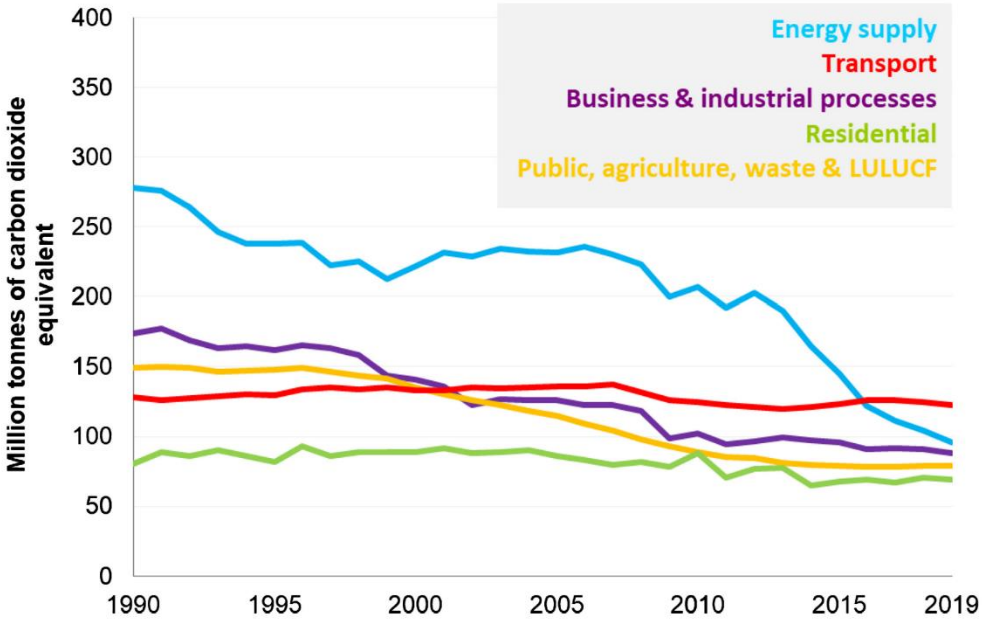

Figure 1-4: UK greenhouse gas emissions by divisions [22].

The worldwide energy supply consisted of 80% fossil fuels in 2019. Oil included the largest portion of energy supply amidst coal and gas. Although, despite coal holding a modest 23% in quantity, it produced the greatest amount of greenhouse gas emissions globally of 42% (Figure 1-5).

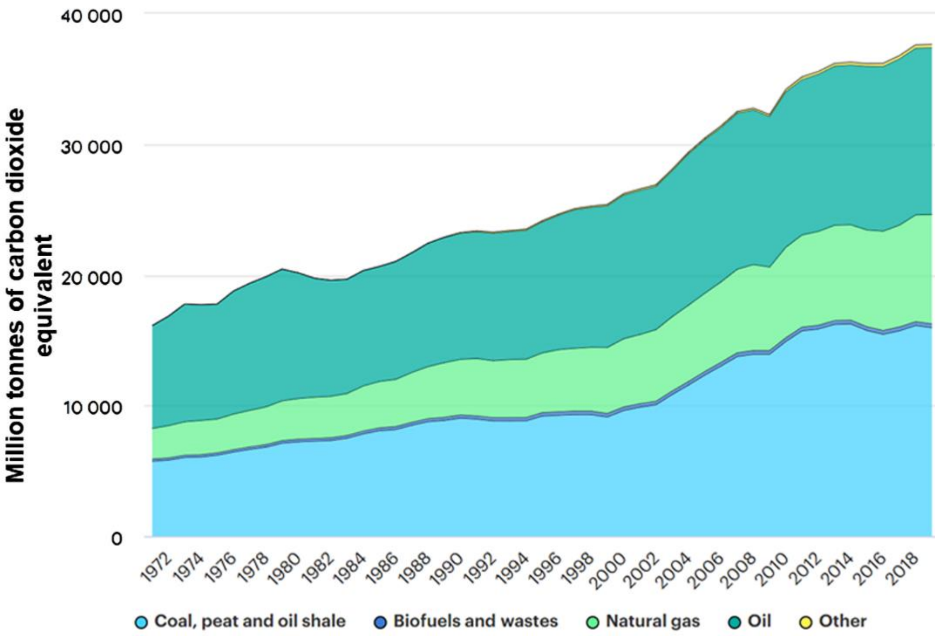

Figure 1-5: Global greenhouse gas emissions per energy type [23].

The global greenhouse gas emissions were dominated by the USA and China amounting to over 40% (Figure 1-6). Roughly 10% of all global energy associated emissions are methane related. It has been shown by the International Energy Agency methane tracker in 2021, that a decline in methane emissions may be the most economical and profitable routes to decreasing the long-term emissions caused by the gas and oil industry [23]. Furthermore, economies generating vast amounts of methane emissions as well as fossil fuels could explain the greater portion of the overall greenhouse gases produced from the energy sector [23].

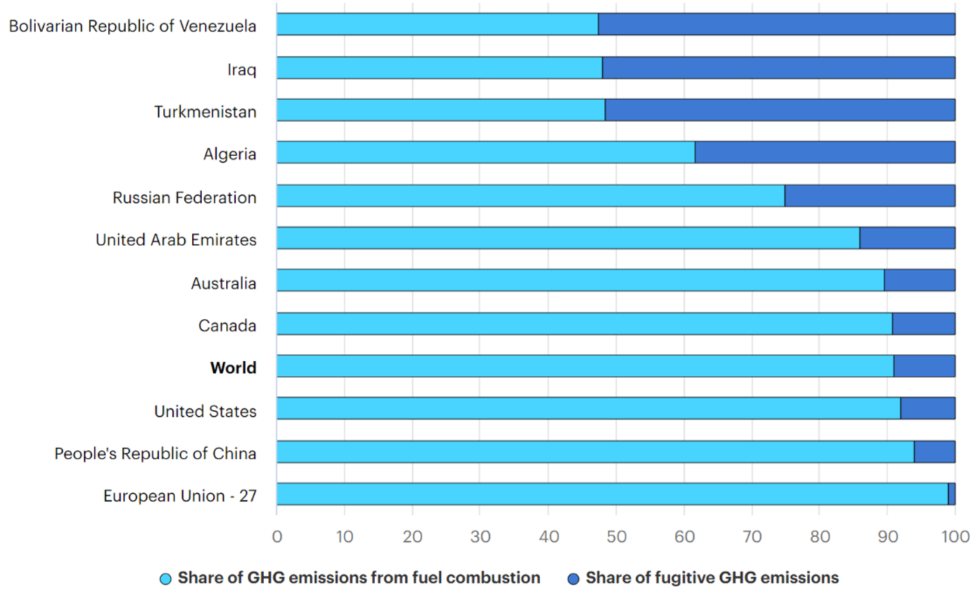

Figure 1-6: Overall greenhouse gas emissions from energy as a % of fuel combustion and fugitive emissions [23].

1.1.2 UK and Worldwide targets for reducing greenhouse gas emissions

The burning of fossil fuels for heating and petrol for cars results in the production and release of greenhouse gases. Consequently, an increase in flooding has been observed in recent years, for example at the London underground in summer 2021 [24]. Furthermore, reports by Intergovernmental Panel on Climate Change have shown that a lack of action to restrict the temperature of global warming by at least 1.5°C over that of pre-industrial standard, will result in far more constant and severe catastrophic natural disasters such as fires and flooding [25]. Hence, emissions released would need to be reduced to as low as possible (nil), allowing the limited surplus to be consumed via naturally occurring carbon sources. In doing this, a significant reduction in greenhouse gases can be witnessed in the UK [24]. Other methods, that aim to help achieve the imperative goal of 'net zero' are, to halt the use of petrol and diesel car engines, end deforestation and coal fuelled source generators [24]. Moreover, in 2015, the 'Paris Agreement' [26] was adopted to tackle climate change. The aim being to restrict the rising temperature of global warming to below at least 2°C, with a more desirable goal of 1.5°C. In order to accomplish this endeavour, countries all over the world are attempting attain climate neutrality before 2050, by quickly reaching global peeking of greenhouse gases.

Currently, the UK has acted in reaching 'net zero' through steps such as accelerating the ceasing of new petrol/diesel car sales to 2030, investing in carbon capture, wind power and hydrogen as well as production in electric vehicles. The UK has also provided efforts in promoting the use of public transport, walking, and cycling as well as recycling and upscaling to help decrease the carbon footprint. Efforts to protect the natural environment are also being made by improving biodiversity to promote healthy ecosystems, aiding a more sustainable economy, and arranging protection from the effects of climate change such as flooding and overheating [24]. Moreover, the UK has endorsed the development of new innovative low carbon technologies, produced zero emission vehicles (trains, ships, and planes) running on novel decreased sourced of carbon energy and adopted using cleaner affordable energy to heat homes [24].

1.2 Decarbonisation of heat

Regardless of attempts in decarbonising the power division, the generation of heat and electricity correlates to above 40% of the CO_2 emissions globally, from fuel combustion alone, with 70% of allied emissions being emitted by coal fired power stations (Figure 1-7). The generation of electricity CO_2 emissions are decided by the subsequent factors: production efficiency, electrical output, portion of fossil in total production as well as carbon intensity of fossil production.

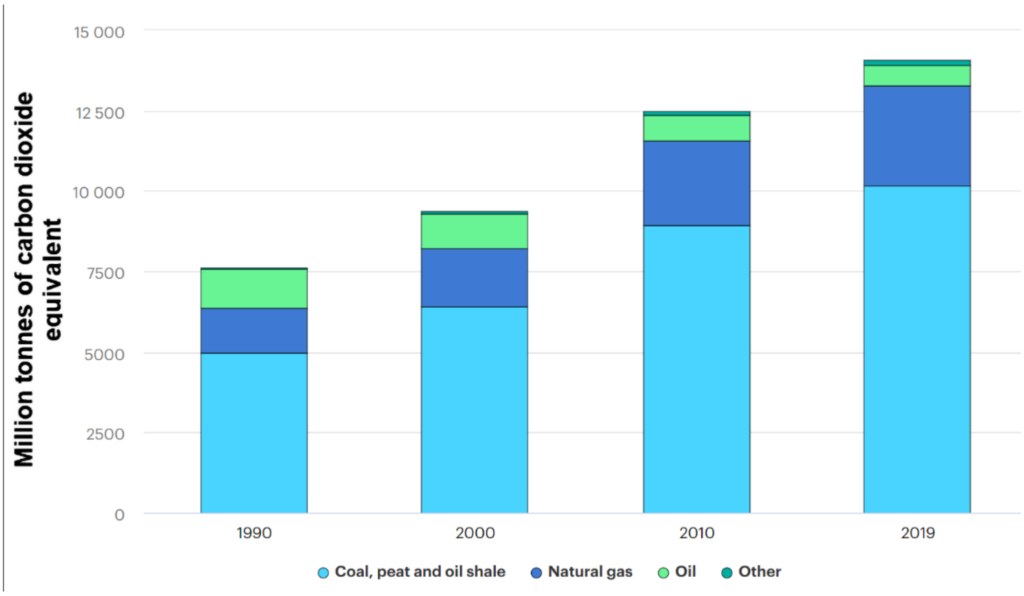

Figure 1-7: CO_2 emissions from electricity and heat generation by energy source [23].

1.2.1 Fuels for heat generation

At least 54% of the overall global energy generated is produced by the industrial sector and is continuously increasing by 1.2% every year. Many industries in this sector make use of fossil fuels in order to meet their heat demands [27]. From the burning of fossil fuels, the steam generated is used for heat applications of industrial processes [28]. Applications with the process industry favour heat as opposed to that of electrical energy in order to attain the energy requirements needed.

Metal manufacturing is a conspicuous industry known for depleting extensive quantities of energy. This industry is comprised of aluminium, steel, and iron. In the case of melting metal, the temperature needed can increase to 1500ºC [29], which renders both heat pumps as well as electrical heating counterproductive. The worldwide need for steel has been steadily increasing throughout recent years due to the rise in population and GDP. Figure 1-8 illustrates the proportion of CO_2 emissions in steel production in the 'net zero' scenario.

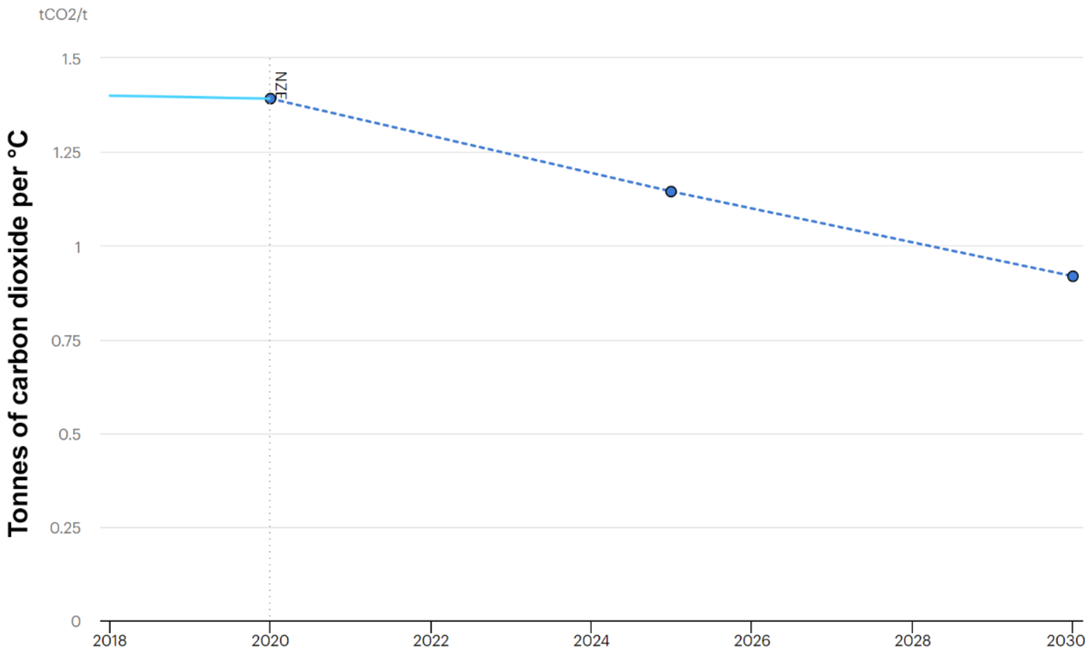

Figure 1-8: CO_2 of steel production in Net Zero Scenario (2018-2030) [30]

The cement sector accounts for roughly 12-15% of the overall energy used. As a result, a large proportion of carbon emissions are produced (1.8 gigatons per year [31]) due to fossil fuel burning to sustain high temperatures [32]. Within the cement industry, coal, petroleum coke as well as fuel oils are the primary components of the energy supply. Lately, alternative fuels and natural gases are being made use of as substitute energy sources [33]. Despite this 7% of the overall CO_2 emissions are caused by the cement industry [34] and this is rapidly increasing as the production of cement is accelerating quicker than the speed by which emissions are being decreased [35].

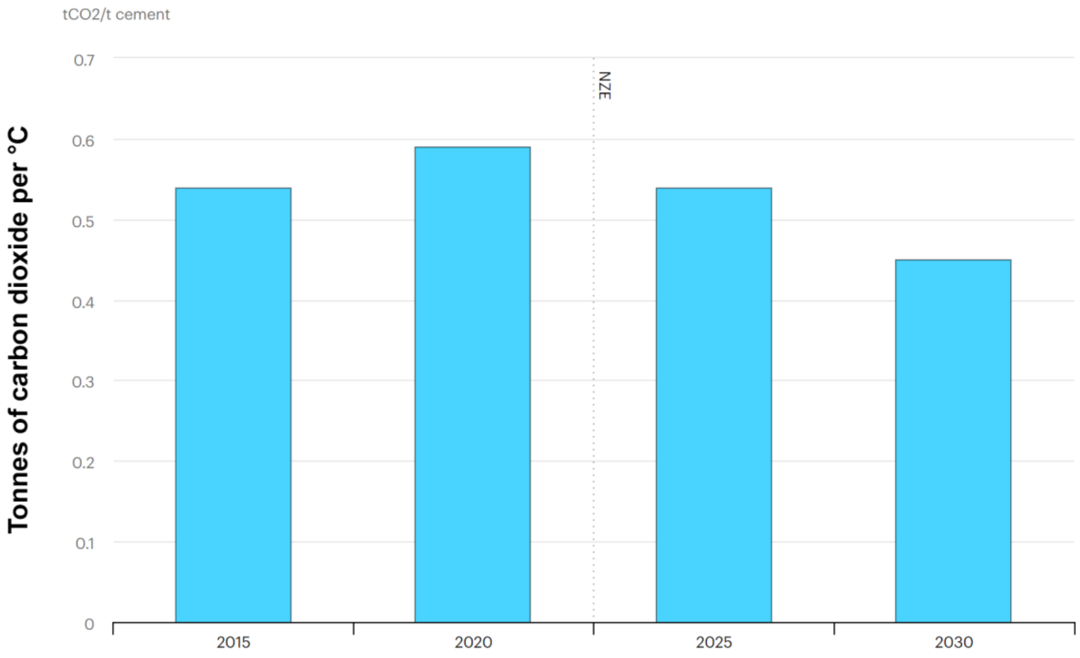

Figure 1-9: CO_2 of cement production in Net Zero Scenario (2015-2030) [36]

Figure 1-9 depicts an ideal reduction in cement production to achieve 'net zero'. Also, with high temperature heating a key necessity for these industries, replacement of fossil fuels by perhaps carbon neutral fuels may be a promising option.

1.2.2 Carbon neutral fuels

The CO_2 in the atmosphere does not rise nor decrease through the burning of carbon-neutral fuels and such fuels are created using CO_2 as the raw material supply. There are a variety of groups of carbon-neutral fuels such as biosynthetic fuels – produced via biomass gasification – and biofuels. One of the most prominent categories of carbon neutral fuels are biogas, biodiesel, bioethanol, bio-syngas and bio-butanol, all of which are produced from waste product and crops. Deriving biofuel from biomass is rather appealing due to biomass being cost effective and readily available over the passage of time. The generation of biomass can occur using materials or organisms that are either living or dead. Moreover, algal biomass is exposed to high temperatures to form bio-syngas [37]. Components of bio-syngas include hydrogen, carbon monoxide, carbon dioxide and methane. On the other hand, the main components of biogas are carbon dioxide and methane, and its production is made possible through the anaerobic digestion of organic compounds such as waste and food [38] (Figure 1-10).

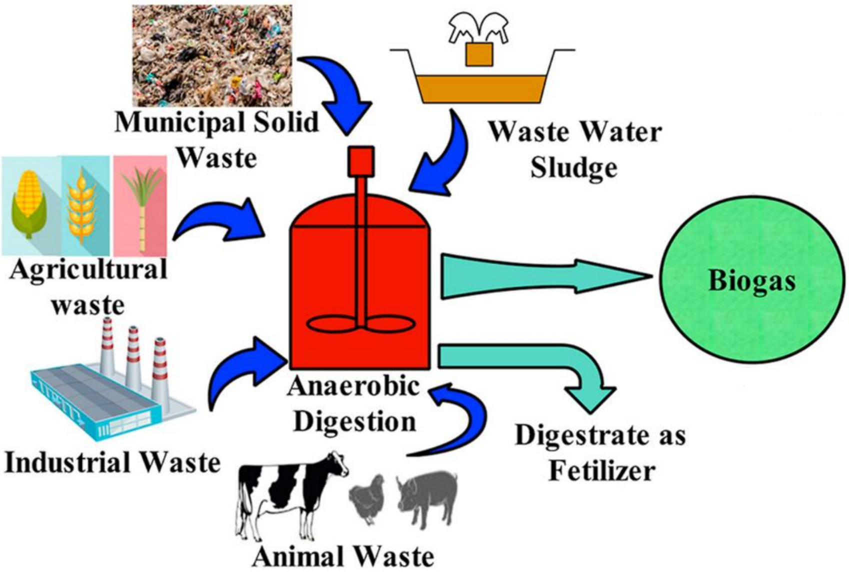

Figure 1-10: Bio-gas production [39]

The renewable energy market is continually growing and developing, and biogas usage has significantly risen from 14.5 GW in 2012 to 29.5 GW in 2022 [40]. One of the primary reasons renewable fuels have gained such importance is because of the global aim to reduce the world's greenhouse gas emissions. The global power from biogas alone is about 18 GW, with many power stations found in Europe (UK and Germany) and America [41,42]. An increase in the total number bio-gas plants worldwide has been witnessed due to the movement towards a greener economy (Table 1-1) [43].

Table 1-1: Total Number of Bio-gas plants [43]

Country	Number of plants in 2014	Number of plants in 2016	Number of plants in 2019
France	8	30	47
Denmark	12	32	34
United Kingdom	37	85	96
Italy	5	7	8
Finland	9	12	17
Switzerland	24	31	45
Netherlands	21	26	53
Germany	178	194	203
Austria	14	15	13
Sweden	59	63	69
Hungary	2	2	n/a
Luxembourg	3	3	3
Spain	1	1	n/a
Norway	n/a	n/a	9
Australia	0	0	0
South Korea	n/a	n/a	10
Japan	n/a	6	6
China	n/a	n/a	2
USA	n/a	n/a	50

A study in the UK was carried out looking at potential syngas production from biogas by dry reforming of methane and found that the capacity for renewable energy generation in the UK can be assisted with the production of syngas from biogas [44].

1.2.3 Issues associated with switching to carbon neutral fuels

The most common issues faced with changing to carbon neutral fuels include lack of government policies, access to viable technology, and initial investment for set-up. Governments should deliberate on such policies by providing incentives and subsidising technology transfer between developed and developing nations. This is ought to be crucial for countries that are impacted by climate change the most and for countries like the UK, where international policies have been signed and endorsed to reduce greenhouse gas emissions by mid-century [44].

The UK government has recently published a Hydrogen strategy in August 2021 [45] to develop a low carbon hydrogen sector to build a cleaner and greener energy system to aid the UK's transition to Net-Zero. The UK Hydrogen strategy aims to deliver 5GW production by the year 2030. It sets out a roadmap to enable production, distribution, storage of hydrogen whilst ensuring economic growth. In order to accelerate the use of hydrogen, the UK government has committed itself to gas blending[45]. The aim is to introduce 20% of hydrogen into the gas grid mixed with natural gas by 2023 (subject to trials). The UK government believes mixing hydrogen into existing gas networks could accelerate technical, regulatory and commercial changes that could facilitate a smoother transition to the potential use of pure hydrogen as a heating fuel. Figure 1-11 depicts the projected hydrogen demand in 2030 and 2035 in various sectors.

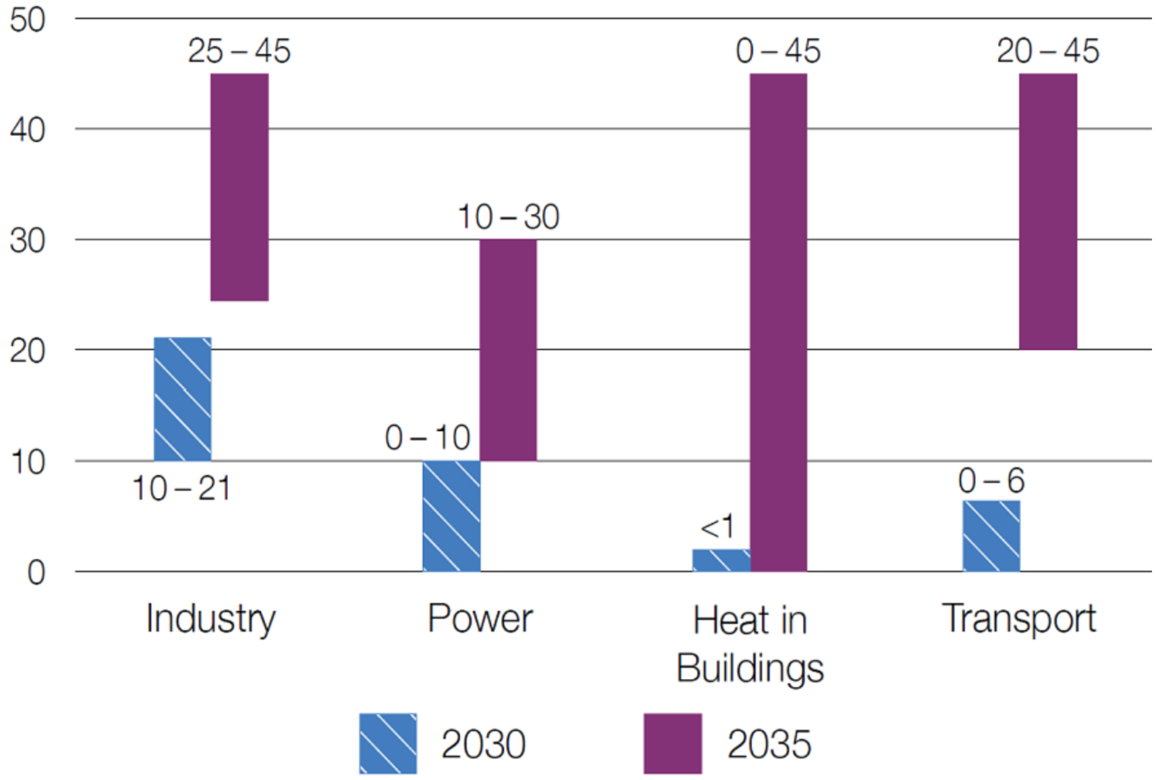

Figure 1-11: Illustrative Hydrogen demand in 2030 and 2035 (%) [45]

1.2.4 Problems of burning carbon neutral fuels

The burning of carbon neutral fuels is a daunting challenge. A considerable proportion of ingredients in biofuels are incombustible gases [46]. One of the key obstacles for biogas growth in heat and power generation industries has been due to its low calorific value [47]. Processing and refinement of biofuels are costly and are mostly conducted in sensitive applications [46].

1.2.4.1 Low-calorific fuels

Biogas and biosyngas can be described as carbon neutral fuels with low-calorific values - also known as lean gases. These renewable fuels have potential for substituting or replacing petroleum fuels; in particular for heat generation [47]. Such low reactivity fuels are gaining a lot of attention due to their low cost production but their combustion under certain operating conditions is challenging for conventional burners. Low-calorific fuels tend to contain a significant quantity of inert gases such as carbon dioxide and nitrogen [46]. Due to these characteristics conventional combustion often do not guarantee sufficient flame stability and also produce a large quantity of harmful emissions[48,49]. With such challenges in mind it is imperative to combust low-calorific fuels in an efficient combustion system whereby the burner design/material selection is as such that prolonged heat retention within the burner or pre-heating of fuel mixture can play a key role in complete/stable combustion of low calorific carbon neutral fuels [49]. Combustion within a porous medium is a probable solution where such fuels can comfortably burn within the cavities of the solid matrix [48].

1.2.5 Porous media

A porous medium is a material consisting of a solid matrix with an interlinked void. The voids – also known as pores – allow the flow of one of more fluids through the material. In single-phase flow the pores are filled by a fluid whereas in two-phase flow a liquid and a gas contribute to the pore space as shown in Figure 1-12 [50]. Naturally developed porous media are more likely to have a non-uniform size and shape. These can include sandstone, wood, a slice of bread or even the human lung (Figure 1-13). Porous media created by man, however, mostly is uniform and designed for a particular application or size which can include metallic foams, ceramics, and composite materials (Figure 1-13). The fraction of the total volume of the solid matrix that is occupied by void space defined as the porosity [50].

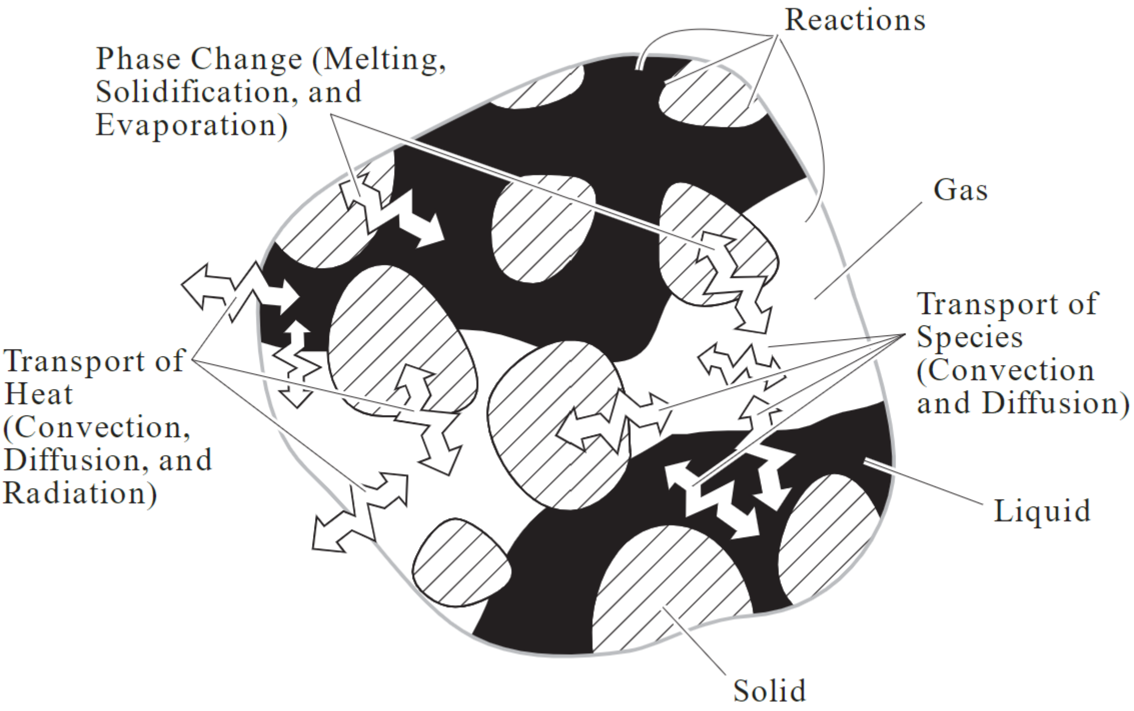

Figure 1-12: Pore-level diagram showcasing two phase flow in porous media [50]

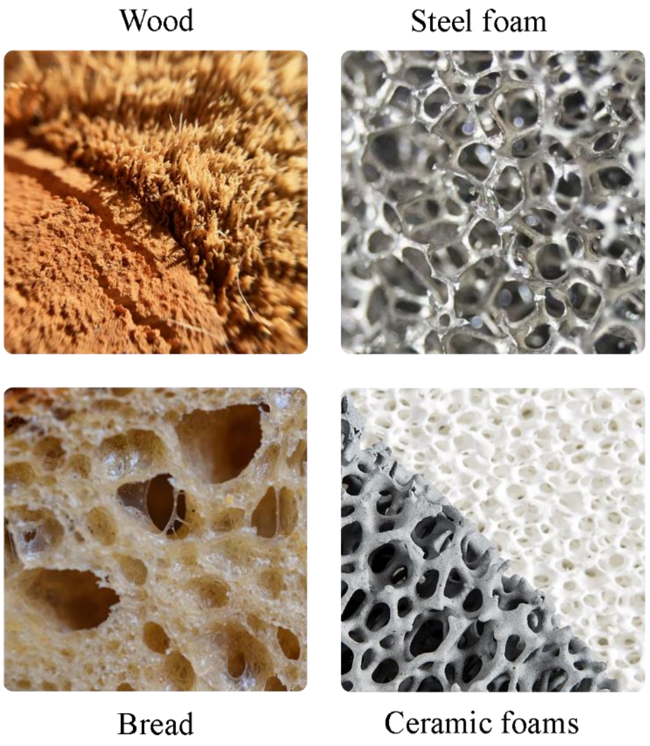

Figure 1-13: Natural porous media vs man-made porous media

Ceramic porous media have the ability to withstand high temperatures, are chemically stable and resistant to erosion. The most popular ceramic foams for high temperature applications are silicon carbide, zirconia and alumina [49]. Hence, they are the preferred choice of material employed in porous burners.

1.2.6 Porous burner for combustion of carbon neutral fuels

A low-cost technological solution to combust carbon neutral fuels for thermal energy are porous burners. Porous burners are a technology with the capability to combust low-calorific and carbon neutral fuels such as biogas and syngas [49] (Figure 1-14). This technology allows a carbon neutral fuel mixed with air to burn within the voids of a solid porous material instead of an open flame like traditional gas burners.

Figure 1-14: Porous burner

One of the key design considerations for a porous burner is the choice of porous material. The material choice is commonly based around, cost, thermal conductivity, resistance to thermal shock and the maximum temperature the material can withstand; thus, making ceramic foams a popular choice [49]. The solid ceramic foams have excellent heat retention properties which can allow carbon neutral fuels to burn comfortably without flame extinction [49]. This is due to the internal heat recirculation of the solid matrix. The incoming cool reactants of the fuel mixture are pre-heated allowing for easy ignition and for stable combustion within the solid matrix to take place, despite variation in fuel flow rate [49] (Figure 1-15). Consequently, making porous burners suitable for combustion of carbon neutral fuels.

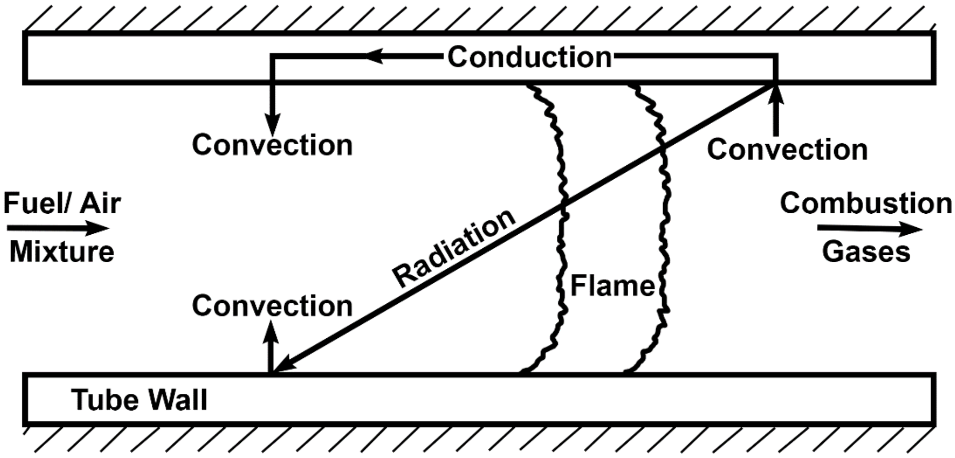

Figure 1-15: Schematic representation of heat recirculation in a porous medium idealised as an insulated refractory tube [49]

Combustion in porous media is known to be dominated by heat transfer, therefore it is imperative to investigate heat transfer individually within a porous medium. Also, combustion is drastically impacted by the variations in the inlet flow, making it ever so important to investigate the dynamic response of such systems. The use of porous media in emerging technologies requires an understanding of their dynamic responses as in such applications the inlet fluid flow rate can become strongly time dependent [51,52]. But most studies of forced convection in porous media look at only the steady phenomena [53,54] and over the last 20 years, majority of studies on porous media have been based on the Darcy model and its extensions [55,56]. However it is generally understood that the Darcy model might not be suitable for periodic flow systems [57] and that a pore-scale approach can be used for greater accuracy. Not many numerical studies have investigated unsteady and oscillatory flows in porous media in the two-dimensional domain [57,58] and even less studies have done so in the three-dimensional domain [59]. Therefore, to understand porous media flow, which entails small voids within which the fluid can pass; thus affected by wall boundary conditions, it is imperative to understand the dynamic response of heat transfer in porous media to time-varying flows in the three-dimensional domain to interpret the results in a realistic situation. Furthermore, it is understood that combustion of carbon neutral, low calorific fuels can play a huge role in improving energy efficiency and lowering CO_2 emissions [60], but such fuels incur challenges regarding flame stability in conventional burners [61]. Thus, a porous burner with strong heat recirculation properties can allow combustion of fuel mixtures which might not be flammable [62]. However, in most industrial applications combustion occurs under steady state conditions [63,64] whereby switching from fossil fuels to biogas or bio syngas often includes using unsteady fuel sources [65]. The variability could be in the fuel flow rate and/or chemical composition due to the temporal change in the feedstock that produce renewable fuels [66]. Moreover, studies of combustion in inert and catalytic porous media are largely focused on steady combustion [67,68], dominated by methane mixtures [69] with very little attention to ultra-lean operation [70]. Thus, understanding the dynamic response of porous burners operating under time-varying and ultra-lean conditions can help lower CO_2 emissions and improve energy efficiency by using low calorific, carbon neutral fuels.

1.3 Objectives

The objective of this thesis is to gain deep fundamental understanding about time-dependent heat transfer and combustion in porous media. This has been achieved through a combined numerical and experimental approach. Firstly, a numerical analysis of fluid flow and heat transfer in porous media has been carried out in chapter 2, chapter 3 and chapter 4. It was imperative to investigate heat transfer in porous media independently as heat transfer plays a dominant role in porous media combustion whereby a three-dimensional pore-scale model was created to interpret the results in a realistic situation; implementing wall boundary conditions. The numerical investigations include a systematic approach whereby the inputs - pore diameter, velocity, fluid type – were varied. Furthermore, an experimental analysis using a custom-built porous burner with conventional and bio-driven gaseous fuels at constant and dynamic flow rates was carried out in chapter 5 and chapter 6. CO_2 and CO emissions as well various temperature readings were noted. Moreover, a dynamic approach was crucial as majority of existing numerical and experimental studies have extensively investigated steady flow and the dynamic response of such systems remains relatively unexplored under ultra-lean operation; allowing the reduction of CO_2 emissions and improving energy efficiency. Finally, a summary of the findings of thesis and future works are given in chapter 7.

Chapter 2 A pore-scale assessment of the dynamic response of forced convection in porous media to inlet flow modulations

International Journal of Heat and Mass Transfer – Rabeeah Habib, Nader Karimi, Bijan Yadollahi, Mohammad Hossein Doranehgard, Larry K.B. Li

2.1 Introduction

The use of porous media in emerging technologies [52,60], including electrochemical systems [71,72] combustion of carbon-neutral and renewable fuels [59,73], and micro chemical reactors [53,74], requires an understanding of their dynamic responses. This is because in these applications the inlet fluid flow rate can become strongly time dependent [49]. It is, further, essential to predict the thermal response of the system to the temporal disturbances superimposed on the inlet flow [75]. Yet, the existing investigations of forced convection in porous media have focused largely on the steady phenomena. This trend could be readily observed in studies that conducted macroscopic modelling (e.g. [55,76,77]) as well as in those taking a pore-scale approach to the analysis of heat convection in porous media (e.g. [78,79]).

Over the last two decades, most theoretical and numerical studies on porous media have been based on the Darcy model and its extensions [80,81]. Nevertheless, it has been implied that the application of this model to periodic flow systems is not straightforward [71] and thus a pore-scale approach is sometimes used for greater accuracy. A small number of studies have investigated unsteady and oscillatory flows in porous media in two-dimensional domains [59,72,73], and even fewer studies have examined three-dimensional domains [53]. As a result, there appears to be a gap in understanding the dynamic response of heat transfer in porous media to time-varying flows. To evaluate the status of steady and unsteady pore-scale modelling, here a concise review of the literature on microscopic studies in porous media is put forward.

Inspired by the macroscopic study of Kuwahara et al. [82], Gamrat et al. [83] numerically investigated heat transfer over banks of square rods in aligned and staggered arrangements with a varying porosity between 0.44 and 0.98. The two-dimensional laminar flow model focussed on low Reynolds number flows and with two thermal boundary conditions: constant wall temperature and constant volumetric heat source. The effects of bank arrangements, porosity, Prandtl and Reynolds number upon the value of the Nusselt number were examined. Gamrat et al. [83] showed that the convective heat transfer coefficient obtained with a constant wall temperature was significantly higher than previously reported results. In a similar context, Teruel and Diaz [84] simulated a microscopic laminar flow developed through a porous medium formed by staggered square cylinders. They modelled multiple representative elementary volumes (REV) to validate their calculations of macroscopic parameters, such as the interfacial heat transfer coefficient by employing a unit periodic cell. The steady flow regime was varied with Peclet numbers in the range of 10–1000 and porosities between 0.55–0.95. The interfacial heat transfer coefficient was also calculated as a function of the REV positions in the porous structure showing position dependency or pore-scale fluctuations.

Two-dimensional square and circular cross-sectional models in a staggered arrangement were developed by Torabi et al. [85]. A steady laminar flow was numerically simulated with a constant inlet temperature and solid phase temperature. These authors [85] performed a thermodynamic analysis of forced convection through porous media with a particular focus on entropy generation. A range of Reynolds numbers and porosities were considered for both Darcy and Forchheimer flow regimes. In keeping with the findings of macroscopic models, the results showed that increasing the Reynolds number or decreasing the porosity of the medium enhances the rate of heat transfer.

Ozgumus and Mobedi [86] examined the effects of the pore- to-throat size ratio on the interfacial heat transfer coefficient for a periodic, two-dimensional porous media containing an inline array of rectangular rods. The velocity and temperature distributions in the voids between the rods were calculated numerically for the REV using the Navier Stokes equations. The effects of variations in the pertinent parameters including porosity, the Reynolds number and the pore-to-throat size ratio were considered. Ozgumus and Mobedi [86] found that the pore-to-throat size ratio could considerably affect the interfacial convective heat transfer coefficient. According to their results, an increase in porosity increases the Nusselt number for low pore-to-throat size ratios, but it decreases the Nusselt number for high pore-to-throat size ratios.

In an attempt to gain further insight into combustion in porous media, Jouybari et al. [87] conducted a pore-scale simulation of turbulent reacting flow of air/methane mixture. This study was mainly concerned with the investigation of multi-dimensional effects and turbulence on the flame within the pores of a reticulated porous medium. The investigated two-dimensional medium consisted of a staggered arrangement of square cylinders, similar to that of Teruel and Diaz [84]. The stationary Reynolds averaged Navier-Stokes, energy conservation, the species conservation, and a turbulence model were solved using a finite volume technique. In this study, the turbulence kinetic energy, turbulent viscosity ratio, temperature, flame speed, convective heat transfer, and thermal conductivity were compared for laminar and turbulent simulations. Jouybari et al. [87] showed that unlike the previous volume-averaged simulations (macroscopic) which predicted a flat flame in the porous medium, a highly curved flame anchored to the square cylinders was detected in their study.

Wu et al. [88] numerically simulated convective heat transfer between air flow and ceramic foams to optimise the volumetric solar air receiver performances. They computed the local convective heat transfer coefficient between the air flow and ceramic porous foam for which the flow momentum and energy balance were solved inside the porous ceramic foam. A sensitivity study on the heat transfer coefficient was conducted with the porosity, velocity and mean cell size parameters. The Reynolds number based on the pore diameter was between 240–1600, where part of the flow regime was laminar, and the solid was kept at a uniform temperature. Wu et al. [88] stated that the difference between the laminar flow and the turbulence model was insignificant and therefore their study considered only a turbulent flow. The inlet temperature was kept smaller than the constant temperature of the ceramic foam to study the convective heat transfer coefficient values. The flow field and heat transfer characteristics were analysed in detail, and based on the results, a correlation for the volumetric local convective heat transfer coefficient was developed.

A numerical investigation of turbulent fluid flow and heat transfer in porous media was carried out by Yang et al. [79]. They considered a T-junction mixing where a flow is vertically discharged in a three-dimensional fully developed channel flow. The governing equations were also solved at the pore level using a turbulence model. An in-line and a staggered arrangement of pores were investigated over a wide range of Reynolds numbers similar to that of Gamrat et al. [83]. Gaseous nitrogen with a uniform free stream velocity and a constant temperature entered a clear channel with a square cross-section. Similarly, nitrogen gases with uniform velocity and constant temperature (higher or lower than the channel inlet) were injected through the porous structure and mixed with the channel flow in a T-junction arrangement. The surfaces of the solid porous structure were kept at a constant temperature, equal to the channel flow whereas all other walls in the model were considered adiabatic. Heat transfer examination of the flow domain revealed that the temperature distribution in the porous structure was more uniform for the staggered array. Yang et al. [79] further found that the average Nusselt number in the porous medium increased drastically with increasing Reynolds number in the flow under an in-line array, while for the staggered array, it remained insensitive to Reynolds number.

Kim and Ghiaasiaan [89] modelled two-dimensional laminar, steady and pulsating flow through porous media. Their investigated system included several unit cells of porous structures with sinusoidal temporal variations in inlet flow. The porous media consisted of periodic arrays of square cylinders with the porosity ranging from 0.64-0.84. The Navier-Stokes equations were solved for pore-level simulations (microscopic equations) and the obtained results were compared with the volume-averaged equations (macroscopic equations) such as the Darcy-Forchheimer momentum equation. The Reynolds number, based on the unit cell length, of 0.1-1000 was set for steady flow while, that based on the mean superficial velocity (0.11 and 560) was used for unsteady simulations. The oscillatory flow consisted of pulsating frequencies ranging between 20-64 Hz with a fixed amplitude of 0.4 for all cases. Kim and Ghiaasiaan [89] stated that although the inlet velocity was sinusoidal, the calculated velocity was not exactly sinusoidal, indicating the existence of a non-linearity in the behaviour of the system. They concluded that the application of Darcy-extended Forchheimer momentum equation with coefficients representing steady flow to pulsating flow conditions is only adequate at very low-flow (low frequency) conditions and is otherwise incorrect [89].

Alshare et al. [90] computed laminar steady and unsteady fluid flows and heat transfer for a spatially periodic array of square rods representing two-dimensional isotropic and anisotropic porous media. Uniform heat flux boundary conditions were imposed on the solid-fluid interface where the Reynolds number was varied between 1 and 1000. The microscopic details of the rod arrangement and flow angularity were used to determine the effective anisotropic properties of the porous medium. The flow was varied from 0-90° relative to the unit cell where the working fluid was air. Alshare et al. [90] argued that the permeability of the isotropic medium was uniform and independent of the flow angle, while for the anisotropic medium, the permeability varied nearly linearly between the two principal permeabilities.

Using the same geometry as Kim and Ghiaasiaan [89], Pathak and Ghiaasiaan [91] investigated solid-fluid heat transfer and thermal dispersion in laminar pulsating flow through porous media. Two dimensional, laminar flows in porous media were composed of periodically configured arrays of square cylinders with sinusoidal temporal disturbances on the inlet flow. Detailed numerical data was obtained for porosities of 0.64-0.84, frequencies of 0-100Hz, and Reynolds numbers of 70-980. Pore-scale volume-averaged heat transfer coefficients and the thermal dispersion term were found to be strong functions of porosity, Reynolds number, and most importantly, the flow pulsation frequency. Based on the obtained numerical data, correlations were developed for cycle-averaged, pore-scale Nusselt number and the dimensional thermal dispersion term. Pathak et al. [92] presented a numerical investigation of the hydrodynamics and conjugate heat transfer in porous media with the unidirectional-steady and oscillatory flows. The pore-scale simulations considered helium as the inlet fluid with steady and oscillatory flow at two amplitudes and varying frequencies between 0-60Hz for velocity. The obtained data was then used for the calculation of numerous parameters including the unit cell length based Nusselt number. It was concluded that the predictive methods and correlations based on unidirectional steady flow should be avoided in the analysis of periodic flow systems in porous media.

Penha et al. [78] developed a transport model subject to periodic boundary conditions that describe incompressible fluid flow through a uniformly heated porous solid. The transport model used a pair of pore scale energy equations to define conjugate heat transfer. To cope with the geometrically complex domains, Penha et al. [78] developed a numerical method for solving the transport equations on a Cartesian grid. The results obtained by Penha et al. [78] corresponded to two structured models of porous media: an inline and a staggered arrangement of square rods on fully developed flows with isothermal walls. The approximation was modelled as a three-dimensional array with a REV where the Reynolds number was defined with respect to the reference length of the model as was the Nusselt number. The effects of various system parameters were studied on the Nusselt number for both arrangements of square rods. A reasonable agreement was shown with the results of Kuwahara et al. [82] and other studies for Reynolds number ≥ 10 with the inline arrangement and for the staggered arrangement, while the two models were almost identical for $10 <$ Reynolds number ≤ 100.

It follows from the review of literature that the existing pore-scale studies on unsteady heat convection in porous media are chiefly concerned with the accurate evaluation of Nusselt number. Unsurprisingly, this demands conduction of rather extensive computations which are often highly expensive and time consuming. However, a number of evolving technologies [49,59] require prediction of heat transfer rates in short durations with limited computational power and under highly dynamic conditions. Hence, there is a pressing need for the development of low-cost predictive tools to evaluate the dynamic response of heat transfer in porous media. Yet, as of now, there exists almost no systematic study on such tools. The current work aims to address this issue by using the outcomes of a pore-scale computational model for the development of a predictive heat transfer tool introduced by the classical theory of control. The study further determines the applicability range of the developed tool through evaluating the non-linearity of the dynamic response of heat convection in porous media.

The rest of this paper is organised as follows. First, the theoretical and numerical methods utilised by the investigation is presented. This is followed by the discussion of the results and a summary of the key findings and conclusions of the work.

2.2 Methodology

Determining the heat transfer characteristics inside porous media can be a cumbersome task [48,93]. Unsteady, multi-dimensional, pore-scale, simulations are necessary to understand the complex transport and the thermal dynamic response of these systems.

2.2.1 Problem configuration

A general sketch of the system modelled in this investigation is shown in Figure 2-1 and a schematic diagram is shown in Figure 2-2. A porous medium is represented by a series of staggered cylinders over which the fluid flows. Figure The working fluid enters the domain through a uniform flow moving from left to right. The computational domain has a total length, *l*, height, *H*, while *l* / *H* = 20 and a flow obstacle (cylinder) diameter, *D*, for which *D*/*H* = 0.4. The base configuration has a porosity, ε, of 0.874. However, the porosity of the porous structures changes with the cylinder diameter. The working fluids are air, hydrogen and carbon dioxide as they mimic fluids from the experimental investigations (Chapter 5, Chapter 6) and are most commonly found in combusting flows (Chapter 5, Chapter 6). Figure 2-3 highlights the importance of the third-dimension showcasing strong flow interaction on the boundary layers.

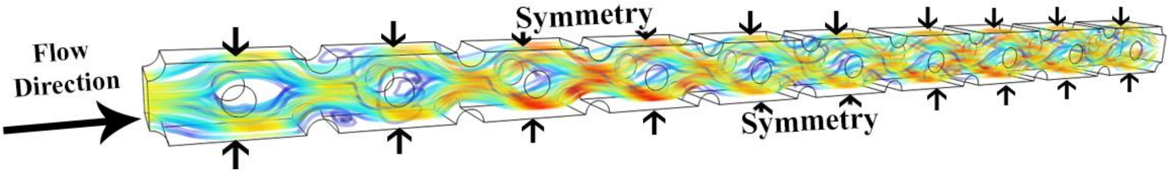

Figure 2-1: General sketch of the 3-D pore scale model

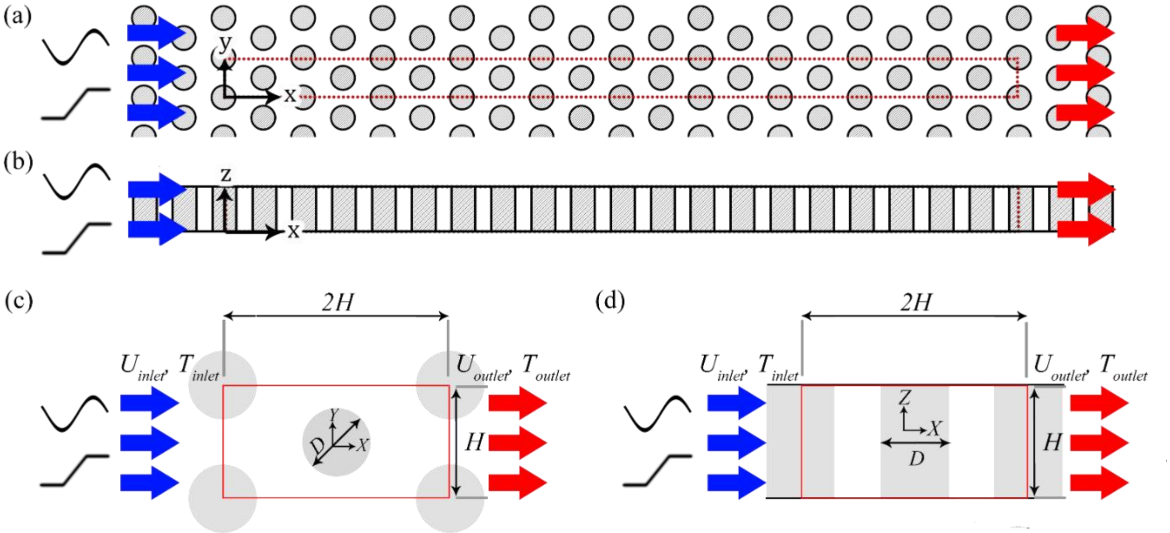

Figure 2-2: Physical model and the coordinate system (a) coordinate system in x-y plane (b) coordinate system in x-z plane (c) single pore structural unit with boundaries in x-y plane (d) single pore structural unit with boundaries in x-z plane.

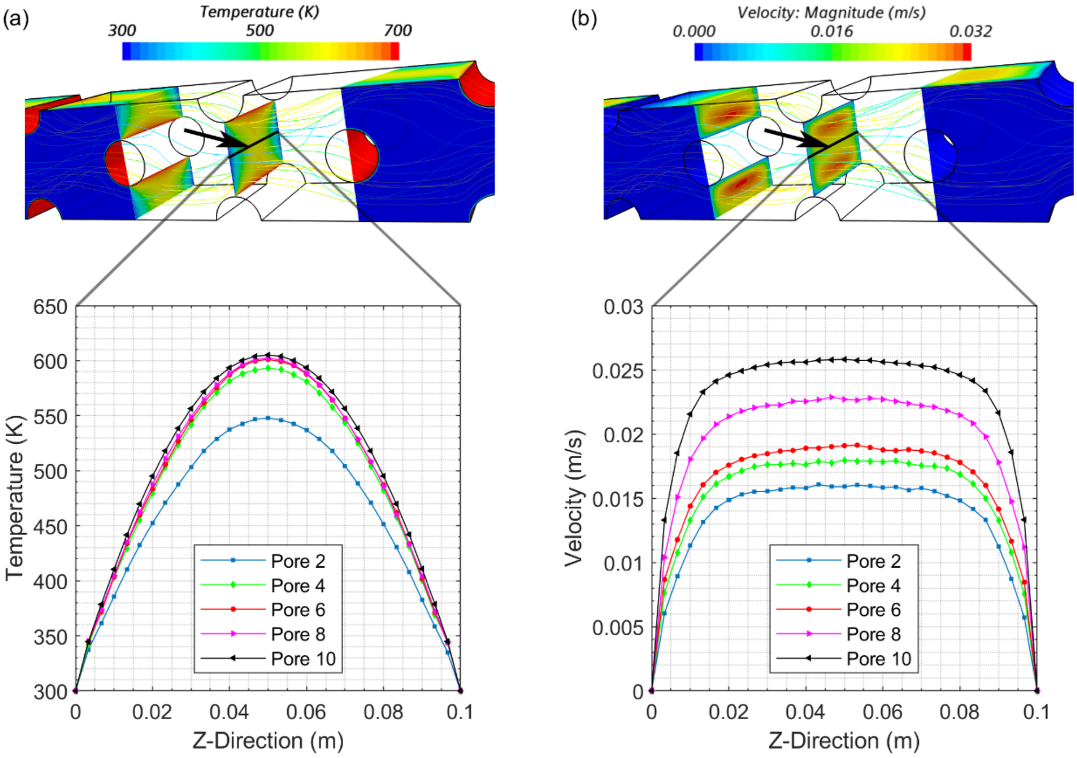

Figure 2-3: Flow interaction on the boundary layers in the third dimension (Z-Direction) Fluid type: Air, $\varepsilon = 0.874$, $Re_L=50$, $f=0.25$ Hz, $a=30\%$. (a) Temperature Profile (b) Velocity Profile

Ten cylinders are employed along the x-axis. Extensive numerical tests revealed that increasing the number of cylinders beyond this number does not change the statistics of the flow and thus the flow at the end of the current computational domain can be deemed fully developed.

To determine the minimum required number of flow obstacles, simulations were performed on a unit cell model (based on Saito and de Lemos [94] approach) with periodic boundary conditions at the inlet and outlet with an obstacle diameter of 0.05m. The solid walls were set to isothermal boundary conditions with a temperature 300K where no slip conditions were imposed. The inlet temperature was set to 200K assuming uniform fluid flow. It is noted that although the unit cell model is representative of the inner element in a porous medium, its application is restricted to steady state conditions. As a result, a carefully devised approach was taken to generate a numerical model suitable for unsteady simulations. This involved utilising the steady unit cell model as a foundation and then generating a script to re-insert the velocity and temperature profiles from the outlet to the inlet. These simulations were run continuously till the variance between the inlet and outlet fell under a designated threshold, described by Relative Profile Change, $RPC = \left(\sum_{profile} \frac{|\psi_{outlet} - \psi_{inlet}|}{\psi_{outlet}}\right) \times 100$ in which ψ is either the velocity or temperature. Table 2-1 displays the results of this study for three different values of Reynolds number. Evidently, after approximately 9 iterations and for all Reynolds numbers the change in RPC falls below 5%. Hence, it was decided to model the REV using ten identical obstacles. To ensure validation, the new model was investigated with the exact same conditions as the unit cell model. The tests showed the pressure and temperature profiles to be almost identical to the profiles after nine level of injections. Thus, a ten obstacle configuration (as shown in Figure 2-1 and Figure 2-2) was selected to carry out the investigations reported in the rest of this paper.

Table 2-1: Relative Profile Change Vs Re-injection iteration at different Reynolds numbers

	Relative Profile Change %		
Injection Level (-)	**Re_L=50**	**Re_L=200**	**Re_L=300**
1	75.6	93.6	90
2	27.6	58.3	58.4
3	10.1	36.9	40.6
4	3.8	23.6	28.6
5	1.3	15.2	19.9
6	0.6	9.5	14.1
7	0	6.1	9.9
8	0	4	7.1
9	0	2.6	5
10	0	1.4	3.4
11	0	1.1	2.1
12	0	0.5	1.8

Steady state and unsteady responses are considered for the operation of the pore-scale model. This study focuses on the thermal dynamic response at the pore level, with the introduction of sinusoidal disturbances on the velocity fluctuations at the inlet (see Figure 2-2a, Figure 2-2b, Figure 2-2c). Two symmetry planes are imprinted above and below the working model along the y-axis to reduce the computational costs and time.

The numerical simulations were conducted using the computational fluid dynamics package STAR-CCM+ 12.04.010 – a finite volume based Computational Fluid Dynamics software. An unsteady, three-dimensional, laminar flow model, coupled with the energy equation, was implemented within the fluid region for higher stability.

The following assumptions are made throughout the current analysis.

- The flow is assumed to be laminar. This is justified by noting that the Reynolds numbers used in this study remain always below 325. This assumption is made by the analysing the investigations carried out by Saito and de Lemos [95–97] where $Re_L > 1000$ the flow is deemed fully turbulent and $Re_L \approx 300$ the flow begins to transition towards turbulence. As in this study the flow spends only a small fraction of time at $Re_L > 300$, any transitional flow is ignored.

- The boundary conditions are time independent, and the temporal variations are imposed on the inlet flow.
- As shown in Figure 2-1 and Figure 2-2, a consolidated porous medium is considered [98].

2.2.2 Governing equations, boundary conditions and numerical flow solver

The conservation of mass for the fluid flow between the inlet and outlet is given by

$$\frac{\partial \rho}{\partial t}+\frac{\partial \rho u_x}{\partial x}+\frac{\partial \rho u_y}{\partial y}+\frac{\partial \rho u_z}{\partial z}=0, \tag{2-1}$$

as the mass flux enters and leaves the model. Conservation of momentum [99] for the fluid flow through the pores in x, y and z directions read

$$\begin{aligned}\left(\frac{\partial \rho u_x}{\partial t}+u_x\frac{\partial \rho u_x}{\partial x}+u_y\frac{\partial \rho u_x}{\partial y}+u_z\frac{\partial \rho u_x}{\partial z}\right)\\ =-\frac{\partial p}{\partial x}+\frac{\partial}{\partial x}\left[2\mu\frac{\partial u_x}{\partial x}-\frac{2}{3}\mu\left(\frac{\partial u_x}{\partial x}+\frac{\partial u_y}{\partial y}+\frac{\partial u_z}{\partial z}\right)\right]\\ +\frac{\partial}{\partial y}\left[\mu\left(\frac{\partial u_x}{\partial y}+\frac{\partial u_y}{\partial x}\right)\right]+\frac{\partial}{\partial z}\left[\mu\left(\frac{\partial u_x}{\partial z}+\frac{\partial u_z}{\partial x}\right)\right],\end{aligned} \tag{2-2}$$

$$\begin{aligned}\left(\frac{\partial \rho u_y}{\partial t}+u_x\frac{\partial \rho u_y}{\partial x}+u_y\frac{\partial \rho u_y}{\partial y}+u_z\frac{\partial \rho u_y}{\partial z}\right)\\ =-\frac{\partial p}{\partial y}+\frac{\partial}{\partial x}\left[\mu\left(\frac{\partial u_x}{\partial y}+\frac{\partial u_y}{\partial x}\right)\right]\\ +\frac{\partial}{\partial y}\left[2\mu\frac{\partial u_y}{\partial y}-\frac{2}{3}\mu\left(\frac{\partial u_x}{\partial x}+\frac{\partial u_y}{\partial y}+\frac{\partial u_z}{\partial z}\right)\right]\\ +\frac{\partial}{\partial z}\left[\mu\left(\frac{\partial u_y}{\partial z}+\frac{\partial u_z}{\partial y}\right)\right],\end{aligned} \tag{2-3}$$

$$\left(\frac{\partial \rho u_z}{\partial t}+u_x\frac{\partial \rho u_z}{\partial x}+u_y\frac{\partial \rho u_z}{\partial y}+u_z\frac{\partial \rho u_z}{\partial z}\right)$$
$$=-\frac{\partial p}{\partial z}+\frac{\partial}{\partial x}\left[\mu\left(\frac{\partial u_x}{\partial z}+\frac{\partial u_z}{\partial x}\right)\right]+\frac{\partial}{\partial y}\left[\mu\left(\frac{\partial u_y}{\partial z}+\frac{\partial u_z}{\partial y}\right)\right] \qquad (2\text{-}4)$$
$$+\frac{\partial}{\partial z}\left[2\mu\frac{\partial u_z}{\partial z}-\frac{2}{3}\mu\left(\frac{\partial u_x}{\partial x}+\frac{\partial u_y}{\partial y}+\frac{\partial u_z}{\partial z}\right)\right],$$

The conservation of energy for the heat transferring flow is written as

$$\rho c_p\left(\frac{\partial T}{\partial t}+\frac{\partial u_xT}{\partial x}+\frac{\partial u_yT}{\partial y}+\frac{\partial u_zT}{\partial z}\right)=k_f\left(\frac{\partial^2 T}{\partial x^2}+\frac{\partial^2 T}{\partial y^2}+\frac{\partial^2 T}{\partial z^2}\right), \qquad (2\text{-}5)$$

where all symbols have been defined in the nomenclature.

The pertinent boundary conditions include no slip condition on the external surface of the cylindrical obstacles. Further, the top and bottom of the model in the y-direction are selected as the symmetry planes (Figure 2-2a). The external surfaces of the ten obstacles of the model are all set to a constant temperature of 700K. The outlet has an initial condition with the ambient temperature (300K) and is under atmospheric pressure. The coupled flow solver was employed to model the fluid flow, while steady and implicit unsteady solvers were used throughout this study.

Under steady conditions, the flow of the fluid at the inlet was modelled as a uniform velocity and an inlet temperature of 300K. The inlet flow velocity was then modulated by superimposing a temporal sinusoidal with variable amplitude and period (frequency). The sinusoidal disturbance superimposed on the inlet flow is a sine wave with a prescribed amplitude and frequency:

$$u(0,t)=u_{in}\cdot\left(1+a_f sin(2\pi\cdot f\cdot t)\right). \qquad (2\text{-}6)$$

The Reynolds number based on the obstacle diameter is obtained by the following relation.

$$Re_L = \frac{u_{in}\rho D}{\mu}. \tag{2-7}$$

within the pore-scale model, heat is transferred by forced convection complying with the Newton's law of cooling. That is

$$q''_f = h_o\left(T_f - T_{ref}\right). \tag{2-8}$$

The surface-averaged, time-dependent Nusselt Number was calculated over each obstacle of the porous structure to evaluate the thermal response of the system. The following relation was considered to obtain the numerical value for Nusselt Number [83].

$$Nu_L = \frac{q''_f D}{k\left(T_f - T_{ref}\right)}. \tag{2-9}$$

A second order discretization method was applied to all equations and the converged solutions from alike steady state solutions were used as the starting point for the unsteady simulations. The steady state investigations were achieved for residual levels of 10^{-6} for all equations. The base time step was designated to be two orders of magnitude lower than the physical time scale and a refined time step was implemented for unsteady cases for attaining greater precision. Additionally, a considerably large value was set for the maximum time step in unsteady cases. Furthermore, the average temperature at the outlet was observed to check the convergence in time. If the simulations deviated in the final 1000-time steps by less than 0.5K the simulations were set to be terminated.

A parametric study was subsequently conducted in which the Reynolds numbers, porosity, working fluids and frequency of the inlet velocity disturbances were varied systematically. Table 2-2 displays the operating conditions and the parameters in this study. It should be noted that the frequencies of the inlet disturbances in the current study are quite low ($f \leq 2\mathrm{Hz}$). This is because only low flow velocities are considered in this work and therefore the porous system will be slow in responding to temporal disturbances superimpose on the inlet flow.

Table 2-2: Operating Conditions

Other conditions							
Ambient temperature (K)	T_{amb}	300					
Frequency (Hz)	f	0.25	0.5	0.75	1	1.5	2
Reynolds Number	Re_L	50		150		250	
Geometry							
Pore scale model length (m)	l	2.0					
Obstacle diameter (cm)	D	4		5		6	
Porosity	ε	0.717		0.804		0.874	
Fluid		air		hydrogen		carbon dioxide	
Inlet temperature (K)	T_{in}	300					
Inlet pressure (MPa)	p_{in}	0.1					
Obstacle temperature (K)		700					

2.2.3 Validation and grid independency

As shown in Figure 2-4, a polyhedral staggered mesh was used with prism layers and finer spacing around the inlet, outlet and external surfaces of the obstacles. Computational tests were performed using a mesh with varying base size to determine the grid density that would achieve an adequate balance between computational power and accuracy. The base size specifies the reference length value for all relative size controls such as the surface size, maximum cell size, and total prism layer thickness. The value of base size varies depending on the model dimensions. To verify the grid independency of the numerical solution, the Nusselt number over the obstacles was investigated for seven different base sizes. This was performed with Re_L= 50 and ε = 0.717 and the outcomes are summarised in Table 2-3. As the mesh density is increased, there is a convergence of the solution. The coarsest mesh, cell size of 0.1m, fails to accurately capture the outlet temperature and Nusselt number on each obstacle. However, solutions obtained with the grids consisting of hundreds of thousands of cells are reasonably accurate. Higher grid densities, up to a cell size of 0.001m, yield no obvious advantage in accuracy of the results. Hence, for the three-dimensional pore-scale model, all solutions presented in this work are achieved using a mesh with a cell size of 0.005m. Precautions were taken to ensure enough mesh refinement, and adequate mesh resolution.

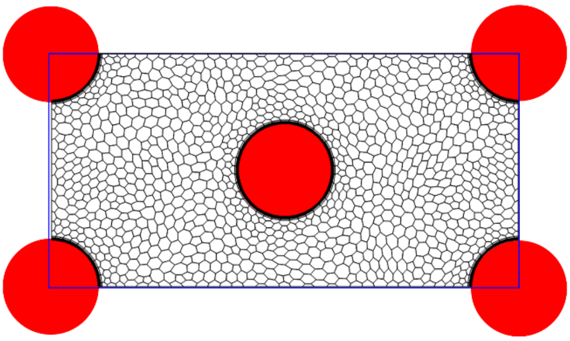

Figure 2-4: Polyhedral staggered mesh of a single pore structural unit as implemented in the current simulations.

Table 2-3: Grid Independency

	Cell Size (m)	Number of cells
Test 1	0.1	204,354
Test 2	0.05	543,607
Test 3	0.02	586,929
Test 4	0.01	611,772
Test 5	0.005	838,353
Test 6	0.003	1,662,417
Test 7	0.001	15,662,124

The current study is validated using the data reported in Ref. [85] with the use of a circular cross-section configuration, with varying Reynolds number. The Reynolds number and Nusselt number are calculated by using the Darcian velocity and the bulk temperature as the reference instead of the obstacle diameter. Table 2-4 shows a good agreement between the current results and those of Ref. [85]. Further,

Figure 2-5 depicts favourable comparisons of the current results with the numerical data of Kawahara et al. [82] and Chen and Wung [100]. Furthermore, to evaluate the unsteady performance of the simulations, the current configuration without cylinders were exposed to different ramp disturbances in the flow temperature. The predicted flow temperatures at different locations along the domain by the laminar flow model were compared to those predicted by direct numerical simulation (DNS) of the same problem [101]. The very good agreements observed in Figure 2-5a and Figure 2-5b confirm the validity of the current unsteady numerical simulations.

Table 2-4: Validation for Nusselt Number with Torabi et al. [85]

Re_D	Nu ($\varepsilon = 0.717$)	Nu (Torabi et al. [85])	% error
1	6.26	6.8	8.6
10	6.9	7	1.4
50	10.42	10.9	4.6
100	12.29	13	5.8
200	15.33	15.9	3.7

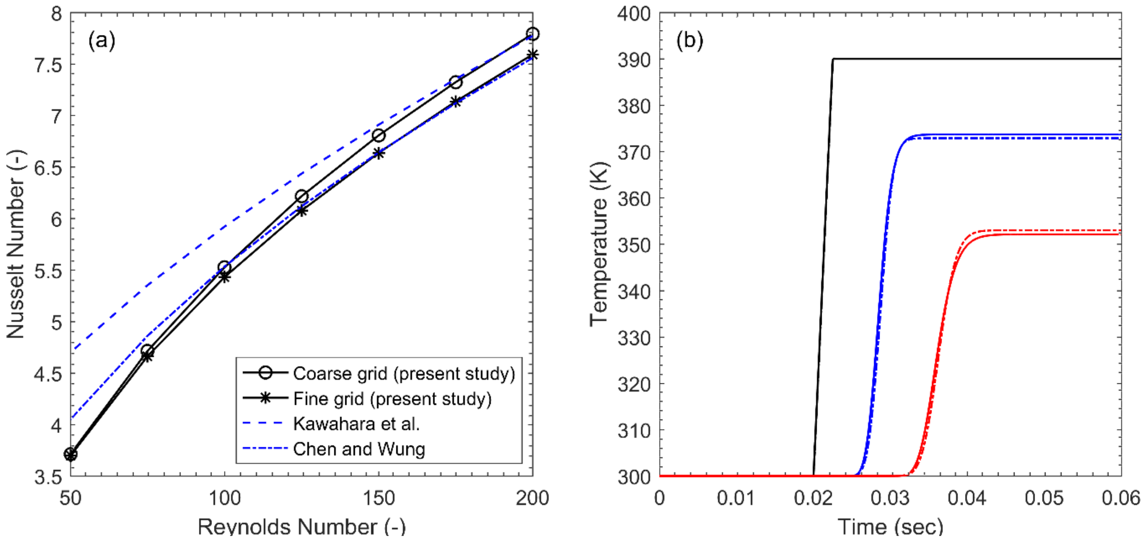

Figure 2-5: a) Comparison between Nusselt Number calculated by the current simulation and those reported in Refs. [82] [100] *over a single obstacle; b) Temporal variations of temperature at inlet (black), centre (blue) and outlet (red) for unsteady response, solid and dash-dot lines represent DNS and the current simulations, respectively.*

2.3 Results and discussion

Figure 2-6 illustrates the spatiotemporal response of the investigated flow field to a sinusoidal velocity disturbance superimposed on the inlet flow. The figure corresponds to a case with high porosity and low Reynolds number in which the wake of each obstacle is shorter than the distance between two neighbouring obstacles. The steady flow includes low velocity wake regions behind the cylinders surrounded by relatively higher velocity regions formed by the passage of the flow between the cylindrical obstacles. As clearly shown in Figure 2-6, modulation of the inlet flow by a sine wave results in a noticeable change in the magnitude of the velocity around the obstacles. This alteration in the flow velocity is advected by the mean flow and thus propagates downstream throughout the domain. Figure 2-6 shows two advective sinusoidal disturbances. These include one shown on the left-hand side of the figures advecting through the first few pores of the systems (marked by an arrow), while the other disturbance has already proceeded towards the outlet. Clearly, influences of the disturbance upon the velocity field has decayed during the downstream propagation process. This is to be expected as the fluid viscosity tends to smear out the stronger velocity gradients induced by the flow disturbance. Modulations of the flow velocity alters the local heat loss coefficient, which in turn forms a temporal heat transfer response on the external surface of each obstacle. The dynamics of this response will be investigated in the later parts of this section.

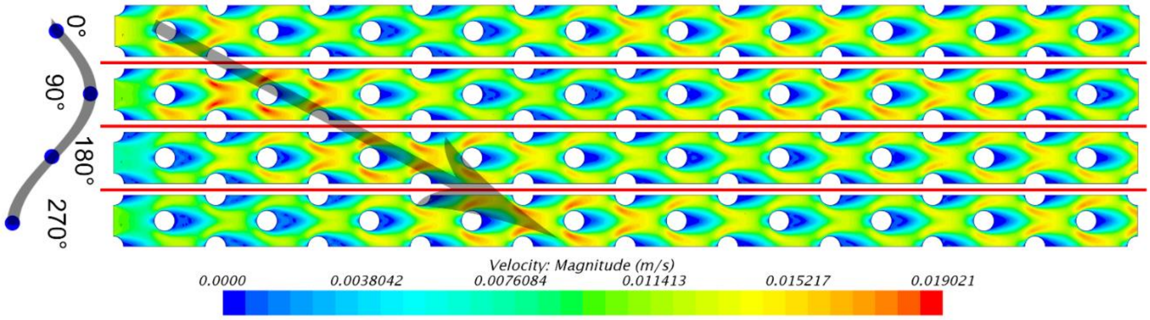

Figure 2-6: Spatiotemporal evolution of the flow field exposed to a sinusoidal inlet velocity disturbance. Fluid type: CO_2, $\varepsilon = 0.874$, $Re_L=50$, $f=0.25$ *Hz,* $a=30\%$.

Figure 2-7 shows the temperature and velocity fields of an investigated porous medium exposed to sinusoidal disturbance at the inlet velocity. Development of the steady temperature field has been shown in Figure 2-7a. This represents a typical convective system with constant temperature boundaries in which the flow temperature approaches that of the boundaries towards the outlet. Introduction of the velocity disturbance does not appear to have any obvious effect upon the flow field. It will be later shown that this is because the velocity disturbance in this case induces a relatively small perturbation in the heat loss coefficient. Nonetheless, it will be argued that the heat transfer and subsequently the temperature fields are affected by the disturbance. Figure 2-7b shows the spatiotemporal evolution of the flow field during a full period of inlet velocity modulation by a sine wave. The trends shown in this figure are qualitatively similar to those discussed in Figure 2-6. However, the changes in the fluid type and the porosity of the medium have resulted in the intensification of the velocity effects of the flow disturbance. It is worth noting that the local maximum velocity in Figure 2-7b and Figure 2-6 are well below 1m/s (Reynolds numbers below 325) and thus the transition to turbulence in any part of the flow remains unlikely.

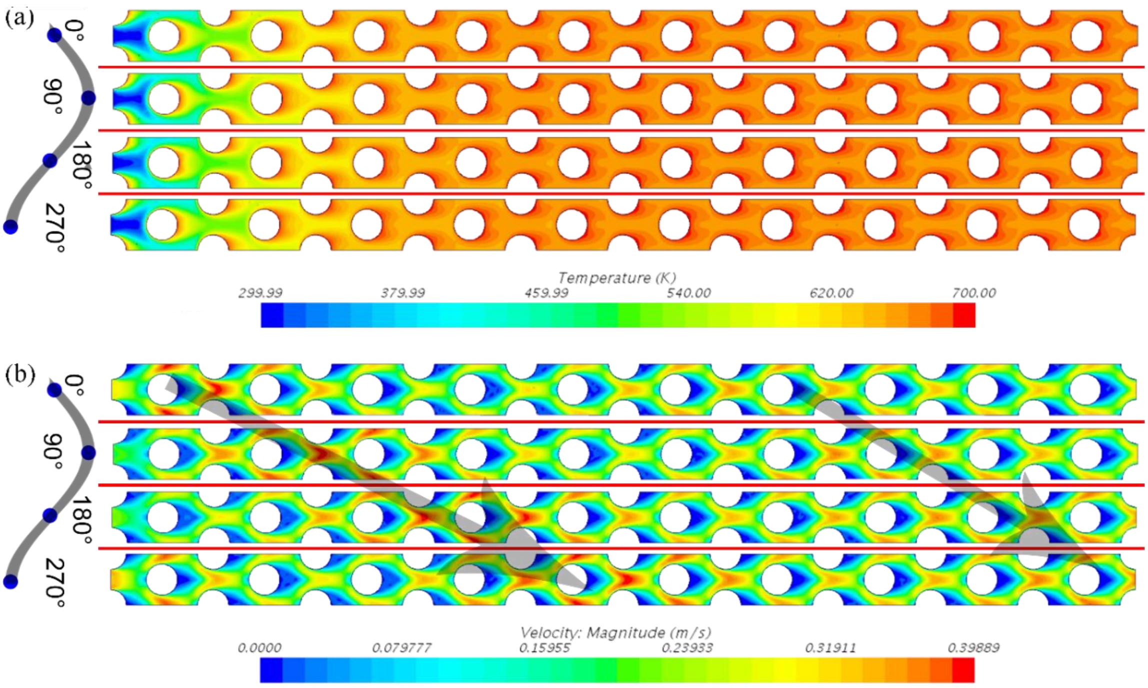

Figure 2-7: Spatiotemporal evolution of the flow temperature and velocity fields exposed to a sinusoidal inlet velocity disturbance. Fluid type: H_2, $\varepsilon = 0.717$, $Re_L=50$, f=0.25 Hz, a=30% (a) temperature field (b) velocity field.

The normalised Nusselt number on each obstacle is defined as $Normalised\ Nu = Nu_L \div \overline{Nu_L}$ where $\overline{Nu_L}$ is the mean Nusselt number averaged over the entire external surface area of the obstacle in the steady flow. Figure 2-8 shows the time trace of the normalised Nusselt number when the flow is modulated by a sinusoidal disturbance with a frequency of 0.25 Hz. It is clear that the temporal response of the Nusselt number over the three examined obstacles closely resembles a sine wave, while there is a significant drop of the amplitude for those obstacles that are located farther from the inlet. This observation is further confirmed by the spectra of the traces of Nusselt numbers' response (calculated through using fast Fourier transform, FFT) shown in Figure 2-8b. The occurrence of response at the same frequency as the input excitation is a classical sign of a linear system [102,103]. It is, therefore, inferred that in this case heat transfer in the porous medium can be approximated as a linear dynamic system.

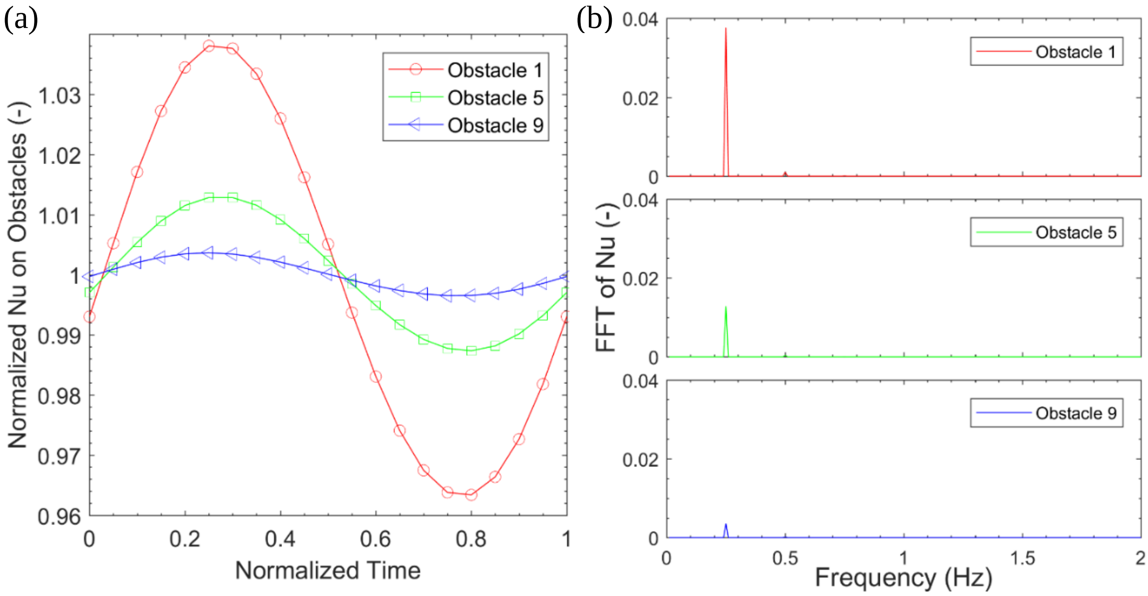

Figure 2-8: (a) Temporal evolution of the normalised Nusselt number over three different obstacles (normalised time=time (s)/period of sine wave(s)), (b) Spectrum of Nusselt number. Fluid: air $\varepsilon = 0.874$ Re_L=50 f=0.25 Hz.

The dynamics of a linear system can be readily predicted by a transfer function, which gives information on both amplitude and phase of the response [102]. Transfer function of a linear dynamical system offers a major convenience in predicting the responses of such system to any input disturbance. This is because any arbitrary disturbance at the system input can be decomposed into a series of sinusoidal disturbances by utilising Fourier transform. The transfer function enables predicting the system response to each of those sinusoids and the linearity of the system allows adding them to figure out the system response to the arbitrary input disturbance. The concept of transfer function is usually used for a single input, single output system. Here, we consider the oscillating inlet flow as the input of a dynamic system for which the oscillating normalised Nusselt number at a given obstacle is the output. As a result, in the current problem ten transfer functions can be defined for the ten considered obstacles (see Figure 2-2). The amplitude of these transfer functions is defined as $a(\omega) = |Normalised\ Nu_{L_i}(\omega)|$ in which i denotes the obstacle number. The amplitude and phase of these transfer functions were calculated for all obstacles and two representative set of results are shown in Figure 2-9. The amplitudes of transfer function shown in Figure 2-9a and Figure 2-9b clearly indicate that the system is most responsive to the lowest excitation frequencies. As expected, the amplitude of the response for the obstacles situated farther from the inlet is significantly smaller than those located upstream. This is due to the decay of disturbance throughout the advection process (see Figure 2-6 and Figure 2-7). As the frequency of the input sine wave increases, the amplitude of the response drops considerably. This behaviour can be consistently observed for all considered obstacles in Figure 2-9 and Figure 2-9b. The strong response of the normalised Nusselt number to low frequency sinusoids is in keeping with those already reported for other mechanical [104] and thermal systems [105,106]. In general, low frequency disturbances provide a longer time for a physical system to respond and thus a larger amplitude is often obtained at low frequencies of the input disturbance. In the current case, the low frequency sinusoidal disturbances provide enough time for the process of heat convection on the surface of the obstacle to be completed. Yet, as the frequency of the flow disturbance increases, the available time for the interactions between the disturbance and heat convection becomes shorter and thus the amplitude of the response diminishes. Although not shown in Figure 2-9, a simple extrapolation reveals that at certain high frequency, the system response drops to almost zero. This is where the disturbance is temporally so short that the heat convection process essentially cannot respond to it. Once again, this feature is analogous to those reported for other thermofluid systems [105,106].

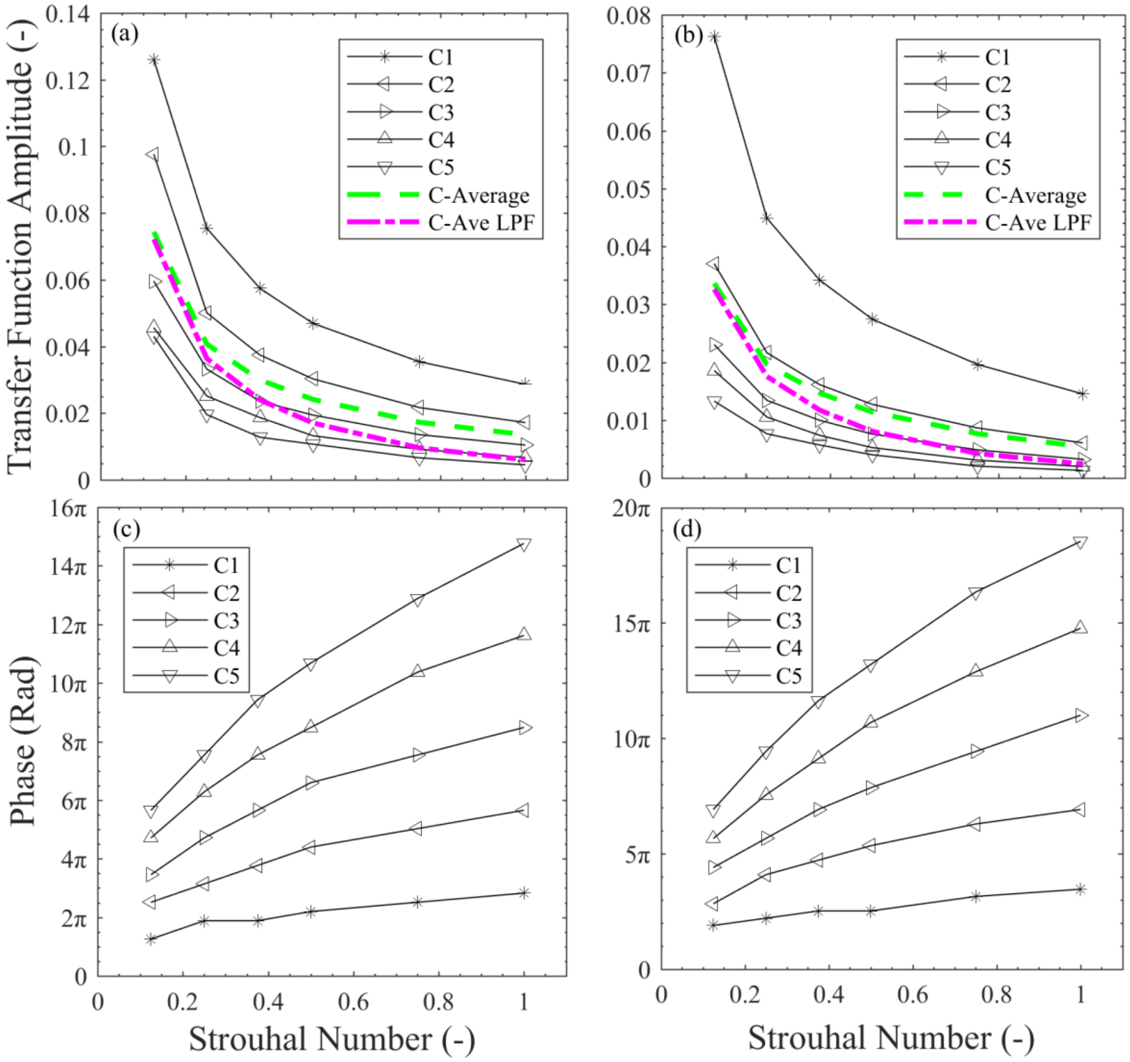

Figure 2-9: Transfer functions of heat convection evaluated over different obstacles (C1-C5), (a) Fluid: CO_2, $\varepsilon = 0.874$ $Re_L = 50$– Transfer function amplitude, (b) Fluid: H_2, $\varepsilon = 0.804$ $Re_L = 50$– Transfer function amplitude, (c) Fluid: CO_2, $\varepsilon = 0.874$ $Re_L = 50$– Phase of transfer function, (d) Fluid: H_2, $\varepsilon = 0.804$ $Re_L = 50$– Phase of transfer function.

Figure 2-9c and Figure 2-9d indicate that the phase of the transfer function resembles that of a classical convective lag [103]. This is the time elapsed for the flow disturbance to move from the inlet to a given obstacle. For a system with constant convective lag, the phase will be a straight line. The deviation from this implies changes in the advective velocity of the disturbance. As already discussed, this is because of the decay and annihilation of the initial disturbances during the process of advection over flow obstacles. Considering these trends, the transfer function of the thermal system including all ten obstacles can be approximated in two different ways. First, the responses of all obstacles can be simply averaged. Second, the amplitude of the thermal system can be approximated as a ‘low-pass filter’ [107–109] while, the phase is governed by a convective lag. It is well established that many thermofluid systems are practically low-pass filters [110,111] as such they respond only to low frequencies and become irresponsive to any excitation that exceeds a certain frequency. The low pass filter only allows low frequency signals from 0Hz to a cut off frequency, f_c to pass whilst blocking those any higher. With visual inspection, it can be seen in Figure 2-9a and Figure 2-9b that the cut-off frequency is around the Strouhal number of 0.5. Equation (2-10 and Equation (2-11 are the modified relations used to create a low pass filter for the average amplitude of the thermal system [110,111].

$$Low\ pass\ filter = \overline{a_f} \cdot \frac{X_C}{\sqrt{R^2 + X_C^2}}, \tag{2-10}$$

$$X_C = \frac{1}{2\pi f C}, \tag{2-11}$$

where all terms are defined in the nomenclature. The low pass filter introduced in Equation (2-10) and Equation (2-11) and illustrated in Figure 2-9 represents an approximation of the heat transfer dynamics of the porous system. Figure 2-8 further shows that the amplitude of the transfer function predicted by the low-pass filter is close to the average response. The phase of the system can be simply approximated by that of $e^{i2\pi f(t+\tau_j)}$ in which τ_j is the time taken for the disturbance to travel from the inlet to obstacle j.

The foregoing findings on transfer function were entirely based upon the assumption of linearity of the system, as confirmed by Figure 2-8. However, there are cases for which the system dynamics are no longer linear. For example, Figure 2-10 shows the time trace and spectrum of Nusselt number for a case similar to that shown in Figure 2-8 but with a different type of fluid and a higher Reynolds number. The appearance of two peaks in the spectra, particularly for the obstacles located farther from the inlet, is a clear indication of deviation from linearity. This is further supported by Figure 2-11 which shows the phase portrait (Lissajous pattern) of the normalised Nusselt number calculated for three different cases. Figure 2-11a corresponds to a case with a linear response in which the oval shapes in phase portrait are axisymmetric. However, this feature disappears in Figure 2-11b and Figure 2-11c indicating a progressive departure from the linear response. Figure 2-11c corresponds to a strongly nonlinear system for which the phase portrait can become significantly asymmetric [112]. Prediction of the dynamics of nonlinear systems is quite involved and, in many instances, the only way for predicting the behaviours of such systems is through high order modelling, which can be computationally expensive. This is, of course, very different to the linear approach discussed previously in which the whole dynamics could be inferred from the transfer function with little computational cost. It is therefore essential to identify under which conditions the system can be approximated as a linear system. This, in turn, calls for the quantification of nonlinearity.

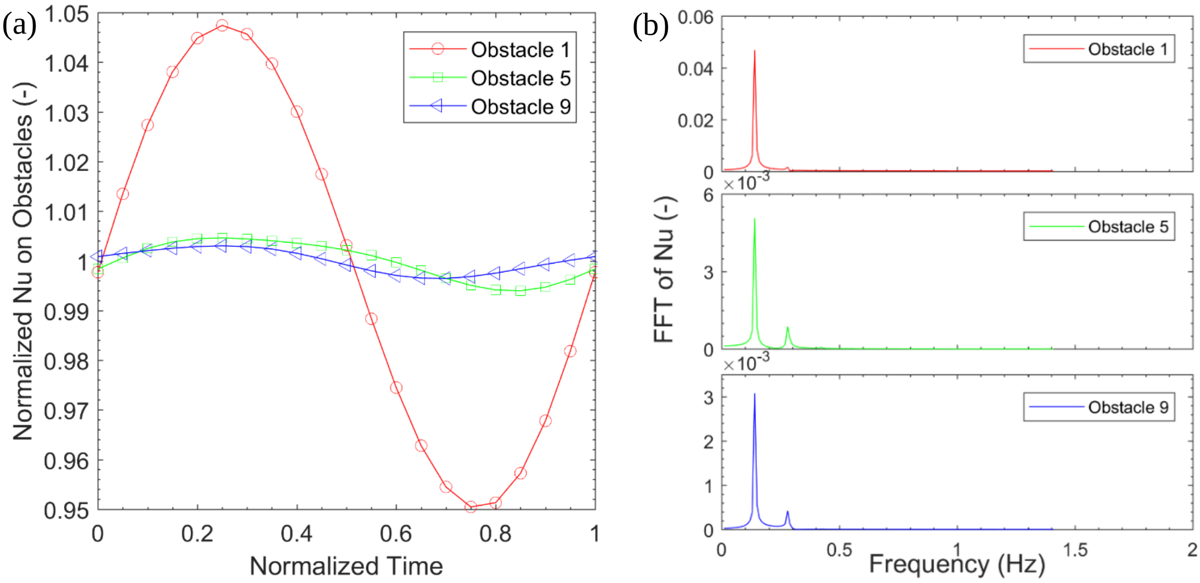

Figure 2-10:(a) Temporal evolution of the normalised Nusselt number on three different obstacles (normalised time=time (s)/period of sine wave(s)), (b) Spectrum of Nusselt number. Fluid: CO_2 $\varepsilon = 0.804$, $Re_L = 150$, f=0.25 Hz.

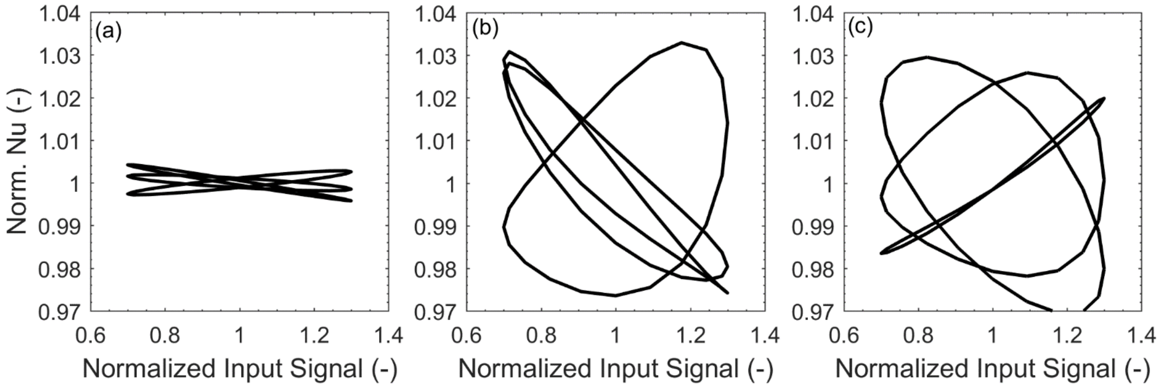

Figure 2-11: Phase Portrait (Lissajous pattern), (a) linear case: Air, ε = 0.804, Re_L =50, f=0.25 Hz, (b) mildly non-linear case: Air, ε = 0.804, Re_L =250, f=0.25 Hz, (c) non-linear case: CO_2, ε = 0.804, Re_L =250, f=0.75 Hz.

Here, a measure of non-linearity is introduced to evaluate deviation from linearity of the response. This is given by

$$\delta = \frac{n}{n-o}, \qquad (2\text{-}12)$$

where δ is the measure of non-linearity, n, Euclidean norm of the normalized Nusselt number recorded at each obstacle and o is the discrete Fourier transform single-sided amplitude spectrum of the normalized Nusselt number at each obstacle [113]. Equation (2-12 assigns value of 0 to a completely linear system and gives value of 1 to a completely nonlinear system. Thus, any real dynamic system will be assigned a value between 0 and 1. Figure 2-12 shows the values of the measure of non-linearity (δ) calculated for all ten obstacles, indicating that the extent of nonlinearity can vary significantly with frequency. That is to say that for a given obstacle, the Nusselt number can respond almost linearly to a disturbance at one frequency and strongly nonlinearly to another frequency. Figure 2-12 shows that the response of all obstacles to high frequency disturbances remains nearly linear. However, the response to the lowest frequency can be strongly nonlinear. The physical origin of nonlinearly in the current problem is due to the interactions between the flow disturbances and the boundary layers around the obstacles as well as those with the wake region behind the obstacle. Such interactions are very complex, and their predictions require detailed analysis. The current results indicate that the long duration (low frequency) disturbances have sufficient time to go through these interactions and thus can render a nonlinear response. However, the short term, high frequency, disturbances somehow by-pass the fluid dynamic interactions and provide almost linear response with a smaller amplitude.

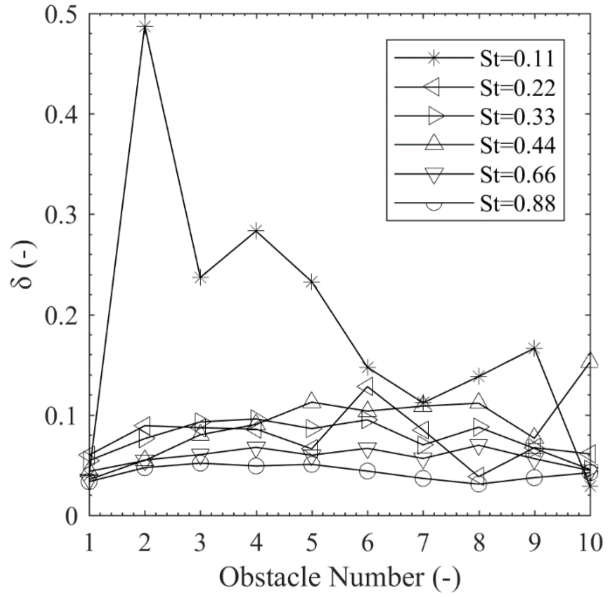

Figure 2-12: The value of measure of nonlinearity of Nusselt Number over different obstacles – Fluid: Air, ε = 0.874, Re_L =250.

Here, the focus is on identifying the conditions for which the nonlinear response can be safely ignored and thus the dynamics of heat transfer system can be predicted by the straightforward transfer function approach. Figure 2-13 represents the maximum non-linearity factor with changes in porosity and Reynolds number for all six investigated Strouhal number and across all ten obstacles with the working fluid of air. This figure shows the maximum value of the measure of nonlinearity for each combination of Reynolds number and porosity (total of 9). It also specifies the obstacle number and Strouhal number for which the maximum is reached. This figure clearly shows that there is no monotonic trend with the Reynolds number and porosity. For example, the maximum value of the measure of nonlinearity at Re_L=50 is close to zero and it increases to a higher value as the Reynolds number increases to 150. However, it drops down again when Reynolds number increases to 250. This is an important result, as there is often a notion that lower Reynolds numbers render linear response and higher Reynolds number contribute to nonlinearity. Such expectation stems from the macroscopic models of fluid flow in porous media (e.g. Darcy and Darcy-Brinkmann-Forchheimer models) which add nonlinearity only to the higher

Reynolds number flows. However, the current results indicate that for a dynamic problem the situation can be more complicated and Reynolds number and porosity can both affect the level of nonlinearity in a non-monotonic fashion. Figure 2-13, nonetheless, shows that regardless of the value of porosity the level of nonlinearity always remains reasonably small at the lowest investigated Reynolds number (Re_L=50). It can be then postulated that for low enough Reynolds numbers, the system is almost linear and thus the transfer function approach can be utilised to predict the dynamics of heat transfer. Yet, increases in Reynolds number does not necessarily push the system towards a nonlinear response.

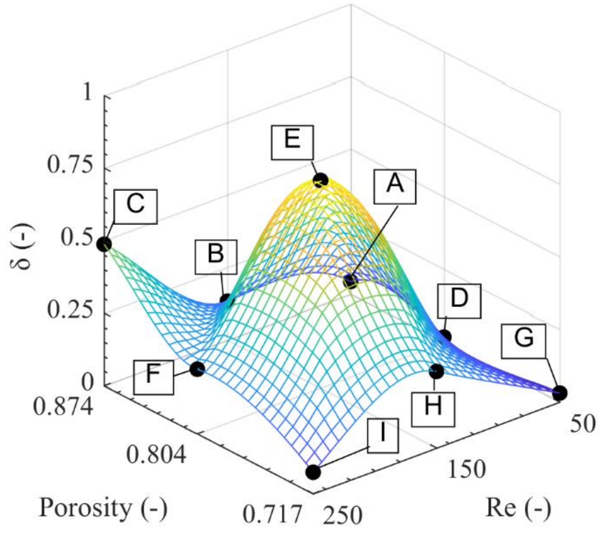

Figure 2-13: The maximum value of measure of nonlinearity in Nusselt Numbers, for air. A) St=0.125, C9 B) St=0.125, C7 C) St=0.125, C2 D) St=0.125, C2 E) St=0.125, C8 F) St=0.125, C2 G) St=1, C2 H) St=0.125, C6 I) St=0.25, C2.

2.4 Summary and conclusions

Unsteady forced convection in porous media can happen in the systems subject to time-varying inlet flows. Examples of such systems can be readily found in electrochemical systems and porous burners used for the combustion of renewable fuels. In these applications, it is necessary to predict the heat transfer response of the system to arbitrary disturbances superimposed upon the inlet flow. Although it is possible to numerically model such responses, they are likely to be computationally quite demanding. However, usually heat transfer predictions should be made over a short period of time and through using a limited computational power. It is, therefore, desirable to use the classical methods of predicting the system dynamics without conducting a detailed computational study for every disturbance that the system may become exposed to. Nonetheless, such methods (e.g. transfer functions) are mostly limited to linear dynamical systems. This raises an important need to critically assess the linearity of the dynamic response of heat convection in porous media and find out under which conditions a transfer function approach can be used. To address this issue, a pore-scale analysis of unsteady forced convection was conducted in a reticulated porous medium consisting of several flow obstacles and subject to a temporally modulated inlet flow by a sinusoidal disturbance. The spatio-temporal evolutions of the flow disturbances within the investigated porous medium were simulated numerically. Further, the Nusselt number on each flow obstacle was considered as the output of a dynamic system for which the assessment of linearity was subsequently carried out. The key findings of this study can be summarised as follows.

- At low Reynolds numbers, the heat transfer response remains almost linear and therefore, a transfer function approach can be taken to predict the system dynamics.
- The transfer functions of all obstacles are most responsive to low frequency excitation and nearly insensitive to higher frequencies and, therefore closely resemble a low-pass filter.
- Low frequency disturbances appeared to be more likely to lead to nonlinear response. This can be attributed to the availability of enough time for the flow disturbance to interact with the boundary layers formed around the obstacles.
- For linear cases, the average amplitude and phase response of the porous medium can be approximated by a low-pass filter and a convective lag, respectively.
- Calculation of the measure of nonlinearity revealed that, rather counterintuitively, increases in Reynolds number do not necessarily enhance nonlinearity of the heat transfer response. In fact, non-monotonic trends in the level of nonlinearity were observed with respect to Reynolds number and porosity of the medium.

As established in the current chapter, transfer functions are mostly limited to linear dynamical systems. Thus, the need to assess the linearity of the dynamic response of heat convection in porous media and the criteria under which the transfer function approach is applicable is of utmost importance. Therefore, chapter 3 is a continuation of the existing study with varied initial conditions/working fluids.

Chapter 3 On the unsteady forced convection in porous media subject to inlet flow disturbances – A pore-scale analysis

International Communications in Heat and Mass Transfer – Rabeeah Habib, Bijan Yadollahi, Nader Karimi, Mohammad Hossein Doranehgard

3.1 Introduction

The dynamic response of forced convection in porous media to imposed disturbances is of high practical significance. Many natural and manmade systems involve forced convection within porous media in which the inlet flows are time dependent. Examples include fuel cells [114,115], heat exchangers [116] Stirling engines and pulse tube cryo-coolers as well as human circulatory systems [59]. The most conventional way of characterising the response of any physical system to input temporal disturbances is by working out the frequency response or transfer function [103]. This provides a strong means of predicting the system response to any arbitrary temporal disturbance with minimal computational effort. In this approach the response of system to harmonic inputs are measured/computed for a range of frequencies. Through using Fourier transformation, any arbitrary intake can be deconstructed into a group of harmonics. Since transfer function provides the response of the system to each of those harmonics, the total response can be readily devised through superposition.

Although transfer functions are very helpful in predicting the dynamic response, they are limited to linear systems. For that reason, prediction of the response of a nonlinear system to input disturbances often involves full simulations, which can be highly demanding. Hence, it is essential to evaluate linearity of different systems and determine the applicability of transfer function approach to prediction of their dynamics. This is particularly the case for thermofluid systems as the strong nonlinearity of momentum transfer often tends to dominate the dynamics of these systems [117,118]. Nonetheless, slowly moving fluid systems can be, sometimes, modelled as linear systems [50]. Given the major convenience that linear dynamics offer, it is crucial to figure out under which conditions a system can be approximated as linear. The current work aims to answer this question addressing forced convection within a porous structure for which the fluid flow is relatively slow and therefore the dynamics might remain nearly linear.

A number of articles reported studies on forced convection in porous media [119,120]. The general area of macroscopic analysis of forced convection in porous media has already received substantial attention. Numerous examples of steady ([121,122]), unsteady ([116,123]), turbulent flow ([124–126]) and local non-equilibrium ([127–129]) studies can be readily found in the literature. It is, however, known that macroscopic approach to heat convection in porous media is an approximative method and that a pore-scale understanding of the underlying physics is an important necessity. This is particularly the case for unsteady processes as they are more prone to being smeared out in the averaging exercises leading to macroscopic formulations [50,130]. Here, a brief review of the literature on the pore-scale analyses of forced convection of heat is put forward. The studies have been arranged in a chronological order to better represent the historical evolution of this branch of research on convection in porous media.

Fujii et al. [131] numerically investigated heat transfer in a two-dimensional model. Incorporating a steady laminar flow, they modelled a square bank consisting of five cylindrical obstacles with an in-line arrangement and solved Navier Stokes and energy equations. Isothermal boundary conditions were imposed on the tube wall and Reynolds number, Re_L, was varied between 60-300. Fujii et al. [131] discovered a connection between flow and heat transfer and the type of flow obstacles in the porous configuration. Ma and Ruth [132] conducted a numerical analysis of high Forchheimer number flow in a two-dimensional porous model. Their problem consisted of an interconnected three unit-cell capillary configuration in which Navier Stokes equations were solved. Ma and Ruth [132] developed the macroscopic momentum equations by applying the volume averaging concept and calculated macroscopic parameters such as permeability and Forchheimer number. They altered the Reynolds number, Re_D, between 0.01-100, and argued that the macroscopic response of the system involves nonlinear flow when $Re_D \approx 10$.

Nakayama et al. [133] examined steady heat and fluid flow in a two-dimensional anisotropic configuration. These authors modelled an inline arrangement of square obstacles to represent a microscopic porous system. The square obstacles were set to constant temperature; higher than that of the inlet temperature. Navier Stokes and energy equations were solved numerically for a single unit cell structure and laminar flow regime. The results procured were then subject to volume averaging to analyse the macroscopic parameters similar to those of Ma and Ruth [132]. Nakayama et al. [133] compared the effects of increasing the Reynolds number with respect to the Nusselt number at two different modes of anisotropy. They concluded that when the system is modelled as isotropic, at 0° of anisotropy, there is very little augmentation in Nusselt number, $Nu,$ as Reynolds number, Re, is increased. However, when the system has 45° anisotropy there is a sharp incline in Nu when $Re_L \geq 10$. More recently and inspired by Saito and Lemos [134] and Kuwahara et al. [82], Gamrat et al. [83] numerically studied heat transfer over square obstacles with low Reynolds number ranging between $0.05 \ \leq Re_D \leq 40$. Modelling the two-dimensional square obstacles in an in-line and staggered arrangement for a periodic unit cell, the flow was steady and laminar also, isothermal and isoflux boundary conditions were implemented. Gamrat et al. [83] found that, for a staggered arrangement, there is a greater change in Nusselt number by increasing Reynolds number compared with an inline arrangement. For both arrangements, higher porosities resulted in lower Nusselt numbers.

In a dynamic analysis, Kim and Ghiaasiaan [89] considered square particles in an inline arrangement with six unit cells simulating unsteady laminar flow, modulated by the external flow pulsations. The oscillatory flow had a frequency range of $20\ \mathrm{Hz} \leq f \leq 64\ \mathrm{Hz}$. Navier Stokes equations were solved using the commercial software FLUENT followed by the application of the volume averaging concept to calculate the macroscopic parameters for each unit cell. Kim and Ghiaasiaan [89] showed that the value of the cycle-averaged permeability coefficients were similar between steady and unsteady flows. However, the cycle averaged Forchheimer coefficients were reported to be quite responsive to flow pulsation. As a result, the values recorded for steady flow were naturally greater. Variable parameters such as ε and Re_D were found to be the core cause of phase change between the velocity and pressure oscillations.

A two-dimensional laminar model containing square obstacles in an inline arrangement was analysed by Alshare et al. [90]. The Representative Elementary Volume (REV) was designated as a unit cell, subject to steady and unsteady flows in both isotropic and anisotropic conditions. The square obstacles were set to constant heat generating thermal boundary conditions. The flow angle was varied between 0° and 90° and Re was altered between 1-1000. For steady flows, the results were similar to those of Nakayama et al. [133] where the increase of Reynolds number led to a gradual increase of Nusselt number under isotropic conditions. Additionally, for anisotropic conditions there was a drastic increase in Nusselt number with Reynolds number. Alshare et al. [90] further showed that the isotropic model was unaffected by the flow angle. However, permeability of the anisotropic model changed between the two principal permeabilities. Subsequently, Pathak and Ghiaasian [91] studied the effects of thermal dispersion and convective heat transfer in a laminar oscillating flow. Pathak and Ghiaasian [91] argued that a single unit cell model neglects the entrance effects complications and the phase lag, making the periodic boundary conditions unsuitable for oscillatory flows. As a result, they modelled an inline arrangement of two-dimensional square particles [91]. The oscillatory flow frequency was set between 0-100 Hz and the Reynolds number varied between 70-980. It was found that as the frequency increases there is an augmentation in the average convection coefficient and, for a higher Reynolds number a large average convection coefficient was reported. However, the average Nusselt number dropped at higher porosities.

Penha et al. [78] proposed a computational method to solve conjugate heat transfer with isothermal conditions for a three-dimensional porous medium including periodic REVs. The system was arranged in an aligned and staggered way; similar to that of Nakayama et al. [133,135] and Kuwahara et al. [82]. A pair of pore-scale energy equations were solved for fluid and solid regions to characterise the conjugate heat transfer. This further allowed Penha et al. [78] to average the heat transfer coefficient as the temperature of the solid altered gradually, with respect to timescale of the developing fluid. In a study of fuel cells, Yuan and Sundén [114] analysed heat transfer in a porous medium with the use of pore-scale energy equations. A simplified two-dimensional porous model was developed within a parallel plate; with the top wall subject to a constant heat flux and the lower wall set to adiabatic conditions. This included a set of 5 × 5 cylindrical solid particles in an inline arrangement subject to a uniform flow. Yuan and Sundén [114] altered the operating conditions to simulate various scenarios and showed that Knudsen number was minuscule to overlook the rarefaction effect.

In a different work, Pathak et al. [92] studied conjugate heat transfer like that of Penha et al. [78] but with exposure to a laminar pulsating flow. This involved simulation of a two-dimensional system with seven aligned square rods which were considered as the REV and, pulsating frequency was altered between 0-60 Hz (at two different amplitudes). The pore-scale results were then used to work out the volume-averaged Darcy permeability, Nusselt number and Forchheimer coefficient showing that these parameters were highly responsive to pulsating flow and change in amplitude. Amongst other findings, Pathak et al. [92] stated that extrapolative approaches and relationships which are built on uniform consistent flow are not suitable for investigating periodic flow systems. In a similar study, Mulcahey et al. [136] examined the effects of oscillatory flows upon heat transfer and drag in a two-dimensional array of square obstacles imitating a heat exchanger. Extending the model from Pathak et al. [92] to ten unit-cells as the REV, the square particles were set to a constant temperature of 300K whilst the inlet temperature was 200K. Mulcahey et al. [136] found the drag coefficient plummeted with higher porosities and Re_L but had little or no sensitivity to the changes in the oscillation frequency of the flow. The Nusselt number was reported to augment with the decrease in the period of the pulsating flow and with the increase in Re_L. It was concluded that oscillatory flows could enhance heat transfer in heat exchanger tube bundles.

In their numerical investigation, Imani et al. [137] analysed the effects of ε, Re, Pr, thermal conductivity ratio and heat conduction on heat flux splitting at the boundary of a porous medium. They designed a channel with parallel plates, consisting of three different porous configurations of random, inline and staggered. The inlet was set to uniform velocity with the working fluid being air and water. The square obstacles were set to a constant heat flux and the parallel plates were assumed to be thermally insulated. The system was modelled under steady conditions with laminar flow ($1 \leq Re_L \leq 50$). Imani et al. [137] employed

Lattice Boltzmann Method to solve for fluid flow and heat transfer and found that all the investigated parameters could influence heat flux splitting at the external boundary of the porous medium. However, the effects of some parameters were reliant on those of others such as the thermal conductivity ratio between solid and fluid.

Teruel [138] studied the entrance effects on heat transfer between the solid and fluid regions through porous media. They investigated a porous medium consisting of two-dimensional square obstacles in a staggered arrangement. The inlet temperature was set to be higher than the constant temperature at the fluid/solid interface. The system was modelled under microscopic laminar flow and periodic boundary conditions were applied to the outlet of the model. The volume averaging concept was utilised to obtain the interfacial heat transfer coefficient. The results showed that the flow was characterised by a developing region which could be multiple REVs in length showing agreement with Pathak and Ghiaasian [91]. Teruel concluded that the macroscopic energy equation model might show large discrepancies if the entrance effect was to be neglected [138].

Pore-scale, turbulent heat convection in a three-dimensional channel filled with porous media at a T-junction was numerically analysed by Yang et al. [79]. The porous media was modelled as square rectangular obstacles in both inline and staggered arrangements and fully developed flows were passed through the T-junction. The results showed that Nusselt number for the inline arrangement was less than that of the staggered arrangement. However, it was found that with increasing the flow rate, inline arrangement featured a dramatic increase in Nusselt number while, little increase was recorded for a staggered arrangement. Most recently, Jafarizade et al. [139] analysed heat convection in a metal foam geometry with the use of micro-tomography. The aluminium foam was simulated through a three-dimensional unsteady model with a Re_L of 10-200. The authors [139] presented the laminar model in terms of a structural factor to calculate the heat transfer coefficient. They found that with the addition of this new parameter, the accuracy of Nusselt number correlation was affected for application through ranges of pore diameter and porosity. However, Jafarizade et al. [139] argued that the developed correlation could still decently represent convection coefficient of the porous metallic foams. In another recent work by the same group, Afshari et al. [140] numerically studied thermal dispersion in granular porous media using a pore-scale model. Microscopic governing equations were used to solve the steady laminar flow of granular porous media. A direct numerical simulation was then carried out to calculate the macroscopic thermal dispersion. The system under investigation was simulated as a three-dimensional configuration with circular grains and varying diameters. Afshari et al. [140] discovered that when under advection dominated regime, normalised longitudinal dispersion coefficient increased with increases in the fluid to solid thermal conductivity ratio [141].

Ahmed et al. [142] investigated the thermal performance of a pipe partially filled with metal foams. A grooved metal foam was used to observe heat transfer and fluid flow characteristics. It was reported that the aspect ratio of 0.55 results in the optimal Nusselt number. Chakkingal et al. [143] studied the combined effects of natural and forced convection in a heated cavity filled with porous media. Richardson number was altered between 0.025-500 and it was found that heat transfer improves when forced convection is travelling in the same direction as natural convection. The reverse behaviour was noted for opposing forced and natural convection. Qin et al. [144] analysed the effects of flow boiling in a two-dimensional open-cell metal foam using Lattice Boltzmann method. The pore-scale study systematically varied Reynolds number, porosity and Rayleigh number, and showed that convective heat transfer is suppressed due to the bubble motion confinement within the metal foam.

It follows from the review of literature that, except for a few studies ([89-92,136]), the response of forced convection within porous media to oscillating flows at the inlet has not been investigated at pore-scale. Further, the existing studies are mostly attentive to the value of Nusselt number and the factors influencing that under oscillating flow conditions. Consequently, the dynamics of heat transfer have comparatively received much less attention. As a result, our understanding of the dynamic response of porous media to incoming flow disturbances is still largely incomplete. The current study aims to address this issue.

3.2 Methodology

3.2.1 Problem configuration, governing equations and assumptions

A visual representation of the analysed pore-scale configuration is depicted in Figure 3-1. This includes a three-dimensional model consisting of cylindrical obstacles in staggered arrangement in which a steady or temporally modulated flow enters from left-hand side. This configuration is subject to periodic boundary conditions on the upper and lower boundaries. The reason for the selection of such configuration will be discussed later.

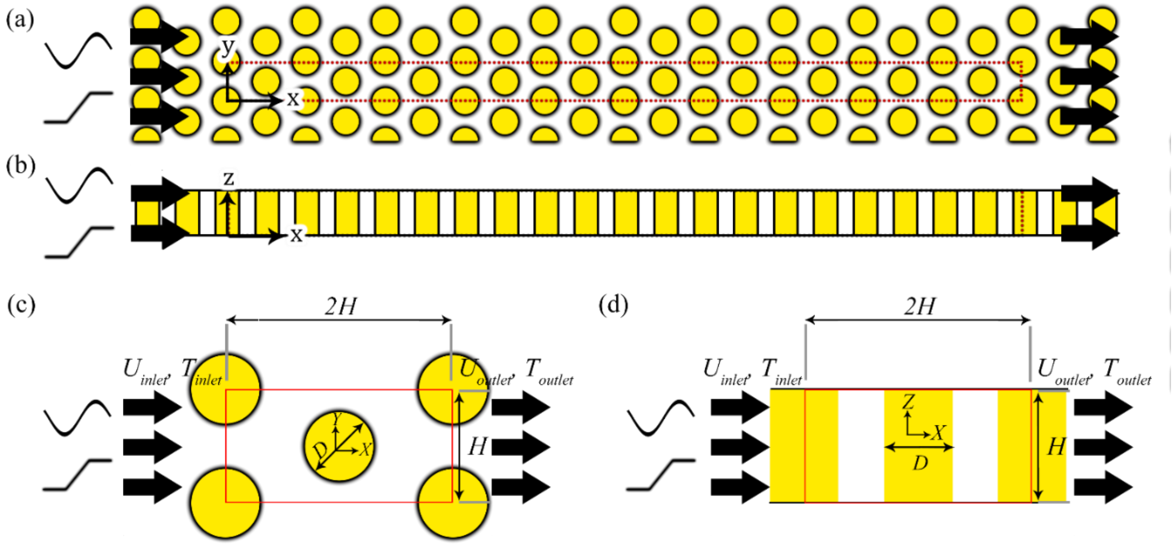

Figure 3-1: A view of the terrain model used for unsteady investigations (a) x-y coordinate system (b) x-z coordinate system (c)computational unit for a single pore in x-y plane (d) computational unit for a single pore in x-z plane

Assuming a laminar flow, for the low Reynolds number considered in this study, the governing equations are as follows. The unsteady equations for the continuity of mass, momentum and energy are obtained from Ref. [145] and are expressed, respectively, as shown below.

$$\frac{\partial \rho}{\partial t} + \frac{\partial \rho u_x}{\partial x} + \frac{\partial \rho u_y}{\partial y} + \frac{\partial \rho u_z}{\partial z} = 0, \qquad (3\text{-}1)$$

$$\begin{aligned}\left(\frac{\partial \rho u_x}{\partial t}+u_x\frac{\partial \rho u_x}{\partial x}+u_y\frac{\partial \rho u_x}{\partial y}+u_z\frac{\partial \rho u_x}{\partial z}\right)&\\ =-\frac{\partial p}{\partial x}+\frac{\partial}{\partial x}\left[2\mu\frac{\partial u_x}{\partial x}-\frac{2}{3}\mu\left(\frac{\partial u_x}{\partial x}+\frac{\partial u_y}{\partial y}+\frac{\partial u_z}{\partial z}\right)\right]&\\ +\frac{\partial}{\partial y}\left[\mu\left(\frac{\partial u_x}{\partial y}+\frac{\partial u_y}{\partial x}\right)\right]+\frac{\partial}{\partial z}\left[\mu\left(\frac{\partial u_x}{\partial z}+\frac{\partial u_z}{\partial x}\right)\right],&\end{aligned}\tag{3-2}$$

$$\begin{aligned}\left(\frac{\partial \rho u_y}{\partial t}+u_x\frac{\partial \rho u_y}{\partial x}+u_y\frac{\partial \rho u_y}{\partial y}+u_z\frac{\partial \rho u_y}{\partial z}\right)&\\ =-\frac{\partial p}{\partial y}+\frac{\partial}{\partial x}\left[\mu\left(\frac{\partial u_x}{\partial y}+\frac{\partial u_y}{\partial x}\right)\right]&\\ +\frac{\partial}{\partial y}\left[2\mu\frac{\partial u_y}{\partial y}-\frac{2}{3}\mu\left(\frac{\partial u_x}{\partial x}+\frac{\partial u_y}{\partial y}+\frac{\partial u_z}{\partial z}\right)\right]&\\ +\frac{\partial}{\partial z}\left[\mu\left(\frac{\partial u_y}{\partial z}+\frac{\partial u_z}{\partial y}\right)\right],&\end{aligned}\tag{3-3}$$

$$\begin{aligned}\left(\frac{\partial \rho u_z}{\partial t}+u_x\frac{\partial \rho u_z}{\partial x}+u_y\frac{\partial \rho u_z}{\partial y}+u_z\frac{\partial \rho u_z}{\partial z}\right)&\\ =-\frac{\partial p}{\partial z}+\frac{\partial}{\partial x}\left[\mu\left(\frac{\partial u_x}{\partial z}+\frac{\partial u_z}{\partial x}\right)\right]+\frac{\partial}{\partial y}\left[\mu\left(\frac{\partial u_y}{\partial z}+\frac{\partial u_z}{\partial y}\right)\right]&\\ +\frac{\partial}{\partial z}\left[2\mu\frac{\partial u_z}{\partial z}-\frac{2}{3}\mu\left(\frac{\partial u_x}{\partial x}+\frac{\partial u_y}{\partial y}+\frac{\partial u_z}{\partial z}\right)\right],&\end{aligned}\tag{3-4}$$

$$\rho c_p\left(\frac{\partial T}{\partial t}+\frac{\partial u_xT}{\partial x}+\frac{\partial u_yT}{\partial y}+\frac{\partial u_zT}{\partial z}\right)=k_f\left(\frac{\partial^2 T}{\partial x^2}+\frac{\partial^2 T}{\partial y^2}+\frac{\partial^2 T}{\partial z^2}\right),\tag{3-5}$$

All parameters and variables have been reported in the nomenclature.

Furthermore, the porosity of the configuration could be controlled by adjusting the obstacle dimensions. In this case, circular obstacles with diameter of 0.05 m were fitted in the domain and porosity was varied by changing the axial and transversal distances of the obstacles. No-slip condition along with 300K constant temperature were applied on all solid walls. The fluid properties were set to those of air or hydrogen under standard settings. The velocity of the fluid at the entrance was assumed to be constant and the temperature was 200K. Also, the surface averaged Nusselt number over the flow obstacles were monitored to evaluate the heat transfer amongst the fluid, as well as the solid region.

To find out the minimum number of the required flow obstacles, an initial set of simulations were performed whereby the entrance and exit were set to periodic boundary conditions, while other settings were unchanged. This would reproduce the unit element (see Figure 3-1c) for the porous structure based on the approach presented by Saito and de Lemos [94]. It should be noted that although this model is the closest representation of an internal component inside a porous medium, it's limited to a steady state environment. Therefore, a step-by-step methodology was developed to generate a representative model which could be used for unsteady simulations. The basic steady state unit model was used as a starting point, with velocity inlet and pressure outlet boundaries. A script was developed whereby the velocity and temperature profiles were re-injected from the exit to the entrance of the model. The simulations were re-run till the difference amid the entrance and exit profiles falls under a certain limit, denoted by Relative Profile Change (RPC):

$$RPC = \left(\sum_{profile} \frac{|\psi_{outlet} - \psi_{inlet}|}{\psi_{outlet}} \right) \cdot 100, \tag{3-6}$$

in which ψ is either temperature or velocity, and the RPC is summed over every point on the boundary as a percentage value. The results of the investigation for the selected Reynolds numbers have been summarised in Figure 3-2. It could be seen that the profiles drop under 5% after 9 iterations have surpassed for the investigated Reynolds numbers. Beyond this point, the profiles effectively remain the same. Therefore, it was concluded that the representative model could be generated using a terrain made up of ten identical flow obstacles as shown in Figure 3-1. To ensure the validity of this, the terrain geometry was tested at the same conditions as the periodic model. Investigations showed that the temperature and pressure profiles at the outlet almost exactly match those profiles after nine levels of injection. Furthermore, the results were very close to the profiles obtained using periodic boundary conditions confirming the proper build-up of the new model. The rest of the investigations reported in this study were performed on the model shown in Figure 3-1a.

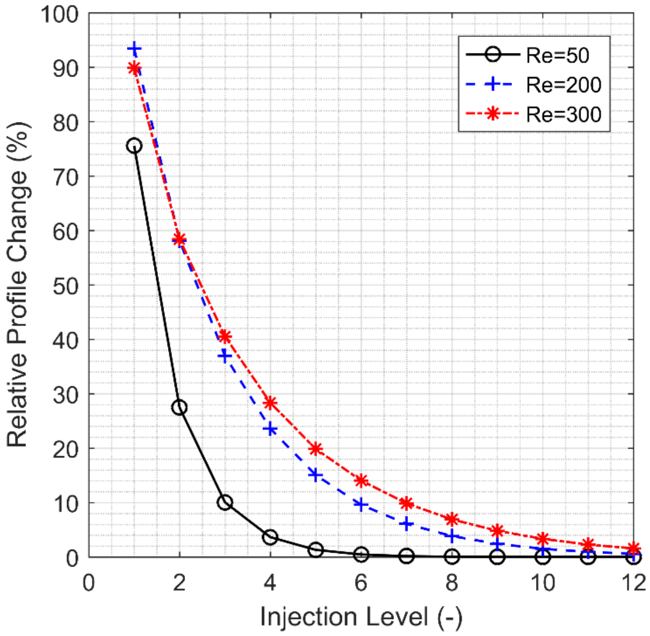

Figure 3-2: Changes in the relative profile versus re-injection iterations for varying values of Reynolds numbers.

The inlet flow was modulated by varying the frequency and amplitude of the sinusoidal wave employed on the inlet velocity. That is:

$$u(0,t) = u_L \cdot \left(1 + a_f sin(2\pi \cdot f \cdot t)\right). \tag{3-7}$$

It is well-known that any arbitrary temporal disturbance can be decomposed into a series of sine waves through application of Fourier transform. As a result, sine waves are the building blocks of temporal disturbances of all kinds and, for that reason here they are used as the primary input disturbances.

The Reynolds number was defined by the following relation [146].

$$Re_L = \frac{u_L \rho D}{\mu}. \tag{3-8}$$

Inside the pore-scale numerical model, heat is transported by forced convection complying with the Newton's law of cooling. That is [145]

$$q_f'' = h_o\left(T_f - T_{ref}\right). \tag{3-9}$$

which is defined at the surface of the obstacle. In order to assess the thermal response of the model, the surface-mean, time-dependent Nusselt Number was determined over all individual obstacles of the terrain model. The numerical value of the Nusselt number was acquired by the use of Equation (3-10), as shown below [83].

$$Nu_L = \frac{q_f'' D}{k_f\left(T_f - T_{ref}\right)}. \tag{3-10}$$

Three various values of Reynolds number (50,150,250) and porosity (0.87, 0.8 and 0.72) and six different frequencies between 0 and 2Hz were investigated along with an inlet velocity disturbance with an amplitude of 30% of its steady value. Simulations were repeated for fluids of air, carbon dioxide and hydrogen, resulting in the total number of 162 unsteady simulations. The choice of the low frequencies is due to the low fluid velocity in the system which slows down the heat convection response. Thus, only long period (low frequency) flow disturbances are of interest.

3.2.2 Numerical methods

3.2.2.1 Computational techniques

A three-dimensional numerical model was developed in STAR-CCM+ V12.04, which is a finite volume based Computational Fluid Dynamics (CFD) software. An adequately refined mesh of polyhedral cells was generated in the bulk region. Further, a number of tetrahedral or the so called “prism layer” cells were implemented near all solid surfaces with large gradients of flow properties (see Figure 3-3). A second order discretization technique was employed to every equation along with a coupled solver which was adopted for achieving higher stability. For the unsteady simulations, the converged solution from similar steady state simulation was used as the initial condition. The foundation time-step was selected so that it was a factor of 100 below than that of the physical timescale. An improved time step was adopted for non-steady simulations for achieving higher accuracy. The steady state investigations were simulated until the residuals count fell under 10^{-6} for every equation. Furthermore, a very high value was selected for the maximum time-step number in unsteady cases, and the mean temperature at the exit of the model was monitored to check the convergence in time. The stoppage criterion was to terminate the simulations if the deviation in the last 1000 time-steps was under 0.5 K.

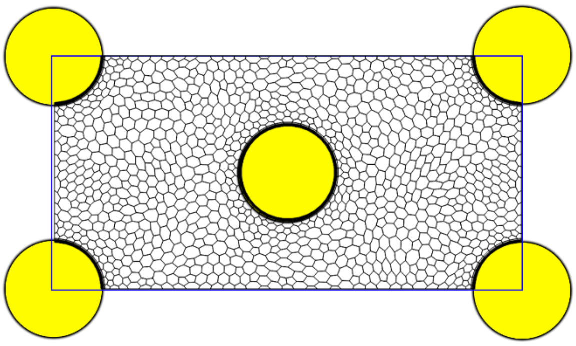

Figure 3-3: Polyhedral staggered mesh with prism layers of a single pore.

3.2.2.2 Grid independency and validation

Nusselt numbers were calculated separately on each circular obstacle. These values were a single quantity for steady state simulations and a temporal variations plot was generated for unsteady cases. Temporal variations in the flow velocity were introduced at the inlet. The system response was represented by the temporal variations of Nusselt number over the obstacles. A series of successive refinements were undertaken on the computational mesh resulting in grids of roughly 2600, 45000, 225000, 377000, 445000, 613000 and 2570000 cells, respectively. Examination of a single Reynolds number indicated that Nusselt number varied slightly with changing the grid in the range of 225000 – 2570000 cells. Further refinement in the grid size did not show any noticeable change in the results. In fact, the changes in Nusselt number were minor even in the 225000 – 613000 cell range, and therefore a grid including 613000 cells was used in this study.

To validate the numerical results, the calculated Nusselt numbers under steady state condition were compared with the empirical correlations of Chen and Wung [100] and Kuwahara et al. [82] developed for heat transfer in structures similar to that of the current study. These correlations are expressed by

$$\overline{Nu} = 0.78Re^{0.45}Pr^{0.38}, \tag{3-11}$$

$$Nu = \left(1 + \frac{4(1+\varepsilon)}{\varepsilon}\right) + \frac{1}{2}(1+\varepsilon)^{1/2}Re^{0.6}Pr^{1/3}. \tag{3-12}$$

The former has been derived for staggered arrangement of pores while the latter was essentially extracted for square obstacles. Both correlations are valid in a wide range of Reynolds numbers and porosities. The settings are quite similar to the simulations discussed in section 3.2.1.

Table 3-1: Comparison between Nusselt Number

Re_D	Nu (simulated)	Nu (Kuwahara et al. [82])	Nu (Chen and Wung. [100])
50	3.71	4.71	4.06
100	5.43	5.92	5.54
150	6.65	6.89	6.65
200	7.61	7.80	7.58

For further validation, the results of an unsteady simulation using an in-house direct numerical simulation (DNS) code [101] were compared against the predictions made by the current simulations. The investigated geometry was a channel of 0.02 m × 0.002 m in dimensions. The air flow was laminar (Re=150), and wall temperatures were maintained at 300 K. A 30% ramp-up variable temperature was applied at the inlet, and the temperature at three locations, namely $x = 0.0$, 0.01, and 0.02 m were monitored. Figure 3-4 shows a comparison between the two datasets, featuring an excellent agreement. Although not shown here, comparison of the velocity profiles across the channel resulted in the same level of agreement. Therefore, it is concluded that the developed unsteady numerical model could predict the flow and heat transfer processes with adequate accuracy and resolution.

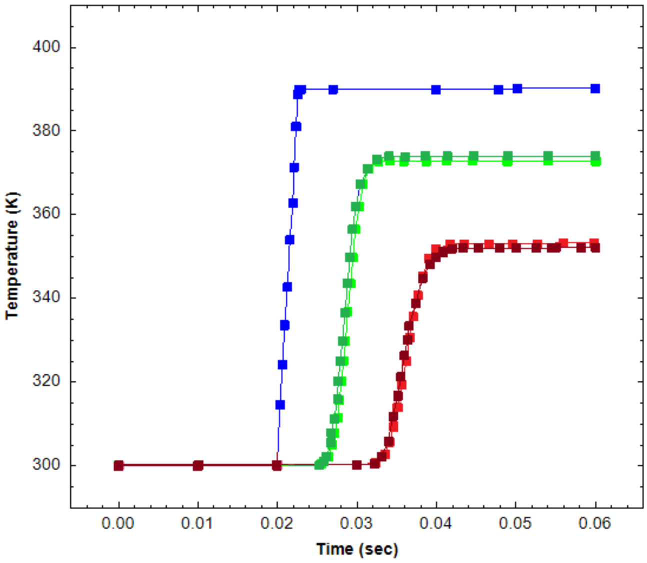

Figure 3-4: Time trace of flow temperature at the inlet (blue), centre (green) and outlet (red), dark and light colour lines show the results of DNS and present simulations, respectively.

3.3 Results and discussion

The system shown in Figure 3-1a, consisting of ten flow obstacles, can be considered as ten single-input single output (SISO) sub-systems [103]. In each of these, the velocity modulation at the far left of the figure is considered as the input and the resultant oscillations of the surface averaged Nusselt number over each flow obstacle is the output. The spatio-temporal response of the porous configuration to a sinusoidal perturbation of the inlet flow velocity has been shown in Figure 3-5. This figure includes snapshots of the flow field in four equally spaced points during one flow modulation cycle over a period of four seconds. The flow disturbance is advected by the mean flow and influences the flow field around and behind the obstacles. The effects are strong for those obstacles that are positioned close to the flow inlet. Nonetheless, they decay as the disturbance further penetrates the porous system and the viscous effects annihilate the imposed velocity perturbation. An increased *Re* in Figure 3-5a is reflected as the oscillation travels further downstream when compared to Figure 3-5b. Temporal modification of the flow velocity around the obstacles perturbs the heat convection coefficient and leads to the oscillation of Nusselt number. These oscillations are expected to be more pronounced for the obstacles closer to the inlet and decrease in amplitude as the outlet is approached. This can be confirmed by visual inspection as a second oscillation (towards the outlet) within each system is recorded at a lower velocity. The analyses presented in this section aim to evaluate the linearity of the relation between the fluctuations in Nusselt number on different flow obstacles and those of the inlet flow.

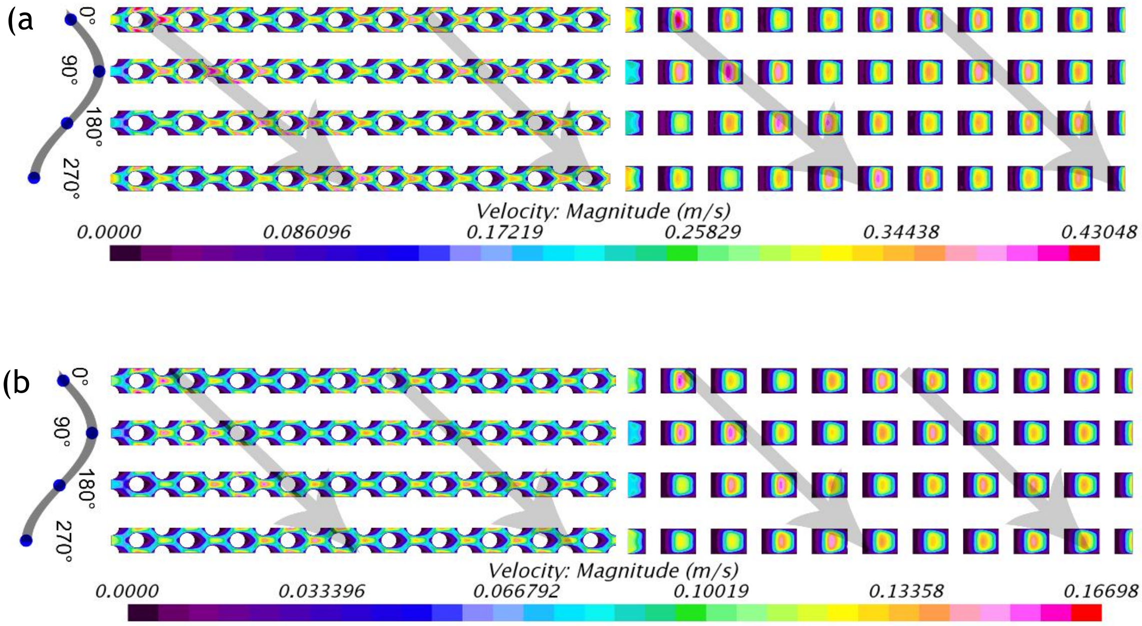

Figure 3-5: Spatiotemporal evolution of the flow disturbance during advection throughout the system, left column: side view, right column: top view, (a) H_2, $\varepsilon = 0.804$ Re=150 (b) H_2, $\varepsilon = 0.804$ Re=50.

Figure 3-6a and Figure 3-6b show a typical time trace of the flow velocity, along the centreline, as well as that of the surface averaged Nusselt number over the first flow obstacle. Figure 3-6b displays an obvious lag when the oscillation is compared with the flow velocity. The spectra of these traces are depicted in Figure 3-6c and Figure 3-6d, demonstrating that the frequency content of the system output (surface-averaged Nusselt number) is almost identical to that of the input (flow velocity oscillations). This is a clear indication of a linear system to which the classical theory of system dynamics could be applied [102]. However, Figure 3-7 indicates that this is not always the case. This figure shows the spectrum of the Nusselt number fluctuations under three different conditions specified in the figure caption. In this figure, frequency has been non-dimensionalised through introducing a Strouhal number defined as $St = (f \cdot D)/u$. Clearly, the frequency response can include other harmonics different to that of the input. That is to say that although the flow velocity input contains only one frequency, the Nusselt number response involves two, or more, frequencies and hence it is nonlinear [117]. The same conclusion can be made through analysis of the phase portrait of Nusselt number and flow velocity traces at a selected frequency and over three different obstacles (see Figure 3-8). The right column of Figure 3-8 shows the cases for which the response remains nearly linear as the portraits are nearly axisymmetric. However, asymmetry of the phase portraits in the left column of this figure demonstrates a strong nonlinearity [112].

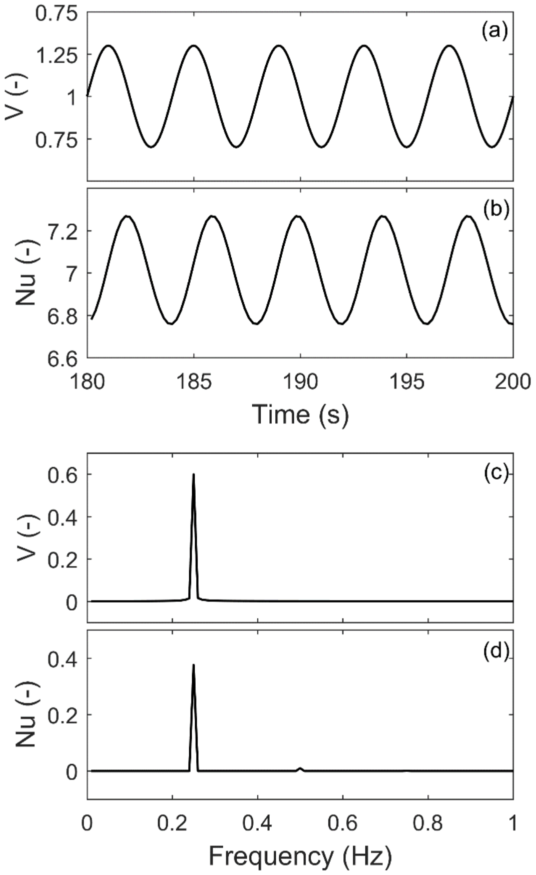

Figure 3-6: (a) time trace of the inlet flow (b) time trace of the surface-averaged Nusselt number (c) spectrum of the inlet flow (d) spectrum of the surface-averaged Nusselt number for H_2, $\varepsilon = 0.804$ Re=50.

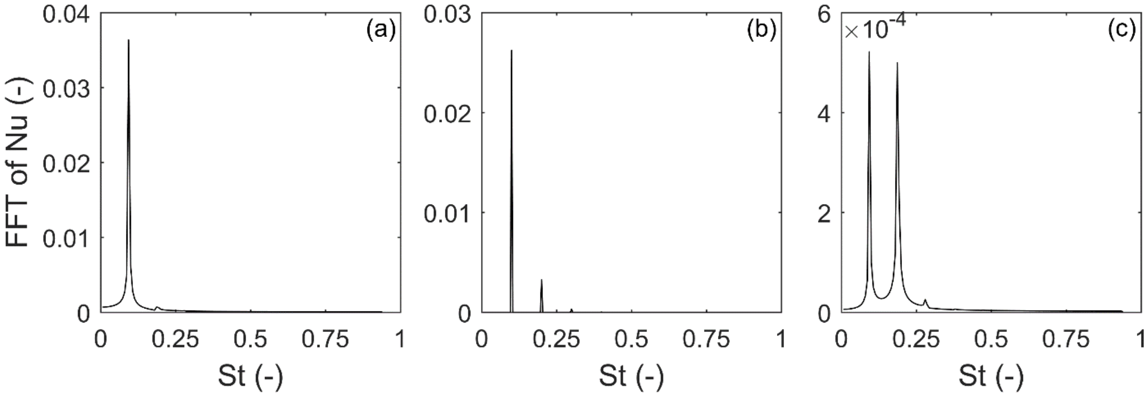

Figure 3-7: Frequency content (spectrum) of Nusselt number oscillations (a) CO_2, ε = 0.874 Re=50 f=0.25 Hz, (b) Air, ε = 0.874 Re=150 f=0.25 Hz, (c) CO_2, ε = 0.804 Re=150 f=0.25 Hz.

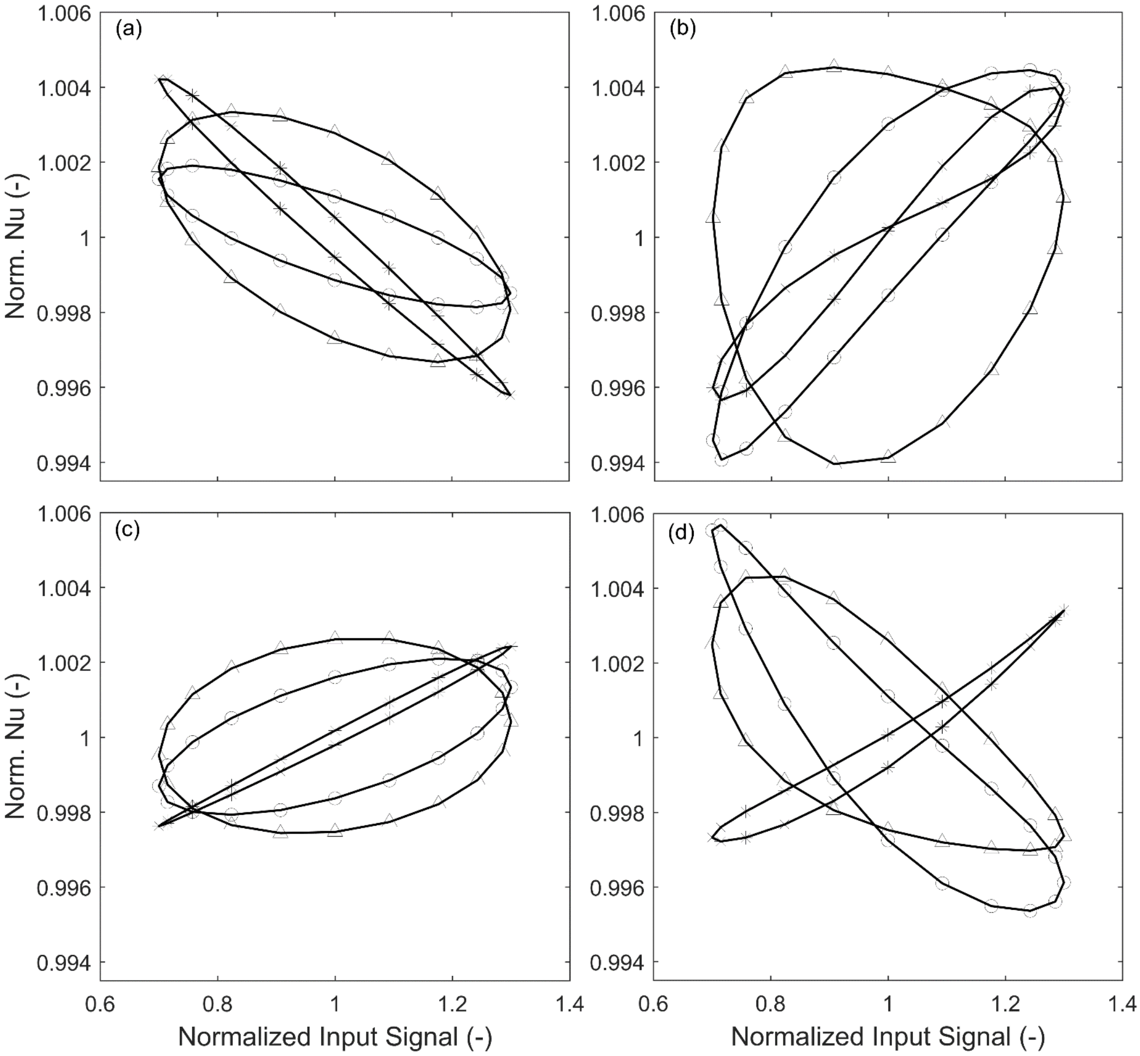

Figure 3-8: Phase portrait of Nusselt number oscillations at f=0.25 Hz, plus: first obstacle, circle: fifth obstacle, diamond: tenth obstacle. (a, c) H_2, ε = 0.804 Re=50 & Air, ε = 0.717 Re=50 -Linear dynamics (b, d) CO_2, ε = 0.804 Re=150 & H_2, ε = 0.804 Re=150-Nonlinear dynamics.

The spectral and phase portrait analyses shown in Figure 3-6, Figure 3-7 and Figure 3-8 can detect nonlinear dynamics. However, they do not quantify the extent of nonlinearity. As shown in Figure 3-7b, there could be situations in which the spectrum involves a relatively insignificant second peak. Yet, it is not obvious whether such cases can be still approximated as a linear response or not. It is therefore necessary to develop a rigorous quantitative measure of nonlinearity through which the linear and nonlinear responses of the system can be clearly distinguished. To resolve this issue, calculation of non-linearity was imported in order to assess alteration from a purely linear behaviour. The latter is conveyed through

$$\delta = \frac{n}{n - o} \tag{3-13}$$

in which δ is the extent of non-linearity, *n*, denotes Euclidean norm of the normalized Nusselt number logged over all obstacles and *o* is the discrete Fourier transform of that [113]. Here, the normalised Nusselt number is defined as $Normalised\ Nu = Nu_L \div \overline{Nu_L}$ where $\overline{Nu_L}$ is the surface averaged Nusselt number over the obstacle under steady state condition. Equation (3-13 assigns the value of zero to a truly linear system and sets one to an entirely nonlinear system. As a result, it always assigns a value between zero and one to any dynamical system [113]. A threshold can be then considered and the systems with the values of δ below that can be regarded as linear, while those with a measure of nonlinearity higher than the threshold are deemed nonlinear.

The numerical values of δ were evaluated for all obstacles and modulation frequencies and for all simulated configurations. For any given set of porosity or Reynolds number, the upper limit of δ (denoted by Max (δ)) was then found. Figure 3-9 shows these maxima with changes in porosity and Reynolds number for the six inspected Strouhal numbers over each obstacle for CO_2. The figure caption also specifies the obstacle and Strouhal numbers where the upper limit was achieved. According to Figure 3-9, changes in porosity and Reynolds number can majorly affect the upper limit of the degree of nonlinearity. For the lowest porosity, the maximum values of δ remains almost indifferent to Reynolds number. However, at higher values of porosity the maxima of δ can either increase or decrease by increases in Reynolds number. Figure 3-9 shows that, in general, the variation of Max (δ) with porosity and Reynolds number is convoluted. It is, nonetheless, observed that regardless of porosity, for the lowest value of Reynolds number (Re=50) the values of Max (δ) are the smallest in the figure and around 0.25. Physically, this can be explained by noting that nonlinearity in the current problem is dominated by the nonlinearity of momentum transfer (Eq. (2-2, (2-3, (2-4). Lowering the value of Reynolds number implies lower flow velocity which in turn weakens the nonlinearity of momentum transfer. This argument is qualitatively in keeping with the rationale behind Darcy and Darcy-Brinkmann models of flow in porous media which ignore the nonlinearity of momentum transfer [50]. However, unlike the general notion of macroscopic modelling, Figure 3-9 shows that rises in Reynolds number do not inevitably result in stronger nonlinearity. Interestingly, the lowest value of Max (δ) in Figure 3-9 is encountered at the highest Reynolds number.

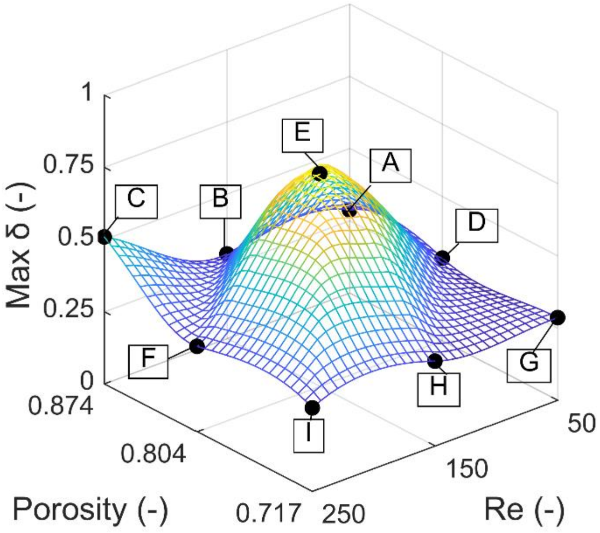

Figure 3-9: The maximum values of the measure of nonlinearity for CO_2 simulations changing with porosity and Reynolds number A) St=1, C2 B) St=0.375, C3 C) St=0.125, C2 D) St=0.375, C5 E) St=0.125, C8 F) St=0.375, C3 G) St=0.375, C5 H) St=0.125, C6 I) St=0.375, C7. C_i denotes flow obstacle i.

Considering the value of δ=0.25 as the threshold of nonlinearity and sketching figures similar to Figure 3-9 for other investigated fluids, the linear cases could be readily distinguished. For these, the classical theory of system dynamics and in particular the concept of transfer function can be developed to describe the response of thermal system to inlet flow modulations. Figure 3-10 shows the transfer function of the thermal response for which the amplitude is defined as $|\mathcal{F}(Nu_i(St))|/|\mathcal{F}(u_{inlet}(St))\ |$. In this relation, $\mathcal{F}(Nu_i(St))$ is the Fourier transform of the surface averaged Nusselt number for obstacle i and $\mathcal{F}(V_{inlet}(\mathrm{St}))$ is the Fourier transform of the flow velocity at the inlet.

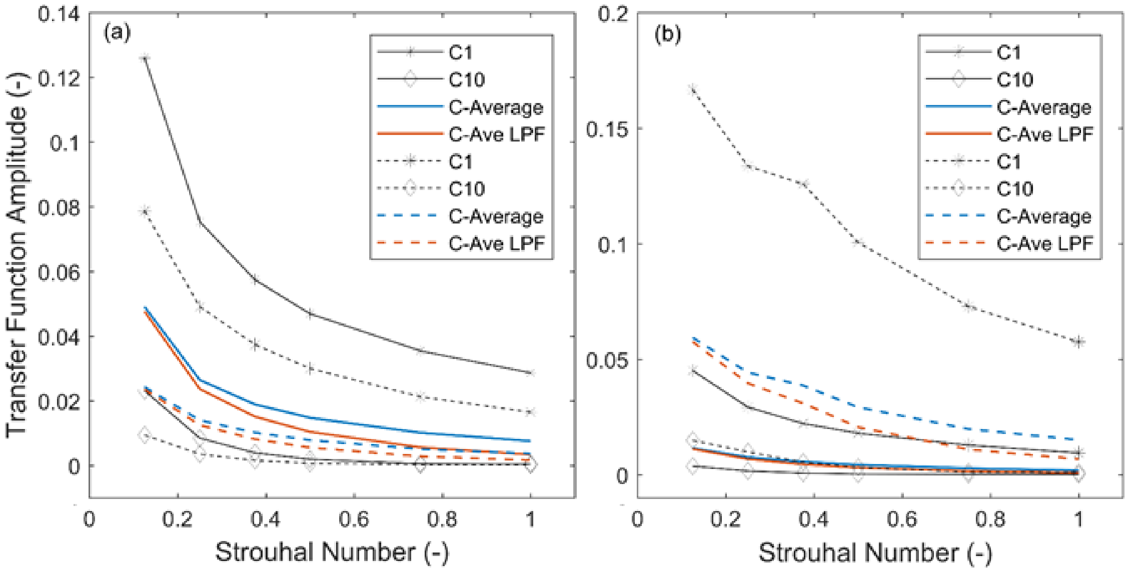

Figure 3-10: Amplitude of transfer function (a) Fluid: Air, ε = 0.874 Re=50 (solid line) & Air, ε = 0.804 Re=50 (dashed line). (b) Air, ε = 0.717 Re=50 (solid line) & Air, ε = 0.717 Re=250 (dashed line). C_i denotes obstacle i.

Figure 3-10 shows the amplitude and non-dimensional delay of the transfer functions calculated for four linear cases. The data have been presented for the first and tenth flow obstacles as well as the average data for all ten obstacles. As a general trend, the rapid reduction of the amplitude with frequency is completely evident. That is to say that the surface averaged Nusselt numbers over all obstacles respond more strongly to low frequency modulations. This behaviour is often regarded as low pass filtering and stems from the fact that the small frequency modulations deliver a lengthier time for the process of heat transfer to take place. As the frequency increases, the available duration for heat transfer declines and at certain frequency the system becomes essentially irresponsive to modulation and the amplitude approaches zero. This behaviour has been already reported in other thermofluid systems [106,118]. The low-pass filtering characteristic of the response allows for the development of an approximative formulation for the transfer function. A low pass filter allows passage of low frequency signals from 0Hz to a cut-off frequency, f_c to pass and attenuates higher frequencies. This cut-off frequency can be found visually from the transfer function and following a procedure detailed in Refs. [108,109], the general formulation for low pass filter is given by

$$Low\,pass\,filter = \bar{a} \cdot \frac{X_C}{\sqrt{R^2 + X_C^2}}, \tag{3-14}$$

$$X_C = \frac{1}{2\pi f C}, \tag{3-15}$$

whereby all terms are reported in the nomenclature. For the transfer functions shown in Figure 3-10, this results in $A_{OUT} = A_{IN} \times \frac{\left(\frac{1}{2\pi f C}\right)}{\sqrt{1000^2 + (\frac{1}{2\pi f C})^2}}$ in which *A_{in}* and

A_{out} refer to the amplitude of the input (velocity) and output (Nusselt number). Figure 3-10 shows that the developed low-pass filter closely approximates the average response across all ten obstacles and for the four investigated cases. Figure 3-10 further shows that the amplitude of the response of the first obstacle grows in magnitude when the Re_L and of the structure increase. However, the frequency responses of the tenth obstacle are almost the same regardless of the values of Reynolds number and porosity. The strong dependency of the transfer function amplitude upon Reynolds number is to be expected as, in general, forced convection over a cylinder is significantly influenced by Reynolds number. Convergence of the responses over the tenth obstacle implies the existence of a global but negligibly low-amplitude response farther from the inlet.

Figure 3-11 illustrates the outcomes of a statistical analysis conducted on all linear cases detected in this study (a total of 13 cases each consisting of 6 frequencies). To construct this figure, the amplitudes of the transfer function (as explained earlier) calculated for each obstacle were averaged over all investigated frequencies and the process was repeated for all detected linear cases. The arithmetic mean and standard deviation of the results are shown in Figure 3-11. As expected, the first obstacle features the strongest average response and further shows the largest standard deviation amongst all obstacles. Moving towards the outlet of the system, the average amplitude drops quickly and so does the standard deviation of the amplitude. The rate of this drop is, however, non-uniform and the average amplitude decreases sharply over the first three obstacles. Yet, the amplitude decline slows down and after the fifth particle it becomes quite gradual. As a result, most of the amplitude dissipation occurs over the first three flow obstacles and the farther situated obstacles are of much less significance. This behaviour is an important result as it demonstrates that the problem under investigation is highly dependent upon pore-scale processes. Porous media macroscopic models of heat convection are often based on averaging over several pores with an inherent assumption that no sharp changes occur within those pores. Nonetheless, the current results show that response of the porous structure to flow modulations could vary strongly from one pore to another. Hence, adopting a pore-scale method appears to be an essential necessity in the problems that involve dynamic response of heat convection in porous media.

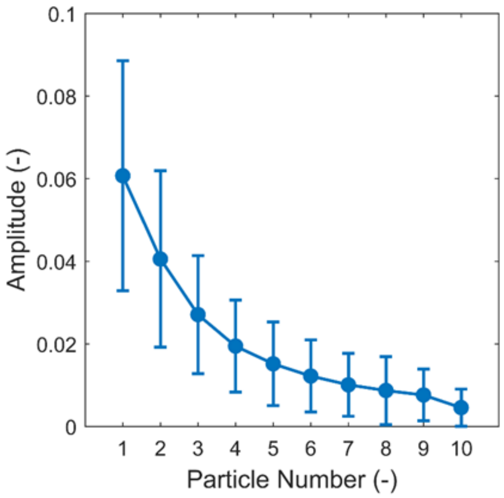

Figure 3-11: Average and standard deviation of the amplitude of transfer function for all linear cases each consisting of 6 frequencies.

3.4 Conclusions

The dynamic response of forced convection in porous media to imposed oscillations on the inlet flow velocity was investigated through conduction of a pore-scale analysis. A porous-structure including several flow obstacles subject to constant wall temperature was exposed to harmonic oscillations of the flow velocity at the inlet. The dynamic relations between these oscillations and the resultant fluctuations in the surface averaged Nusselt number over each obstacle were examined in detail. In particular, a novel measure of nonlinearity was introduced to quantify the nonlinearity of the Nusselt number response. The ultimate aim was to determine the transfer function of the porous medium so that the dynamic response of the medium to any arbitrary velocity disturbance could be figured out. Further, the limitations of transfer function were formally evaluated through measuring the linearity of the thermal response.

The crucial discoveries of this study can be summarised as below.

- Increases in pore-scale Reynolds number can push the dynamics towards nonlinearity. However, in contrast with a notion implied by the macroscopic models, further increases in Reynolds number may result in retrieving the linear response.
- The Nusselt number transfer functions developed for the linear cases, can be similar to a classical low-pass filter. This highlights the fact that the dynamics of heat convection are influenced most significantly by the low-frequency flow disturbances.
- The statistical analysis of the cases with linear dynamics showed that the thermal response of the porous structure is dominated by those of the first few obstacles. This clearly reflects the importance of utilising pore-scale modelling in the analysis of unsteady forced convection in porous media.

Chapter 2 and chapter 3 both comprise of a pore-scale analysis of unsteady convection subject to temporally modulated inlet flow by a sinusoidal disturbance. Expanding the pore-scale analysis further, chapter 4 investigates the transient response to inlet ramp inputs using the existing pore-scale model as transient response of porous media has grown in importance with its widespread use in emerging technologies [147,148].

Chapter 4 A pore-scale investigation of the transient response of forced convection in porous media to inlet ramp inputs

ASME – Journal of Energy Resources Technology – Rabeeah Habib, Bijan Yadollahi, Nader Karimi

4.1 Introduction

Comprehending the transient response of porous media has grown in importance with its widespread use in emerging technologies [149–153]. Cases can be found in the use of heat exchangers [116], micro chemical reactors [53,154], fuel cells [114,115] and electrochemical systems [71,72]. Understanding the response of these systems is vital as the inlet fluid flow rate can be highly time dependent [49]. It is fundamental to have the ability to predict the thermal response of the pertinent model subject to time-dependent disturbances at the inlet [75] . Steady flow has been the predominant focus of majority of existing studies of forced convection in porous media. This pattern is clearly visible in numerical investigation that were conducted using a pore-scale approach (e.g. [85,86]); and especially in those studies that took a macroscopic modelling approach (e.g. [54,155]).

A smaller amount of macroscopic investigations have analysed unsteady and pulsating flows in porous media as will be discussed in the core part of this literature review. Fewer studies reported results using the pore-scale approach; with most studies being in the two-dimensional domain [59,156] and even less in the three-dimensional domain [53,157]. In order to fully comprehend steady and unsteady macroscopic modelling, a brief examination of literature on macroscopic studies in porous media is carried out using the Darcy model and its extensions. It is generally understood that a macroscopic model might be lacking for the analysis of periodic flow systems [71] therefore a pore-scale approach is employed in this paper.

Saito and de Lemos [134] proposed two-macroscopic-energy equation models for conduction and convection for packed beds of porous media assuming local thermal non equilibrium. The authors modelled a two-dimensional unit cell model with square cylinders in a staggered arrangement; replicating Kuwahara et al. [82] physical model. Saito and de Lemos [134] numerically solved for the interfacial heat transfer coefficient; discretizing the macroscopic governing equations using the control volume method. These authors [134] found their work to be in agreement with Kuwahara et al. [82]. They concluded that a higher porosity medium could reduce the energy transfer between the solid and fluid phase [134]. Lu et al. [158] simulated temperature disturbances during the mixing process of a T-junction filled with and without porous media. They implemented local thermal equilibrium model and concluded that the addition of porous media within the T-junction model lowers the temperature fluctuations during the mixing process [158].

Kim et al. [159] numerically simulated a two-dimensional channel filled with porous media to investigate the effects of forced oscillatory flow on the Nusselt number. Isothermal boundary conditions were set to the channel walls where the porosity of the porous media was fixed to 0.6. The authors [159] compared the temperature and flow fields with ranges of pertinent parameters and discovered oscillatory flow to reduce heat transfer in the entrance region of the model when compared to steady flow. They further reported enhanced heat transfer in the central region of the model. A similar study was conducted by Guo et al. [160] who considered the effects of pulsating flow on heat transfer in a pipe partially filled with porous media. The system was modelled as two-dimensional with porous media attached to the walls of the pipe. Guo et al. [160] found that Nusselt number monotonically increases with the growth in the porous layer thickness.

Bhargava et al. [161] present finite element solutions for a non-Newtonian fluid experiencing pulsations. The analysis was conducted by adopting a one-dimensional transient model depicting a porous medium conduit. The pulsatile effects of the pressure gradient on the model flow were examined by altering parameters such as Reynolds number, pulsating amplitude and frequency. Bhargava et al. [161] discovered the velocity to augment with an increase in permeability and a reduction of non-Newtonian behaviour. Huang and Yang [162] studied forced oscillatory convection in a parallel plate channel with porous blocks mounted to the lower wall. They described the effects of varying the amplitude, frequency and porous blockage ratio on the flow field and heat transfer of the model. An oscillatory flow was introduced to improve flow mixing and greater thermal transport, revealing that heat transfer augments from the heat sources with the rise of the oscillation amplitude.

A numerical study was conducted by Dhahri et al. [163] to find the effects of pulsating flow on entropy generation within a pipe partially filled with porous media. The authors monitored the response of the amplitude, frequency, porous layer thickness and thermal conductivity ratio with respect to entropy generation. They discovered the temperature difference in the fluid region to be greater than that of the porous region. Farooghi et al.[123] studied steady and oscillating flow in a parallel plate channel partially composed with porous media in the upper and lower walls of the channel; subject to a constant heat flux. The authors employed the Brinkman-Forchheimer-extended Darcy model and implemented the LTNE method and reported that LTE method overestimates the heat transfer. Farooghi et al. [123] suggested that augmenting the amplitude of flow oscillation could result in an increase in the time-averaged Nusselt number. They further noted the thermal conductivity ratio to increase heat transfer between the solid and fluid, if the porous media thickness is kept constant.

Ghafarian et al. [164] computed pulsating flow through a channel filled with a porous medium to analyse heat transfer. Various studies were conducted by altering the frequency, amplitude, and Reynolds number of the working fluid as well as a change of porosity. The local Nusselt number was calculated for a laminar model to monitor heat transfer, showing that the Nusselt number to augment with the use of a high amplitude and high frequency. Targui and Kahalerras [116] numerically simulated oscillatory flow through a double pipe heat exchanger coupled with porous baffles. It was found that the oscillation has a profound effect on heat transfer and maximises it when only the hot fluid flow oscillates. Zaman et al. [165] numerically examined the flow of blood induced with pulsatile flow within a porous-saturated overlapping stenosed artery. The study depicted a pathological solution where the blood travels through an artery comprising of blood clots and fatty cholesterol. The numerical simulation showed the effects of flow rate, velocity, and wall shear stress on the porous medium. It was found that with a larger permeability the resistance of the flow is smaller whilst the flow rate and velocity augments.

It is observed that the existing studies on unsteady forced convection are mostly concerned with the macroscopic analysis by using the extended Darcy models. Further, most studies include two-dimensional simulations and gave little attention to the transient response of the system. Therefore, there is currently a gap in understanding the thermal transient response at pore-scale in a three-dimensional domain. The current investigation aims to address this issue.

4.2 Methodology

4.2.1 Problem configuration, governing equations and assumptions

In the current pore-scale model, the flow is assumed to be unsteady and laminar. The mass, momentum, and energy conservations [145] for such flow are written as follows.

$$\frac{\partial \rho}{\partial t}+\frac{\partial \rho u_x}{\partial x}+\frac{\partial \rho u_y}{\partial y}+\frac{\partial \rho u_z}{\partial z}=0, \tag{4-1}$$

$$\begin{aligned}
&\left(\frac{\partial \rho u_x}{\partial t}+u_x\frac{\partial \rho u_x}{\partial x}+u_y\frac{\partial \rho u_x}{\partial y}+u_z\frac{\partial \rho u_x}{\partial z}\right)\\
&\qquad=-\frac{\partial p}{\partial x}+\frac{\partial}{\partial x}\left[+2\mu\frac{\partial u_x}{\partial x}-\frac{2}{3}\mu\left(\frac{\partial u_x}{\partial x}+\frac{\partial u_y}{\partial y}+\frac{\partial u_z}{\partial z}\right)\right]\\
&\qquad+\frac{\partial}{\partial y}\left[\mu\left(\frac{\partial u_x}{\partial y}+\frac{\partial u_y}{\partial x}\right)\right]+\frac{\partial}{\partial z}\left[\mu\left(\frac{\partial u_x}{\partial z}+\frac{\partial u_z}{\partial x}\right)\right],
\end{aligned} \tag{4-2}$$

$$\begin{aligned}
&\left(\frac{\partial \rho u_y}{\partial t}+u_x\frac{\partial \rho u_y}{\partial x}+u_y\frac{\partial \rho u_y}{\partial y}+u_z\frac{\partial \rho u_y}{\partial z}\right)\\
&\qquad=-\frac{\partial p}{\partial y}+\frac{\partial}{\partial x}\left[\mu\left(\frac{\partial u_x}{\partial y}+\frac{\partial u_y}{\partial x}\right)\right]\\
&\qquad+\frac{\partial}{\partial y}\left[2\mu\frac{\partial u_y}{\partial y}-\frac{2}{3}\mu\left(\frac{\partial u_x}{\partial x}+\frac{\partial u_y}{\partial y}+\frac{\partial u_z}{\partial z}\right)\right]\\
&\qquad+\frac{\partial}{\partial z}\left[\mu\left(\frac{\partial u_y}{\partial z}+\frac{\partial u_z}{\partial y}\right)\right],
\end{aligned} \tag{4-3}$$

$$\left(\frac{\partial \rho u_z}{\partial t} + u_x \frac{\partial \rho u_z}{\partial x} + u_y \frac{\partial \rho u_z}{\partial y} + u_z \frac{\partial \rho u_z}{\partial z}\right) = -\frac{\partial p}{\partial z} + \frac{\partial}{\partial x}\left[\mu\left(\frac{\partial u_x}{\partial z} + \frac{\partial u_z}{\partial x}\right)\right] + \frac{\partial}{\partial y}\left[\mu\left(\frac{\partial u_y}{\partial z} + \frac{\partial u_z}{\partial y}\right)\right] + \frac{\partial}{\partial z}\left[2\mu \frac{\partial u_z}{\partial z} - \frac{2}{3}\mu\left(\frac{\partial u_x}{\partial x} + \frac{\partial u_y}{\partial y} + \frac{\partial u_z}{\partial z}\right)\right], \tag{4-4}$$

$$\rho c_p\left(\frac{\partial T}{\partial t} + \frac{\partial u_x T}{\partial x} + \frac{\partial u_y T}{\partial y} + \frac{\partial u_z T}{\partial z}\right) = k_f\left(\frac{\partial^2 T}{\partial x^2} + \frac{\partial^2 T}{\partial y^2} + \frac{\partial^2 T}{\partial z^2}\right), \tag{4-5}$$

where all terms have been defined in the nomenclature.

A representative elementary volume (REV) similar to the structure used in Ref. [166] is taken into consideration. The REV contains a single pore around an obstacle [167]. Such a unit is periodically repeated in each direction to create the large-scale porous structure. Therefore, it is safe to assume nearly identical flows in each REV unit. As a result, the boundaries of this unit element are treated as periodic and symmetric.

The first set of investigations incorporated the REV as a separate unit. The porosity of the unit could be regulated by changing the pore dimensions as obstacle dimensions. In this instance, the pore was selected to be of $0.1 \times 0.2\, m^2$ and a circular obstacle of diameter 0.05 m was designed in the domain. The flow was assumed to be steady state. All solid walls were set to a constant temperature of 300K with no slip boundary conditions. The fluid properties were established to be standard air. Uniform velocity boundary conditions applied at the inlet, and the temperature was set to 200K and atmospheric pressure at the outlet. Top and bottom of the pore were treated as symmetry boundaries. Periodic boundary conditions were set at the inlet and outlet for another batch of simulations. All other settings were kept the same as the previous investigations. This replicated the unit structure for the porous media model based on the approach obtained by Saito and de Lemos [94] . It should be devised, however, that while this model is near-identical depiction of the internal structure in a porous medium, it is restricted to steady state conditions. Consequently, it was decided to follow a systematic approach to produce a representative model which could be employed for unsteady simulations. The rudimentary steady state REV unit model was devised as a foundation model, with velocity entrance and pressure exit boundaries. In this instance, a script was created where the velocity, as well as the temperature profiles were re-inserted from the exit to the entrance of the model [101]. Therefore, the simulation continued till the variance amongst the inlet and outlet fell beneath a certain value, defined as Relative Profile Change (RPC) as below:

$$RPC = \left(\sum_{profile} \frac{|\psi_{outlet} - \psi_{inlet}|}{\psi_{outlet}} \right) \cdot 100, \qquad (4\text{-}6)$$

where ψ is either velocity or temperature. The RPC is collated upon every position on the boundary as a percentage unit. The effect of three Reynolds numbers were tested in this part of the study. The outcomes of the investigation have been depicted in Figure 4-1. It is clear that the difference in profiles falls below 5% after 9 iterations for all three Reynolds numbers. After this, the profiles remain almost the same. Thus, it was settled that representative model could be produced using a terrain made up of ten REVs (see Figure 4-2). The terrain geometry was then verified at identical conditions as the periodic model showing that the temperature and pressure profiles at the outlet almost match those profiles after nine levels of insertion. Further, with the use of periodic boundary conditions the results were found to be almost identical. This confirmed the proper construction of the computational model used in the rest of the current study.

A series of steady state investigations were performed on the terrain model to study the effects of main variables affecting the fluid flow inside the system. Three porosities of 0.87, 0.8 and 0.72 were considered. Uniform velocity and 300K constant temperature were set at the inlet and atmospheric pressure was set at the outlet. Three wall temperatures of 500, 600 and 700K were also tested with 300K inlet temperature. The effects of circular obstacle geometries were investigated and Nusselt number was calculated separately on each obstacle to enable a more detailed evaluation of the results.

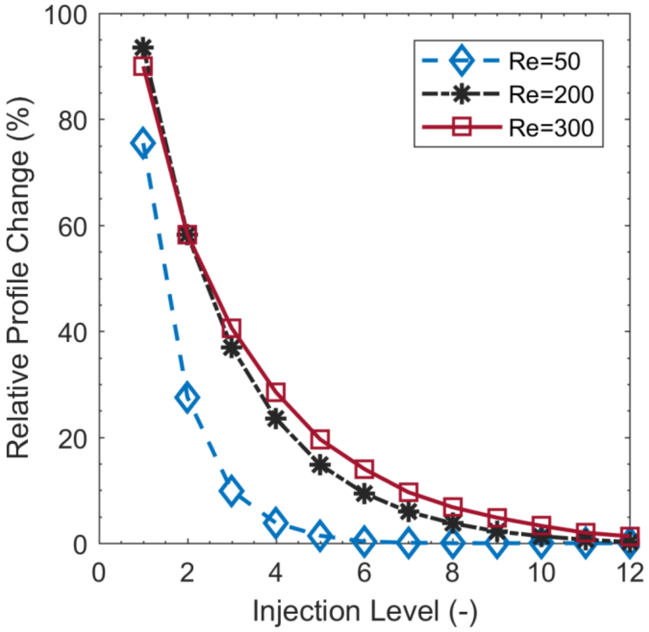

Figure 4-1: Accumulative relative profile change versus re-injection iteration at different Reynolds numbers.

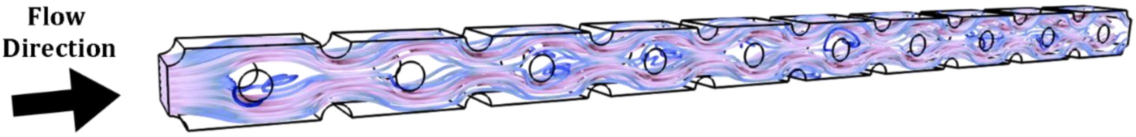

Figure 4-2: A 3-D view of the terrain model used for unsteady investigations visualising fluid flow.

Under unsteady condition, a ramp-up was selected as the method for temporal variations as one of the most common scenarios in real applications. The inlet flow was modulated by superimposing a ramp-up on the inlet velocity after 5 seconds. That is:

$$u(0,t) = u_{in} \cdot \left(1 + \frac{t}{t_{ramp} \cdot a_r}\right). \qquad (4\text{-}7)$$

The Reynolds number [146] was defined by the following relation.

$$Re_L = \frac{u_{in}\rho D}{\mu}. \qquad (4\text{-}8)$$

Newton's law of cooling [145] is expressed as

$$q_f'' = h_o(T_f - T_{ref}). \tag{4-9}$$

The Nusselt number is surface-averaged for all obstacles to assess the thermal response of the pore-scale model. The following equation is employed to calculate the Nusselt Number [83].

$$Nu_L = \frac{q_f'' D}{k_f(T_f - T_{ref})}. \tag{4-10}$$

Along with the aforementioned Re and porosity values, three ramp durations of 10, 20 and 30 seconds were investigated along with three ramp-up levels of 10, 20 and 30% of the base value. All the investigations were tested for ramp-ups in inlet temperature and velocity. Furthermore, three fluids as air, CO_2 and H_2 were tested. A total of around 500 different settings were investigated in the course of this investigation.

4.2.2 Numerical methods

4.2.2.1 Computational techniques

A numerical model was developed using the commercial software STAR-CCM+. A satisfactory refined mesh of polyhedral cells was formed for the bulk region (Figure 4-3a). In total, 15 high quality, tetrahedral or “prism layer” cells were generated per solid surface to ensure higher accuracy of gradient calculations. All equations were solved using a second order discretization technique where a coupled solver was implemented for greater stability. The boundary conditions were set according to each case as described in section 4.2.1. Stagnant flow along with ambient pressure and temperature were set as the initial conditions for all cases except for the unsteady simulations. For these cases, the converged solution from similar steady state simulation was used instead. The central time step chosen was that in which the magnitude was lesser by a factor of 100 in comparison to that of the physical time scale. In order to reduce the runtime of ramp cases, a variable time-step approach was adopted. These time steps were refined around the ramp section for more accuracy.

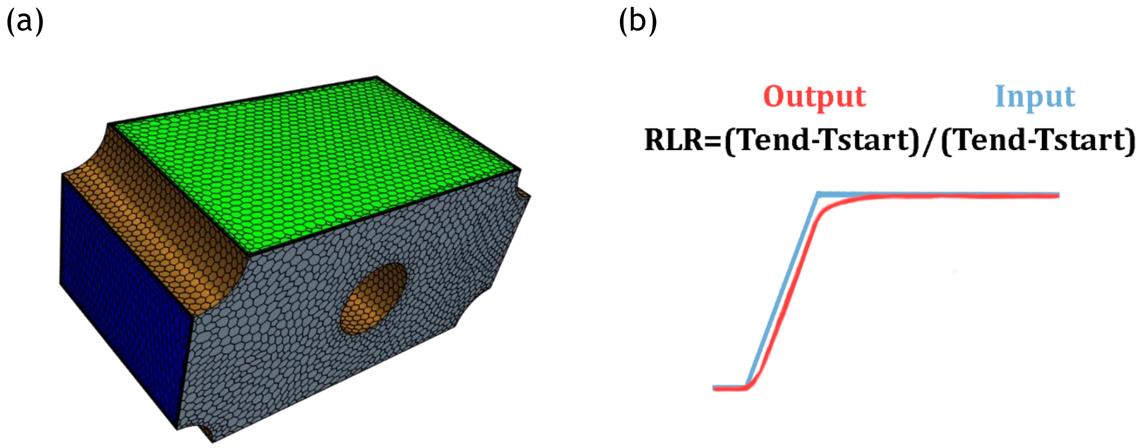

Figure 4-3: (a) Single pore structural unit as implemented in the current simulations (b) Schematic representation for the definition of RLR.

A minimum magnitude of 10^{-6} for all equations residual levels were achieved for all steady state simulations. Furthermore, a sizeable parameter was selected for upper limit time-step number in ramp cases, and mean temperature at the exit was analysed to monitor convergence with respect to time. A new stoppage criterion was defined to terminate the simulations if the deviation in the last 1000 time-steps is lower than 0.5 K [168]. These proved to be adequate convergence criteria for almost all cases.

4.2.2.2 Grid independency and validation

Surface-averaged Nusselt numbers were calculated individually for each obstacle. Although these values are a single measure for steady state simulations, a temporal variations plot was produced for unsteady simulations. Steady state results were normalized with their final settled value on each pore. Temporal variations in either velocity or temperature were introduced to entrance of the model. System response was checked via Nusselt number over obstacles. Ideally, the same variation profile should convect to each obstacle at a speed of bulk velocity. However, this is not the case in real flows because of the lags incorporated by the viscous flow. A lag could be introduced as the flow-induced elongation in the ramp section, designated as Response Lag Ratio (RLR):

$$RLR = \frac{(t_{end} - t_{start})_{output}}{(t_{end} - t_{start})_{input}}. \tag{4-11}$$

RLR is a non-dimensional quantity, calculated for the Nusselt number response of each obstacle. A graphical representation for the RLR definition is shown in Figure 4-3b.

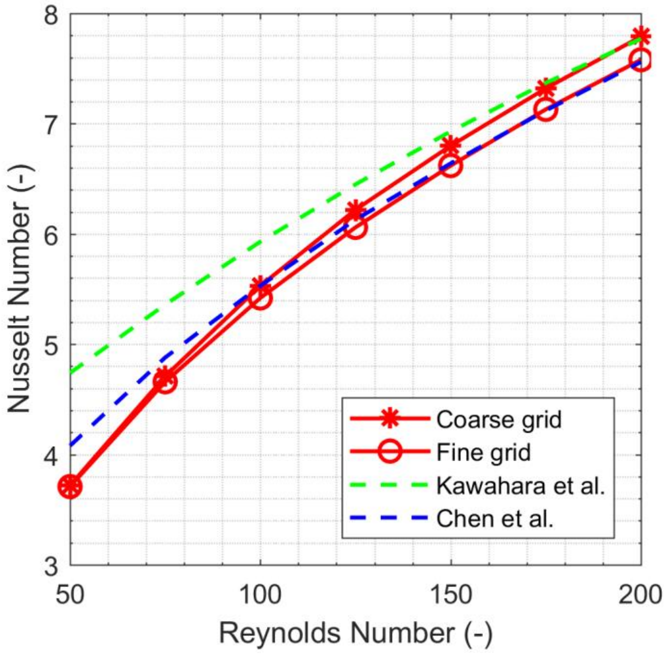

Figure 4-4: A comparison of Nusselt Number values in heat transfer validation case.

Figure 4-4 shows the validation case performed on Nusselt number predictions. Two separate studies of Chen and Wung [100] and Kawahara et al. [82] were selected. A correlation for heat transfer in structures similar to the current study has been proposed in each of these studies. These correlations are based on experimental and numerical data defined by:

$$\overline{Nu} = 0.78Re^{0.45}Pr^{0.38}, \tag{4-12}$$

$$Nu = \left(1 + \frac{4(1+\varepsilon)}{\varepsilon}\right) + \frac{1}{2}(1+\varepsilon)^{1/2}Re^{0.6}Pr^{1/3}. \tag{4-13}$$

Equation (4-12 was derived to represent a staggered arrangement whereas Equation (4-13 was extracted particularly for square obstacles. Both correlations can be used for a large range of properties and Reynolds numbers. The close similarity of the simulated results and the correlations confirms validity of the numerical simulations.

The computational mesh was systematically refined to find the ideal balance between relative accuracy and low computational costs. A total of seven grids were created between a range of 2600-2,570,000 cells. Early investigations on a single Reynolds number showed that the Nusselt number shows minimal variance for grid ranges between 225,000 – 2,570,000 cells. However, further refinement in the grid sizes did not show any significant change in the results (as shown in Figure 4-4). Therefore, it is safe to argue that the results are grid independent using the 613,000 cell grid.

4.3 Results and discussion

Figure 4-5 illustrates the spatial response of the ten obstacles pore-scale model to a steady inlet flow velocity. This figure displays snapshots of three configurations where the wall temperature alters at intervals of a 100K for their respective converged solutions. The inlet flow enters at ambient temperature from the left-hand side and exits towards the right. As the inlet flow travels downstream, the constant temperature around the circular obstacles influences the flow field around and behind the obstacles, creating wake regions. This effect is readily observed in the flow field where there is a larger temperature difference between the inlet flow and the circular obstacles and, is particularly visible when the wall temperature is at its lowest. Such effects decay after the third obstacle as the flow travels downstream almost appearing to have reached thermal equilibrium. However, the diffusion effects are the strongest throughout the porous configuration when the obstacle temperature is the largest. This can be seen when the wall temperature is 700K, the flow field appears to reach very close to thermal equilibrium further downstream at the tenth obstacle. The flow field behaviour and temperature change are monitored throughout the system by the surface-averaged Nusselt Number around each circular obstacle. The analyses discussed in this section aim to understand the transient response by observing the response lag ratio of the pore-scale model subject to an unsteady ramp input.

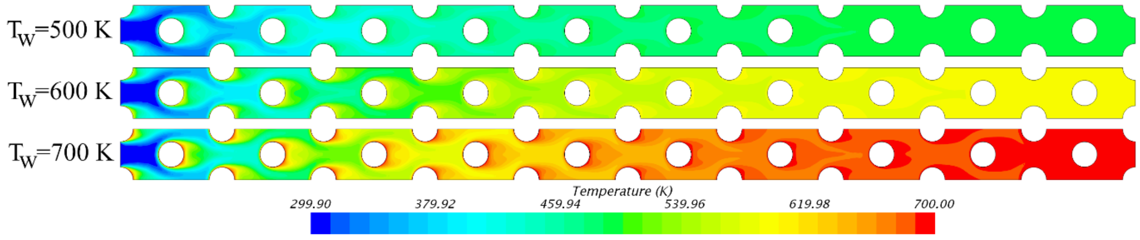

Figure 4-5: The effect of wall thermal boundary conditions on steady temperature fields, Fluid type: H_2, $\varepsilon = 0.804$, *Re=250*

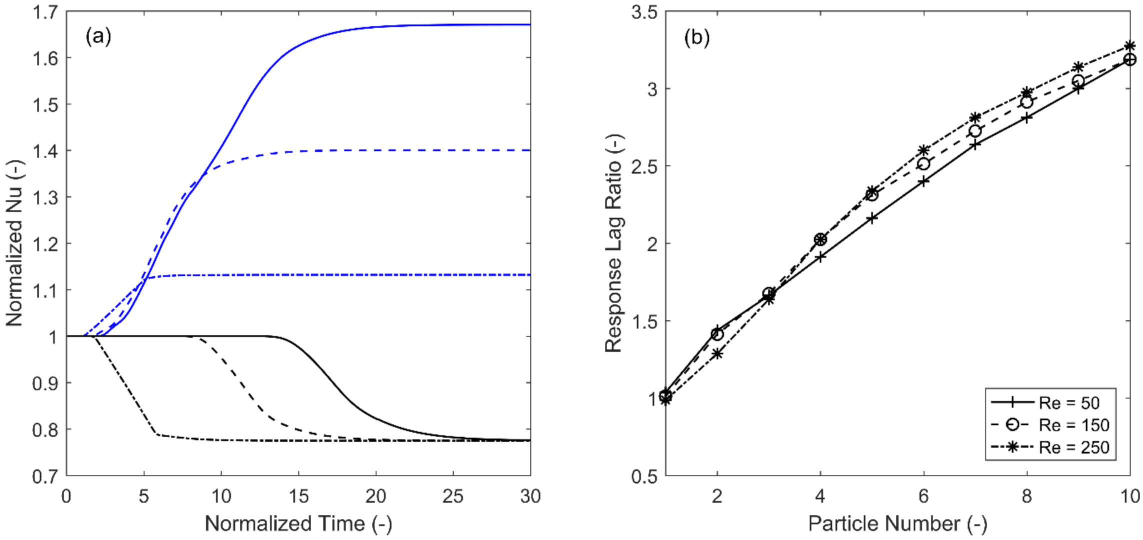

Figure 4-6: a) A comparison between normalized Nu results for ramp in velocity (blue) and temperature (black) on first (solid), sixth (dash) and tenth (dash-dot) pores, Fluid type: CO_2, $\varepsilon = 0.874$, $Re_L=150$, *R=30 s, a=30%; b) The effect of Reynolds number on RLR, Fluid type:* H_2, $\varepsilon = 0.804$, *R=20 s, a=20%.*

A comparison of Nusselt numbers is made for the inlet flow subject to a ramp between inlet temperature and inlet velocity in Figure 4-6a. As the velocity ramp is introduced, the first obstacle responds gradually albeit the largest increase in Nusselt number is also reported. The opposite is observed at obstacles closer to the outlet with quicker response time and lesser augmentation in Nusselt number. This is expected to be due to the thermal boundary conditions set for the circular obstacles. As the time-dependent ramp travels throughout the model the viscous effects continue to decay with the rate of heat transfer plummeting as it reaches the outlet. A similar trend is observed when the system is subject to an inlet temperature ramp. To achieve constant convective heat transfer the system requires less time when the flow is closer to the outlet when compared to the inlet. As the inlet temperature rises, the local temperature difference between the fluid and solid surfaces decreases. This limits the rate of heat transfer and reduces Nusselt number when compared with the steady state value. It is noteworthy that the heat transfer rate per obstacle and response time both change when the system is subject to a velocity ramp whereas only response time differs when the system is subject to a temperature ramp. Figure 4-6b displays the response lag ratio for each obstacle. The lag augments as the fluid travels downstream of the model where the viscous effects resist the inertial forces of the fluid flow. As the Reynolds number increases the viscous effects are also amplified; inflating the overall lag of the system. This phenomenon is further analysed in Figure 4-7 visualising the spatiotemporal flow field snapshots equally split over the respective ramp duration. The time-dependent inlet temperature is subject to an increase of 30% of its base value. In Figure 4-7a it can be seen before the introduction of the ramp, the flow field of the obstacles closer to the exit of the system exhibit higher temperature readings; almost matching the temperature of the surface of the obstacles (700K). As the inlet ramp in temperature is introduced, the overall flow field temperature surges, forcing the higher temperatures to move further upstream. This is because the convective heat transfer diminishes as the gap between the temperature difference narrows; decreasing the Nusselt number.

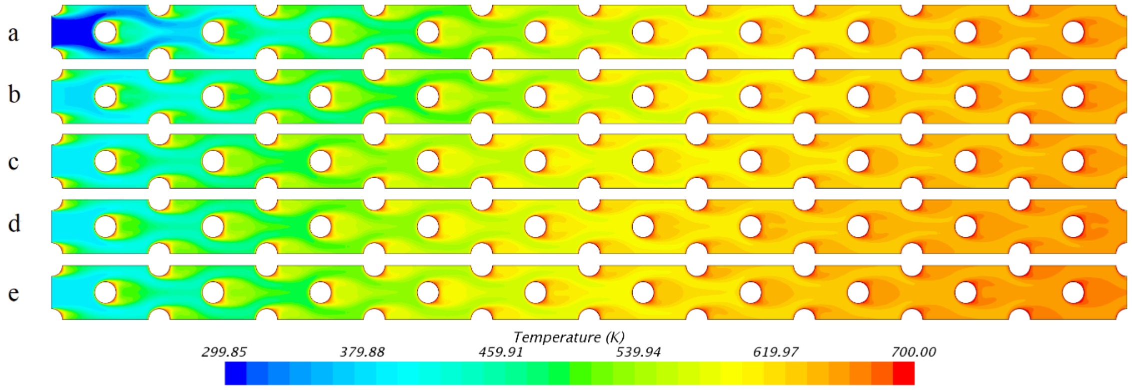

Figure 4-7: Temporal evolution of the temperature field with 10 sec. ramp duration (on Temperature) for air at Re=250 ε = 0.874.

However, the opposite is observed in Figure 4-8 where the temporal evolutions for the velocity field are introduced by a 10 seconds ramp input. Thus, the increase in velocity and constant temperature at the circular obstacles provide a streamlined contour pattern where convective heat transfer is increasing. Also, as the Reynolds number increases further with the ramp so does the inertial effects of the flow, combined with the thermal diffusion occurring at the circular obstacles, the wake region expands gradually with the passage of time. It is apparent from Figure 4-8, that there is a greater wake flow when compared to Figure 4-9; which is lower in Reynolds number. This can also be observed between Figure 4-9a and Figure 4-9e where the wake flow contours surge in velocity as the Reynolds number augments. A similar pattern is also observed in the general flow between the two configurations. Where a more streamline contour pattern is observed as the flow moves towards the outlet for a high Reynolds number and a more scattered wider flow pattern for the lower Reynolds number.

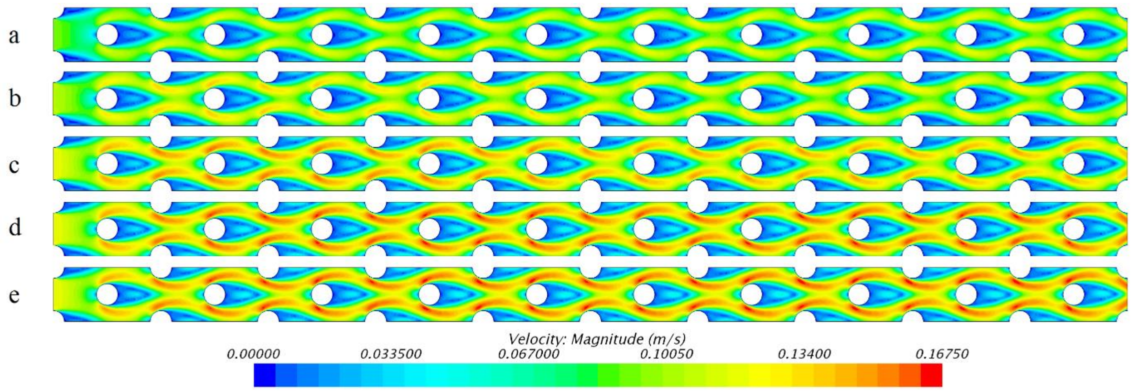

Figure 4-8: Temporal evolution of the velocity field with 10 sec. ramp duration (on Velocity) for air at Re=250 ε = 0.874.

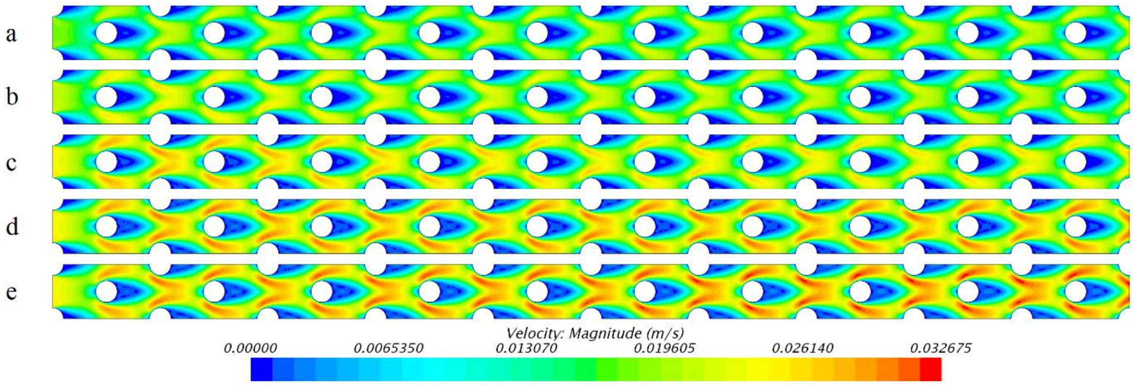

Figure 4-9: Temporal evolution of the velocity field with 10 sec. ramp duration (on Velocity) for air at Re=50 ε = 0.874.

An identical configuration to Figure 4-8 is presented in Figure 4-10 where the working fluid has been switched from air to hydrogen. A similar streamlined contour flow field is observed to that of air, however there is a drastic increase in the system's velocity albeit the same Reynolds number. This is primarily due to the fluid properties. Hydrogen inhibits a lower density than air, making the fluid lighter therefore more responsive to the identical Reynolds number. This trend is clearly observed during the general flow of the model and within the wake region as the ramp input is implemented. It is understood for a high-density working fluid with identical configuration in the pore-scale model, the system will exhibit a lower fluid velocity, therefore making it less sensitive to inlet disturbances in comparison to a low-density fluid.

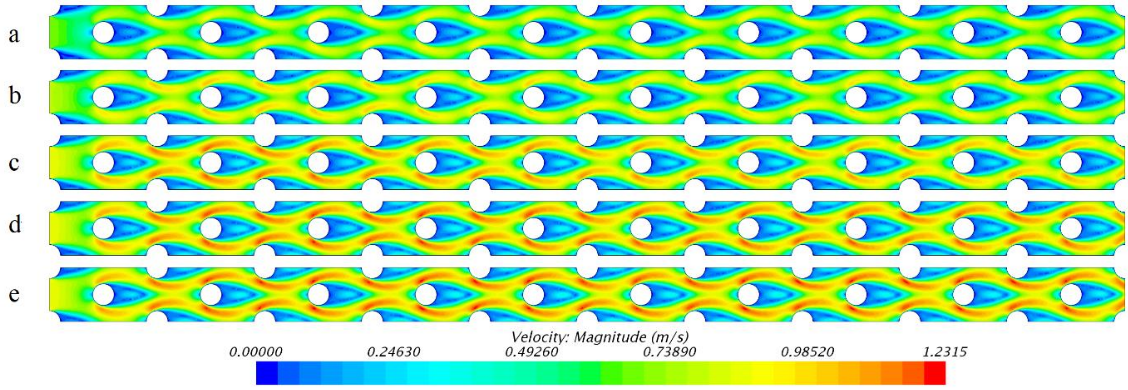

Figure 4-10: Temporal evolution of the velocity field with 10 sec. ramp duration (on Velocity) for H_2 at Re=250 $\varepsilon = 0.874$

Although the fluid properties of hydrogen make it more sensitive to inlet disturbances, it also appears to be a lot more responsive to the thermal diffusion and viscous effects incurred around the obstacles when compared with air. This is observed in the response lag ratio of hydrogen in Figure 4-11a, where all respective porosities report a higher response lag ratio when compared with its counterpart, air. A monotonic increase in the response lag ratio is observed for air across all three porosities of the system. However, hydrogen exhibits a response lag ratio further downstream for larger porosities. The change in porosity amongst different working fluids is further analysed in Figure 4-11b. The common trend changed where the largest porosity outputs a higher response lag ratio for high density fluids (carbon dioxide and air) and the opposite is noted for hydrogen when compared with the lowest porosity. As the Reynolds number is increased with decreasing porosity the RLR decreases rather than increasing for air and carbon dioxide due to their fluid properties. With hydrogen being more sensitive and less dense the change in Reynolds number with porosity has little or no effect in the overall RLR.

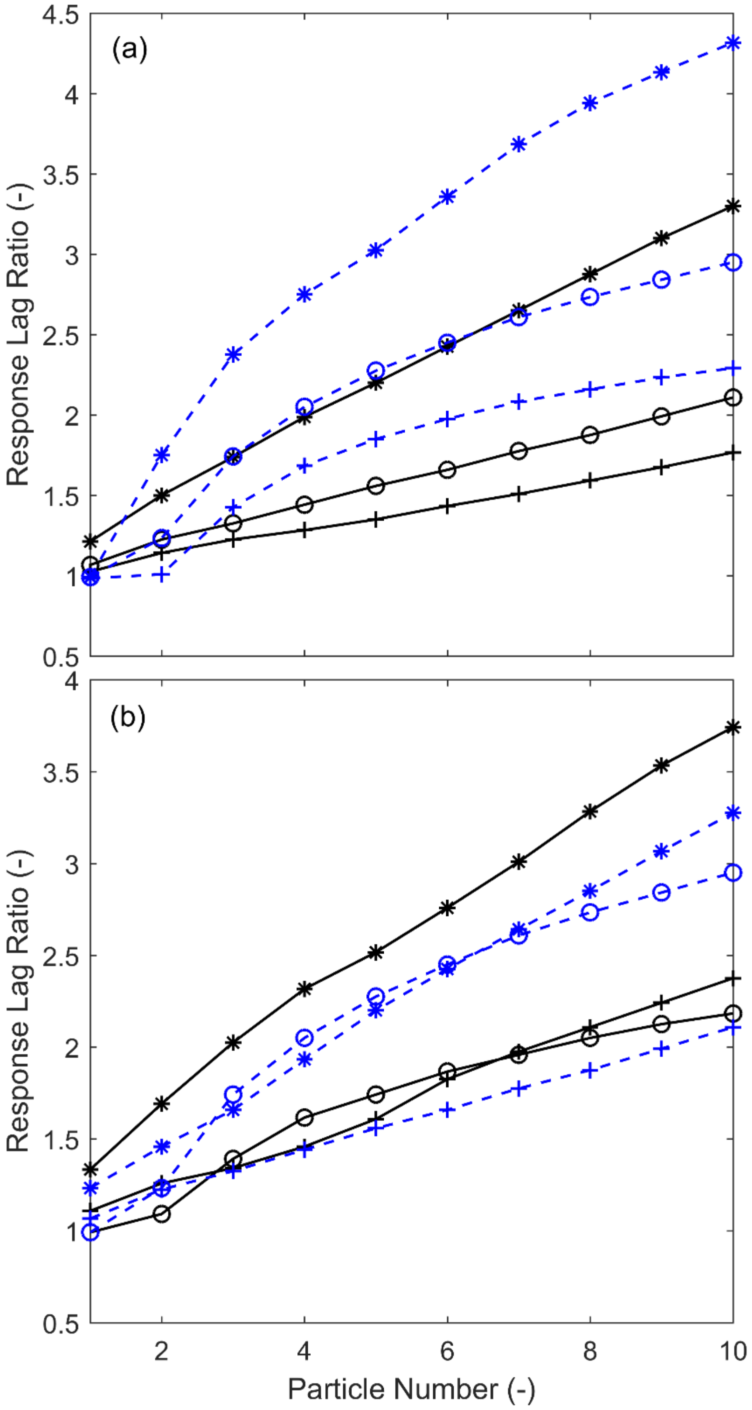

Figure 4-11: a) The RLR for air (black) and H_2 (blue) at porosities of 0.87 (+), 0.80 (o) and 0.72 (*) when Re=250; b) The RLR for 0.87 (black, Re=150) and 0.80 (blue, Re=250) porosities and air (+), H_2 (o) and CO_2 (*)

The RLR is further discussed under the variable parameters of amplitude and ramp duration for the different working fluids. Figure 4-12a shows the increase in amplitude augments the inlet velocity therefore increasing forced convective heat transfer and viscous effects around the obstacles; resulting in a higher response lag ratio. Fluid properties continue to impact the degree of RLR reported, with hydrogen (lower density fluid) showcasing larger increases in RLR as the amplitude increases. However, for air (higher density fluid), although there is an increase in RLR; it is minimal. A general trend is also observed in Figure 4-12b, as the ramp duration is prolonged amongst the working fluid the RLR is noted to decrease. The lower RLR is reported as the gradual increase in velocity due to longer ramp duration decays the viscous effects and allows more time for heat to transfer from the circular obstacles to fluid with ease. Contrary to the previous trend reported in Figure 4-12a, Figure 4-12b showcases higher RLR for air than hydrogen in general. Yet, it is also more responsive to the increase in ramp duration allowing the system to adapt to a higher density fluid resulting in a lower RLR than hydrogen for a 30 seconds ramp duration. The RLR being the response lag ratio is representative of the attenuation effect of the porous medium upon an input disturbance. Such attenuation is generally more intense when the disturbance includes strong gradients. For a ramp disturbance, strong gradients imply higher amplitude and shorter duration. That is why in Figure 4-12 increase of Ramp amplitude results in higher values of RLR while increases in ramp duration reduces that.

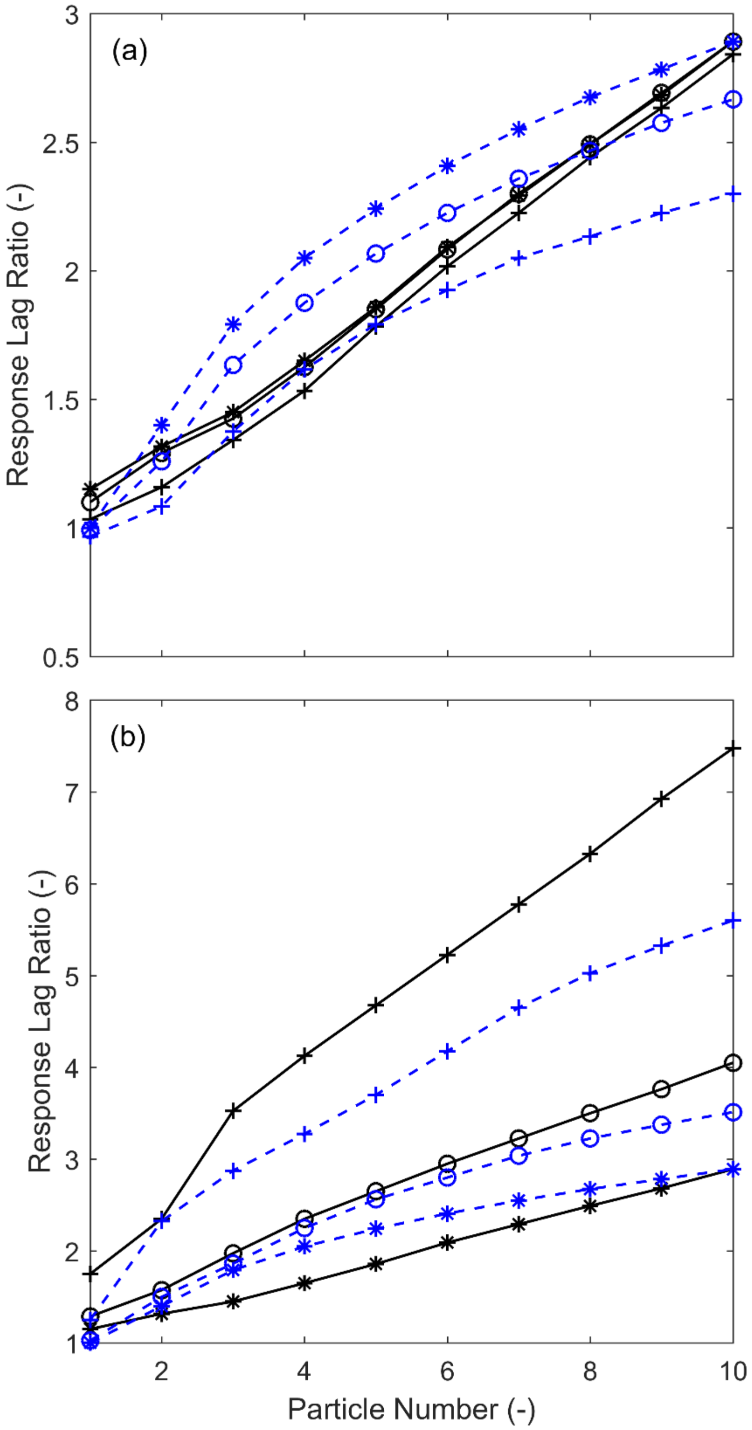

Figure 4-12: a) The effect of ramp amplitude on RLR for air (solid black) and H_2 *(dash blue) at 10% (+), 20% (o) and 30% (*) amplitudes during a 30 second ramp duration; b) The effect of ramp duration on RLR for air (solid black) and* H_2 *(dash blue) at 10 sec. (+), 20 sec. (o) and 30 sec. (*) durations for 30% amplitude.*

4.4 Conclusions

A pore-scale analysis was conducted to study the effects of forced convection in porous media subject to a ramp disturbance superimposed on the entrance of a reticulated porous structure. Comprehending the transient response of porous media has grown in importance with its widespread use in numerous emerging applications. This study allows the prediction of thermal response of the pertinent system subject to time dependent disturbances at the inlet. The porous model was made up of ten consecutive cylindrical obstacles with set isothermal boundary conditions and was subject to ramp disturbance for the flow velocity and temperature at the inlet. The RLR and transient behaviour at each obstacle was examined in detail by monitoring the spatiotemporal evolution of the flow and temperature fields as well as the surface averaged Nusselt number.

The key findings are as follows:

- An imposed ramp temperature disturbance at the inlet has an identical thermal response throughout the system, where an inlet velocity ramp input shows a varying response for each cylindrical obstacle. This makes a pore-scale analysis essential to monitor the transient thermal response of a porous structure.
- An increase in Reynolds number has a minuscule rise on the RLR.
- An increase in porosity decreases the RLR. Yet, when Reynolds number is decreased for a structure with a large porosity, RLR increases for high density fluids only (air and carbon dioxide).
- An increase in amplitude increases the RLR.
- An increase in ramp duration decreases the RLR, more strongly for high density fluids.

After extensive numerical investigations into the temporal disturbances introduced at the inlet within the pore-scale model, an experimental study was devised with various fuel mixture blends to investigate the dynamic response of ultra-lean combustion in a porous burner.

Chapter 5 Unsteady ultra-lean combustion of methane and biogas in a porous burner – An experimental study

Applied Thermal Engineering – Rabeeah Habib, Bijan Yadollahi, Ali Saeed, Mohammad Hossein Doranehgard, Larry K.B. Li, Nader Karimi

5.1 Introduction

Utilisation of low-calorific fuels can improve energy efficiency and reduce carbon emissions by combustion systems [49]. In particular, combustion of carbon neutral, low-calorific fuels is of high significance in lowering CO_2 emissions [61,169,170]. Yet, combustion of low-calorific fuels often involves significant challenges regarding flame stability in most conventional burners [171,172]. Porous burners offer a practical technological route to address this issue [63,64,173]. Strong heat recirculation in porous burners allows premixed combustion of fuel mixtures that might not otherwise be flammable [48,174]. Currently, many industrial applications employ porous burners [175,176]. Examples include glass and chemical processing [177], gas turbines and propulsion [65,66] as well as heat exchangers [178]. In all these applications, combustion occurs under steady state conditions. However, switching from fossil fuels to biogas and biosyngas often includes utilisation of unsteady sources of fuels [179,180]. The unsteadiness could be in the fuel flow rate and/or chemical composition and is largely due to the temporal change in the feedstock that produce renewable fuels [67,180]. Unlike that under steady state, time-dependent combustion in porous media has, so far, received very little attention.

The general area of combustion in inert and catalytic porous media has already received substantial attention, see for example [70,181,182]. However, existing investigations have predominately focussed on steady combustion ([182,183]) where most studies have analysed burner operation with the use of methane mixtures ([184,185]) and very few incorporate ultra-lean operation [186]. As a result, there appears to be a gap in understanding the dynamic response of porous burners operating under time-varying and ultra-lean conditions. An air and fuel mixture is considered to be lean when $\phi < 1$. However, in ultra-lean combustion the fuel concentration is at or below the lean flammability limit for a free flame, i.e. for methane $\phi \leq 0.5$ [49]. Hence, it is imperative to understand unsteady combustion in porous burners. Here, a concise review of literature on the experimental studies related to premixed combustion in porous media over the past decade is put forward in a chronological order. Reviews of earlier works can be found in Refs. [187,188].

Bubnovich et al. [189] carried out an experiment with the aim of achieving flame stabilisation of premixed air and methane mixture within a porous burner between alumina balls of different sizes. A packed bed of alumina balls was utilised throughout the burner with a shorter diameter upstream (2.5mm) and larger diameter downstream (5.6mm). The burner was covered with insulation material to minimise heat losses and inserted thermocouples were utilised to measure the temperature inside the porous medium. CO and NO_x emissions were also measured at the exit of the burner using a gas analyser. Bubnovich et al. [189] found the flame to stabilise at the interface of the Alumina balls for the flow rates between 7.01-19.00 l/min where $0.6 < \phi < 0.7$. The authors [189] also found the pollutant emissions to be extremely low within this stability range where the maximum flame temperature was recorded to be 1675 K. Mujeebu et al. [190] investigated the combustion and emission characteristics of two novel porous burners with that of a conventional burner. The surface burner was made-up of two sheets of alumina foam; with the lower sheet consisting of a higher porosity and the upper sheet of a lower porosity. The authors [190] measured the temperature at four different locations by inserting thermocouples in the axial direction and the inlet fuel was a pre-vaporised liquid petroleum gas mixture. The flame stability, thermal efficiency, pollutant emissions and maximum flame temperature were compared with that of a conventional burner. A reduction of NO_x emissions of up to 75% for both porous burners compared with a conventional burner was reported.

A two-layer porous burner for low pollutant emissions was developed by Keramiotis et al. [191] who monitored its thermal efficiency and operational limits. A silicon carbide ceramic foam was used as the solid matrix with a density of 10ppi and methane and liquefied petroleum gas were chosen as the input fuels.

The authors [191] varied different input parameters including equivalence ratio for lean combustion (0.625-0.83), excess air and thermal load output (200-1000 $\mathrm{kW/m^2}$). The burner response was monitored by measuring the solid phase temperature and pollutant emissions. Keramiotis et al. [191] discovered excellent fuel interchangeability between liquefied petroleum gas and methane with respect to pollutant emissions and burner operation. It was concluded that for both fuels the burner is more sensitive to the changes in thermal load rather than equivalence ratio.

Robayo et al. [192] studied the enhancement of combustion in porous media by introducing perovskite catalysts to the ceramic matrix. A large porosity silicon carbide ceramic foam was utilised as the burner matrix with a steady lean methane/air mixture as the inlet fuel. Temperature was measured via thermocouples across eight axial points. Robayo et al. [192] found that all perovskite catalysts enhance the burner performance. Dehaj et al. [193] conducted an experimental study of premixed combustion of methane in a porous burner with the addition of a heat exchanger for household heating application. They [193] found the pressure to decrease within the burner as there is an increase in power and the excess air ratio.

A variable porosity porous burner was built by Song et al. [61] to operate on ultra-low calorific gas combustion. Silicon carbide was utilised as the ceramic foam whereby it gradually increases in pore density throughout, from the entrance to the exit of the burner. The purpose was to combust ultra-low calorific fuels lower than 6.28 $\mathrm{MJ/m^3}$. In order to accommodate this, the authors [61] preheated the burner by igniting liquefied petroleum gas then switched to a CH_4+N_2/air (ultra-low calorific) mixture, burning the ultra-low calorific fuel within the porous burner. Song et al. [61] discovered their annular porous burner increased the flame stability limit with a further reduction in CO emissions. The authors [61] managed to successfully combust a mixture with a calorific value as low as 1.4 $\mathrm{MJ/m^3}$.

In an experimental study, Ghorashi et al. [194] compared pollutant emissions of a conventional and a custom-built porous burner. These authors [194] monitored the effects of pore density and porous material on the pollutant emissions when the burner was fed by a steady flow of natural gas/air mixture. Silicon carbide and alumina were chosen as the solid porous matrix with pore density ranging between 10-30ppi and the burner operation was between ϕ=0.65-0.83. Ghorashi et al. [194] found the CO emissions to reduce by the use of alumina instead of silicon carbide. They also reported a surge in CO emissions with the increase in pore density. Chaelek et al. [195] developed a novel pre-heating air porous medium burner to compare its performance with a conventional burner. They designed an annular burner filled with alumina spheres whereby pre-heated air recirculates towards the inlet of the burner. The authors [195] measured the temperature at 14 different points via thermocouples to monitor the thermal performance of the burner and the exhaust gases were fed into a gas analyser. Chaelek et al. [195] found the maximum thermal efficiency of the burner to reach 51% whereby a reduction in energy consumption by 28.6% was noted when compared to a conventional burner.

In their experimental investigation, Devi et al. [196] ran a porous burner on a power range between 5-10 kW and a stable lean operating range of $0.75 < \phi < 0.97$ with biogas as fuel. These authors [196] analysed the performance of a conventional burner using the identical input parameters for comparative analysis. Devi et al. [196] discovered that their porous radiant burner reduced CO and NO_x emissions up to 95% and 85% respectively when compared to a conventional burner. Uniform temperature distribution on the surface of the burner was considered as a sign of enhanced combustion performance. Hongsheng et al. [197] designed a porous burner operating on diesel fuel subject to pulse combustion. The core part of the burner consisted of alumina filled spheres filled within a quartz tube with a ceramic foam upstream to form the pre-heating zone. Hongsheng et al. [197] fed air and liquid diesel into the burner and once flame stability was achieved, the air flow was adjusted, and the fuel was injected at intervals to create pulse combustion. It was shown that the propagation of the flame was similar to subsonic combustion under transient operation.

Most recently, Habib et al. [157,168,198] conducted extensive pore-scale modelling and demonstrated that the response of heat transfer in porous media to fluctuations in the inlet flow could involve complex dynamics. As combustion in porous media is dominated by heat transfer, it is anticipated that combustion is also significantly affected by fluctuations in the inlet flow. However, as clearly reflected by the preceding review of literature there is currently almost no systematic study of such effects. The present work aims to fill in this gap through an experimental approach.

5.2 Methodology

5.2.1 Experimental setup and instrumentation

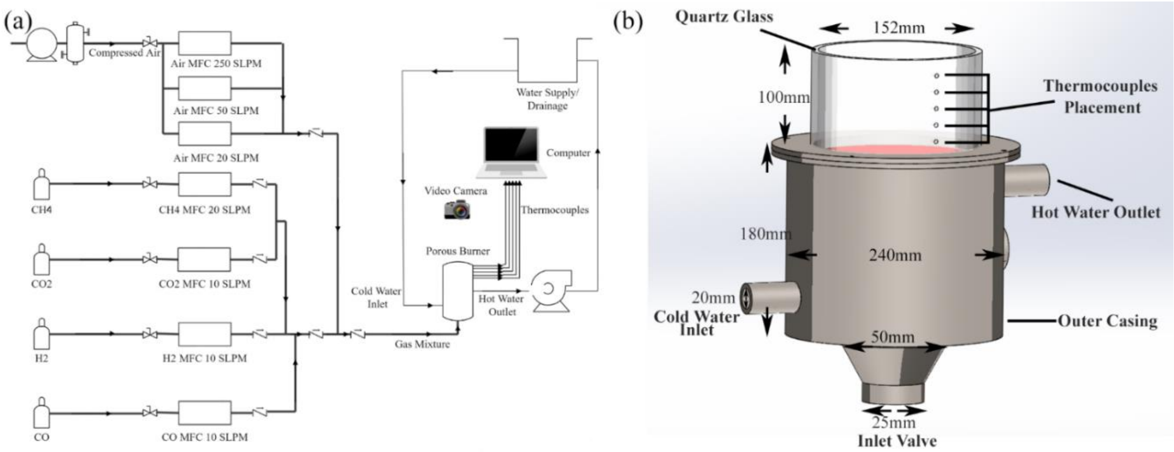

Figure 5-1: (a) Schematic of the experimental setup (b) 3-D model of the porous burner.

Figure 5-1 shows a schematic diagram of the employed experimental setup. The test rig and apparatus can be divided into four major parts; the fuel/air supply system, porous burner, water cooling supply and, data collection and measurement equipment.

5.2.1.1 Fuel/Air supply system

An air filter was used to extract moisture from compressed air. A quarter turn hand valve was installed upstream of air mass flow controllers (MFC) to manually operate the supply of air whereby an identical arrangement was made for fuel transmission between respective gas cylinders and MFCs with the installation of manual valves. ALICAT Scientific programmable MFCs were used for both fuel and air with an error margin of $\pm 0.6\%$. Flow Vision SC software from ALICAT was utilised to alternate the mass flow rate (standard litres per minute – SLPM) of each MFC via a computer. Different ranges of MFCs (Figure 5-1a) were operated to supply the steady and time-varying flows of air and fuel. Fuel was transported within a 6.35mm diameter stainless steel pipe linking to a 25.4mm outer diameter thick rubber pipe. The premixing of fuel and air took place within the rubber pipe before being fed into the porous burner.

5.2.1.2 Porous burner

The porous burner is comprised of four primary components including inlet valve, outer casing, combustion chamber and quartz glass. Figure 5-1b displays a 3-D model of the burner and provides the key dimensions. All components were manufactured from stainless steel. A quartz glass was fixed on top of the burner with high temperature resistant sealant to visually observe the combustion process in porous media. The combustion chamber sits within the outer casing of the porous burner, leaving a gap for water to flow in-between for the cooling process. The water cooling process occurs around the exterior of the combustion chamber and interior of the outer casing of the porous burner. The empty void paves way for a water tank with attached inlet and outlet. Cold water flows from the water supply into the lower side of the burner via the inlet; filling up completely before exiting to ensuring maximum efficiency of the cooling process.

The combustion chamber was filled with layers of porous ceramic comprising of the preheating and combustion zones. Alumina foam (20ppi - $\varepsilon \approx 0.47$) sits at the bottom of the combustion chamber followed by a cone shaped silicon carbide ceramic foam (20ppi) to form the preheating zone and to mitigate the risks of flashback. This is preceded by a packed bed of less dense silicon carbide foams (10ppi - $\varepsilon \approx 0.72$). Further downstream, the quartz glass was filled with high density silicon carbide (20ppi) foams with the exception of two low density silicon carbide foams (10ppi) for flame stabilisation as shown in Figure 5-2.

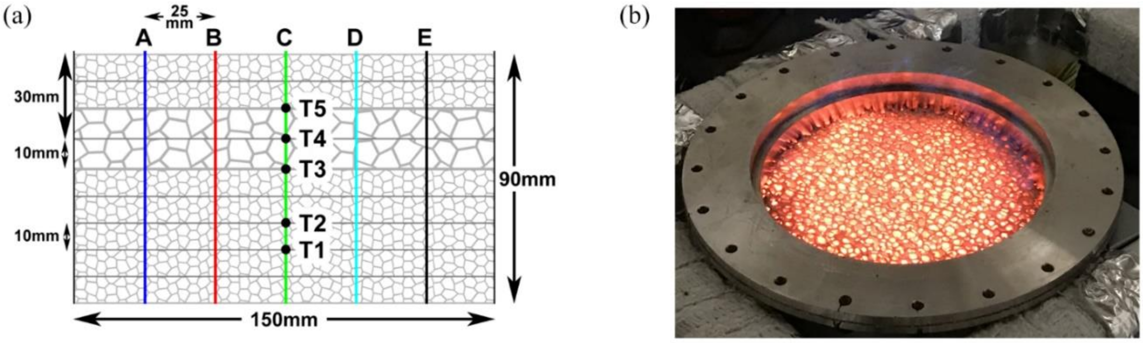

Figure 5-2: a) Schematic of the working section illustrating the position of thermocouples with reference points A, B, C, D, and E, b) Top view of the porous burner during operation.

5.2.1.3 Data collection

Temperature measurements were carried out at five different points at the centre of the ceramic foam as shown in Figure 5-2a. Type-N thermocouples were used with a 0.5mm bead diameter because of their ability to withstand temperatures above 1553K with an error margin of ±2.5K. The thermocouples were fed through the holes drilled in the quartz glass to the centre of the ceramic foam; fixed in place with high temperature resistant sealant. The voltage signals generated by each thermocouple were passed through an amplifier and plotted using Pico software. One hundred data points were recorded per second for each thermocouple to ensure high accuracy at a much higher frequency than that of the inlet fuel oscillations. An Anton Sprint Pro 5 multifunction flue gas analyser was positioned a few centimetres above the burner exit to measure CO, CO_2, and NO_x emissions for steady state cases. The gas analyser error margin was reported to be ±10ppm for CO range of 0-200ppm, ±20ppm for CO range of 200-2000ppm, ±0.3% for CO_2 and ±5ppm for NO_x. A high resolution (1920x1080) digital camera was used to record the flame behaviour and movement at a distance of approximately 1.5m from the burner.

Uncertainty analysis was also calculated to ensure adequate accuracy of the experimental procedure during flow modulation. This included the uncertainty error for mass flow controllers and thermocouples. To define this, thermocouple values were used from case 4x where T3 reported the highest temperature (1363K). Therefore, T3 uncertainty error was assumed across all five thermocouples. Combined with the supplied MFC manufacturer error (±0.6%), the total accumulative uncertainty error in flow measurements= ±2.7%.

5.2.2 Experimental procedure

The fuel mixture equivalence ratio [199] was defined as

$$\phi = \frac{(m_f/m_{air})_{actual}}{(m_f/m_{air})_{stoichiometric}} \tag{5-1}$$

whereby the reactants form a lean mixture when the equivalence ratio is less than unity. The thermal load of the burner [199] [200] is defined as

$$P = \dot{m}_f \times LHV_f \tag{5-2}$$

where $\dot{m}_f$, is the fuel mass flow rate and LHV_f, is the fuel lower heating value whereby the energy produced by the burner is calculated for each respective fuel.

Table 5-1 provides details of the experimental conditions for steady cases and Table 5-2 shows details for the unsteady cases, for both methane and biogas mixtures. Flow Vision SC software was used to program the MFCs to set the fuel flow rate systematically. The burner was ignited under lean conditions and the subsequent decrease in the fuel flow rate resulted in ultra-lean combustion and stabilisation of the flame inside the porous foam. The gas analyser measured pollutant emissions after the steady state cases had completely stabilised and the final temperature were recorded via the thermocouples.

As shown in Table 5-2, after achieving flame stability, the methane flow rate was oscillated between 10-30% of its base value at different frequencies for both mixtures. This was done by programming the digital mass flow controller to change the flow rate of methane according to a sinusoid with variable frequency and amplitude. The axial temperature profile was recorded for the entirety of the flame oscillation. The flame position movement was monitored along the reference points shown in Figure 5-2 with a post-processing code developed in MATLAB.

5.2.3 Image processing

Extensive image processing was conducted to monitor the flame movement/position. Video footage was extracted for each unsteady case for a complete sinusoidal cycle – either 60s or 180s. A compilation of burner snapshots were created using Adobe Premiere Pro at a time interval of 2s for each study to visualise the flame behaviour. Further, a code was developed in MATLAB to process the snapshots. After cropping each image to strictly the ceramic foam (see Figure 5-2a), the image resolution was converted to represent distance whereby 5.34 pixels of each image corresponds to 1mm in physical distance. In order to monitor the vertical flame movement, five equally spaced reference points were created along the x-axis in the y-direction. Each image was converted from colour to black and white, whereby a luminance criterion was set to detect the flame. The luminance value for flame detection differed for each fuel and was validated by visual confirmation. Once the luminance criterion was satisfied, the y-location of these values was calculated (where flame was detected) at the designated reference points. The values were further refined and only the upper and lower y-location was used to identify the top and bottom part of the flame at each reference point. The process was repeated for all snapshots for each case. The upper and lower locations of luminance values were then plotted in time, representing the flame movement in the y-direction of the ceramic foams across the five reference points over a complete sinusoidal cycle.

Table 5-1: Steady Experiments - a-CH_4, b-Biogas (CH_4=70%,CO_2=30%)

	CO_2 (standard L/min)	CH_4 (standard L/min)	Air (standard L/min)	Mixture (standard L/min)	Equivalence Ratio (ϕ)	Thermal Power (kW)
Case 1a		4.35	142.49	146.84	0.275	2.34
Case 2a		5.03	150.88	155.91	0.3	2.7
Case 3a		4.61	150.88	155.49	0.275	2.48
Case 4a		5.59	167.64	173.23	0.3	3
Case 5a		5.12	167.64	172.76	0.275	2.75
Case 6a		5.63	184.4	190.03	0.275	3.02
Case 7a		6.7	201.17	207.87	0.3	3.6
Case 8a		6.14	201.17	207.31	0.275	3.3
Case 9a		6.66	217.93	224.59	0.275	3.57
Case 10a		6.92	226.31	233.22	0.275	3.71
Case 1b	1.41	3.3	99.07	103.78	0.3	2.4
Case 2b	1.29	3.03	99.07	103.39	0.275	2.2
Case 3b	1.59	3.71	111.46	116.76	0.3	2.7
Case 4b	1.45	3.4	111.46	116.31	0.275	2.48
Case 5b	1.76	4.13	123.84	129.73	0.3	3
Case 6b	1.62	3.78	123.84	129.24	0.275	2.75
Case 7b	1.94	4.54	136.22	142.7	0.3	3.3
Case 8b	1.94	4.54	148.61	155.09	0.275	3.3
Case 9b	2.1	4.92	160.99	168.01	0.275	3.57

Table 5-2: Oscillatory Experiments - x-CH_4, y-Biogas (CH_4=70%, CO2=30%)

	CO_2 (Standard L/m)	CH_4 (Standard L/m)	Air (Standard L/m)	Mixture (Standard L/m)	Equivalence Ratio (ϕ)	Thermal Power (kW)	Oscillation period (s) of CH_4 flow	Amplitude (%) of steady CH_4 flow
Case 1x		6.22-7.6	226.3	232.52-233.9	0.2475-0.3024	3.34-4.08	60s	10%
Case 2x		4.84-8.98	226.3	231.14-235.28	0.1925-0.3572	2.6-4.82	60s	30%
Case 3x		6.22-7.6	226.3	232.52-233.9	0.2475-0.3024	3.34-4.08	180s	10%
Case 4x		4.84-8.98	226.3	231.14-235.28	0.1925-0.3572	2.6-4.82	180s	30%
Case 1y	2.1	4.43-5.41	161	167.52-168.5	0.2475-0.3024	3.41-3.74	60s	10%
Case 2y	2.1	3.44-6.4	161	166.53-169.49	0.1925-0.3572	3.07-4.06	60s	30%
Case 3y	2.1	4.43-5.41	161	167.52-168.5	0.2475-0.3024	3.41-3.74	180s	10%
Case 4y	2.1	3.44-6.4	161	166.53-169.49	0.1925-0.3572	3.07-4.06	180s	30%

5.3 Results and discussion

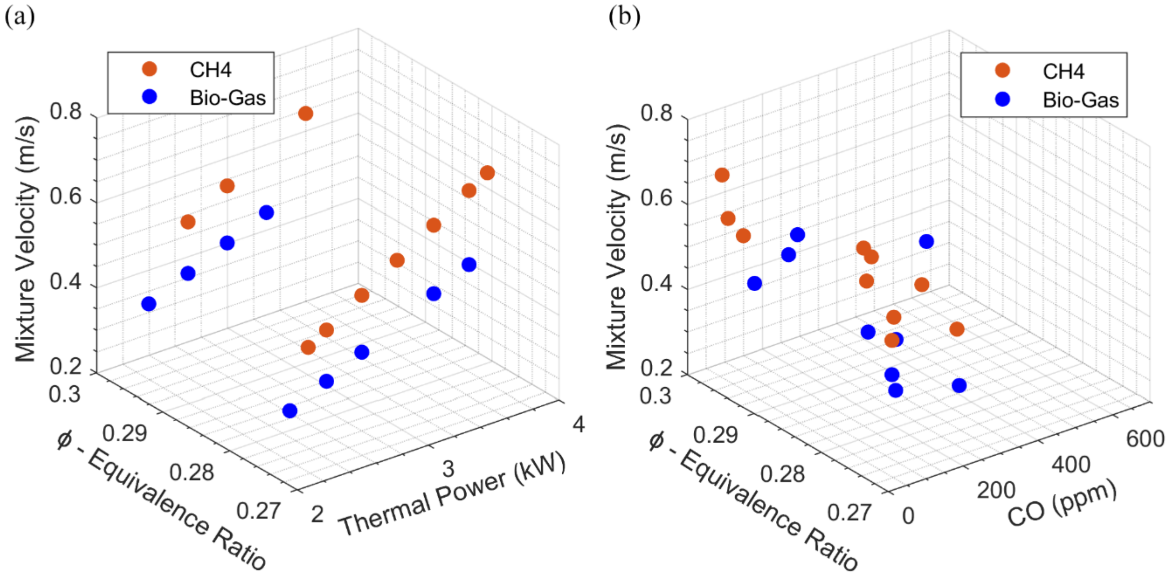

Figure 5-3: Steady CH4/Biogas mixtures (a) Equivalence Ratio vs Thermal Power (b) Equivalence Ratio vs CO emissions.

The right quantity of heat generation, heat recirculation and heat losses are keys to achieving combustion stabilisation within porous media [49]. In general, combustion stabilisation can be achieved when the mixture velocity (air and fuel flow velocity) and flame speed are proportionate. Figure 5-3 displays the burner performance under ultra-lean, steady state cases in which combustion stabilisation for both methane and biogas mixtures (Table 5-1) was achieved. Figure 5-3a illustrates the relations between burner thermal power and mixture equivalence ratio and velocity. Here, the mixture (air and fuel) velocity refers to that inside the quartz tube. Expectedly, the thermal power increases monotonically as the mixture velocity is increased. It is also clear that methane mixtures feature relatively higher thermal power compared to those of biogas, which is simply due to the higher enthalpy of combustion of methane.

Figure 5-3b highlights the effects of mixture velocity and equivalence ratio on CO emissions. The common trend shows the CO emissions plummet for a higher mixture velocity and for a lower equivalence ratio. As the mixture velocity reduces, the temperature within the combustion zone decreases. This is due to reduction in heat release while the heat losses remained almost unchanged. Lower temperatures contribute to incomplete combustion and interrupt oxidation of CO to CO_2. Lower equivalence ratio also reduces the heat generation and brings down the reaction temperature which then results in increase in CO emissions. Evidently, emission of CO is relatively high for biogas. This is because the existence of CO_2 in the mixture decreases the temperature compared to that in methane mixtures and increases the likelihood of incomplete combustion.

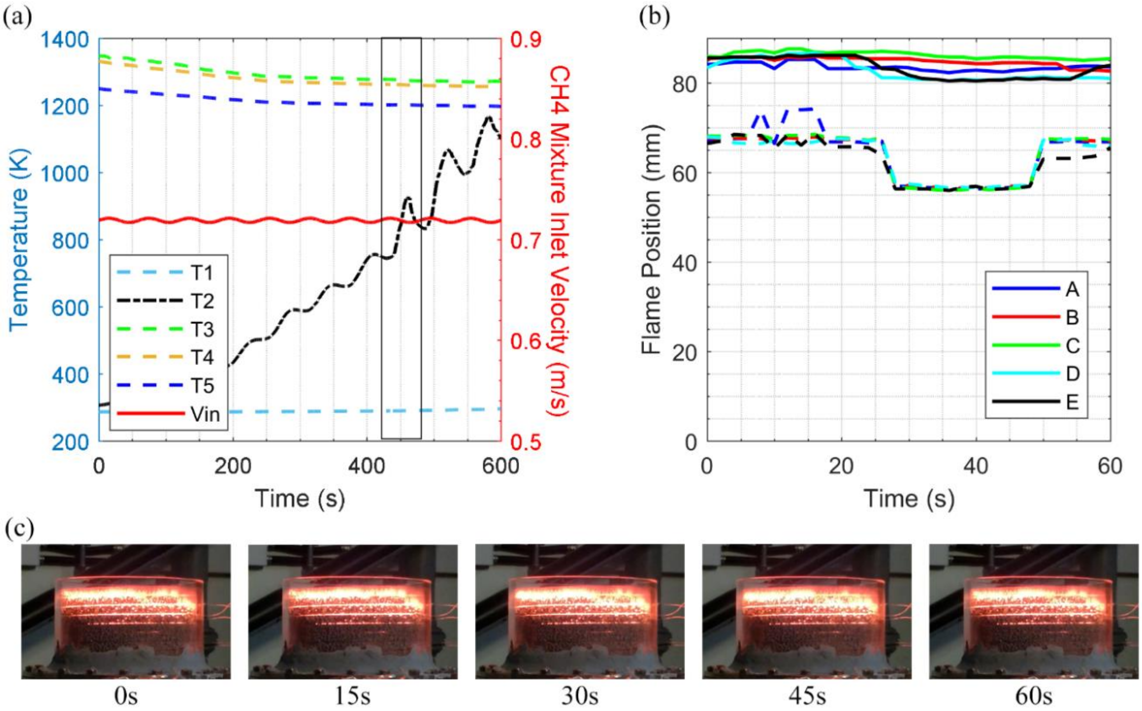

Figure 5-4: Unsteady case 1x, α=10%, t=60s (a) Axial temperature profile vs CH_4 mixture velocity (b) Flame position movement at respective reference points, solid line – upper part of flame, dash line – lower part of flame (c) Snapshots of porous burner subject to unsteady flow at different intervals.

Case 10a (Table 5-1) was the starting point for all unsteady methane cases before introduction of the inlet sinusoidal disturbances. Figure 5-4 illustrates the porous burner performance operating on methane mixture subject to inlet disturbance superimposed on the fuel flow rate with a period of 60s and amplitude of 10%. The axial temperature was monitored throughout the entirety of the experiment whereby a flashback criterion was set at T1=773K by empirical observation. Modulation of fuel flow rate resulted in a visible motion of the reactive front inside the quartz tube. This motion was filmed (see section 5.2) and the subsequent temperature variation were further recorded. In total, ten cycles of oscillation in fuel flow rate were completed with the burner operation remaining stable.

Figure 5-4a shows the temperature traces recorded by the thermocouples (see Figure 5-2a) as well as the calculated fluctuations in the mixture flow velocity. Clearly, the temperature has been recorded by T3, between the interface of high density and low-density silicon carbide ceramic foam. The interface amid the two ceramic foams offers a supplementary means of stabilising the combustion flame whereby the upstream region behaves as a flashback arrestor. This is primarily due to the sudden decrease in pore size upstream of the interface. While throughout the experiment all measured temperatures exhibit almost stationary behaviours, T2 continues to rise as a direct response to the fluctuations in the inlet sinusoidal fuel. The independency of temperature traces upon the fluctuations in fuel flow implies that the flame motion has not been sensed by the thermocouples recording those traces. In the current case, this means that fluctuations in flame location is limited to the vicinity of thermocouple T2. To further investigate this, Figure 5-4b visualises the flame position movement corresponding to the eighth sinusoidal cycle at its designated reference points. After a period of roughly 27s, the lower part of the flame takes a significant dip (12mm) which can be visually observed in Figure 5-4c. This correlates to the temperature recoded by T2 as Figure 5-4b shows that the movement of the flame is around 10mm, which explains why other thermocouples did not sense the motion of the flame. A comparison between the flow velocity signal in Figure 5-4a (the part inside the box) and flame location in Figure 5-4b, reveals that the flame motion more and less follows the fluctuation in the mixture velocity. Indeed, there is a phase lag between the two fluctuations. Yet, this is very much to be expected as time lag between the flow and flame oscillations are well recorded by studies on flame dynamics, e.g. [106].

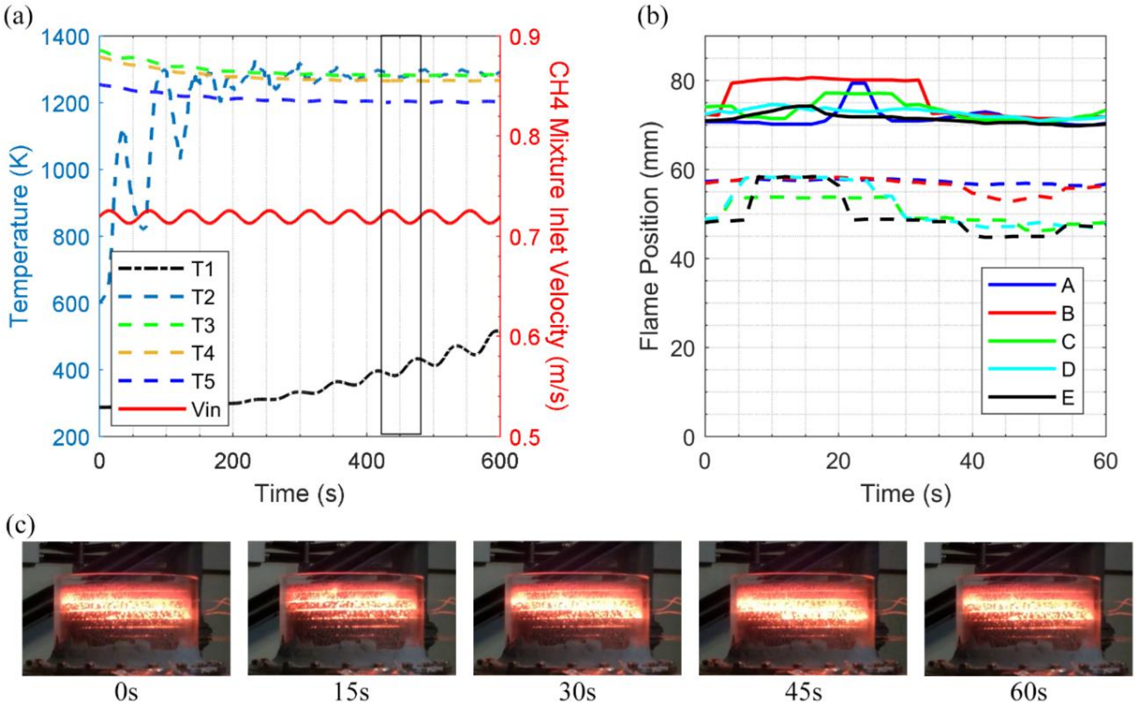

Figure 5-5: Unsteady case 2x, α=30%, t=60s (a) Axial temperature profile vs CH_4 mixture velocity (b) Flame position movement at respective reference points, solid line – upper part of flame, dash line – lower part of flame (c) Snapshots of porous burner subject to unsteady flow at different intervals.

Figure 5-5 shows a similar case to case 1x albeit with a 30% inlet fuel flow rate illustrated in red. In Figure 5-5a, the temperature is initially observed at T3, but as the time elapses, the temperature traces recorded by T2 and T3 as T2 become more responsive to the inlet disturbance. Heat recirculation is increased with the amplification of the inlet fuel flow rate. Downstream of the reaction zone, the combustion products are likely to have a higher temperature than the low-density ceramic foam, thus convective heat transfer takes place between the hot gases and the solid matrix. The solid foam then radiates and conducts heat upstream of the combustion zone. Since the temperature of the solid is larger than that of the inlet mixture; convective heat transfer takes place between the solid and gas. As a result, the incoming cold reactants are preheated. However, due to the lower pore size and high-density ceramic foam upstream, the rate of conductive heat transfer is increased as direct impact of large inlet fuel disturbance over a relatively short time. Consequently, the upstream thermocouple, T1 highlights the thermal response of the inlet disturbance over ten oscillatory cycles. Figure 5-5c demonstrates the flame movement of the eighth cycle of the inlet fuel fluctuations (marked by the box in Figure 5-5a). A broken oscillatory pattern is visible as the flame position again directly correlates to the thermal response of the system. With the introduction of an increased amplitude the flame travels further upstream when compared to case 1x. As the core part of the flame has settled within the lower density silicon carbide, the flame thickness has also increased uniformly as can be seen in Figure 5-5c.

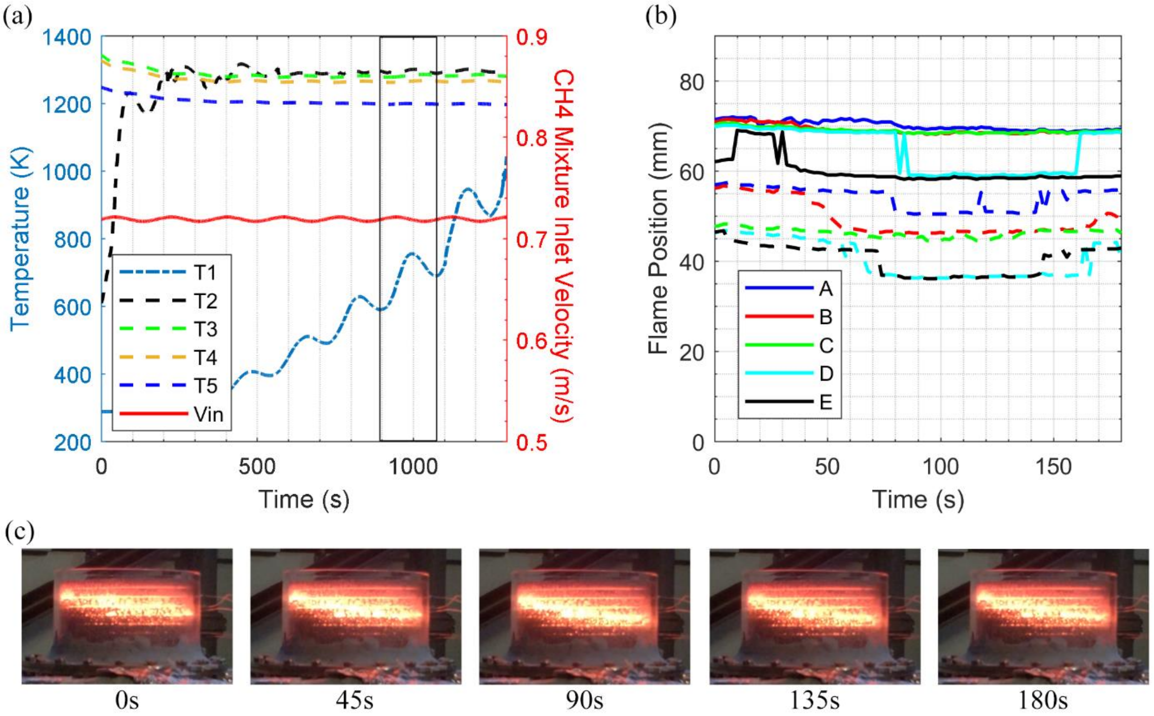

0s 45s 90s 135s 180s

Figure 5-6: Unsteady case 3x, α=10%, t=180s (a) Axial temperature profile vs CH_4 mixture velocity (b) Flame position movement at respective reference points, solid line – upper part of flame, dash line – lower part of flame (c) Snapshots of porous burner subject to unsteady flow at different intervals.

Next, the period of fuel flow oscillation was extended to 180s to provide a longer time for the combustion system to respond. Figure 5-6a (case 1c) shows the temperature transitions from T3 to T2 post 500s of the experiment. At this point, the combustion zone transitions into the upstream high density ceramic foam. Although the inlet disturbance is at a minimal amplitude of 10%, the prolonged fluctuation period extends the internal heat recirculation of the hot combustion products to the incoming cold reactants and minimises heat losses even when the inlet velocity is brought to low values. The oscillatory temperature response at T1 can be seen to increase rapidly as the combustion zone moves to the lower porosity silicon carbide foam, improving heat conduction and thermal radiation with the increase in foam density. Figure 5-6b provides a visual of the sixth cycle of the inlet velocity impact upon the flame movement. Although, the flame position oscillates according to the imposed sinusoidal disturbance, a non-uniform movement is detected. This is further verified by Figure 5-6c whereby the flame features a roughly 30-degree tilt. This behaviour could be due to the existence of small imperfections in the ceramic foam orientation with the insertion of thermocouples allowing the preheating of incoming cold reactants to accelerate on one side of the burner foam. Nonetheless, such tilting was not observed in steady state cases and its inception is related to long-period forcing.

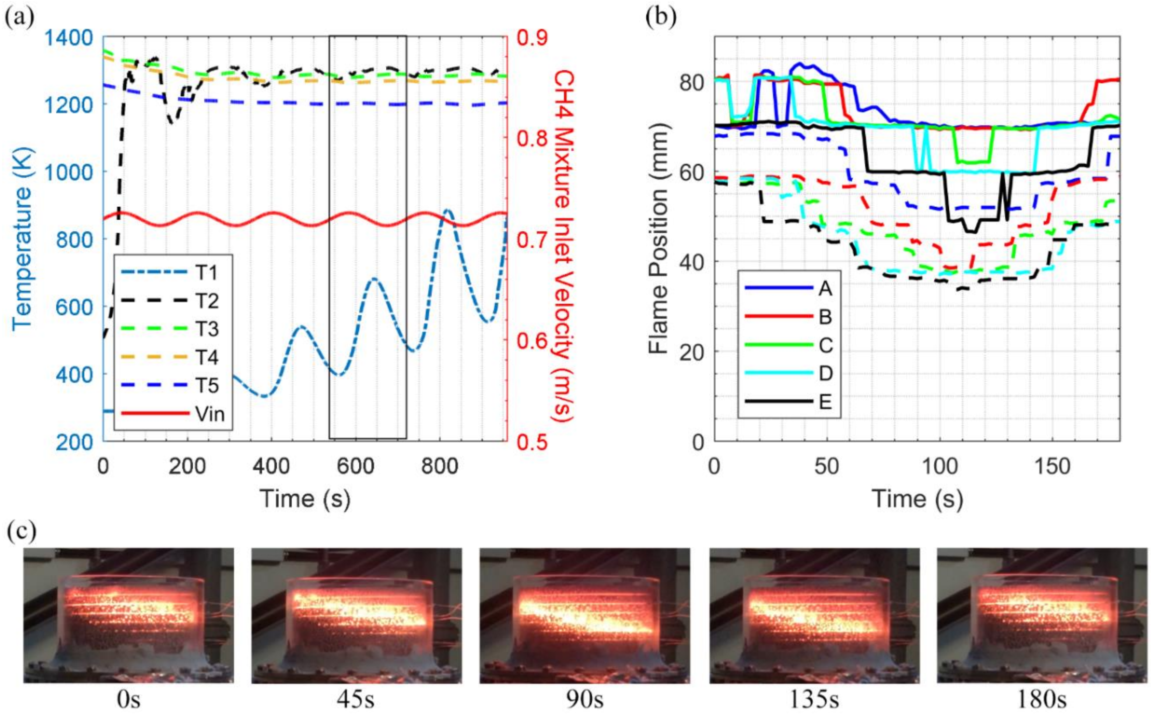

Figure 5-7: Unsteady case 4x, α=30%, t=180s (a) Axial temperature profile vs CH_4 mixture velocity (b) Flame position movement at respective reference points, solid line – upper part of flame, dash line – lower part of flame (c) Snapshots of porous burner subject to unsteady flow at different intervals.

Figure 5-7 highlights (case 4x) the thermal response and flame oscillations as a result of a modulation of fuel flow with the amplitude of 30% over a cycle period of 180s. With the increase of amplitude in the methane fuel rate, the equivalence ratio surges to 0.3572 at the peak of the sinusoidal wave, far higher than the stable operating range for the burner for a methane mixture. At the trough of each sinusoidal wave, the equivalence ratio drops to 0.1925, quenching the local flame. Yet, with an increased period of fluctuations, in each cycle the porous burner stores the heat and with the increase of the fuel flow rate; accelerates the excess enthalpy combustion. As a result, in Figure 5-7a, after five cycles the fuel flow is cut off as the burner reaches the flashback criterion within 900s, far quicker than when the amplitude was set at 10% (1300s). Figure 5-7b portrays the fourth sinusoidal cycle of the flame movement. It can be seen that the non-uniform movements of the flame augments amongst the reference points with an increase in amplitude. Figure 5-7c displays this behaviour where the flame not only causes a further tilt but also visualises the further spread of the flame amongst the porous burner within the ceramic foam.

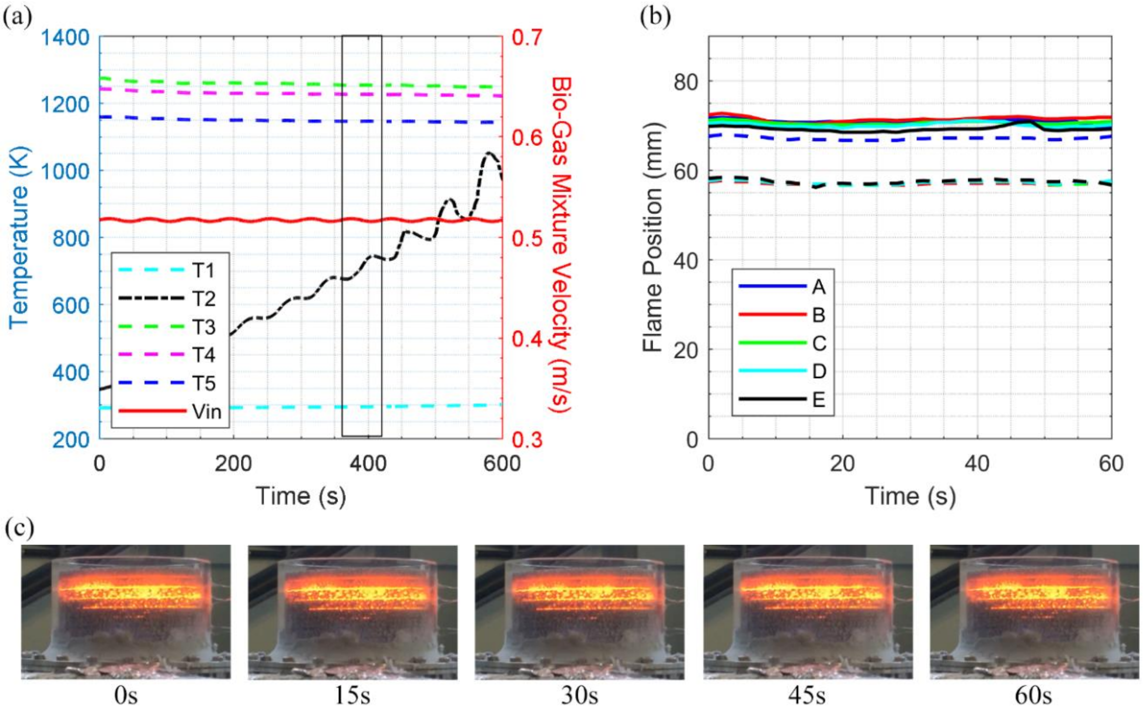

Figure 5-8: Unsteady case 1y, a=10%, t=60s (a) Axial temperature profile vs Biogas mixture velocity (b) Flame position movement at respective reference points, solid line – upper part of flame, dash line – lower part of flame (c) Snapshots of porous burner subject to unsteady flow at different intervals.

Case 9b (see Table 5-1) is used as the foundation for all unsteady biogas mixture cases before the inlet sinusoidal disturbances are introduced. Figure 5-8 represents biogas mixture subject to sinusoidal disturbance of 10% amplitude of methane flow over a period of 60s (case 1y). The carbon dioxide composition of the mixture and air are kept constant amongst all biogas experiments. Upon initial observation, Figure 5-8a shows the inlet fuel oscillations have little or no effect across all thermocouples except T2. For this case, the flame was subject to 10 forcing cycles while maintaining stable operation. A comparison between biogas and methane mixture displays a similar pattern with the rate of increase in temperature at T2, however from the eighth cycle onwards, a noticeably lesser temperature increase is observed in biogas mixture. This can be primarily attributed to the chemical composition of the mixture; as a smaller amount of fuel is being burned of the incoming reactants, less heat is generated. This led to smaller temperature rises and a longer time for heat to transfer. As a domino effect, this also increases the time to heat up the silicon carbide foam. Figure 5-8b displays that the flame movement is minimal within the seventh cycle as the reaction rate of biogas mixture is slower. A 10% amplitude has minimal impact, albeit due to the extensive thermal properties of silicon carbide it manages to withhold heat. Figure 5-8c depicts the biogas flame showing no obvious flame movement over the relevant period. However, it is noted that the flame colour and luminance is less intense when compared with the methane mixture due to the dilution of the mixture.

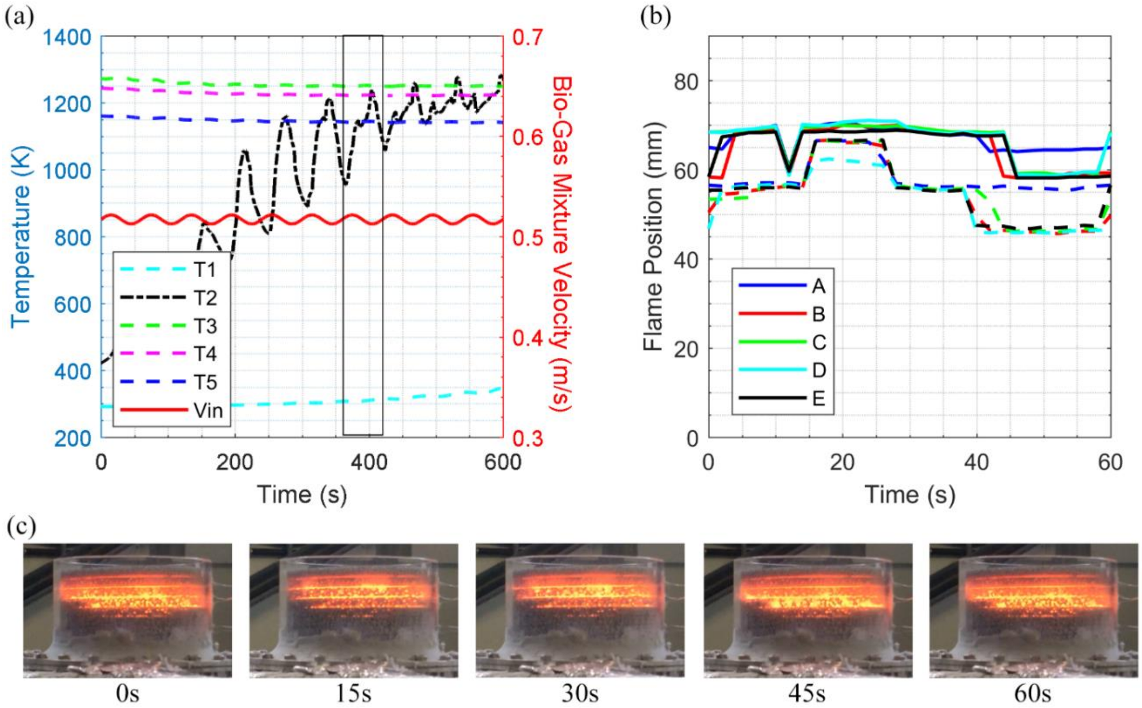

Figure 5-9: Unsteady case 2y, α=30%, t=60s (a) Axial temperature profile vs Biogas mixture velocity (b) Flame position movement at respective reference points, solid line – upper part of flame, dash line – lower part of flame (c) Snapshots of porous burner subject to unsteady flow at different intervals.

Figure 5-9 displays (case 2y) the trend of biogas flame as the amplitude of fluctuations in fuel flow is increased to 30% of its base value over a period of 60s. Figure 5-9a highlights stable burner operation throughout the experiment, completing ten cycles of the superimposed disturbances on fuel flow. The flame realigns itself with T2 being the most responsive thermocouple to the inlet disturbance whereby a sporadic oscillatory pattern is observed post cycle six of the experiment. During this period, a gradual increase in temperature at T1 is observed. It should be noted that due to the increase of amplitude of the fuel flow rate a greater increase and decrease in temperature is detected whereby a larger temperature amplitude is visible in T2 when compared to case 1y. Further, as a result of the short period of fluctuations, the silicon carbide foam is able to retain heat. Extending the gradual reduction in reaction rate, the burner overcomes flame extinction as the fuel flow rate rebounds into a surplus value from the foundation model (case 9b). This borderline uncertainty is also visible in Figure 5-9b and Figure 5-9c where the flame thickness is minimal for the seventh cycle of the experiment as the burner responds to the reduction in the flow rate from the previous cycle. After recovery, the temperature increases, the flame thickness widens, and the flame position moves upstream.

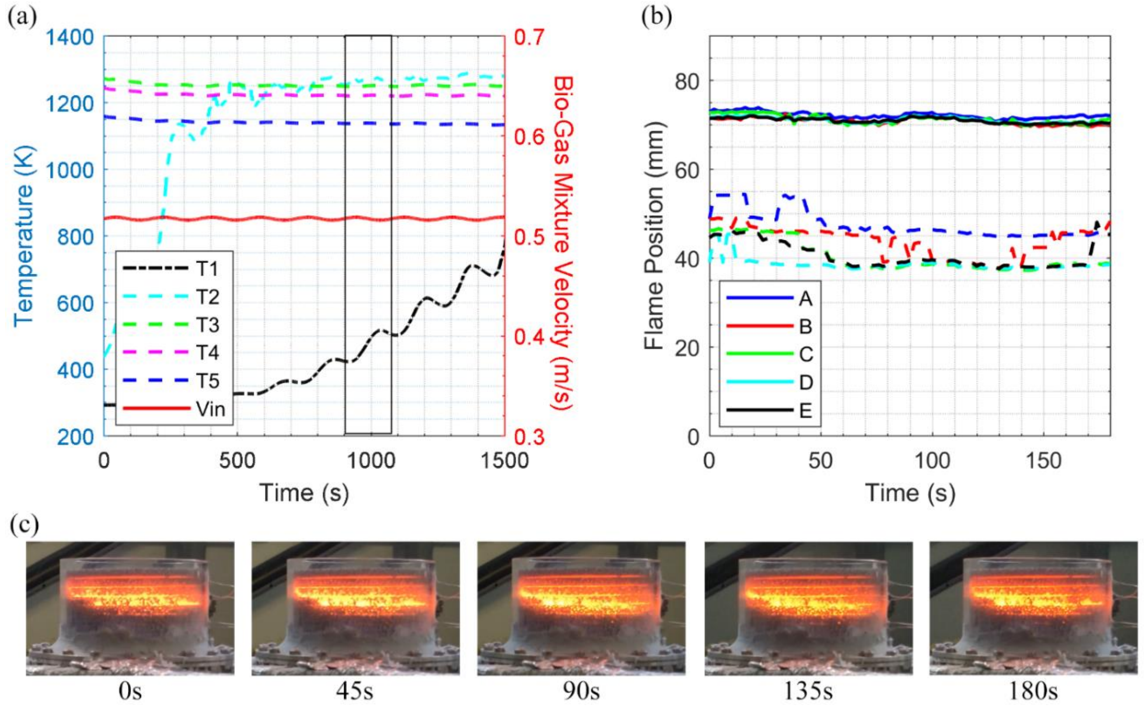

Figure 5-10: Unsteady case 3y, a=10%, t=180s (a) Axial temperature profile vs Biogas mixture velocity (b) Flame position movement at respective reference points, solid line – upper part of flame, dash line – lower part of flame (c) Snapshots of porous burner subject to unsteady flow at different intervals.

Figure 5-10 shows (case 3y) the effect of increasing the time period of the inlet fuel flow rate disturbance to 180s with a 10% amplitude. Overall, the system (Figure 5-10a) is able to complete 8 cycles of oscillatory flow amidst experiencing gradual flashback and the flame travelling upstream. Biogas mixture was able to prevent flashback for an additional 6 minutes when compared to methane mixture for similar conditions. This is primarily due to a variety of factors such as lower inlet velocity, lower flame speed and dilution of fuel composition; all lowering the flame temperature and speed. As a result, heat transfer within the ceramic foam also occurs at a slower pace due to the weaker temperature gradient between the flame and foam. Further, prolonging the flashback effects with the ceramic foam taking longer to achieve thermal equilibrium with the flame moving upstream. T1 directly responds to the induced disturbance almost taking the shape of an asymptotic curve if allowed to continue. The flame position of the sixth cycle of the experiment is shown in Figure 5-10b. The flame movement appears to be minimal due to the low amplitude fluctuation albeit there is a significant increase in flame thickness, indicating a slower reaction rate. This is further confirmed by visual inspection by Figure 5-10c at various time intervals whilst the burner is subject to modulation of the fuel flow.

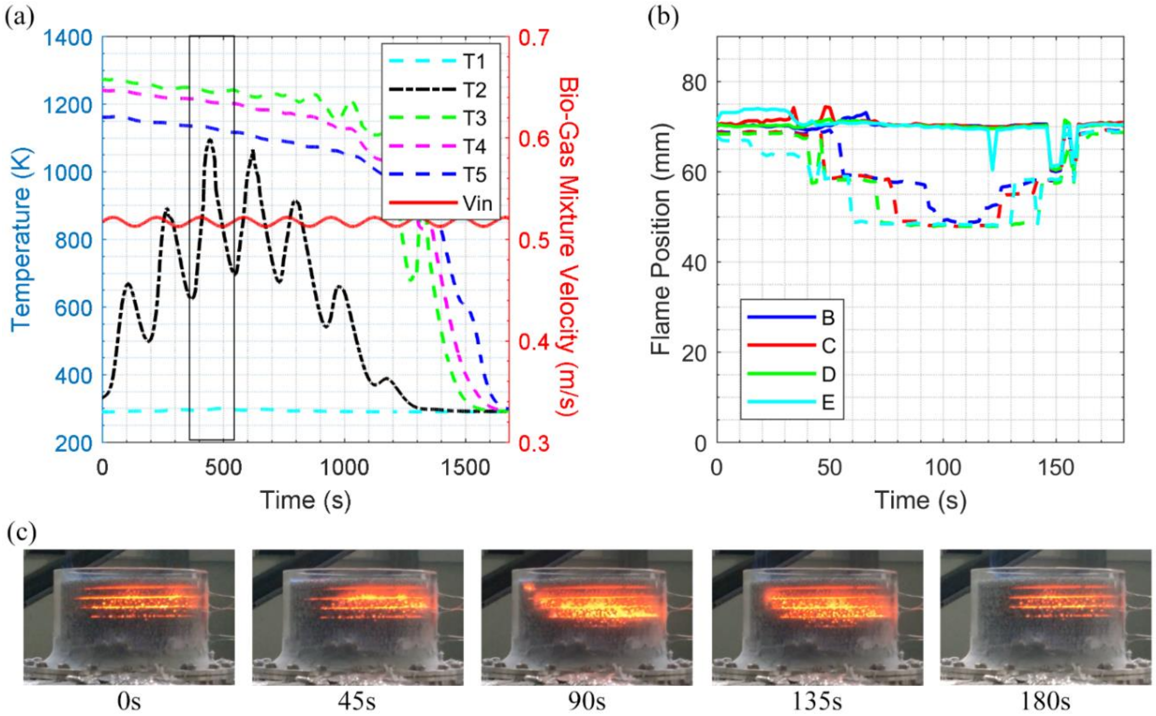

Figure 5-11: Unsteady case 4y, a=30%, t=180s (a) Axial temperature profile vs Biogas mixture velocity (b) Flame position movement at respective reference points, solid line – upper part of flame, dash line – lower part of flame (c) Snapshots of porous burner subject to unsteady flow at different intervals.

Figure 5-11 represents case 4y whereby the amplitude is increased to 30% of the inlet fuel flow rate at a period of 180s per cycle. Figure 5-11a shows the burner response commences with T2 recording temperature gains of the first three cycles and then the system begins to experience more heat loss than heat addition. As a result, complete flame extinction via blow off occurs at the seventh cycle. As the fuel flow rate was adjusted for the methane mixture only, the equivalence ratio was altered but for biogas both the equivalence ratio and ratio of methane to carbon dioxide were affected. At the trough of the highest amplitude (30%) of fuel modulation, the equivalence ratio drops to 0.1925. With such a low ratio of fuel compared to the rest of the mixture over a longer time, the burner is not able to recover the lost heat when the inlet inputs a surplus flow of methane into the system. Furthermore, with each cycle the overall temperature continues to drop, with the combustion gas transferring little or less heat to the pre-heating zone. This process continues to repeat until the overall temperature drop is so significant that it can no longer ignite the incoming mixture within the conduits of the ceramic foam; resulting in flame extinction. Figure 5-11b further clarifies this as no flame is detected at reference point A during the third cycle, where a gradual blow off is underway. Although, due to the higher amplitude a larger flame thickness is detected albeit very minimal flame movement [201]. A drastic heat loss during the imposed sinusoidal disturbance is visible at various time intervals as can be seen in Figure 5-11c.

5.4 Conclusions

An experimental study was conducted on a porous burner under ultra-lean condition to investigate the effects of sinusoidal fluctuations in the inlet fuel flow upon the flame dynamics. Such burners can be used in heating applications where very high temperatures are not needed. Burner operation with biogas often involves unsteadiness in fuel flow rate because of the inherent fluctuations in the gas supply of small-scale anaerobic digesters. Methane and a mixture of methane and carbon dioxide, mimicking biogas, were used as fuel. The fluctuations were superimposed on the fuel flow via programmable mass flow controllers. The response of the porous burner was evaluated by measuring the temperature at different axial locations along the burner centreline and by capturing the flame movement through imaging. It was shown that, under steady conditions, the burner could be operated for equivalence ratios as low as 0.275 for both methane and biogas. Further, biogas ultra-lean flames generated more CO emissions than methane flames. Under unsteady conditions, the porous burner was able to stabilise combustion when the methane mixture was subjected to inlet sinusoidal disturbances with amplitudes between 0 and 30% of the steady values over a period of 60 s. It was found that the vertical motion of the flame roughly follows the dynamics of the imposed oscillations. This was the case for both methane and the biogas mixture. However, the extent of flame movement for methane was significantly greater than that for biogas, whereas the flame thickness increase/decrease for biogas was more responsive than for methane. Finally, for both fuels, long exposure of the burner (180 s) to fuel flow modulations led to flame destabilisation, resulting in flashback or blow-off.

Chapter 6 On the response of ultra-lean combustion of CH_4/H_2 blends in a porous burner to fluctuations in fuel flow- An experimental investigation

ACS – Energy and Fuels – Rabeeah Habib, Bijan Yadollahi, Ali Saeed, Mohammad Hossein Doranehgard, Nader Karimi

6.1 Introduction

Natural gas is currently used widely throughout the world and is expected to continue being a major source of energy in the foreseeable future [202]. Production of carbon dioxide by combustion of natural gas is smaller than that of other fossil fuels. Nonetheless, this still poses a substantial concern and hence, there exist active plans for decarbonisation of gas grids [93,203]. Injection of hydrogen to natural gas pipelines has been identified as a practical approach to reducing carbon emissions [204,205]. As a result, in recent years, there has been a surge of research interest in the combustion of hydrogen and methane mixtures, e. g. [206,207]. Although these studies [208,209] have provided a wealth of insight into the problem, they are chiefly focused on lean premixed and partially premixed flames [210]. This makes them pertinent to high temperature applications typically more than 1500K. There are, however, an increasing number of applications in which large temperatures are not needed and generation of heat at moderate temperatures is preferred [211]. Ultra-lean combustion may provide a solution to the problem of heat generation at moderate temperatures [128,185]. Yet, some important challenges should be addressed first. These include management of carbon monoxide emissions and flame stability issues [183,212]. The current work is focused on the latter through analysis of ultra-lean combustion of CH_4/H_2 blends in a porous burner.

An ultra-lean blend of air and fuel is inherently a low-calorific value mixture [213]. The resultant reduction in the temperature makes the flame susceptible to blow-off and extinction [214]. It has been already shown that porous burners can significantly enhance the flame stability [49]. Excellent thermal properties of a porous ceramic foam enable combustion of premixed low calorific fuels that would not be otherwise possible [215,216]. At present, the use of porous burners can be found in several engineering applications [175,176]. These include propulsion and gas turbine systems [65,66], heat exchangers [178], and chemical processing [217]. A fundamental issue in stability of combustion system operating under lean and ultra-lean conditions is their response to temporal changes in the fuel flow rate [218]. Such changes can occur during the start-up and shut-down and can be also encountered when the fuel composition varies [187,218]. Further, due to the small flow rates of hydrogen and methane in ultra-lean burners, mechanical defects can cause flow fluctuations. Robustness of the ultra-lean burner is heavily influenced by its response to such fluctuations in fuel flow rate.

The literature on combustion in chemically inert porous media is rather large (see for example [69,219]) and reviewers of literature can be found in Refs. [220,221]. Importantly, however, most of the existing studies on combustion in porous media are concentrated on steady condition ([222,223]). The majority of experiments in this area evaluated the burner performance ([184,224]), and only few considered the ultra-lean condition [186,225]. Thus, a very small fraction of the vast literature on reacting flows in porous media is related to the unsteady combustion and flame stabilisation issues. In the followings, these studies are briefly discussed. Further, due to the peculiarities of hydrogen flames, combustion of hydrogen in porous media is also included in the discussion.

Kakutkina et al. [226] experimentally investigated hydrogen-air combustion inside a porous burner. The mixture was ignited upstream of a quartz tube containing porous medium, which also provided partial optical access to the flame [226]. The flame movement was recorded via a digital camera and the temperature was measured by a thermocouple at the designated parameters of the hydrogen-air mixture. Kakutkina et al. [226] found that for a 70% hydrogen mixture, the flame propagates upstream at a distance of 100mm in 2000s and the maximum temperature recorded was around 950K at approximately 1750s under steady conditions. Fuel interchangeability was studied by Alavandi and Agrawal [227] by combusting lean blends of hydrogen-syngas and methane fuel mixtures inside a porous burner. The air flow rate was kept constant for all tests, while the methane concentration was lowered for each test as the hydrogen and carbon monoxide fuel rates were adjusted to produce the required thermal power under steady conditions. The authors [227] reported reduced carbon monoxide and nitrogen oxides emissions at any flame temperature for hydrogen and carbon monoxide mixtures compared to those produced by a pure methane flame.

Gauthier et al. [228] studied pollutant emissions when hydrogen was added to a natural gas mixture inside a porous burner. The burner was first operated with a natural gas-air mixture, once the combustion had stabilised a gradual addition of hydrogen was made. The experiments were conducted for $0.3 \leq \phi \leq 0.95$, $100 \leq P \leq 700$ and an interchangeable hydrogen concentration of up to 100% within the natural-gas and hydrogen fuel composition. Gauthier et al. [228] reported that as natural gas is slowly replaced by hydrogen a reduction in carbon monoxide, carbon dioxide, and nitrogen oxides took place. Also, they found that when the hydrogen content exceeds 80% the flame becomes unstable.

Peng et al. [229] experimentally examined combustion of a premixed hydrogen-air mixture by varying the size of the combustion chamber inside the porous burner. The purpose of the study was to monitor the flame stability with the inclusion and exclusion of porous media in the combustion chamber. The authors [229] chose a stainless-steel mesh to represent the porous media whereby the hydrogen-air mixture was operated for different mass flow rates and equivalence ratios. Peng et al. [229] found that as the diameter of combustor chamber diminished, the flame front within the porous media enlarged across the flow direction. Also, with the insertion of porous media, an increase in heat transfer accelerated the combustion process. Inspired by Alavandi and Agrawal [227], Arrieta et al. [230] studied the combustion of mixtures of methane and syngas inside a porous burner. Their experiments were focused on the emissions of CO and NOx, flame stability response to assigned thermal power, and the effects of volume fraction of the syngas mixtures under steady conditions. Arrieta et al. [230] used methane as the basic fuel for all tests where the hydrogen to carbon monoxide ratio was varied. It was concluded that the addition of hydrogen-rich syngas to methane did not impact the flame stability or temperature profile drastically. Yet, a considerable reduction in CO and NOx emissions was reported.

The most recent work of the current authors showed that an ultra-lean mixture of methane and carbon dioxide burning inside a porous foam could strongly respond to fluctuations in methane flow rate [225]. Upon introduction of fluctuations, the flame featured hydrodynamic motion inside the porous foam. It was observed that there were certain amplitude and frequency of the flow modulation under which the flame could survive [225]. As the characteristics of CH_4/H_2 blends are quite distinctive to those of CH_4/CO_2, the burner stability for combustion of methane and hydrogen blends needs to be re-examined. This is particularly due to the high reactivity of hydrogen which can significantly affect flame blow-off and extinction.

As heat transfer dominates combustion in porous media, the latter is expected to be influenced by variations in the inlet flow. This is particularly the case in ultra-lean combustion in which changes in the temperature can have a profound effect on the flame stability. Nevertheless, as seen in the preceding survey of literature, currently there is no systematic experimental study on CH_4/H_2 mixtures subject to inlet flow disturbances under ultra-lean conditions. In an attempt to address this shortcoming, the current work investigates experimentally the unsteady ultra-lean hydrogen combustion of different blends of methane and hydrogen.

6.2 Methodology

6.2.1 Experimental setup and instrumentation

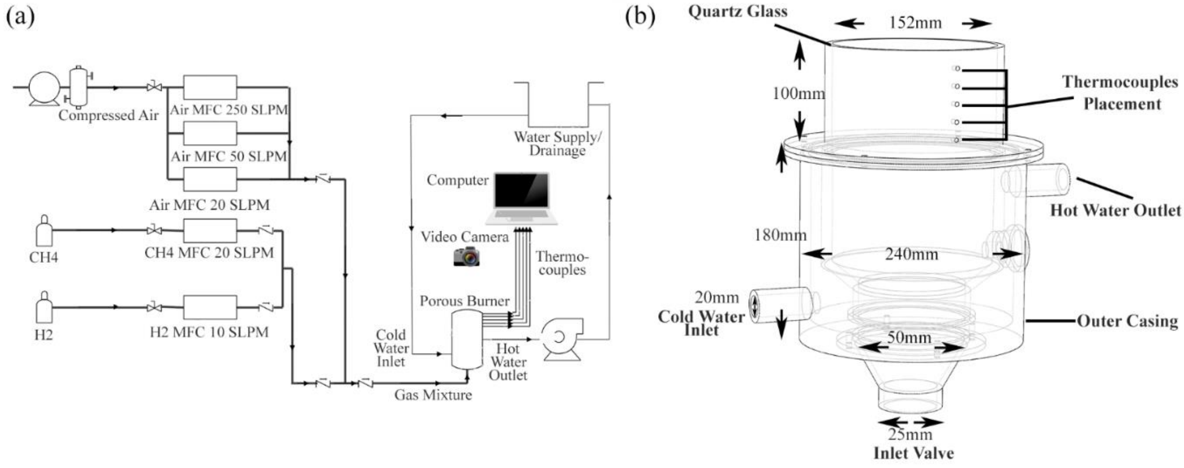

Figure 6-1: (a) Diagram representation of the experimental setup (b) 3D transparent view of the employed porous burner.

A schematic representation of the experimental setup is illustrated in Figure 6-1a. This consists of four key components; the porous burner (Figure 6-1b), water coolant system, fuel mixture supply, and data harvesting and measurement apparatus.

6.2.1.1 Porous burner

Figure 6-1b illustrates the vital sizes of the porous burner in a transparent 3-D model. The model was made up of four main parts consisting of a quartz glass tube, an inlet valve, a combustion compartment, and an outer casing. The flame in porous media was observed through the quartz glass tube by securing it above the burner with a sealant able to withstand temperatures up to 1500K. The remaining parts were made of stainless steel.

The combustion compartment was made up of two separate sections; the combustion and preheating regions. Both regions consisted of porous ceramic layers stacked one atop the other vertically. The preheating section (designed to reduce the probability of flashback) entailed an Al_2O_3 foam (20ppi - $\varepsilon \approx 0.47$) positioned nearest to the inlet valve preceded by a funnel-shaped SiC ceramic foam (20ppi - $\varepsilon \approx 0.47$). This was followed by a stack of low-density SiC foams (10ppi - $\varepsilon \approx 0.72$) completing the preheating region. The combustion region (visible through the quartz glass tube) consisted of predominately high-density SiC foams (20ppi - $\varepsilon \approx 0.47$). Two layers of low-density SiC foams (10ppi - $\varepsilon \approx 0.72$) were placed near the centre of the combustion region to provide further flame stability as illustrated in Figure 6-2.

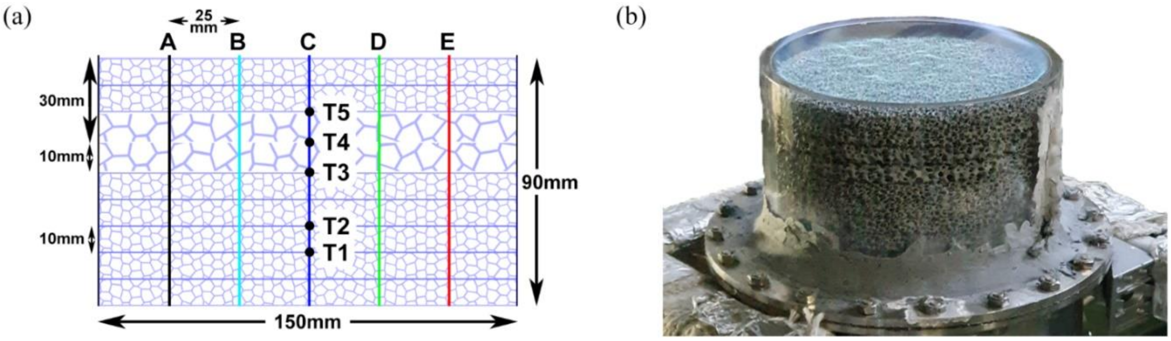

Figure 6-2: a) Combustion region schematic highlighting the placement of thermocouples with reference points A, B, C, D, and E, b) Quartz glass tube visualising the flame before entering the porous foam.

6.2.1.2 Water coolant system

An opening was created between the internal side of the outer casing and the external side of the combustion compartment for the water cooling to take place. The vacant gap acted as a water reservoir with an integrated inlet and outlet within the porous burner. The water coolant system drew cool water from the water source filling the water reservoir from the inlet located near the bottom of the burner. Once the reservoir was full, the water departed from the outlet (located near the top of the burner) warranting a thorough cooling of the stainless-steel burner.

6.2.1.3 Fuel mixture supply

The mixture entering the burner consisted of a blend of hydrogen and methane diluted with air. Fuel was supplied from the corresponding gas cylinders and digital mass flow controllers (MFC) equipped with manually operated valves. Moisture was removed from the compressed air with the use of an air filter and the air was supplied in an arrangement similar to that of the fuel where a quarter-turn hand valve was installed before the air MFCs. Flow Vision SC software was obtained from ALICAT to vary the mass flow rate of each MFC using a computer. The programmable MFCs from ALICAT Scientific operated under an uncertainty of $\pm 0.6\%$ for both air and fuel. A number of MFCs were installed with relevant operational ranges (Figure 6-1a) for fuel and air to operate under steady and time-varying flows. The fuel mixture was premixed within the transmission system before being supplied to the porous burner. Air was supplied via a rubber pipe with an outer diameter of 25.4mm, which was connected to a 6.35mm diameter stainless steel pipe carrying fuel further downstream where the premixing occurred. The rubber pipe fed the fuel mixture to the inlet valve of the porous burner.

6.2.1.4 Data harvesting

Figure 6-2a depicts the five key points wherein temperature measurements were conducted at the midpoint of the ceramic foam. Five respective holes were drilled on the side of the quartz tube glass to secure each thermocouple midpoint of the porous media with the use of a high-temperature resistant sealant. To measure flame temperatures, type N thermocouple was deployed with uncertainty error of

$\pm 2.5\mathrm{K}$, minute diameter size of 0.5mm, and the capability of withstanding temperatures up to 1553K. Pico software was utilised to plot temperature with respect to time by translating the voltage signals produced by the thermocouples. In order to capture the temperature change accurately, data were logged at much larger frequency (100Hz) than the set frequency of the inlet fuel disturbances (≈0.02Hz). The exhaust gases of the porous burner were monitored by installing a gas analyser - Anton Sprint Pro 5 - above the outlet of the burner (≈10cm) for cases described in Table 6-1. The error was stated to be $\pm 0.3\%$ for CO_2 and ± 20ppm for CO. A full high-definition video camera (1920×1080) was mounted ≈1.5m from the burner to record the flame performance and migration.

6.2.2 Experimental procedure

The equivalence ratio [199] was noted to be

$$\phi = \frac{(m_f/m_{air})_{actual}}{(m_f/m_{air})_{stoichiometric}} \tag{6-1}$$

where the mixture is described as lean when $\phi < 1$. The thermal power of the system [199] [200] is given by

$$P = \dot{m}_f \times LHV_f \tag{6-2}$$

in which the energy produced by each fuel is determined.

Table 6-1 presents the operating conditions for steady experiments and Table 6-2 shows those for the unsteady experiments, for varying fuel concentrations of methane and hydrogen mixtures. The mixture blends consist of a mole percentage of each respective fuel. The flow rates of both fuels were systematically altered by programming the MFCs using Flow Vision SC software. Under lean operation ($\phi \approx 0.55$) the porous burner was ignited using a long-nosed lighter. The mixture flow rate was then gradually lowered to achieve ultra-lean combustion ($0.25 \leq \phi \leq 0.275$) and flame stability within the porous media. A gas analyser (Anton

Sprint Pro 5) was employed to record the final values of CO, CO_2, and NO_x of the cases described in Table 6-1 after flame stability had been achieved. It was found that NO_x emissions are almost negligible. This is to be expected as the current low-temperature combustion system strongly suppresses formation of thermal NO_x. Once the flame had been stabilised, the concluding temperature values were noted from the Pico software.

After the flame had stabilised, as described in Table 6-2, the hydrogen and methane flows were subject to a sinusoid disturbance with a varying amplitude of 10-50% of its initial value for both fuel concentrated mixtures with a single forcing frequency. This was conducted by programming the MFCs to oscillate the fuel flow rates at the designated amplitude and frequency. As the flame inlet disturbance was introduced, the temperature traces were recorded using the Pico software at the thermocouple locations illustrated in Figure 6-2a. The digital camera recorded the flame movement, which was then reported along with the designated reference points (Figure 6-2a) with an image processing code developed in MATLAB.

Uncertainty error was also calculated to ensure adequate accuracy of the experimental procedure during flow modulation. This included the uncertainty error for mass flow controllers and thermocouples. To determine this, thermocouple values were used from case 6x where T3 reported the highest temperature (1384K). Therefore, T3 uncertainty error was assumed across all five thermocouples. Combined with the supplied MFC manufacturer error ($\pm 0.6\%$), the total accumulative uncertainty error in flow measurements= $\pm 2.7\%$.

6.2.3 Image processing

An in-depth image analysis was carried out to observe the change in flame position. The video recording of an entire oscillation of 60s was cut out from the footage of each case described in Table 6-2. Using video editing software Adobe Premier Pro, screenshots of the oscillation were saved every 2s from the video recordings of all cases to examine the flame operation. Additionally, an image processing code was developed in MATLAB to examine the screenshots. Each screenshot was initially cropped to represent only the ceramic foam within the quartz tube glass (see Figure 6-2a). To monitor flame movement, the screenshot pixels were converted to a distance where 12.8 pixels were noted to be the equivalent of 1mm. The referenced points were generated vertically along the x-axis to determine the flame migration in the y-direction. Every picture was transformed from an RGB image to black and white where a brightness criterion was introduced for flame detection. The luminosity value for each concentration of fuel varied thus authenticated by visual validation. As the brightness conditions were fulfilled, the vertical position of the parameter was determined (i.e. where the flame had been identified) at the specified reference points. The designated values were reduced by filtering out only the top and bottom y-location. These values served to define the upper and lower section of the flame across all reference points. This procedure reoccurred until all pictures had been processed by the code. The final top and bottom positions of the brightness criterion were then plotted with respect to time, illustrating migration of the flame vertically within the porous media along the five reference points over a full oscillatory cycle.

Table 6-1: Steady Experiments - a-CH_4 (90%) H_2(10%), b-CH_4 (70%) H_2(30%)

	H_2 (standard L/min)	CH_4 (standard L/min)	Air (standard L/min)	Mixture (standard L/min)	Equivalence Ratio (ϕ)	Thermal Power (kW)
Case 1a	0.57	5.16	190.86	196.59	0.25	2.5
Case 2a	0.69	6.24	209.94	216.87	0.275	3.02
Case 3a	0.76	6.81	229.03	236.6	0.275	3.3
Case 4a	0.82	7.37	248.12	256.31	0.275	3.575
Case 1b	2.11	4.91	178.03	185.05	0.275	2.47
Case 2b	2.34	5.46	197.81	205.61	0.275	2.75

Table 6-2: Oscillatory Experiments - x-CH_4 (90%) H_2(10%), y-CH_4 (70%) H_2(30%)

	H_2 (Standard L/m)	CH_4 (Standard L/m)	Air (Standard L/m)	Mixture (Standard L/m)	Equivalence Ratio (ϕ)	Thermal Power (kW)	Oscillation period (s) of fuel flow	Amplitude (%) of steady fuel flow
Case 1x	0.82	6.63-8.11	248.1	255.57-257.05	0.2481-0.3016	3.221-3.926	60s	CH_4 =10%
Case 2x	0.82	5.16-9.58	248.1	254.10-258.52	0.1945-0.3550	2.514-4.629	60s	CH_4 =30%
Case 3x	0.82	3.69-11.06	248.1	252.63-260	0.1413-0.4088	1.8130-5.3380	60s	CH_4 =50%
Case 4x	0.74-0.9	7.37	248.1	256.23-256.39	0.2743-0.2755	3.571-3.577	60s	H_2 =10%
Case 5x	0.57-1.09	7.37	248.1	256.04-256.54	0.2725-0.2770	3.556-3.587	60s	H_2 =30%
Case 6x	0.41-1.23	7.37	248.1	255.88-256.7	0.2712-0.2780	3.549-3.593	60s	H_2 =50%
Case 1y	2.11	4.42-5.4	178.03	184.56-185.54	0.25-0.3	2.238-2.711	60s	CH_4 =10%
Case 2y	2.11	3.44-6.38	178.03	183.58-186.52	0.2005-0.3490	1.770-3.1750	60s	CH_4 =30%
Case 3y	2.11	2.46-7.37	178.03	182.60-187.51	0.1508-0.3992	1.3-3.649	60s	CH_4 =50%
Case 4y	1.90-2.32	4.91	178.03	184.84-185.26	0.2722-0.2774	2.4610-2.4850	60s	H_2 =10%
Case 5y	1.48-2.74	4.91	178.03	184.42-185.68	0.2672-0.2830	2.438-2.513	60s	H_2 =30%
Case 6y	1.06-3.17	4.91	178.03	184-186.11	0.2615-0.2882	2.41-2.537	60s	H_2 =50%

6.3 Results and discussion

The burner was operated under steady state as well as fluctuating fuel flow. Here, the outcomes of these two modes of operation are presented separately.

6.3.1 Steady condition

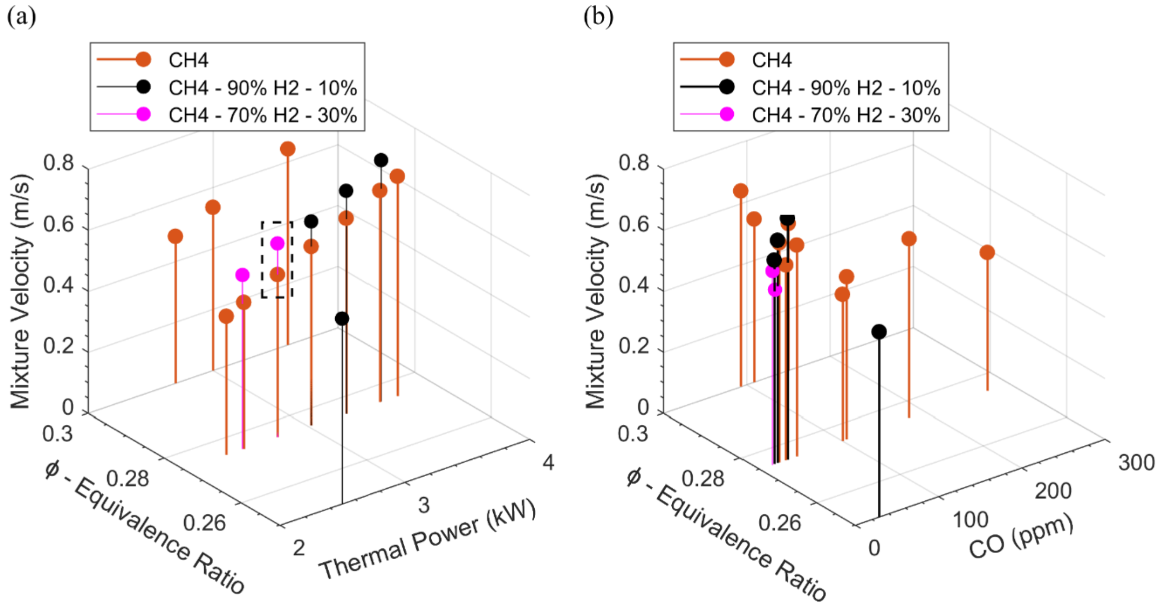

Figure 6-3: Steady fuel mixtures (a) ϕ vs P (b) ϕ vs CO emissions.

In order to achieve stable combustion inside the ceramic foam, a fine balance between heat production, heat deficit, and heat recirculation is required [49]. Flame stabilisation is most commonly attained when the flame speed matches the upstream flow velocity of air and fuel mixture [218]. Figure 6-3 depicts the effectiveness of stable combustion within the porous burner functioning in an ultra-lean setting for various fuel mixtures. Habib et al. [225] have extensively discussed the response of methane and bio-gas mixtures within the burner shown in Figure 6-1. Therefore, the focus of the current discussion will be primarily on methane and hydrogen mixtures (Table 6-1). Figure 6-3a displays the correlation between mixture velocity, equivalence ratio and thermal power. The unburned mixture velocity can be considered as the filter velocity within the quartz tube upstream of the flame. Noticeably, there exists a uniform pattern amongst all fuel mixtures where the thermal power augments constantly as the mixture velocity is increased. It is also clear that CH_4(90%)+H_2(10%) mixture exhibits a larger thermal power when compared to its counterpart CH_4(70%)+H_2(30%); which is predominantly due to its larger concentration of methane as (per unit volume) methane has a higher enthalpy of combustion compared to hydrogen. Further, CH_4 (90%)+H_2(10%) is able to operate at ϕ=0.25 as hydrogen provides a higher flame temperature than methane alone to preheat the incoming cold reactants and avoid flame extinction.

Figure 6-3b illustrates the impact of equivalence ratio and mixture velocity on carbon monoxide emissions. An apparent pattern is visible where the carbon monoxide emissions drop as the mixture velocity is increased and the equivalence ratio is decreased. The temperature in the combustion region plummets when mixture velocity curtails. This is typically due to a decline in heat generation whereas the loss of heat continues uninterruptedly. The reduced temperature increases the risk of incomplete combustion and retards the process of oxidation of carbon monoxide to carbon dioxide. Carbon monoxide emissions also increase at smaller equivalence ratios as it chokes the heat release and reduces the reaction temperature.

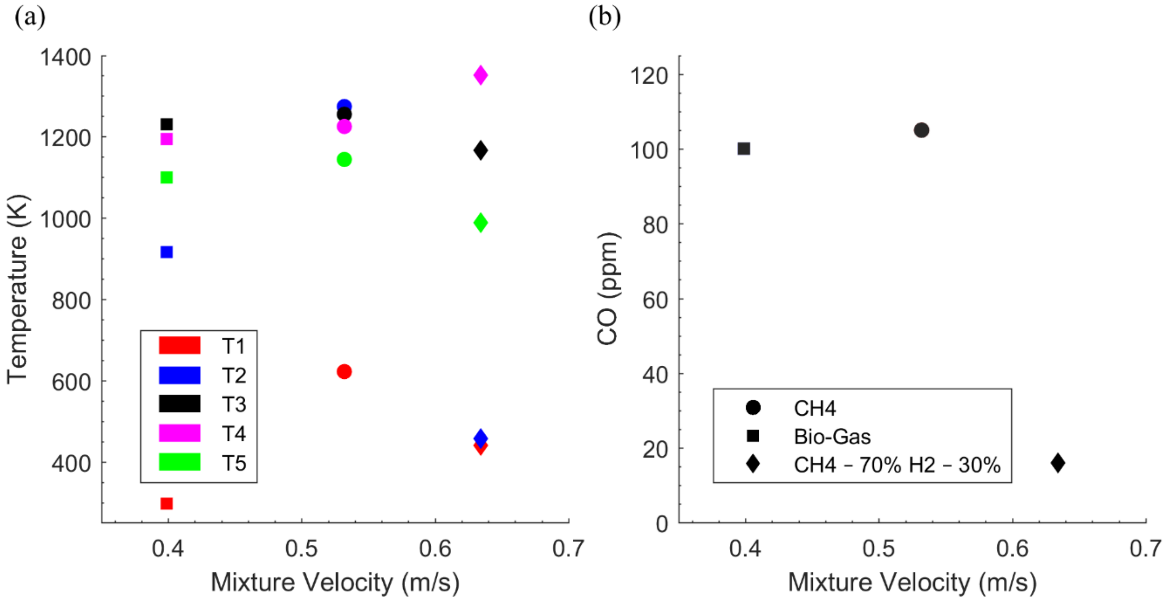

Figure 6-4: Temperatures and CO production vs mixture flow velocity under steady state condition (no modulation of the fuel stream). CH_4 - (circle), Biogas (CH_4(70%)-CO_2(30%))- (square), CH_4(70%)-H_2(30%) – (diamond), ϕ=0.275 (a) Mixture Velocity vs Temperature (b) Mixture Velocity vs CO emissions.

Figure 6-4 depicts the temperature and carbon monoxide emissions plotted with mixture velocity. The three fuel mixtures operate on an identical equivalence ratio of 0.275 and produce the same thermal power of 2.75kW. Figure 6-4a shows the five thermocouple readings when stable combustion has been achieved for the selected fuel mixtures. It is evident that higher unburned mixture velocities result in the larger temperatures. The fuel composition also strongly affects the temperature where biogas outputs the lowest temperature for similar operating conditions. This occurs as a response to the initial presence of carbon dioxide, which dilutes the fuel mixture and lowers the flame temperature. Further, the CH_4(70%)-H_2(30%) mixture produces the highest temperature (1340K), followed by CH_4 (1291K) and then biogas (1233K). This is due to the addition of hydrogen to methane, as hydrogen produces a greater flame temperature when compared to pure methane. It is also noted that the peak temperature for each mixture is detected at a different thermocouple point as the flame location within the burner differs between the fuel mixtures. In Figure 6-4b, the carbon monoxide emissions follow a similar trend as Figure 6-3b, where a greater mixture velocity produces lower emissions. In addition to mixture velocity, hydrogen plays a key role in reducing the carbon monoxide emission for the CH_4 (70%) - H_2 (30%) mixture. The CH_4 (70%) - H_2 (30%) mixture shows 85% reduction in carbon monoxide emissions in contrast to CH_4. This could be primarily attributed to the higher flame temperatures of CH_4/H_2 blends compared to those of CH_4 and biogas. High temperature facilitates the oxidation of carbon monoxide into carbon dioxide and thus reduces CO emissions.

6.3.2 Fluctuating fuel flow

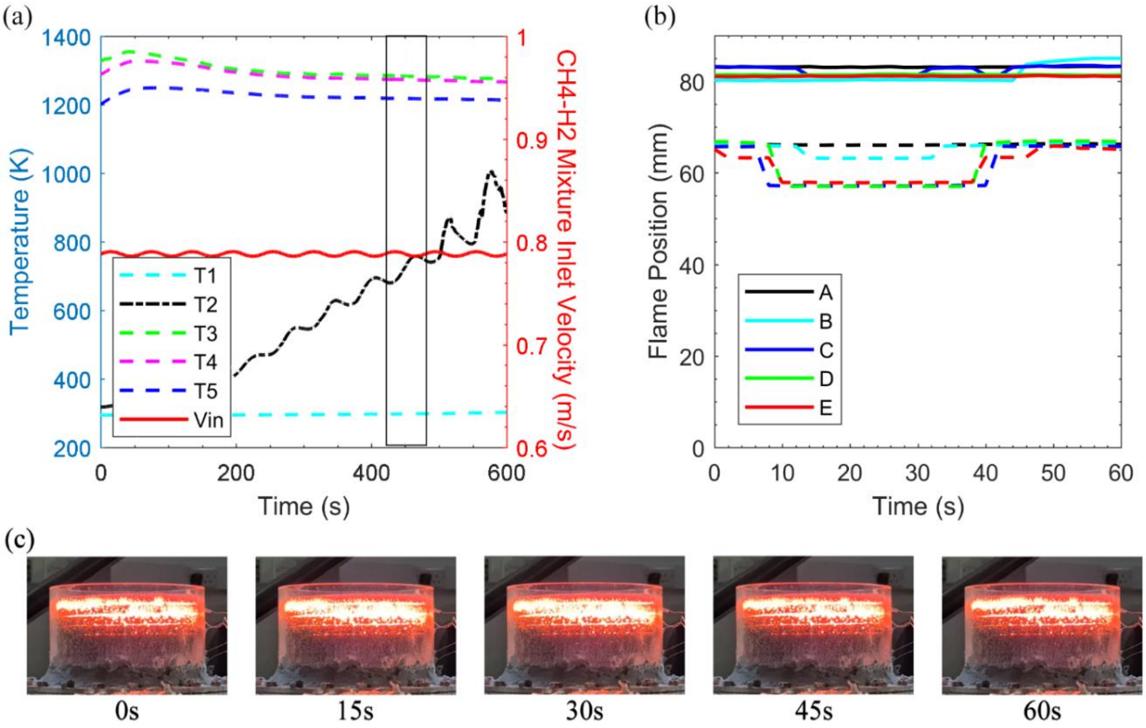

Figure 6-5: Forced response of the burner to modulation of fuel streams. Case 1x, amplitude of oscillation in methane flow:10% (a) Temperature + $CH_4(90\%)$-$H_2(10\%)$ mixture velocity vs Time (b) Flame position motion at reference points, top section of the flame (-) , bottom section of the flame (- -) (c) Screenshots of burner responding to oscillatory flow during complete cycle.

Case 4a was incorporated as a foundation for unsteady CH_4 (90%) - H_2 (10%) cases before superimposing oscillatory disturbances at the inlet. Figure 6-5 displays the porous burner operation with CH_4(90%)-H_2(10%) mixture subject to an oscillatory disturbance introduced on the methane flow with an amplitude of 10% of its steady value, over a period of 60s. The thermocouples were used to record the temperature of each case where the cut-off temperature to detect flashback was defined as T=773.15K. The temporal variation of methane flow leads to a distinct movement of the reaction region within the ceramic foam. This flame movement was video recorded (section 6.2.2) and the change in temperature were also recorded. Ten cycles of fuel flow modulation were applied while no flame flashback/blow-off was observed.

Figure 6-5a illustrates the variation in temperature for case 1x; including the mixture velocity trace. Evidently, the third thermocouple displays the highest temperature recorded (1354K) in between the varying density of the SiC foams. This boundary surrounded by the two SiC foams grants additional flame stability during burner operation as the high-density SiC foam operates as a flashback arrestor. Further, the thermocouples report predominately fixed temperatures in response to the oscillatory methane fuel apart from the second thermocouple. This indicates that the flame movement was not detected by the temperature measurement apparatus. For the current experiment, this implies that the flame movement being restricted around the location of two adjacent thermocouples. This phenomenon was also reported for CH_4 and biogas by Habib et al [217]. As a complimentary analysis, Figure 6-5b depicts the change in location of the flame fluctuation during the eighth oscillatory cycle (marked by the box in Figure 6-5a) at the nominated y-direction reference points. Approximately 8s later, the bottom section of the flame expands about 7mm upstream as shown by Figure 6-5c (15s, 30s). The flame expansion ties in with the temperature measurement noted at the second thermocouple. Figure 6-5b visualises the flame motion to be roughly 7mm, thus elucidating why the flame movement went undetected by the other thermocouples. An assessment amidst the mixture velocity trace highlighted in Figure 6-5a and flame region in Figure 6-5b, discloses that the flame movement almost accurately trails the changes in the flow velocity. Clearly, a phase lag exists amongst the inlet fuel flow and the highlighted temperature variation. This is to be expected and the time lag between fuel and flame fluctuations has been already reported in the context of flame dynamics [106].

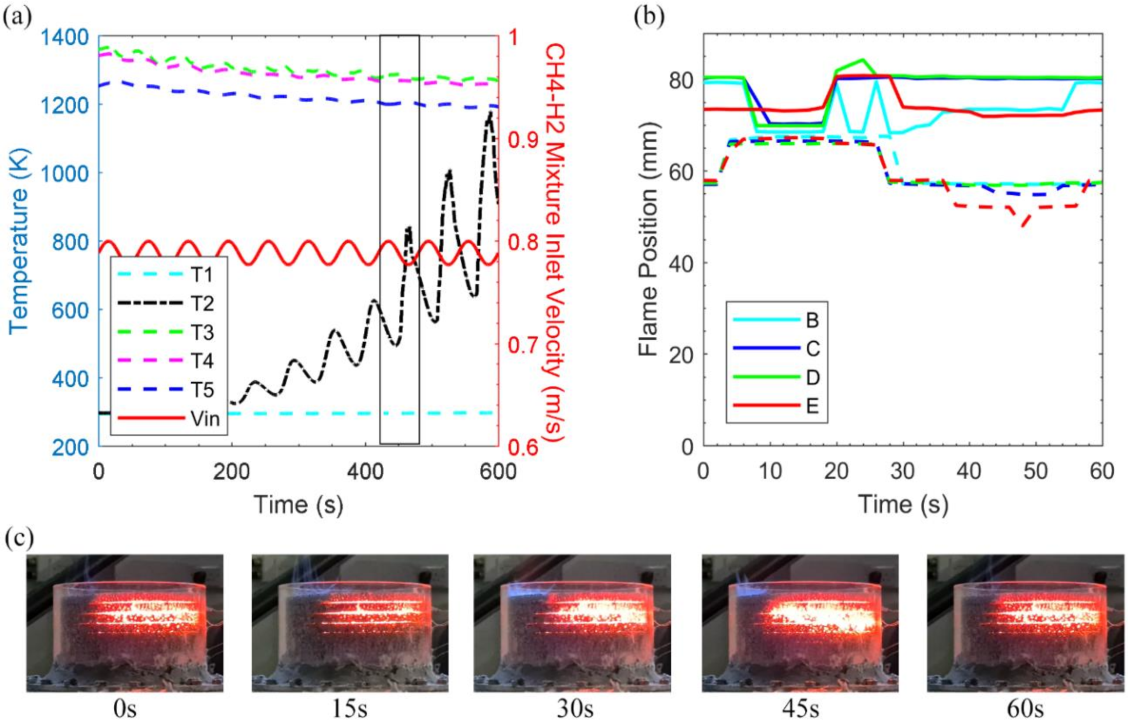

Figure 6-6:Forced response of the burner to modulation of fuel streams. Case 3x, amplitude of oscillation in methane flow: 50% (a) Temperature + CH_4 (90%) - H_2 (10%) mixture velocity vs Time (b) Flame position motion at reference points, top section of the flame (-), bottom section of the flame (- -) (c) Screenshots of burner responding to oscillatory flow during complete cycle.

Figure 6-6 displays case 3x where the amplitude has been enlarged to 50% of the methane flow rate with the fluctuation period remaining unchanged. The temperature trace of the second thermocouple in Figure 6-6a records successive gains for the entirety of the experiment. However, in reality, the overall system is experiencing greater heat loss than heat generation. Consequently, if the present case was to continue for further methane oscillatory cycles, the flame would inevitably extinct. The alarm of blow-off is raised in Figure 6-6b, as no flame is found within the brightness criterion at reference point A, at which a slow process of flame extinction is ongoing. This process remains undetected by the thermocouples due to their central placement within the ceramic foams. Additionally, modulation of methane flow has a direct impact on the concentration of hydrogen and methane while it also alters the equivalence ratio of CH_4(90%)-H_2(10%) mixture. As a result, during the trough at an amplitude of 50% of methane oscillation, the equivalence ratio plummets to 0.1413. Due to this drop, the porous burner struggles to retain heat even after supply of the excess methane to the combustion chamber. A similar phenomenon was also reported by Habib et al [217] whilst operating the same burner on biogas. Yet, it was observed that an amplitude of 30% of the fuel flow rate for biogas was sufficient to incur greater heat loss. Further, for case 3x, an overall temperature reduction is observed at thermocouples 3, 4, and 5 with time as the pre-heating region receives minimal quantities of heat from the combustion region. As this continuous cycle of heat loss progresses, the substantial reduction in temperature roles out the possibility of sustaining a flame within the pores of the ceramic foam. Yet, a thicker flame is visible as a result of greater forcing amplitude despite very little flame motion [201]. The heat loss can be monitored by the reduction in flame visibility in Figure 6-6c. It should be noted that a similar response was found for case 2x.

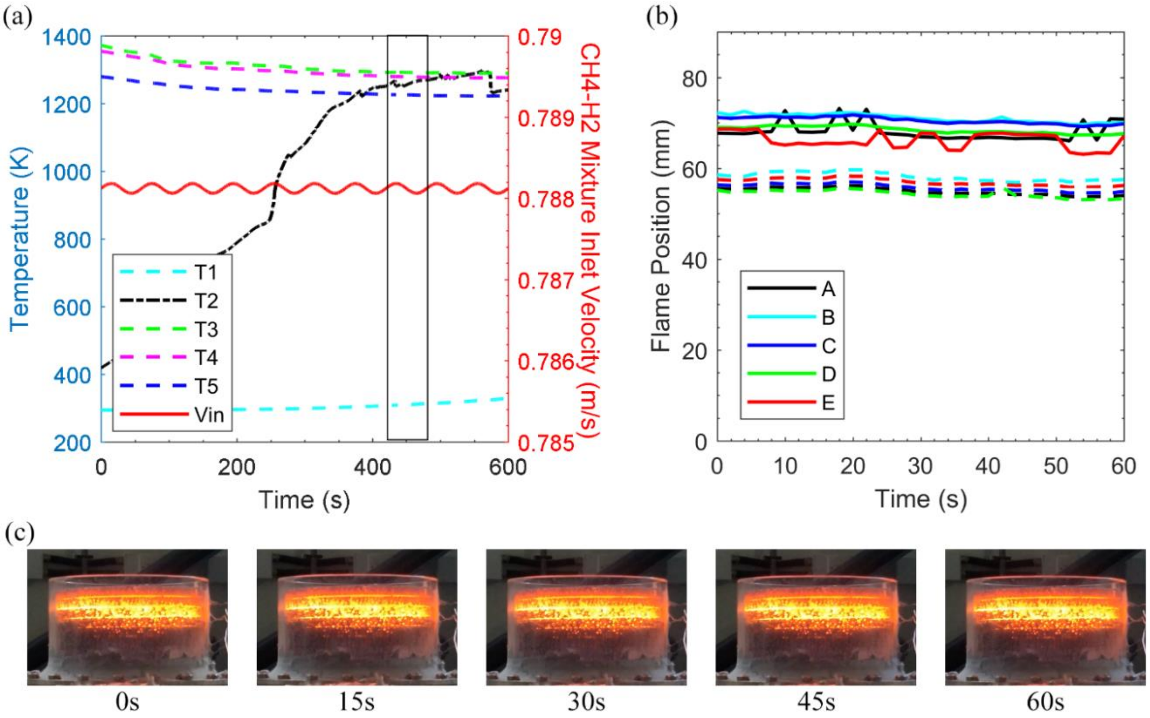

Figure 6-7: Forced response of the burner to modulation of fuel streams. Case 6x, amplitude of oscillation in hydrogen flow: 50% (a) Temperature + CH_4(90%)-H_2(10%) mixture velocity vs Time (b) Flame position motion at reference points, top section of the flame (-), bottom section of the flame (- -) (c) Screenshots of burner responding to oscillatory flow during complete cycle.

Next, the fuel concentration of hydrogen in the CH_4 (90%) - H_2 (10%) mixture was subjected to inlet sinusoidal disturbances. Figure 6-7 displays case 6x where the methane and air composition remain unchanged, and the hydrogen component of the mixture undergoes oscillations at an amplitude of 50%. Case 6x was chosen for discussion due to its higher amplitude value as case 4x and 5x delivered a similar flame/temperature response. Because of the initial low concentration of hydrogen (10%), there is very small changes in the CH_4 (90%) - H_2 (10%) mixture velocity even with the hydrogen amplitude set as high as 50%. Therefore, it is noted that, with the exception of the second thermocouple, most thermocouples are insensitive to the oscillations in hydrogen flow with the third thermocouple recording the highest temperature (1384K) early on in the experiment. It can be seen that the porous burner withstands the introduced inlet disturbances without any visible signs of flame flashback or blow-off. A distinct contrast in the temperature trace of the second thermocouple emerges between the flow modulation of methane and hydrogen. The temperature trace in Figure 6-7 not only obtains a greater temperature but does so in a shorter time. However, the temperature response does not show any clear sign of large oscillations when compared to methane cases. This phenomenon can be attributed to the greater adiabatic flame temperature of hydrogen and its wider flammability limits. Even though the change in fuel flow is minimal, as a larger quantity of hydrogen fuel is burnt, greater heat is produced. Inevitably, this reduces the time for the heat to be transferred whilst substantiating the increase in temperature. Also, due to the superior thermal properties of SiC foam, heat is retained when hydrogen concentration is decreased. Figure 6-7b confirms minor flame motion at the eighth cycle of the experiment as temperature changes are minimal near the end of the experiment, displaying the insignificant impact of hydrogen oscillation. Figure 6-7c depicts the CH_4 (90%) - H_2 (10%) mixture shows insignificant flame motion during the eighth cycle. It is noted that in this case, the brightness and colour of the flame are not as vivid as related to the methane modulation due to hydrogen flame being nearly invisible.

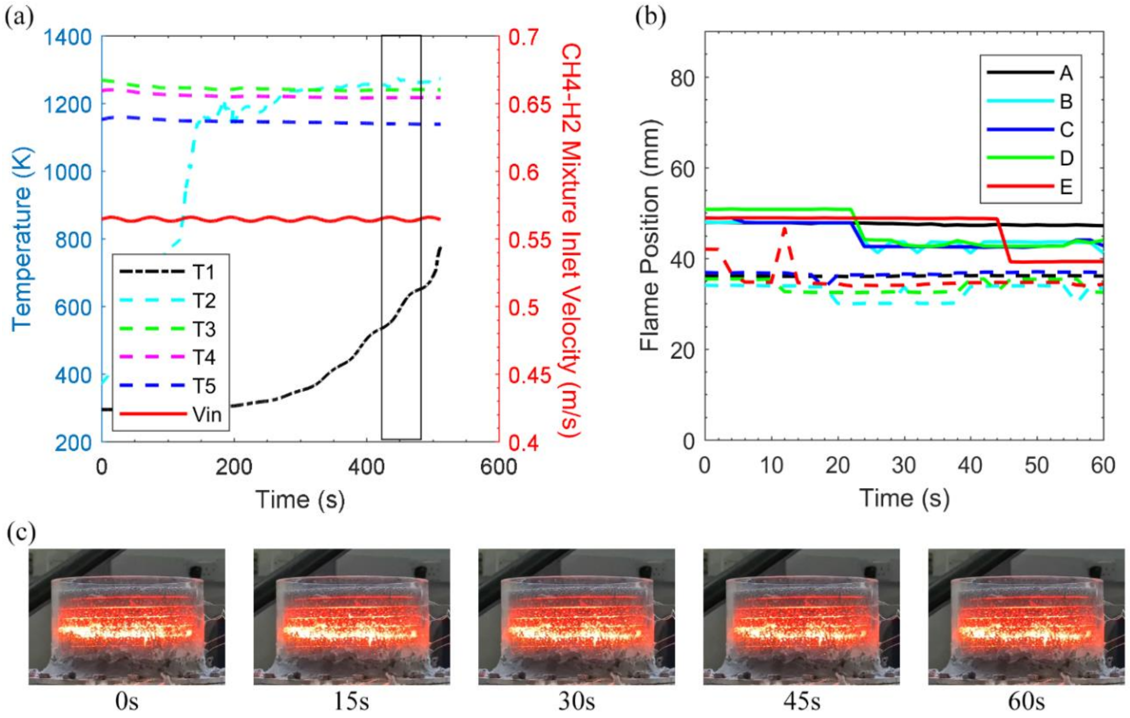

Figure 6-8: Forced response of the burner to modulation of fuel streams. Case 1y, amplitude of oscillation in methane flow:10% (a) Temperature + CH_4 (70%) - H_2 (30%) mixture velocity vs Time (b) Flame position motion at reference points, top section of the flame (-), bottom section of the flame (- -) (c) Screenshots of burner responding to oscillatory flow during complete cycle.

Figure 6-8 illustrates (case 1y) the temperature response and flame position of the CH_4 (70%)-H_2 (30%) mixture when methane flow is modulated with amplitude of 10%. The starting point before introducing disturbances at the inlet was selected to be case 1b for additional safety. As the amplitude of oscillation is 10% for the methane flow rate, the equivalence ratio increases to 0.3 at the peak point of the oscillatory cycle; much greater than the value at which steady CH_4 (70%) - H_2 (30%) mixture operates stably. However, the local flame is choked when the equivalence ratio falls to 0.25 at the lowest point of the oscillatory cycle. Still, as the oscillatory cycle period is limited to 60s, the system not only holds onto the heat but as the methane flow rate augments the excess enthalpy combustion is fast-tracked. Consequently, in Figure 6-8a during the ninth cycle, the fuel supply is cut as the flashback condition is met within 540s. Flashback was also observed by Habib et al. [217] as the same porous burner was operated solely on a CH_4 mixture. However, despite the CH_4 mixture having an identical amplitude of oscillation, it was noted the flashback occurred due to a longer oscillation cycle (180s). Figure 6-8b highlights the eighth oscillatory cycle of the flame motion. The flame motion appears to plummet along the respective reference points as the amplitude augments; with the flame size shrinking as much as 9mm at point E. Figure 6-8c visualises this occurrence as the flame not only moves further upstream, but the width of the flame expands within the porous foam.

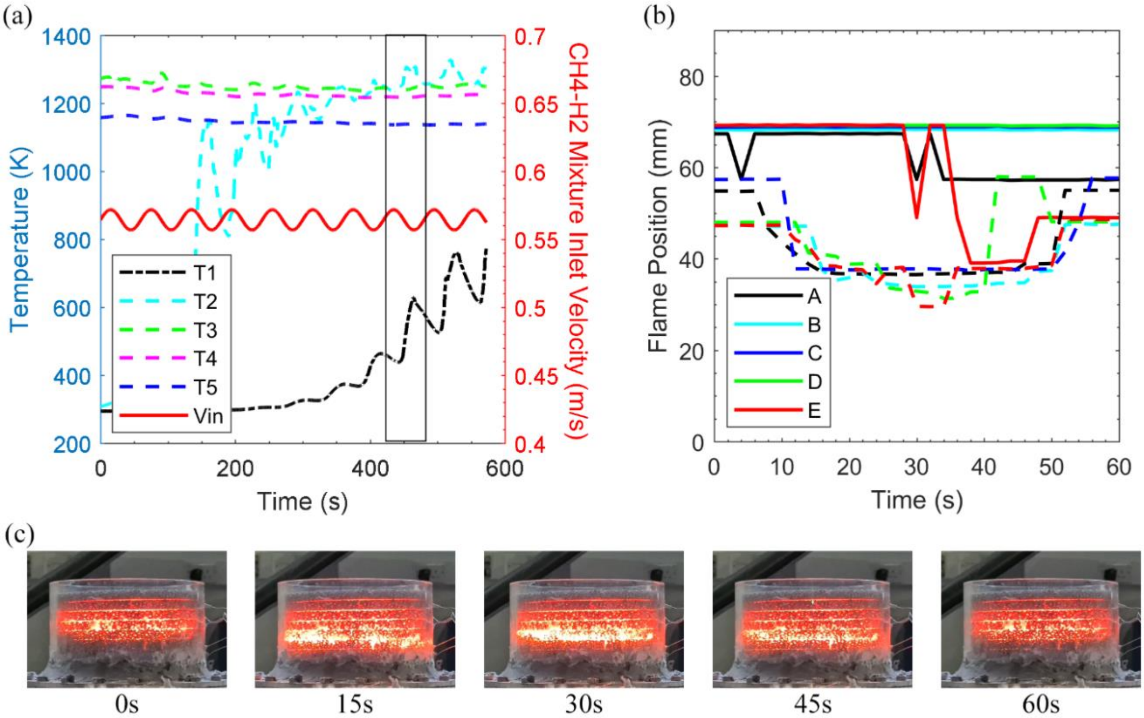

Figure 6-9: Forced response of the burner to modulation of fuel streams. Case 3y, amplitude of oscillation in methane flow:50% (a) Temperature + CH_4(70%)-H_2(30%) mixture velocity vs Time (b) Flame position motion at reference points, top section of the flame (-), bottom section of the flame (- -) (c) Screenshots of burner responding to oscillatory flow during complete cycle.

Figure 6-9 displays a parallel experiment to cases 1y and 2y except with a 50% amplitude. The temperature is primarily reported by the third thermocouple in Figure 6-9a. However, as the experiment proceeds, at the eighth cycle, the second thermocouple becomes the dominant respondent to the inlet fluctuations, followed by the first thermocouple. The recirculation of heat drastically improves as the amplitude of the methane inlet is augmented. This is because of the enhancement of heat convection at higher flow velocities. Downstream of the combustion region, there is a likelihood of a greater temperature at the lesser density porous foam as convective heat transfer takes place between the ceramic foam and the combustion products. Then, conductive, and radiative heat transfer are further involved via the solid SiC foam upstream of the reaction region. As the foam presents a greater temperature than the CH_4 (70%) - H_2 (30%) mixture; convection amid the fluid and solid occurs and warms the cold reactants. Yet, due to the existence of the low porosity ceramic foam downstream of the combustion region, conduction is accelerated in response to significant methane fluctuations. Figure 6-9c highlights the flame motion whereby a somewhat sinusoid resemblance is observed relating to the temperature response of the porous burner.

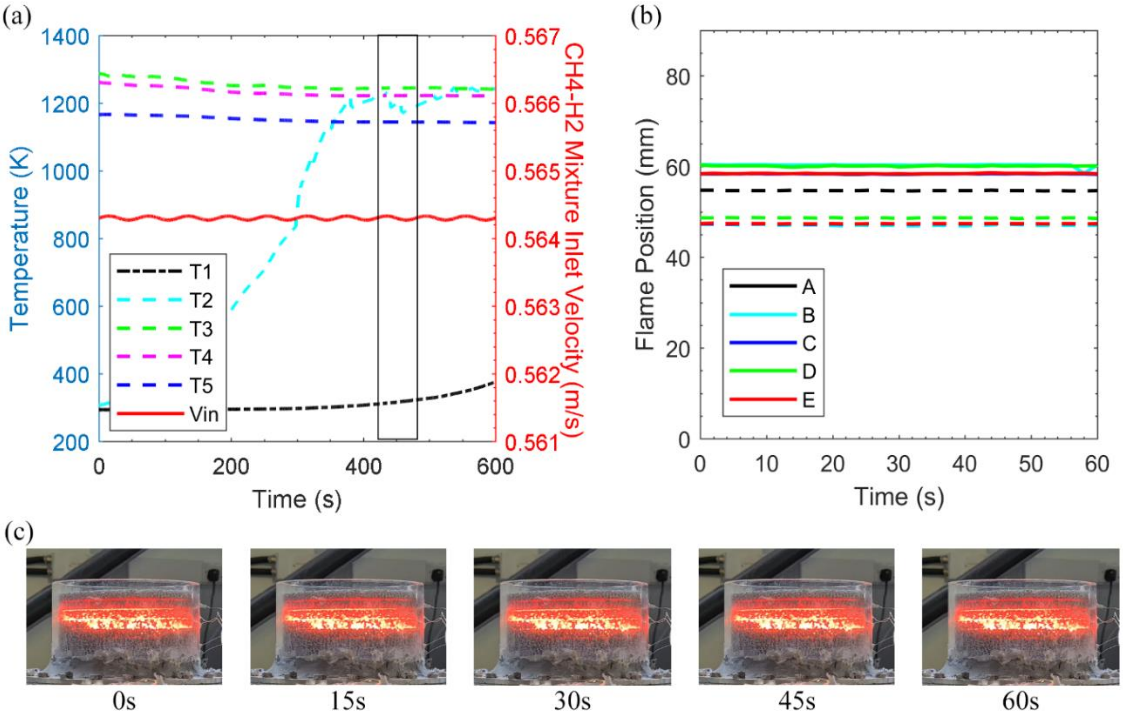

Figure 6-10: Forced response of the burner to modulation of fuel streams. Case 4y, amplitude of oscillation in hydrogen flow:10% (a) Temperature + CH_4(70%)-H_2(30%) mixture velocity vs Time (b) Flame position motion at reference points, top section of the flame (-), bottom section of the flame (- -) (c) Screenshots of burner responding to oscillatory flow during complete cycle.

Figure 6-10 shows the temperature response of the CH_4 (70%) - H_2 (30%) flame as the amplitude of hydrogen flow is modulated by 10%. Figure 6-10a illustrates a similar trend to that reported in case 6x where the system remains stable throughout the experiment and does not distinctly follow the inlet oscillatory behaviour of the fuel flow. The second thermocouple responds directly to the flame movement as it produces erratic behaviour after the sixth sinusoidal wave. As this erratic response continues, a growth in the temperature is noted by the first thermocouple. Further, it is observed that due to the greater initial hydrogen concentration in the fuel composition, the thermal response of case 4y is similar to that of case 6x, even though the current experiment only superimposes an amplitude of 10% as compared to 50%. Figure 6-10a and Figure 6-10b confirm that even when there is a greater portion of hydrogen present in the original fuel composition, a 10% fluctuation in amplitude has an insignificant impact on the flame motion.

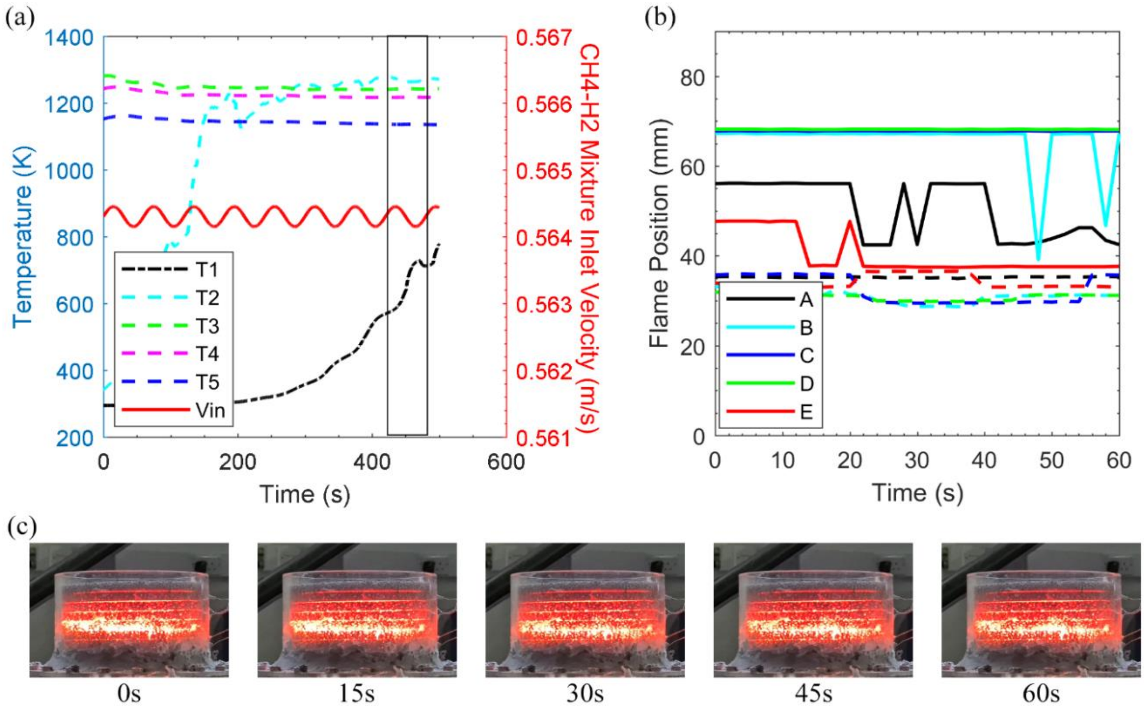

Figure 6-11: Forced response of the burner to modulation of fuel streams. Case 6y, amplitude of oscillation in hydrogen flow: 50% (a) Temperature + CH$_4$ (70%)-H$_2$ (30%) mixture velocity vs Time (b) Flame position motion at reference points, top section of the flame (-), bottom section of the flame (- -) (c) Screenshots of burner responding to oscillatory flow during complete cycle.

Figure 6-11 illustrates the impact of imposing a 50% amplitude inlet disturbance on the hydrogen flow rate within the CH$_4$ (70%) - H$_2$ (30%) mixture. In this case, the porous burner manages to withstand around eight oscillatory cycles (Figure 6-11a) before undergoing flame flashback. It is noted that the thermal response transitions from the second to first thermocouple directly responding to the amplified sinusoidal disturbance at the inlet. Case 6x successfully mitigates the risks of flash back in contrast to case 6y for comparable operating conditions. Flashback occurs in case 6y due to a few reasons including the change in fuel composition and lower inlet mixture velocity; all correlating to the increase in the temperature. The greater portion of hydrogen increases heat transfer inside the SiC foam as a result of the larger temperature gradient amidst the solid matrix and reacting gases. The flame motion during the eighth cycle is displayed in Figure 6-11b, showing a movement of more than 20mm in some instances across the reference points. Subsequently, a wide flame front is detected. This is validated in Figure 6-11c whereby not only the core flame width has been extended but also the external radiation glow has spread throughout the burner.

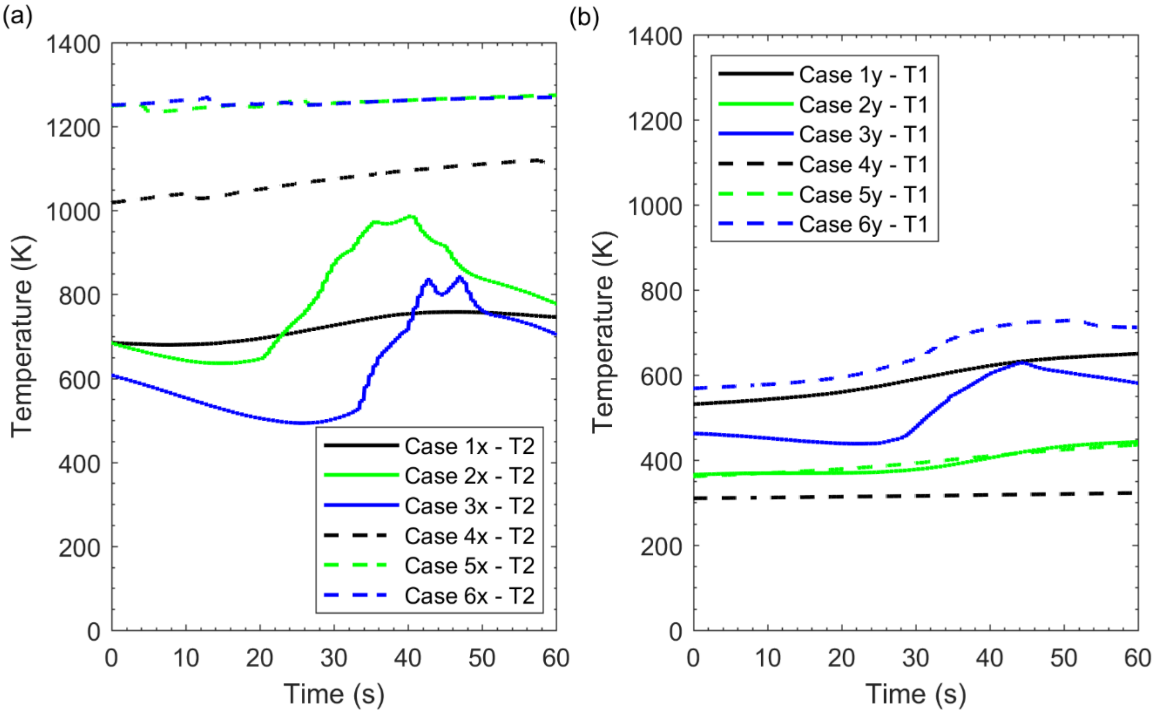

Figure 6-12: Forced response of the burner during an oscillatory cycle, CH4 modulation (solid line), H2 modulation (dashed line) (a) CH4 (90%)-H2 (10%) T2 temperature vs time (b) CH4 (70%)-H2 (30%) T1 temperature vs time.

Figure 6-12 presents a compilation of the temperature traces from the eighth oscillatory cycle of all cases from CH_4 (90%)-H_2 (10%) and CH_4 (70%)-H_2 (30%) mixtures. This comparison provides further clarity to the results reported earlier. Figure 6-12a clearly outlines case 3x undergoing blow-off as T2 records lower temperature against its counterparts - case 1x and case 2x – despite having a greater CH_4 modulation amplitude. Similarly, H_2 fuel modulation outputs larger temperature in comparison to CH_4 modulation without directly responding to the oscillatory pattern. Case 5x and case 6x display a negligible temperature change. Figure 6-12b displays T1 traces of CH_4 (70%)-H_2 (30%) mixture as the flame has moved further upstream with the greater addition of H_2. As a disturbance is superimposed on the fuel inlet, the temperature trace appears to follow a monotonic increase with the increase of H_2 amplitude. However, this pattern is not observed as CH_4 amplitude was increased. Case 1y and Case 3y show greater temperature readings and eventually result in flashback albeit Case 2y which maintains stable operation with a lower temperature.

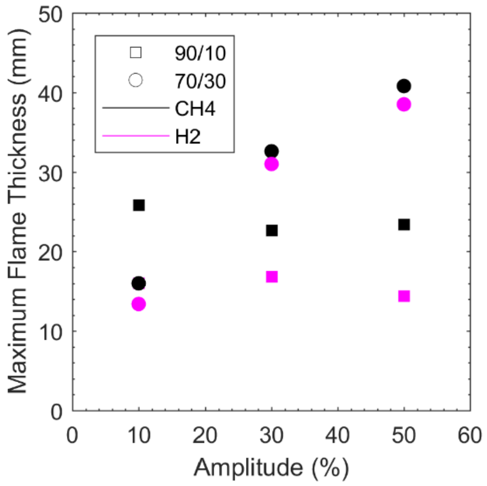

Figure 6-13: Maximum flame thickness vs base value amplitude.

Figure 6-13 depicts a correlation between the flame thickness and the variation of amplitude of hydrogen and methane in both CH_4 (90%) - H_2 (10%) and CH_4 (70%) - H_2 (30%) mixtures. Once again, the flame thickness in this figure was inferred through image processing technique detailed in section 6.2.3. In CH_4 (90%) - H_2 (10%) mixture, it can be seen that as the methane amplitude is increased, mid-way the flame thickness contracts 13% before posting a gradual increase of 4%. An inverse behaviour is observed for hydrogen modulation, as the amplitude increases so do the flame thickness mid-way but then contracts at the maximum amplitude value. However, for the CH_4(70%)-H_2(30%) mixture a monotonic increase in flame thickness is detected for an increase in amplitude for both methane and hydrogen; approximately 300% overall. The exact reason for this behaviour is not immediately obvious, and it calls for further experimental and numerical studies.

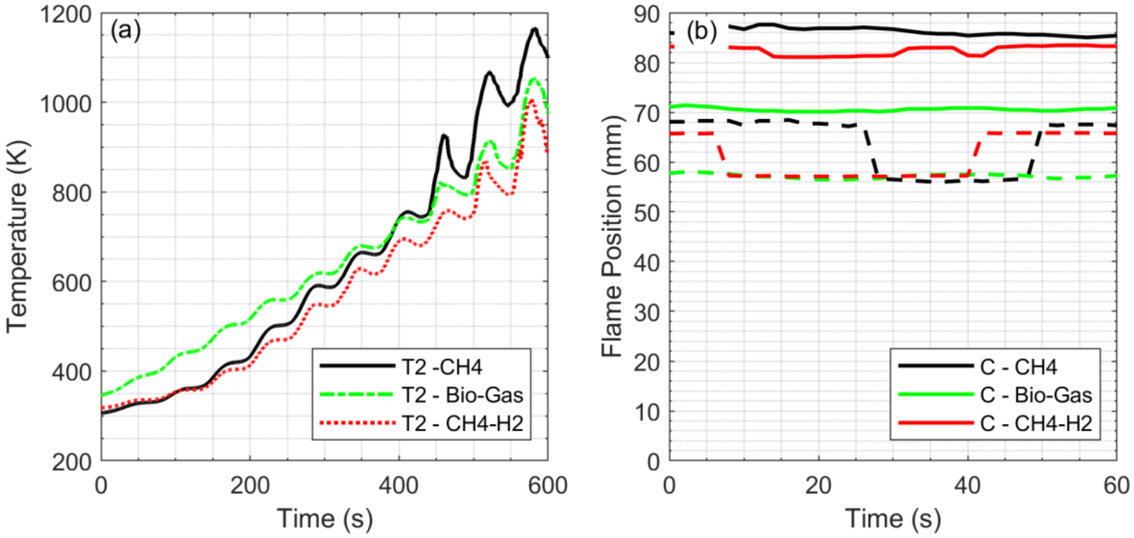

Figure 6-14: Forced response of the burner to modulation of fuel stream of CH4 – Case1x, Bio-Gas – Case1y, CH4 90% H2 10% - Case 1x, amplitude of oscillation in methane flow: 10% (a) Temperature (T2) vs Time (b) Flame position motion at reference point C, top section of the flame (-), bottom section of the flame (- -).

Figure 6-14 illustrates the influence of fuel mixture type on the oscillating flow. The three selected cases are subject to an inlet disturbance superimposed on the methane flow rate with a 10% amplitude, period of 60s, with an identical equivalence ratio (0.275) and maintain stable operation for the entirety of this comparison. Figure 6-14a shows the temperature traces recorded by T2 for various fuel mixture types over ten cycles of oscillation as fluctuations in flame location is limited to the locality of thermocouple T2 . A comparison between the fuel mixtures reveals an akin trend with the rise in temperature at T2, albeit from the eighth cycle forward, a visibly reduced temperature increase is witnessed in Bio-Gas and in particular the CH4-H2 mixture. This can be for the most part ascribed to the chemical composition of Bio-Gas as a reduced amount of fuel is being burned of the incoming reactants, less heat is produced. Consequently, less significant temperature increases occur, and it takes longer for heat to transfer. As a knock-on effect, the silicon carbide foam takes longer to heat up. The T2 CH4-H2 mixture temperature is reported lower than the Bio-Gas mixture, however, this is primarily due to the flame front position being further downstream as the maximum CH4-H2 mixture temperature (1354K) is far greater than its Bio-Gas counterpart (1283K). Figure 6-14b confirms this as the central flame position at point C displays Bio-Gas further upstream when compared with the CH4 and CH4-H2 mixtures. One aspect of the variation in flame position is due to the greater CH4-H2 (≈0.79 m/s) velocity than Bio-Gas velocity (≈0.52 m/s)."

6.4 Conclusions

A custom-designed porous burner was used in an experimental investigation of ultra-lean combustion to investigate the burner response to the oscillations superimposed on the fuel flow. The work was motivated by the possibility of temporal changes in the chemical composition of hydrogen containing fuels including blends of methane and hydrogen. Such variations can strongly influence the flame stabilisation and lead to flame extinction/flashback. It is therefore important to analyse the burner response to imposed oscillations on the fuel streams. CH_4(90%)-H_2(10%) and CH_4(70%)-H_2(30%) mixtures were incorporated as fuel. The inlet sinusoidal disturbances were imposed on the hydrogen and methane flows by programmable MFCs. The thermal response of the system was monitored by using thermocouples positioned at the centre of the burner in different axial locations and, by detecting the flame motion using image processing techniques. It was found that, under steady condition, the CH_4(90%)-H_2(10%) could operate as low as $\phi = 0.25$. Additionally, the CH_4(90%)-H_2(10%) mixture produced greater carbon monoxide emissions when compared to the CH_4(70%)-H_2(30%) mixture. Moreover, NOx emissions were found to be almost negligible. This was expected as the current low-temperature combustion system (maximum temperature $\approx 1384K$) strongly suppressed the formation of thermal NOx [231]. A similar trend was observed by Ferrarotti et al. [232] where the reduction of NOx emissions was closely associated with the reduction in the equivalence ratio. However, the gas analyser's response time of 90 seconds to detect NOx emissions makes it unsuitable to measure NOx emissions in a dynamic experiment. As both mixtures were subject to unsteady inlet flow of hydrogen and methane, the burner remained stable for CH_4(90%)-H_2(10%) mixture when hydrogen was oscillated between 0-50% and for methane between 0-10% over a period of 60s. Similarly, the burner remained stable for the CH_4(70%)-H_2(30%) mixture when hydrogen flow was fluctuated at 0-30% of its steady flow rate and methane fluctuated at 30% for the identical oscillatory period. For both mixtures by in large, it was observed that the flame movement corresponds to the dynamics of the induced disturbances at the inlet. The flame thickness within CH_4(70%)-H_2(30%) mixture was proven to be far greater when compared to CH_4(90%)-H_2(10%) mixture as the hydrogen and methane flows were amplified. Lastly, both fuel mixtures were noted to be rather insensitive to hydrogen fluctuation beneath 30% amplitude.

Chapter 7 Summary and conclusions

The work presented in this thesis has investigated the dynamics of heat transfer and combusting flows in a numerical model and experimental investigation. The numerical study investigated unsteady forced convection in porous media using a microscopic approach in a three-dimensional ten cylindrical obstacle design. An experimental investigation was carried out using a custom-built porous burner to assess the systems behaviour to fluctuations in the inlet flow whilst operating in ultra-lean conditions. The porous burner was operated on different working fuels - methane, biogas and various blends of hydrogen and methane – to draw meaningful results. The findings of these studies are presented in section 7.1 and a recommendation for future works in section 7.2

7.1 Conclusions

Initially heat convection response of a reticulated porous medium to the harmonic and ramp disturbances in the inlet flow was investigated taking a pore-scale approach. A few types of fluids, along with different values of porosity and Reynolds number, were considered. Assuming laminar flow, the unsteady equations of continuity, Navier Stokes and energy were solved computationally. In this model, ten cylindrical obstacles aligned in a staggered arrangement with set isothermal boundary conditions were constructed.

Chapter 2 and Chapter 3 feature the system that was modulated by sine waves superimposed on the inlet flow velocity, and the spatio-temporal responses of the flow and temperature fields were calculated. The results were then utilised to assess the linearity of the thermal response represented by the Nusselt number on the obstacles and compared against existing empirical data. It was observed for linear cases, a transfer function can be approximated by a classic low-pass filter which resembles the average response of the individual obstacles. This indicates that there exists a frequency threshold above which the thermal system is essentially insensitive to flow modulations. However, the dynamical relations between the inlet flow fluctuations as the input and those of Nusselt number as the output, can be non-linear. The extent of encountered non-linearity was determined quantitatively through introduction of a measure of non-linearity. It was found that changes in the pore-scale Reynolds number and porosity of the medium can push the dynamic response of the system towards non-linearity. Yet, further increases in Reynolds number can push the system dynamics back to linear. In general, it was learned that for low Reynolds numbers, the dynamics of heat convection can be predicted decently by taking a transfer function approach. Further, through a statistical analysis, it was shown that the thermal response of the porous medium was strongly dominated by those of the first few obstacles.

Chapter 4 exhibits the thermal system subject to a ramp disturbance superimposed on the entrance flow temperature/velocity. The temporally developing flow and temperature fields as well as the surface averaged Nusselt numbers were used to explore the transient response of the system. Also, a response lag ratio (RLR) was defined to further characterise the transient response of the system. The results revealed that an increase in amplitude increases the RLR. Nonetheless, an increase in ramp duration decreases RLR, particularly for high-density fluids. Interestingly, it was noted that the Reynolds number has almost negligible effects upon RLR.

Chapter 5 and Chapter 6 present the experimental investigation of the response of ultra-lean flames, stabilised in a porous burner, to the fluctuations imposed on the fuel flow rate for various composition of fuels. Chapter 5 is motivated by the likelihood of small biogas generators to produce fuels with temporal variations in their flow rate and chemical composition. Chapter 6 investigates the response to fluctuations in the flow rate of different blends of methane and hydrogen. The employed porous burned includes layers of silicon carbide porous foam placed inside a quartz tube. The burner is equipped with a series of axially arranged thermocouples and was imaged by a digital camera. The fuel streams were measured and controlled separately by programmable mass flow controllers, which impose sinusoidal fluctuations with variable amplitude and frequency on the steady flow. To replicate realistic fluctuations in the fuel flow rate, the period of oscillations were chosen to be on the order of minutes. The temperature inside the ceramic foam was measured using five thermocouples located at the centre of the working section of the burner. The flame embedded in porous media was imaged while the fuel flow is modulated. Analysis of the flame pictures and temperature traces revealed that the forced oscillation of the fuel mixture leads to flame movement within the burner.

In Chapter 5, methane and a blend of methane and carbon dioxide (mimicking biogas) were mixed with air and then fed to the burner at equivalence ratios below 0.3. The flame movement was found to quantitatively follow the temporal variation in the fuel flow for both methane and biogas. Nonetheless, the amplitude of the flame oscillations for methane was to be higher than that for biogas. Further, it was observed that exposure of the burner to the fuel fluctuations for a long time (180s) eventually results in flame destabilisation. However, stabilised combustion was achieved for methane mixtures at amplitudes between 0 and 30% of steady values over a period of 60s.

In Chapter 6, prior to injection into the porous burner, the hydrogen and methane blends were premixed with air at equivalence ratios below 0.275. It was found the flame movement behaved in accordance with the fluctuations in methane and hydrogen flows for both CH_4 (90%)-H_2(10%) and CH_4 (70%)-H_2(30%) mixtures. However, both fuel mixtures were noted to be rather insensitive to hydrogen flow fluctuation with a modulation amplitude below 30% of the steady flow. For the CH_4 (70%)-H_2(30%), the flame in the porous medium can be modulated by fluctuations between 0 and 30% of steady methane flow without any noticeable flame destabilisation. This study revealed the strong effects of unsteady heat transfer in porous media upon the fluctuations in flame position.

7.2 Recommendations for future work

Use of the three-dimensional pore-scale numerical model is still a very open area of research. Future investigations in this area can include

- conjugate heat transfer
- turbulent flow
- reactive flow
- greater variation in porosity

Similarly, the porous burner investigations can be taken further by

- change in porous material
- change in porosity of porous material

- greater proportion of hydrogen in methane and hydrogen blends
- use of carbon-neutral fuels such as syngas and ammonia
- a compact burner design i.e. saving fuel

List of References

[1] S. Piao, P. Ciais, Y. Huang, Z. Shen, S. Peng, J. Li, L. Zhou, H. Liu, Y. Ma, Y. Ding, P. Friedlingstein, C. Liu, K. Tan, Y. Yu, T. Zhang, J. Fang, The impacts of climate change on water resources and agriculture in China, Nature. 467 (2010) 43–51. https://doi.org/10.1038/nature09364.

[2] K.L. Erwin, Wetlands and global climate change: the role of wetland restoration in a changing world, Wetl Ecol Manag. 17 (2009) 71–84. https://doi.org/10.1007/s11273-008-9119-1.

[3] “climate change, n.,” OED Online. Oxford University Press. (n.d.).

[4] S.S. Myers, L. Gaffikin, C.D. Golden, R.S. Ostfeld, K. H. Redford, T. H. Ricketts, W.R. Turner, S.A. Osofsky, Human health impacts of ecosystem alteration, in: Proceedings of the National Academy of Sciences, 2013: pp. 18753–18760. https://doi.org/10.1073/pnas.1218656110.

[5] N. P.Gillett, Malinina Elizaveta, Kaufman Darrell, Nuekom Raphael, Summary for Policymakers of the Working Group I Contribution to the IPCC Sixth Assessment Report - data for Figure SPM.1 (v20210809), (2021).

[6] D.J. Wuebbles, A.K. Jain, Concerns about climate change and the role of fossil fuel use, Fuel Processing Technology. 71 (2001) 99–119. https://doi.org/10.1016/S0378-3820(01)00139-4.

[7] K.P. Shine, J.S. Fuglestvedt, K. Hailemariam, N. Stuber, Alternatives to the Global Warming Potential for Comparing Climate Impacts of Emissions of Greenhouse Gases, Clim Change. 68 (2005) 281–302. https://doi.org/10.1007/s10584-005-1146-9.

[8] M. Janić, Greening Airports, Springer London, London, 2011. https://doi.org/10.1007/978-0-85729-658-0.

[9] K. Zahnle, N. Arndt, C. Cockell, A. Halliday, E. Nisbet, F. Selsis, N.H. Sleep, Emergence of a Habitable Planet, Space Sci Rev. 129 (2007) 35–78. https://doi.org/10.1007/s11214-007-9225-z.

[10] P. Nejat, F. Jomehzadeh, M.M. Taheri, M. Gohari, M.Z. Abd. Majid, A global review of energy consumption, CO2 emissions and policy in the residential sector (with an overview of the top ten CO2 emitting countries), Renewable and Sustainable Energy Reviews. 43 (2015) 843–862. https://doi.org/10.1016/j.rser.2014.11.066.

[11] A.J. McMichael, J.W. Powles, C.D. Butler, R. Uauy, Food, livestock production, energy, climate change, and health, The Lancet. 370 (2007) 1253–1263. https://doi.org/10.1016/S0140-6736(07)61256-2.

[12] S. Cadez, A. Czerny, P. Letmathe, Stakeholder pressures and corporate climate change mitigation strategies, Bus Strategy Environ. 28 (2019) 1–14. https://doi.org/10.1002/bse.2070.

[13] Y. Xu, V. Ramanathan, D.G. Victor, Global warming will happen faster than we think, Nature. 564 (2018) 30–32. https://doi.org/10.1038/d41586-018-07586-5.

[14] C. Bataille, M. Åhman, K. Neuhoff, L.J. Nilsson, M. Fischedick, S. Lechtenböhmer, B. Solano-Rodriquez, A. Denis-Ryan, S. Stiebert, H. Waisman, O. Sartor, S. Rahbar, A review of technology and policy deep decarbonization pathway options for making energy-intensive industry production consistent with the Paris Agreement, J Clean Prod. 187 (2018) 960–973. https://doi.org/10.1016/j.jclepro.2018.03.107.

[15] P. Goglio, A.G. Williams, N. Balta-Ozkan, N.R.P. Harris, P. Williamson, D. Huisingh, Z. Zhang, M. Tavoni, Advances and challenges of life cycle assessment (LCA) of greenhouse gas removal technologies to fight climate changes, J Clean Prod. 244 (2020) 118896. https://doi.org/10.1016/j.jclepro.2019.118896.

[16] K. Du, P. Li, Z. Yan, Do green technology innovations contribute to carbon dioxide emission reduction? Empirical evidence from patent data, Technol Forecast Soc Change. 146 (2019) 297–303. https://doi.org/10.1016/j.techfore.2019.06.010.

[17] M. Sabir, Y. Ali, I. Khan, A. Salman, Plants Species Selection for Afforestation: A Case Study of the Billion Tree Tsunami Project of Pakistan, Journal of Sustainable Forestry. (2020) 1–13. https://doi.org/10.1080/10549811.2020.1830802.

[18] A.A. Jimoh, J. Lin, Biosurfactant: A new frontier for greener technology and environmental sustainability, Ecotoxicol Environ Saf. 184 (2019) 109607. https://doi.org/10.1016/j.ecoenv.2019.109607.

[19] K.L. Ricke, R.J. Millar, D.G. MacMartin, Constraints on global temperature target overshoot, Sci Rep. 7 (2017) 14743. https://doi.org/10.1038/s41598-017-14503-9.

[20] O. Hoegh-Guldberg, D. Jacob, M. Bindi, S. Brown, I. Camilloni, A. Diedhiou, R. Djalante, K. Ebi, F. Engelbrecht, J. Guiot, Y. Hijioka, S. Mehrotra, A. Payne, S.I. Seneviratne, A. Thomas, R. Warren, G. Zhou, S.A. Halim, M. Achlatis, L. v Alexander, M. Allen, P. Berry, C. Boyer, E. Byers, L. Brilli, M. Buckeridge, W. Cheung, M. Craig, N. Ellis, J. Evans, H. Fischer, K. Fraedrich, S. Fuss, A. Ganase, J.P. Gattuso, P. Greve, T.G. Bolaños, N. Hanasaki, T. Hasegawa, K. Hayes, A. Hirsch, C. Jones, T. Jung, M. Kanninen, G. Krinner, D. Lawrence, T. Lenton, D. Ley, D. Liverman, N. Mahowald, K. McInnes, K.J. Meissner, R. Millar, K. Mintenbeck, D. Mitchell, A.C. Mix, D. Notz, L. Nurse, A. Okem, L. Olsson, M. Oppenheimer, S. Paz, J. Petersen, J. Petzold, S. Preuschmann, M.F. Rahman, J. Rogelj, H. Scheuffele, C.-F. Schleussner, D. Scott, R. Séférian, J. Sillmann, C. Singh, R. Slade, K. Stephenson, T. Stephenson, M.B. Sylla, M. Tebboth, P. Tschakert, R. Vautard, R. Wartenburger, M. Wehner, N.M. Weyer, F. Whyte, G. Yohe, X. Zhang, R.B. Zougmoré, Chapter 3: Impacts of 1.5ºC global warming on natural and human systems, 2018. http://hdl.handle.net/10138/311749 (accessed December 14, 2021).

[21] A. Lockley, State Commissioning of Solar Radiation Management Geoengineering, Ethics Policy Environ. 23 (2020) 180–202. https://doi.org/10.1080/21550085.2020.1848176.

[22] UK energy in brief 2021, 2021. https://www.gov.uk/government/statistics/uk-energy-in-brief-2021 (accessed December 16, 2021).

[23] Greenhouse gas emissions from energy – data explorer, IEA, Paris, 2021. https://www.iea.org/articles/greenhouse-gas-emissions-from-energy-data-explorer (accessed December 16, 2021).

[24] Net Zero Strategy: Build Back Greener, 2021. https://assets.publishing.service.gov.uk/government/uploads/system/uploads/attachment_data/file/1033990/net-zero-strategy-beis.pdf (accessed December 22, 2021).

[25] V. Masson-Delmotte, P. Zhai, A. Pirani, S.L. Connors, C. Péan, S. Berger, N. Caud, Y. Chen, L. Goldfarb, M.I. Gomis, M. Huang, K. Leitzell, E. Lonnoy, J.B.R. Matthews, T.K. Maycock, T. Waterfield, O. Yelekçi, R. Yu, B. Zhou, IPCC, 2021: Climate Change 2021: The Physical Science Basis. Contribution of Working Group I to the Sixth Assessment Report of the Intergovernmental Panel on Climate Change, 2021. https://www.ipcc.ch/report/ar6/wg1/#FullReport (accessed December 22, 2021).

[26] The Paris Agreement, 2015. https://unfccc.int/process-and-meetings/the-paris-agreement/the-paris-agreement (accessed December 22, 2021).

[27] K. Ravi Kumar, N.V.V. Krishna Chaitanya, N. Sendhil Kumar, Solar thermal energy technologies and its applications for process heating and power generation – A review, J Clean Prod. 282 (2021) 125296. https://doi.org/10.1016/j.jclepro.2020.125296.

[28] D. Einstein, E. Worrell, M. Khrushch, Steam systems in industry: Energy use and energy efficiency improvement potentials, 2001.

https://escholarship.org/uc/item/3m1781f1 (accessed December 22, 2021).

[29] S. Kalogirou, The potential of solar industrial process heat applications, Appl Energy. 76 (2003) 337–361. https://doi.org/10.1016/S0306-2619(02)00176-9.

[30] IEA: Iron and Steel, Paris, 2021. https://www.iea.org/reports/iron-and-steel (accessed December 22, 2021).

[31] D.J. Barker, S.A. Turner, P.A. Napier-Moore, M. Clark, J.E. Davison, CO2 Capture in the Cement Industry, Energy Procedia. 1 (2009) 87–94. https://doi.org/10.1016/j.egypro.2009.01.014.

[32] M.B. Ali, R. Saidur, M.S. Hossain, A review on emission analysis in cement industries, Renewable and Sustainable Energy Reviews. 15 (2011) 2252–2261. https://doi.org/10.1016/j.rser.2011.02.014.

[33] M.S. Winfield, Marisa Jacott, Cyrus BH Reed, Amy Taylor, Energy Use in the Cement Industry in North America, 2003.

[34] J. Deja, A. Uliasz-Bochenczyk, E. Mokrzycki, CO2 emissions from Polish cement industry, International Journal of Greenhouse Gas Control. 4 (2010) 583–588. https://doi.org/10.1016/j.ijggc.2010.02.002.

[35] B.L. Damineli, F.M. Kemeid, P.S. Aguiar, V.M. John, Measuring the eco-efficiency of cement use, Cem Concr Compos. 32 (2010) 555–562. https://doi.org/10.1016/j.cemconcomp.2010.07.009.

[36] IEA, Direct CO2 intensity of cement production in the Net Zero Scenario, 2015-2030, Paris, 2021.

[37] X.J. Lee, H.C. Ong, Y.Y. Gan, W.-H. Chen, T.M.I. Mahlia, State of art review on conventional and advanced pyrolysis of macroalgae and microalgae for biochar, bio-oil and bio-syngas production, Energy Convers Manag. 210 (2020) 112707. https://doi.org/10.1016/j.enconman.2020.112707.

[38] R. Kadam, N.L. Panwar, Recent advancement in biogas enrichment and its applications, Renewable and Sustainable Energy Reviews. 73 (2017) 892–903. https://doi.org/10.1016/j.rser.2017.01.167.

[39] D. Thiruselvi, P.S. Kumar, M.A. Kumar, C.-H. Lay, S. Aathika, Y. Mani, D. Jagadiswary, A. Dhanasekaran, P. Shanmugam, S. Sivanesan, P.-L. Show, A critical review on global trends in biogas scenario with its up-gradation techniques for fuel cell and future perspectives, Int J Hydrogen Energy. 46 (2021) 16734–16750. https://doi.org/10.1016/j.ijhydene.2020.10.023.

[40] I. Ullah Khan, M. Hafiz Dzarfan Othman, H. Hashim, T. Matsuura, A.F. Ismail, M. Rezaei-DashtArzhandi, I. Wan Azelee, Biogas as a renewable energy fuel – A review of biogas upgrading, utilisation and storage, Energy Convers Manag. 150 (2017) 277–294. https://doi.org/10.1016/j.enconman.2017.08.035.

[41] S.-H. Ho, C. Zhang, F. Tao, C. Zhang, W.-H. Chen, Microalgal Torrefaction for Solid Biofuel Production, Trends Biotechnol. 38 (2020) 1023–1033. https://doi.org/10.1016/j.tibtech.2020.02.009.

[42] M.M. Samy, S. Barakat, H.S. Ramadan, Techno-economic analysis for rustic electrification in Egypt using multi-source renewable energy based on PV/ wind/ FC, Int J Hydrogen Energy. 45 (2020) 11471–11483. https://doi.org/10.1016/j.ijhydene.2019.04.038.

[43] L.N. Nguyen, J. Kumar, M.T. Vu, J.A.H. Mohammed, N. Pathak, A.S. Commault, D. Sutherland, J. Zdarta, V.K. Tyagi, L.D. Nghiem, Biomethane production from anaerobic co-digestion at wastewater treatment plants: A critical review on development and innovations in biogas upgrading techniques, Science of The Total Environment. 765 (2021) 142753. https://doi.org/10.1016/j.scitotenv.2020.142753.

[44] F.M. Baena-Moreno, D. Sebastia-Saez, L. Pastor-Pérez, T.R. Reina, Analysis of the potential for biogas upgrading to syngas via catalytic reforming in the United Kingdom, Renewable and Sustainable Energy Reviews. 144 (2021) 110939. https://doi.org/10.1016/j.rser.2021.110939.

[45] UK hydrogen strategy, 2021.

[46] S.E. Hosseini, M.A. Wahid, Development of biogas combustion in combined heat and power generation, Renewable and Sustainable Energy Reviews. 40 (2014) 868–875. https://doi.org/10.1016/j.rser.2014.07.204.

[47] Y. Qian, S. Sun, D. Ju, X. Shan, X. Lu, Review of the state-of-the-art of biogas combustion mechanisms and applications in internal combustion engines, Renewable and Sustainable Energy Reviews. 69 (2017) 50–58. https://doi.org/10.1016/j.rser.2016.11.059.

[48] J.R. Howell, M.J. Hall, J.L. Ellzey, Combustion of hydrocarbon fuels within porous inert media, Prog Energy Combust Sci. 22 (1996) 121–145. https://doi.org/10.1016/0360-1285(96)00001-9.

[49] S. Wood, A.T. Harris, Porous burners for lean-burn applications, Prog Energy Combust Sci. 34 (2008) 667–684. https://doi.org/10.1016/j.pecs.2008.04.003.

[50] M. Kaviany, Principles of Heat Transfer in Porous Media, 1991.

[51] M. Dejam, Derivation of dispersion coefficient in an electro-osmotic flow of a viscoelastic fluid through a porous-walled microchannel, Chem Eng Sci. 204 (2019) 298–309. https://doi.org/10.1016/j.ces.2019.04.027.

[52] M. Dejam, Hydrodynamic dispersion due to a variety of flow velocity profiles in a porous-walled microfluidic channel, Int J Heat Mass Transf. 136 (2019) 87–98. https://doi.org/10.1016/j.ijheatmasstransfer.2019.02.081.

[53] G. Kolb, Review: Microstructured reactors for distributed and renewable production of fuels and electrical energy, Chemical Engineering and Processing: Process Intensification. 65 (2013) 1–44. https://doi.org/10.1016/j.cep.2012.10.015.

[54] Y. Mahmoudi, N. Karimi, Numerical investigation of heat transfer enhancement in a pipe partially filled with a porous material under local

thermal non-equilibrium condition, Int J Heat Mass Transf. 68 (2014) 161–173. https://doi.org/10.1016/j.ijheatmasstransfer.2013.09.020.

[55] Y. Mahmoudi, N. Karimi, K. Mazaheri, Analytical investigation of heat transfer enhancement in a channel partially filled with a porous material under local thermal non-equilibrium condition: Effects of different thermal boundary conditions at the porous-fluid interface, Int J Heat Mass Transf. 70 (2014) 875–891. https://doi.org/10.1016/j.ijheatmasstransfer.2013.11.048.

[56] C. Dickson, M. Torabi, N. Karimi, First and second law analyses of nanofluid forced convection in a partially-filled porous channel – The effects of local thermal non-equilibrium and internal heat sources, Appl Therm Eng. 103 (2016) 459–480. https://doi.org/10.1016/j.applthermaleng.2016.04.095.

[57] M. Dejam, H. Hassanzadeh, Z. Chen, Shear dispersion in combined pressure-driven and electro-osmotic flows in a capillary tube with a porous wall, AIChE Journal. 61 (2015) 3981–3995. https://doi.org/10.1002/aic.14897.

[58] Y. Deng, C. Feng, J. E, H. Zhu, J. Chen, M. Wen, H. Yin, Effects of different coolants and cooling strategies on the cooling performance of the power lithium ion battery system: A review, Appl Therm Eng. 142 (2018) 10–29. https://doi.org/10.1016/j.applthermaleng.2018.06.043.

[59] Y. Mahmoudi, K. Hooman, K. Vafai, Convective Heat Transfer in Porous Media, CRC Press, 2019.

[60] Z. Kou, M. Dejam, Dispersion due to combined pressure-driven and electro-osmotic flows in a channel surrounded by a permeable porous medium, Physics of Fluids. 31 (2019) 056603. https://doi.org/10.1063/1.5092199.

[61] F. Song, Z. Wen, Z. Dong, E. Wang, X. Liu, Ultra-low calorific gas combustion in a gradually-varied porous burner with annular heat recirculation, Energy. 119 (2017) 497–503. https://doi.org/10.1016/j.energy.2016.12.077.

[62] M. Dejam, H. Hassanzadeh, Z. Chen, Semi-Analytical Solutions for a Partially Penetrated Well with Wellbore Storage and Skin Effects in a Double-Porosity

System with a Gas Cap, Transp Porous Media. 100 (2013) 159–192. https://doi.org/10.1007/s11242-013-0210-6.

[63] S. Rashidi, M.H. Kashefi, K.C. Kim, O. Samimi-Abianeh, Potentials of porous materials for energy management in heat exchangers – A comprehensive review, Appl Energy. 243 (2019) 206–232. https://doi.org/10.1016/j.apenergy.2019.03.200.

[64] M. Siavashi, K. Karimi, Q. Xiong, M.H. Doranehgard, Numerical analysis of mixed convection of two-phase non-Newtonian nanofluid flow inside a partially porous square enclosure with a rotating cylinder, J Therm Anal Calorim. 137 (2019) 267–287. https://doi.org/10.1007/s10973-018-7945-9.

[65] J. Ellzey, M. William, Porous Burner For Gas Turbine Applications, 2003024655, 2003.

[66] M.A. Mujeebu, M.Z. Abdullah, M.Z.A. Bakar, A.A. Mohamad, R.M.N. Muhad, M.K. Abdullah, Combustion in porous media and its applications - A comprehensive survey, J Environ Manage. 90 (2009) 2287–2312. https://doi.org/10.1016/j.jenvman.2008.10.009.

[67] L. Wang, N. Karimi, T. Sutardi, M.C. Paul, Combustion Characteristics and Pollutant Emissions in Transient Oxy-Combustion of a Single Biomass Particle: A Numerical Study, Energy and Fuels. 33 (2019) 1556–1569. https://doi.org/10.1021/acs.energyfuels.8b03602.

[68] M. Toledo, F. Gracia, S. Caro, J. Gómez, V. Jovicic, Hydrocarbons conversion to syngas in inert porous media combustion, Int J Hydrogen Energy. 41 (2016) 5857–5864. https://doi.org/10.1016/j.ijhydene.2016.02.065.

[69] J. Dunnmon, S. Sobhani, M. Wu, R. Fahrig, M. Ihme, An investigation of internal flame structure in porous media combustion via X-ray Computed Tomography, Proceedings of the Combustion Institute. 36 (2017) 4399–4408. https://doi.org/10.1016/j.proci.2016.06.188.

[70] S. Bani, J. Pan, A. Tang, Q. Lu, Y. Zhang, Micro combustion in a porous media for thermophotovoltaic power generation, Appl Therm Eng. 129 (2018) 596–605. https://doi.org/10.1016/j.applthermaleng.2017.10.024.

[71] Y. Deng, C. Feng, J. E, H. Zhu, J. Chen, M. Wen, H. Yin, Effects of different coolants and cooling strategies on the cooling performance of the power lithium ion battery system: A review, Appl Therm Eng. 142 (2018) 10–29. https://doi.org/10.1016/j.applthermaleng.2018.06.043.

[72] G. Xia, L. Cao, G. Bi, A review on battery thermal management in electric vehicle application, J Power Sources. 367 (2017) 90–105. https://doi.org/10.1016/j.jpowsour.2017.09.046.

[73] J.L. Ellzey, E.L. Belmont, C.H. Smith, Heat recirculating reactors: Fundamental research and applications, Prog Energy Combust Sci. 72 (2019) 32–58. https://doi.org/10.1016/j.pecs.2018.12.001.

[74] G. Hunt, N. Karimi, B. Yadollahi, M. Torabi, The effects of exothermic catalytic reactions upon combined transport of heat and mass in porous microreactors, Int J Heat Mass Transf. 134 (2019) 1227–1249. https://doi.org/10.1016/j.ijheatmasstransfer.2019.02.015.

[75] F. He, L. Ma, Thermal management of batteries employing active temperature control and reciprocating cooling flow, Int J Heat Mass Transf. 83 (2015) 164–172. https://doi.org/10.1016/j.ijheatmasstransfer.2014.11.079.

[76] H. Saberinejad, A. Keshavarz, M. Payandehdoost, M.R. Azmoodeh, A. Batooei, Numerical study of heat transfer performance in a pipe partially filled with non-uniform porous media under LTNE condition, Int J Numer Methods Heat Fluid Flow. 28 (2018) 1845–1865. https://doi.org/10.1108/HFF-12-2017-0495.

[77] F. Rong, W. Zhang, B. Shi, Z. Guo, Numerical study of heat transfer enhancement in a pipe filled with porous media by axisymmetric TLB model

based on GPU, Int J Heat Mass Transf. 70 (2014) 1040–1049. https://doi.org/10.1016/j.ijheatmasstransfer.2013.11.028.

[78] D.J. Lopez Penha, S. Stolz, J.G.M. Kuerten, M. Nordlund, A.K. Kuczaj, B.J. Geurts, Fully-developed conjugate heat transfer in porous media with uniform heating, Int J Heat Fluid Flow. 38 (2012) 94–106. https://doi.org/10.1016/j.ijheatfluidflow.2012.08.007.

[79] G. Yang, B. Weigand, A. Terzis, K. Weishaupt, R. Helmig, Numerical Simulation of Turbulent Flow and Heat Transfer in a Three-Dimensional Channel Coupled with Flow Through Porous Structures, Transp Porous Media. 122 (2018) 145–167. https://doi.org/10.1007/s11242-017-0995-9.

[80] M. Dejam, H. Hassanzadeh, Z. Chen, Semi-analytical solution for pressure transient analysis of a hydraulically fractured vertical well in a bounded dual-porosity reservoir, J Hydrol (Amst). 565 (2018) 289–301. https://doi.org/10.1016/j.jhydrol.2018.08.020.

[81] M. Dejam, H. Hassanzadeh, Z. Chen, Pre-Darcy Flow in Porous Media, Water Resour Res. 53 (2017) 8187–8210. https://doi.org/10.1002/2017WR021257.

[82] F. Kuwahara, M. Shirota, A. Nakayama, A numerical study of interfacial convective heat transfer coefficient in two-energy equation model for convection in porous media, Int J Heat Mass Transf. 44 (2001) 1153–1159. https://doi.org/10.1016/S0017-9310(00)00166-6.

[83] G. Gamrat, M. Favre-Marinet, S. le Person, Numerical study of heat transfer over banks of rods in small Reynolds number cross-flow, Int J Heat Mass Transf. 51 (2008) 853–864. https://doi.org/10.1016/j.ijheatmasstransfer.2007.04.038.

[84] F.E. Teruel, L. Díaz, Calculation of the interfacial heat transfer coefficient in porous media employing numerical simulations, Int J Heat Mass Transf. 60 (2013) 406–412. https://doi.org/10.1016/j.ijheatmasstransfer.2012.12.022.

[85] M. Torabi, G.P. Peterson, M. Torabi, N. Karimi, A thermodynamic analysis of forced convection through porous media using pore scale modeling, Int J Heat Mass Transf. 99 (2016) 303–316. https://doi.org/10.1016/j.ijheatmasstransfer.2016.03.127.

[86] T. Ozgumus, M. Mobedi, Effect of Pore to Throat Size Ratio on Interfacial Heat Transfer Coefficient of Porous Media, J Heat Transfer. 137 (2014) 012602-1–9. https://doi.org/10.1115/1.4028764.

[87] N.F. Jouybari, M. Maerefat, M.E. Nimvari, A pore scale study on turbulent combustion in porous media, Heat and Mass Transfer/Waerme- Und Stoffuebertragung. 52 (2016) 269–280. https://doi.org/10.1007/s00231-015-1547-x.

[88] Z. Wu, C. Caliot, G. Flamant, Z. Wang, Numerical simulation of convective heat transfer between air flow and ceramic foams to optimise volumetric solar air receiver performances, Int J Heat Mass Transf. 54 (2011) 1527–1537. https://doi.org/10.1016/j.ijheatmasstransfer.2010.11.037.

[89] S.-M. Kim, S.M. Ghiaasiaan, Numerical Modeling of Laminar Pulsating Flow in Porous Media, J Fluids Eng. 131 (2009) 041203-1–9. https://doi.org/10.1115/1.3089541.

[90] A.A. Alshare, P.J. Strykowski, T.W. Simon, Modeling of unsteady and steady fluid flow, heat transfer and dispersion in porous media using unit cell scale, Int J Heat Mass Transf. 53 (2010) 2294–2310. https://doi.org/10.1016/j.ijheatmasstransfer.2009.11.001.

[91] M.G. Pathak, S.M. Ghiaasiaan, Convective heat transfer and thermal dispersion during laminar pulsating flow in porous media, International Journal of Thermal Sciences. 50 (2011) 440–448. https://doi.org/10.1016/j.ijthermalsci.2010.11.002.

[92] M.G. Pathak, T.I. Mulcahey, S.M. Ghiaasiaan, Conjugate heat transfer during oscillatory laminar flow in porous media, Int J Heat Mass Transf. 66 (2013) 23–30. https://doi.org/10.1016/j.ijheatmasstransfer.2013.06.060.

[93] J. Chen, L. Yan, W. Song, D. Xu, Effect of heat and mass transfer on the combustion stability in catalytic micro-combustors, Appl Therm Eng. 131 (2018) 750–765. https://doi.org/10.1016/j.applthermaleng.2017.12.059.

[94] M.B. Saito, M.J.S. de Lemos, A Correlation for Interfacial Heat Transfer Coefficient for Turbulent Flow Over an Array of Square Rods, J Heat Transfer. 128 (2006) 444. https://doi.org/10.1115/1.2175150.

[95] M.J.S. de Lemos, Turbulence in porous media: modeling and applications, 2nd ed., Elsevier, 2012.

[96] M.B. Saito, M.J.S. de Lemos, Laminar heat transfer in a porous channel simulated with a two-energy equation model, International Communications in Heat and Mass Transfer. 36 (2009) 1002–1007. https://doi.org/10.1016/j.icheatmasstransfer.2009.07.008.

[97] M.B. Saito, M.J.S. de Lemos, A macroscopic two-energy equation model for turbulent flow and heat transfer in highly porous media, Int J Heat Mass Transf. 53 (2010) 2424–2433. https://doi.org/10.1016/j.ijheatmasstransfer.2010.01.041.

[98] A. Nakayama, K. Ando, C. Yang, Y. Sano, F. Kuwahara, J. Liu, A study on interstitial heat transfer in consolidated and unconsolidated porous media, Heat and Mass Transfer. 45 (2009) 1365–1372. https://doi.org/10.1007/s00231-009-0513-x.

[99] C. Pozrikidis, Introduction to Theoretical and Computational Fluid Dynamics., Oxford University Press, 2011.

[100] C.J. Chen, T.-S. Wung, Finite Analytic Solution of Convective Heat Transfer for Tube Arrays in Crossflow: Part II—Heat Transfer Analysis, J Heat Transfer. 111 (1989) 641–648. https://doi.org/10.1115/1.3250730.

[101] L. Christodoulou, N. Karimi, A. Cammarano, M. Paul, S. Navarro-Martinez, State prediction of an entropy wave advecting through a turbulent channel flow, J Fluid Mech. 882 (2020) A8. https://doi.org/10.1017/jfm.2019.799.

[102] K. Ogata, Y. Yang, Modern control engineering, Volume 17, NJ, Upper Saddle River: Pearson, 2010.

[103] K. Ogata, System dynamics, Volume 3, Upper Saddle River, NJ: Prentice Hall, 1998.

[104] N. Luhmann, Introduction to Systems Theory, Cambridge, 2013.

[105] K.R. McManus, T. Poinsot, S.M. Candel, A review of active control of combustion instabilities, Prog Energy Combust Sci. 19 (1993) 1–29. https://doi.org/10.1016/0360-1285(93)90020-F.

[106] N. Karimi, Response of a conical, laminar premixed flame to low amplitude acoustic forcing - A comparison between experiment and kinematic theories, Energy. 78 (2014) 490–500. https://doi.org/10.1016/j.energy.2014.10.036.

[107] M. Gopal, I.J. Nagrath, Control Systems Engineering, 5th Editio, Anshan Ltd, 2009.

[108] A. Banerjee, Automated Electronic Filter Design, Springer International Publishing, Cham, 2018. https://doi.org/10.1007/978-3-319-61554-7.

[109] A. Izadian, Fundamentals of Modern Electric Circuit Analysis and Filter Synthesis, Springer International Publishing, Cham, 2019. https://doi.org/10.1007/978-3-030-02484-0.

[110] S. Candel, Combustion dynamics and control: Progress and challenges, Proceedings of the Combustion Institute. 29 (2002) 1-28. https://doi.org/10.1016/S1540-7489(02)80007-4.

[111] T.C. Lieuwen, Unsteady Combustor Physics, Cambridge University Press, Cambridge, 2012. https://doi.org/10.1017/CBO9781139059961.

[112] H.S. Strogatz, Nonlinear Dynamics and Chaos: With Applications to Physics, Biology, Chemistry, and Engineering, Second Edition, 2nd Editio, CRC Press, 2015.

[113] W.H. Moase, M.J. Brear, C. Manzie, The forced response of choked nozzles and supersonic diffusers, J Fluid Mech. 585 (2007) 281–304. https://doi.org/10.1017/S0022112007006647.

[114] J. Yuan, B. Sundén, On continuum models for heat transfer in micro/nano-scale porous structures relevant for fuel cells, Int J Heat Mass Transf. 58 (2013) 441–456. https://doi.org/10.1016/j.ijheatmasstransfer.2012.11.075.

[115] Y. Wang, K.S. Chen, J. Mishler, S.C. Cho, X.C. Adroher, A review of polymer electrolyte membrane fuel cells: Technology, applications, and needs on fundamental research, Appl Energy. 88 (2011) 981–1007. https://doi.org/10.1016/j.apenergy.2010.09.030.

[116] N. Targui, H. Kahalerras, Analysis of a double pipe heat exchanger performance by use of porous baffles and pulsating flow, Energy Convers Manag. 76 (2013) 43–54. https://doi.org/10.1016/j.enconman.2013.07.022.

[117] A. Fattahi, S.M. Hosseinalipour, N. Karimi, On the dissipation and dispersion of entropy waves in heat transferring channel flows, Physics of Fluids. 29 (2017) 087104. https://doi.org/10.1063/1.4999046.

[118] A. Fattahi, S.M. Hosseinalipour, N. Karimi, Z. Saboohi, F. Ommi, On the response of a lean-premixed hydrogen combustor to acoustic and dissipative-dispersive entropy waves, Energy. 180 (2019) 272–291. https://doi.org/10.1016/j.energy.2019.04.202.

[119] M.M. Bhatti, A. Zeeshan, R. Ellahi, O.A. Bég, A. Kadir, Effects of coagulation on the two-phase peristaltic pumping of magnetized prandtl biofluid through an endoscopic annular geometry containing a porous medium, Chinese Journal of Physics. 58 (2019) 222–234. https://doi.org/10.1016/j.cjph.2019.02.004.

[120] R. Ellahi, S.M. Sait, N. Shehzad, Z. Ayaz, A hybrid investigation on numerical and analytical solutions of electro-magnetohydrodynamics flow of nanofluid through porous media with entropy generation, Int J Numer Methods Heat Fluid Flow. 30 (2019) 834–854. https://doi.org/10.1108/HFF-06-2019-0506.

[121] M. Torabi, N. Karimi, K. Zhang, Heat transfer and second law analyses of forced convection in a channel partially filled by porous media and featuring internal heat sources, Energy. 93 (2015) 106–127. https://doi.org/10.1016/j.energy.2015.09.010.

[122] C. Dickson, M. Torabi, N. Karimi, First and second law analyses of nanofluid forced convection in a partially-filled porous channel – The effects of local thermal non-equilibrium and internal heat sources, Appl Therm Eng. 103 (2016) 459–480. https://doi.org/10.1016/j.applthermaleng.2016.04.095.

[123] P. Forooghi, M. Abkar, M. Saffar-Avval, Steady and Unsteady Heat Transfer in a Channel Partially Filled with Porous Media Under Thermal Non-Equilibrium Condition, Transp Porous Media. 86 (2011) 177–198. https://doi.org/10.1007/s11242-010-9615-7.

[124] J. Yang, Q. Wang, M. Zeng, A. Nakayama, Computational study of forced convective heat transfer in structured packed beds with spherical or ellipsoidal particles, Chem Eng Sci. 65 (2010) 726–738. https://doi.org/10.1016/j.ces.2009.09.026.

[125] M.B. Saito, M.J.S. de Lemos, A macroscopic two-energy equation model for turbulent flow and heat transfer in highly porous media, Int J Heat Mass Transf. 53 (2010) 2424–2433. https://doi.org/10.1016/j.ijheatmasstransfer.2010.01.041.

[126] N.F. Jouybari, M. Maerefat, M.E. Nimvari, A Macroscopic Turbulence Model for Reacting Flow in Porous Media, Transp Porous Media. 106 (2015) 355–381. https://doi.org/10.1007/s11242-014-0405-5.

[127] D.G.P. Guthrie, M. Torabi, N. Karimi, Combined heat and mass transfer analyses in catalytic microreactors partially filled with porous material - The influences of nanofluid and different porous-fluid interface models, International Journal of Thermal Sciences. 140 (2019) 96–113. https://doi.org/10.1016/j.ijthermalsci.2019.02.037.

[128] A. Saeed, N. Karimi, G. Hunt, M. Torabi, On the influences of surface heat release and thermal radiation upon transport in catalytic porous microreactors—A novel porous-solid interface model, Chemical Engineering and Processing - Process Intensification. 143 (2019) 107602. https://doi.org/10.1016/j.cep.2019.107602.

[129] G. Hunt, N. Karimi, M. Torabi, Two-dimensional analytical investigation of coupled heat and mass transfer and entropy generation in a porous, catalytic microreactor, Int J Heat Mass Transf. 119 (2018) 372–391. https://doi.org/10.1016/j.ijheatmasstransfer.2017.11.118.

[130] D.A. Nield, A. Bejan, Convection in porous media, 5th Editio, 2017.

[131] M. Fujii, T. Fujii, T. Nagata, A numerical analysis of laminar flow and heat transfer of air in an in-line tube bank, Numerical Heat Transfer. 7 (1984) 89–102. https://doi.org/10.1080/01495728408961813.

[132] H. Ma, D.W. Ruth, The microscopic analysis of high forchheimer number flow in porous media, Transp Porous Media. 13 (1993) 139–160. https://doi.org/10.1007/BF00654407.

[133] A. Nakayama, F. Kuwahara, T. Umemoto, T. Hayashi, Heat and fluid flow within an anisotropic porous medium, J Heat Transfer. 124 (2002) 746–753. https://doi.org/10.1115/1.1481355.

[134] M.B. Saito, M.J.S. de Lemos, Interfacial heat transfer coefficient for non-equilibrium convective transport in porous media, International Communications in Heat and Mass Transfer. 32 (2005) 666–676. https://doi.org/10.1016/j.icheatmasstransfer.2004.06.013.

[135] A. Nakayama, F. Kuwahara, T. Hayashi, Numerical modelling for three-dimensional heat and fluid flow through a bank of cylinders in yaw, J Fluid Mech. 498 (2004) 139–159. https://doi.org/10.1017/S0022112003006712.

[136] T.I. Mulcahey, M.G. Pathak, S.M. Ghiaasiaan, The effect of flow pulsation on drag and heat transfer in an array of heated square cylinders,

International Journal of Thermal Sciences. 64 (2013) 105–120. https://doi.org/10.1016/j.ijthermalsci.2012.08.017.

[137] G. Imani, M. Maerefat, K. Hooman, Pore-Scale Numerical Experiment on the Effect of the Pertinent Parameters on Heat Flux Splitting at the Boundary of a Porous Medium, Transp Porous Media. 98 (2013) 631–649. https://doi.org/10.1007/s11242-013-0164-8.

[138] F.E. Teruel, Entrance effect on the interfacial heat transfer and the thermal dispersion in laminar flows through porous media, International Journal of Thermal Sciences. 104 (2016) 172–185. https://doi.org/10.1016/j.ijthermalsci.2016.01.005.

[139] A. Jafarizade, M. Panjepour, M. Meratian, M. Davazdah Emami, Numerical Simulation of Gas/Solid Heat Transfer in Metallic Foams: A General Correlation for Different Porosities and Pore Sizes, Transp Porous Media. 127 (2019) 481–506. https://doi.org/10.1007/s11242-018-1208-x.

[140] S. Afshari, S.H. Hejazi, A. Kantzas, Pore-level modeling of effective longitudinal thermal dispersion in non-isothermal flows through granular porous media, Chem Eng Sci. 199 (2019) 451–462. https://doi.org/10.1016/j.ces.2019.01.028.

[141] M. Mottaghi, S. Kuhn, Numerical investigation of well-structured porous media in a milli-scale tubular reactor, Chem Eng Sci. 208 (2019) 115146-1–13. https://doi.org/10.1016/j.ces.2019.08.004.

[142] H.E. Ahmed, O.T. Fadhil, W.A. Salih, Heat transfer and fluid flow characteristics of tubular channel partially filled with grooved metal foams, International Communications in Heat and Mass Transfer. 108 (2019) 104336. https://doi.org/10.1016/j.icheatmasstransfer.2019.104336.

[143] M. Chakkingal, J. de Geus, S. Kenjereš, I. Ataei-Dadavi, M.J. Tummers, C.R. Kleijn, Assisting and opposing mixed convection with conjugate heat transfer in a differentially heated cavity filled with coarse-grained porous

media, International Communications in Heat and Mass Transfer. 111 (2020) 104457. https://doi.org/10.1016/j.icheatmasstransfer.2019.104457.

[144] J. Qin, Z.G. Xu, Z.Y. Liu, F. Lu, C.Y. Zhao, Pore-scale investigation on flow boiling heat transfer mechanisms in open-cell metal foam by LBM, International Communications in Heat and Mass Transfer. 110 (2020) 104418. https://doi.org/10.1016/j.icheatmasstransfer.2019.104418.

[145] Á.L. de Bortoli, G.S.L. Andreis, F.N. Pereira, Equations of Fluid Dynamics, in: Modeling and Simulation of Reactive Flows, 2015: pp. 35–51. https://doi.org/10.1016/b978-0-12-802974-9.00003-9.

[146] H.A. Stone, C. Duprat, Low-Reynolds-Number Flows, in: Fluid-Structure Interactions in Low-Reynolds-Number Flows, 2016: pp. 25–77.

[147] O. Mahian, L. Kolsi, M. Amani, P. Estellé, G. Ahmadi, C. Kleinstreuer, J.S. Marshall, M. Siavashi, R.A. Taylor, H. Niazmand, S. Wongwises, T. Hayat, A. Kolanjiyil, A. Kasaeian, I. Pop, Recent advances in modeling and simulation of nanofluid flows-Part I: Fundamentals and theory, Phys Rep. 790 (2019) 1–48. https://doi.org/10.1016/j.physrep.2018.11.004.

[148] O. Mahian, L. Kolsi, M. Amani, P. Estellé, G. Ahmadi, C. Kleinstreuer, J.S. Marshall, R.A. Taylor, E. Abu-Nada, S. Rashidi, H. Niazmand, S. Wongwises, T. Hayat, A. Kasaeian, I. Pop, Recent advances in modeling and simulation of nanofluid flows—Part II: Applications, Phys Rep. 791 (2019) 1–59. https://doi.org/10.1016/j.physrep.2018.11.003.

[149] J. Cao, N. Djilali, Numerical Modeling of PEM Fuel Cells Under Partially Hydrated Membrane Conditions, J Energy Resour Technol. 127 (2005) 26–36. https://doi.org/10.1115/1.1825048.

[150] V. Dokhani, M. Yu, C. Gao, J. Bloys, Investigating the Relation Between Sorption Tendency and Hydraulic Properties of Shale Formations, J Energy Resour Technol. 140 (2018). https://doi.org/10.1115/1.4037480.

[151] H. Movahedi, M. Vasheghani Farahani, M. Masihi, Development of a Numerical Model for Single- and Two-Phase Flow Simulation in Perforated Porous Media, J Energy Resour Technol. 142 (2020). https://doi.org/10.1115/1.4044574.

[152] N. Shahangian, D. Honnery, J. Ghojel, The Role of Porous Media in Homogenization of High Pressure Diesel Fuel Spray Combustion, J Energy Resour Technol. 136 (2014). https://doi.org/10.1115/1.4024717.

[153] X. Meng, D. Yang, Critical Review of Stabilized Nanoparticle Transport in Porous Media, J Energy Resour Technol. 141 (2019). https://doi.org/10.1115/1.4041929.

[154] G. Hunt, M. Torabi, L. Govone, N. Karimi, A. Mehdizadeh, Two-dimensional heat and mass transfer and thermodynamic analyses of porous microreactors with Soret and thermal radiation effects—An analytical approach, Chemical Engineering and Processing - Process Intensification. 126 (2018) 190–205. https://doi.org/10.1016/j.cep.2018.02.025.

[155] N. Karimi, D. Agbo, A. Talat Khan, P.L. Younger, On the effects of exothermicity and endothermicity upon the temperature fields in a partially-filled porous channel, International Journal of Thermal Sciences. 96 (2015) 128–148. https://doi.org/10.1016/j.ijthermalsci.2015.05.002.

[156] G. Hunt, N. Karimi, M. Torabi, Two-dimensional analytical investigation of coupled heat and mass transfer and entropy generation in a porous, catalytic microreactor, Int J Heat Mass Transf. 119 (2018) 372–391. https://doi.org/10.1016/j.ijheatmasstransfer.2017.11.118.

[157] R. Habib, B. Yadollahi, N. Karimi, M.H. Doranegard, On the unsteady forced convection in porous media subject to inlet flow disturbances-A pore-scale analysis, International Communications in Heat and Mass Transfer. 116 (2020) 104639. https://doi.org/10.1016/j.icheatmasstransfer.2020.104639.

[158] T. Lu, P.X. Jiang, Z.J. Guo, Y.W. Zhang, H. Li, Large-eddy simulations (LES) of temperature fluctuations in a mixing tee with/without a porous medium,

Int J Heat Mass Transf. 53 (2010) 4458–4466. https://doi.org/10.1016/j.ijheatmasstransfer.2010.07.001.

[159] S.Y. Kim, B.H. Kang, J.M. Hyun, Heat transfer from pulsating flow in a channel filled with porous media, Int J Heat Mass Transf. 37 (1994) 2025–2033. https://doi.org/10.1016/0017-9310(94)90304-2.

[160] Z. Guo, S.Y. Kim, H.J. Sung, Pulsating flow and heat transfer in a pipe partially filled with a porous medium, Int J Heat Mass Transf. 40 (1997) 4209–4218. https://doi.org/10.1016/S0017-9310(97)00035-5.

[161] R. Bhargava, H.S. Takhar, S. Rawat, T.A. Bég, O.A. Bég, Finite Element Solutions for Non-Newtonian Pulsatile Flow in a Non-Darcian Porous Medium Conduit, Nonlinear Analysis: Modelling and Control. 12 (2007) 317–327. https://doi.org/10.15388/na.2007.12.3.14690.

[162] P.C. Huang, C.F. Yang, Analysis of pulsating convection from two heat sources mounted with porous blocks, Int J Heat Mass Transf. 51 (2008) 6294–6311. https://doi.org/10.1016/j.ijheatmasstransfer.2008.04.044.

[163] H. Dhahri, K. Slimi, S. Ben Nasrallah, Entropy generation for pulsating flow in a composite fluid/porous system, J Porous Media. 11 (2008) 557–574. https://doi.org/10.1615/JPorMedia.v11.i6.40.

[164] M. Ghafarian, D. Mohebbi-Kalhori, J. Sadeghi, Analysis of heat transfer in oscillating flow through a channel filled with metal foam using computational fluid dynamics, International Journal of Thermal Sciences. 66 (2013) 42–50. https://doi.org/10.1016/j.ijthermalsci.2012.11.008.

[165] A. Zaman, N. Ali, M. Sajid, Numerical simulation of pulsatile flow of blood in a porous-saturated overlapping stenosed artery, Math Comput Simul. 134 (2017) 1–16. https://doi.org/10.1016/j.matcom.2016.09.008.

[166] M.M. Torabi, G.P. Peterson, M.M. Torabi, N. Karimi, A thermodynamic analysis of forced convection through porous media using pore scale

modeling, Int J Heat Mass Transf. 99 (2016) 303–316. https://doi.org/10.1016/j.ijheatmasstransfer.2016.03.127.

[167] G. Hunt, N. Karimi, M. Torabi, Analytical investigation of heat transfer and classical entropy generation in microreactors – The influences of exothermicity and asymmetry, Appl Therm Eng. 119 (2017) 403–424. https://doi.org/10.1016/j.applthermaleng.2017.03.057.

[168] R. Habib, N. Karimi, B. Yadollahi, M. Hossein, L.K.B. Li, A pore-scale assessment of the dynamic response of forced convection in porous media to inlet flow modulations, Int J Heat Mass Transf. 153 (2020) 119657. https://doi.org/10.1016/j.ijheatmasstransfer.2020.119657.

[169] R. Rosa, The Role of Synthetic Fuels for a Carbon Neutral Economy, C (Basel). 3 (2017) 11. https://doi.org/10.3390/c3020011.

[170] L. Wang, N. Karimi, M.C. Paul, Gas-phase transport and entropy generation during transient combustion of single biomass particle in varying oxygen and nitrogen atmospheres, Int J Hydrogen Energy. 43 (2018) 8506–8523. https://doi.org/10.1016/j.ijhydene.2018.03.074.

[171] L. Christodoulou, L. Kabiraj, A. Saurabh, N. Karimi, Characterizing the signature of flame flashback precursor through recurrence analysis, Chaos: An Interdisciplinary Journal of Nonlinear Science. 26 (2016) 013110. https://doi.org/10.1063/1.4940154.

[172] N. Karimi, S. McGrath, P. Brown, J. Weinkauff, A. Dreizler, Generation of Adverse Pressure Gradient in the Circumferential Flashback of a Premixed Flame, Flow Turbul Combust. 97 (2016) 663–687. https://doi.org/10.1007/s10494-015-9695-0.

[173] S. Rashidi, F. Hormozi, M.H. Doranehgard, Abilities of porous materials for energy saving in advanced thermal systems, J Therm Anal Calorim. (2020). https://doi.org/10.1007/s10973-020-09880-9.

[174] P. Gholamalipour, M. Siavashi, M.H. Doranehgard, Eccentricity effects of heat source inside a porous annulus on the natural convection heat transfer and entropy generation of Cu-water nanofluid, International Communications in Heat and Mass Transfer. 109 (2019) 104367. https://doi.org/10.1016/j.icheatmasstransfer.2019.104367.

[175] O. Mahian, L. Kolsi, M. Amani, P. Estellé, G. Ahmadi, C. Kleinstreuer, J.S. Marshall, M. Siavashi, R.A. Taylor, H. Niazmand, S. Wongwises, T. Hayat, A. Kolanjiyil, A. Kasaeian, I. Pop, Recent advances in modeling and simulation of nanofluid flows-Part I: Fundamentals and theory, Phys Rep. 790 (2019) 1–48. https://doi.org/10.1016/j.physrep.2018.11.004.

[176] A. Izadi, M. Siavashi, H. Rasam, Q. Xiong, MHD enhanced nanofluid mediated heat transfer in porous metal for CPU cooling, Appl Therm Eng. 168 (2020) 114843. https://doi.org/10.1016/j.applthermaleng.2019.114843.

[177] S. Mößbauer, O. Pickenäcker, K. Pickenäcker, Application of the porous burner technology in energy- and heat engineering., in: 5th International Conference on Technologies and Combustion for a Clean Environment (Clean Air V), 1999: pp. 519–523.

[178] N. Delalic, D. Mulahasanovic, E.N. Ganic, Porous media compact heat exchanger unit - experiment and analysis, Exp Therm Fluid Sci. 28 (2004) 185–192. https://doi.org/10.1016/S0894-1777(03)00038-4.

[179] C. Mao, Y. Feng, X. Wang, G. Ren, Review on research achievements of biogas from anaerobic digestion, Renewable and Sustainable Energy Reviews. 45 (2015) 540–555. https://doi.org/10.1016/j.rser.2015.02.032.

[180] K. Göransson, U. Söderlind, J. He, W. Zhang, Review of syngas production via biomass DFBGs, Renewable and Sustainable Energy Reviews. 15 (2011) 482–492. https://doi.org/10.1016/j.rser.2010.09.032.

[181] G. Hunt, N. Karimi, B. Yadollahi, M. Torabi, The effects of exothermic catalytic reactions upon combined transport of heat and mass in porous

microreactors, Int J Heat Mass Transf. 134 (2019) 1227–1249. https://doi.org/10.1016/j.ijheatmasstransfer.2019.02.015.

[182] H. Liu, D. Wu, M. Xie, H. Liu, Z. Xu, Experimental and numerical study on the lean premixed filtration combustion of propane/air in porous medium, Appl Therm Eng. 150 (2019) 445–455. https://doi.org/10.1016/j.applthermaleng.2018.12.155.

[183] J. He, Z. Chen, X. Jiang, C. Leng, Combustion characteristics of blast furnace gas in porous media burner, Appl Therm Eng. 160 (2019) 113970. https://doi.org/10.1016/j.applthermaleng.2019.113970.

[184] Y. Liu, D. Ning, A. Fan, H. Yao, Experimental and numerical investigations on flame stability of methane/air mixtures in mesoscale combustors filled with fibrous porous media, Energy Convers Manag. 123 (2016) 402–409. https://doi.org/10.1016/j.enconman.2016.06.058.

[185] A.C. Terracciano, S. De Oliveira, D. Vazquez-Molina, F.J. Uribe-Romo, S.S. Vasu, N. Orlovskaya, Effect of catalytically active Ce0.8Gd0.2O1.9 coating on the heterogeneous combustion of methane within MgO stabilized ZrO2 porous ceramics, Combust Flame. 180 (2017) 32–39. https://doi.org/10.1016/j.combustflame.2017.02.019.

[186] K. Xu, M. Liu, P. Zhao, Stability of lean combustion in mini-scale porous media combustor with heat recuperation, Chemical Engineering and Processing: Process Intensification. 50 (2011) 608–613. https://doi.org/10.1016/j.cep.2011.03.001.

[187] M.M. Kamal, A.A. Mohamad, Combustion in porous media, Proceedings of the Institution of Mechanical Engineers, Part A: Journal of Power and Energy. 220 (2006) 487–508. https://doi.org/10.1243/09576509JPE169.

[188] D. Ingham, A. Bejan, E. Mamut, I. Pop, Emerging Technologies and Techniques in Porous Media, 2012.

[189] V. Bubnovich, M. Toledo, L. Henríquez, C. Rosas, J. Romero, Flame stabilization between two beds of alumina balls in a porous burner, Appl Therm Eng. 30 (2010) 92–95. https://doi.org/10.1016/j.applthermaleng.2009.04.001.

[190] M.A. Mujeebu, M.Z. Abdullah, A.A. Mohamad, Development of energy efficient porous medium burners on surface and submerged combustion modes, Energy. 36 (2011) 5132–5139. https://doi.org/10.1016/j.energy.2011.06.014.

[191] C. Keramiotis, B. Stelzner, D. Trimis, M. Founti, Porous burners for low emission combustion: An experimental investigation, Energy. 45 (2012) 213–219. https://doi.org/10.1016/j.energy.2011.12.006.

[192] M.D. Robayo, B. Beaman, B. Hughes, B. Delose, N. Orlovskaya, R.H. Chen, Perovskite catalysts enhanced combustion on porous media, Energy. 76 (2014) 477–486. https://doi.org/10.1016/j.energy.2014.08.045.

[193] M. Shafiey Dehaj, R. Ebrahimi, M. Shams, M. Farzaneh, Experimental analysis of natural gas combustion in a porous burner, Exp Therm Fluid Sci. 84 (2017) 134–143. https://doi.org/10.1016/j.expthermflusci.2017.01.023.

[194] S.A. Ghorashi, S.A. Hashemi, S.M. Hashemi, M. Mollamahdi, Experimental study on pollutant emissions in the novel combined porous-free flame burner, Energy. 162 (2018) 517–525. https://doi.org/10.1016/j.energy.2018.08.005.

[195] A. Chaelek, U.M. Grare, S. Jugjai, Self-aspirating/air-preheating porous medium gas burner, Appl Therm Eng. 153 (2019) 181–189. https://doi.org/10.1016/j.applthermaleng.2019.02.109.

[196] S. Devi, N. Sahoo, P. Muthukumar, Combustion of biogas in Porous Radiant Burner: Low emission combustion, Energy Procedia. 158 (2019) 1116–1121. https://doi.org/10.1016/j.egypro.2019.01.276.

[197] S. Devi, N. Sahoo, P. Muthukumar, Experimental studies on biogas combustion in a novel double layer inert Porous Radiant Burner, Renew Energy. 149 (2020) 1040–1052. https://doi.org/10.1016/j.renene.2019.10.092.

[198] R. Habib, B. Yadollahi, N. Karimi, A Pore-Scale Investigation of the Transient Response of Forced Convection in Porous Media to Inlet Ramp Inputs, J Energy Resour Technol. 142 (2020) 1–14. https://doi.org/10.1115/1.4047968.

[199] M.J. Moran, H.N. Shapiro, D.D. Boettner, M.B. Bailey, Fundamentals of Engineering Thermodynamics, 7th ed., 2011.

[200] S.R. Turns, An Introduction to Combustion: Concepts and Applications, 2nd ed., McGraw Hill, 2000.

[201] Y. Kazemian, S. Rashidi, J.A. Esfahani, O. Samimi-Abianeh, Effects of grains shapes of porous media on combustion onset—A numerical simulation using Lattice Boltzmann method, Computers & Mathematics with Applications. (2019). https://doi.org/10.1016/j.camwa.2019.10.015.

[202] Energy Supply - International Energy Agency, (2020). https://www.iea.org/data-and-statistics (accessed December 25, 2020).

[203] Z. labidine Messaoudani, F. Rigas, M.D. Binti Hamid, C.R. Che Hassan, Hazards, safety and knowledge gaps on hydrogen transmission via natural gas grid: A critical review, Int J Hydrogen Energy. 41 (2016) 17511–17525. https://doi.org/10.1016/j.ijhydene.2016.07.171.

[204] I.A. Gondal, Hydrogen integration in power-to-gas networks, Int J Hydrogen Energy. 44 (2019) 1803–1815. https://doi.org/10.1016/j.ijhydene.2018.11.164.

[205] M. Ozturk, I. Dincer, Development of renewable energy system integrated with hydrogen and natural gas subsystems for cleaner combustion, J Nat Gas Sci Eng. 83 (2020) 103583. https://doi.org/10.1016/j.jngse.2020.103583.

[206] Y.S. Sanusi, E.M.A. Mokheimer, M.R. Shakeel, Z. Abubakar, M.A. Habib, Oxy-Combustion of Hydrogen-Enriched Methane: Experimental Measurements and Analysis, Energy & Fuels. 31 (2017) 2007–2016. https://doi.org/10.1021/acs.energyfuels.6b03118.

[207] A. Şanlı, İ.T. Yılmaz, M. Gümüş, Experimental Evaluation of Performance and Combustion Characteristics in a Hydrogen–Methane Port Fueled Diesel Engine at Different Compression Ratios, Energy & Fuels. 34 (2020) 2272–2283. https://doi.org/10.1021/acs.energyfuels.9b03033.

[208] S.M. Mousavi, R. Kamali, F. Sotoudeh, N. Karimi, I.-S. Jeung, Numerical Investigation of the Effects of Swirling Hot Co-Flow on MILD Combustion of a Hydrogen–Methane Blend, J Energy Resour Technol. 142 (2020) 112301. https://doi.org/10.1115/1.4047251.

[209] S.M. Mousavi, R. Kamali, F. Sotoudeh, N. Karimi, B.J. Lee, Numerical Investigation of the Plasma-Assisted MILD Combustion of a CH4/H2 Fuel Blend Under Various Working Conditions, J Energy Resour Technol. 143 (2021) 062302. https://doi.org/10.1115/1.4048507.

[210] M.J. Lázaro, J.L. Pinilla, R. Utrilla, I. Suelves, R. Moliner, F. Moreno, M. Muñoz, H2 − CH4 Mixtures Produced by Carbon-Catalyzed Methane Decomposition as a Fuel for Internal Combustion Engines, Energy & Fuels. 24 (2010) 3340–3345. https://doi.org/10.1021/ef901504x.

[211] H. Averfalk, S. Werner, Novel low temperature heat distribution technology, Energy. 145 (2018) 526–539. https://doi.org/10.1016/j.energy.2017.12.157.

[212] N. Karimi, S. McGrath, P. Brown, J. Weinkauff, A. Dreizler, Generation of Adverse Pressure Gradient in the Circumferential Flashback of a Premixed Flame, Flow Turbul Combust. 97 (2016) 663–687. https://doi.org/10.1007/s10494-015-9695-0.

[213] G. Hunt, N. Karimi, B. Yadollahi, M. Torabi, The effects of exothermic catalytic reactions upon combined transport of heat and mass in porous

microreactors, Int J Heat Mass Transf. 134 (2019) 1227–1249. https://doi.org/10.1016/j.ijheatmasstransfer.2019.02.015.

[214] F.A. Williams, A review of flame extinction, Fire Saf J. 3 (1981) 163–175. https://doi.org/10.1016/0379-7112(81)90041-2.

[215] R. Huang, L. Cheng, K. Qiu, C. Zheng, Z. Luo, Low-Calorific Gas Combustion in a Two-Layer Porous Burner, Energy & Fuels. 30 (2016) 1364–1374. https://doi.org/10.1021/acs.energyfuels.5b02399.

[216] N. Djordjevic, P. Habisreuther, N. Zarzalis, Experimental Study on the Basic Phenomena of Flame Stabilization Mechanism in a Porous Burner for Premixed Combustion Application, Energy & Fuels. 26 (2012) 6705–6719. https://doi.org/10.1021/ef3013008.

[217] S. Saraji, L. Goual, M. Piri, Adsorption of Asphaltenes in Porous Media under Flow Conditions, Energy & Fuels. 24 (2010) 6009–6017. https://doi.org/10.1021/ef100881k.

[218] T.C. Lieuwen, Unsteady Combustor Physics, Cambridge University Press, Cambridge, 2012. https://doi.org/10.1017/CBO9781139059961.

[219] M. Toledo, F. Gracia, S. Caro, J. Gómez, V. Jovicic, Hydrocarbons conversion to syngas in inert porous media combustion, Int J Hydrogen Energy. 41 (2016) 5857–5864. https://doi.org/10.1016/j.ijhydene.2016.02.065.

[220] M.A. Mujeebu, M.Z. Abdullah, M.Z.A. Bakar, A.A. Mohamad, M.K. Abdullah, Applications of porous media combustion technology – A review, Appl Energy. 86 (2009) 1365–1375. https://doi.org/10.1016/j.apenergy.2009.01.017.

[221] M.A. Mujeebu, M.Z. Abdullah, M.Z.A. Bakar, A.A. Mohamad, M.K. Abdullah, A review of investigations on liquid fuel combustion in porous inert media, Prog Energy Combust Sci. 35 (2009) 216–230. https://doi.org/10.1016/j.pecs.2008.11.001.

[222] P. Gentillon, J. Southcott, Q.N. Chan, R.A. Taylor, Stable flame limits for optimal radiant performance of porous media reactors for thermophotovoltaic applications using packed beds of alumina, Appl Energy. 229 (2018) 736–744. https://doi.org/10.1016/j.apenergy.2018.08.048.

[223] Q. Peng, W. Yang, J. E, H. Xu, Z. Li, W. Yu, Y. Tu, Y. Wu, Experimental investigation on premixed hydrogen/air combustion in varied size combustors inserted with porous medium for thermophotovoltaic system applications, Energy Convers Manag. 200 (2019) 112086. https://doi.org/10.1016/j.enconman.2019.112086.

[224] H. Wang, C. Wei, P. Zhao, T. Ye, Experimental study on temperature variation in a porous inert media burner for premixed methane air combustion, Energy. 72 (2014) 195–200. https://doi.org/10.1016/j.energy.2014.05.024.

[225] R. Habib, B. Yadollahi, A. Saeed, M.H. Doranehgard, L.K.B. Li, N. Karimi, Unsteady ultra-lean combustion of methane and biogas in a porous burner – An experimental study, Appl Therm Eng. 182 (2021) 116099. https://doi.org/10.1016/j.applthermaleng.2020.116099.

[226] N.A. Kakutkina, A.A. Korzhavin, M. Mbarawa, Filtration combustion of hydrogen-air, propane-air, and methane-air mixtures in inert porous media, Combust Explos Shock Waves. 42 (2006) 372–383. https://doi.org/10.1007/s10573-006-0065-z.

[227] S.K. Alavandi, A.K. Agrawal, Experimental study of combustion of hydrogen-syngas/methane fuel mixtures in a porous burner, Int J Hydrogen Energy. 33 (2008) 1407–1415. https://doi.org/10.1016/j.ijhydene.2007.12.005.

[228] S. Gauthier, E. Lebas, D. Baillis, SFGP 2007 - Natural Gas/Hydrogen Mixture Combustion in a Porous Radiant Burner, International Journal of Chemical Reactor Engineering. 5 (2007) 1–8. https://doi.org/10.2202/1542-6580.1650.

[229] Q. Peng, W. Yang, J. E, H. Xu, Z. Li, W. Yu, Y. Tu, Y. Wu, Experimental investigation on premixed hydrogen/air combustion in varied size combustors inserted with porous medium for thermophotovoltaic system applications, Energy Convers Manag. 200 (2019) 112086. https://doi.org/10.1016/j.enconman.2019.112086.

[230] C.E. Arrieta, A.M. García, A.A. Amell, Experimental study of the combustion of natural gas and high-hydrogen content syngases in a radiant porous media burner, Int J Hydrogen Energy. 42 (2017) 12669–12680. https://doi.org/10.1016/j.ijhydene.2017.03.078.

[231] G.J. Rørtveit, K. Zepter, Ø. Skreiberg, M. Fossum, J.E. Hustad, A comparison of low-NOx burners for combustion of methane and hydrogen mixtures, Proceedings of the Combustion Institute. 29 (2002) 1123–1129. https://doi.org/10.1016/S1540-7489(02)80142-0.

[232] M. Ferrarotti, W. de Paepe, A. Parente, Reactive structures and NOx emissions of methane/hydrogen mixtures in flameless combustion, Int J Hydrogen Energy. 46 (2021) 34018–34045. https://doi.org/10.1016/j.ijhydene.2021.07.161.